Numerical study on viscoelastic Rayleigh-Bénard convection

Xin Zheng

N°d'ordre NNT : 2021LYSEI088

THESE de DOCTORAT DE L'UNIVERSITE DE LYON
opérée au sein de
L'INSA LYON

Ecole Doctorale N° EDA162
Mécanique, Energétique, Génie Civil, Acoustique

Spécialité/ discipline de doctorat : **Thermique Energétique**

Soutenue publiquement le 09/12/2021, par :
Xin ZHENG

Numerical Study on Viscoelastic Rayleigh-Bénard Convection

Devant le jury composé de :

Nouar, Chérif/Directeur de recherche/ENSEM, Nancy	Rapporteur
Castelain, Cathy/Directrice de recherche/Université de Nantes	Rapporteur
Le Quéré, Patrick/Directeur de recherche émérite/Université Paris-Saclay	Examinateur
XIN, Shihe/Professeur des Universités/INSA-LYON	Directeur de thèse
BOUTAOUS, M'hamed/Maître de Conférences/INSA-LYON	Co-directeur de thèse

Département FEDORA – INSA Lyon - Ecoles Doctorales

SIGLE	ECOLE DOCTORALE	NOM ET COORDONNEES DU RESPONSABLE
CHIMIE	**CHIMIE DE LYON** **https://www.edchimie-lyon.fr** Sec. : Renée EL MELHEM Bât. Blaise PASCAL, 3e étage secretariat@edchimie-lyon.fr	**M. Stéphane DANIELE** C2P2-CPE LYON-UMR 5265 Bâtiment F308, BP 2077 43 Boulevard du 11 novembre 1918 69616 Villeurbanne **directeur@edchimie-lyon.fr**
E.E.A.	**ÉLECTRONIQUE, ÉLECTROTECHNIQUE, AUTOMATIQUE** **https://edeea.universite-lyon.fr** Sec. : Stéphanie CAUVIN Bâtiment Direction INSA Lyon Tél : 04.72.43.71.70 secretariat.edeea@insa-lyon.fr	**M. Philippe DELACHARTRE** INSA LYON Laboratoire CREATIS Bâtiment Blaise Pascal, 7 avenue Jean Capelle 69621 Villeurbanne CEDEX Tél : 04.72.43.88.63 **philippe.delachartre@insa-lyon.fr**
E2M2	**ÉVOLUTION, ÉCOSYSTÈME, MICROBIOLOGIE, MODÉLISATION** **http://e2m2.universite-lyon.fr** Sec. : Sylvie ROBERJOT Bât. Atrium, UCB Lyon 1 Tél : 04.72.44.83.62 secretariat.e2m2@univ-lyon1.fr	**M. Philippe NORMAND** Université Claude Bernard Lyon 1 UMR 5557 Lab. d'Ecologie Microbienne Bâtiment Mendel 43, boulevard du 11 Novembre 1918 69 622 Villeurbanne CEDEX **philippe.normand@univ-lyon1.fr**
EDISS	**INTERDISCIPLINAIRE SCIENCES-SANTÉ** **http://ediss.universite-lyon.fr** Sec. : Sylvie ROBERJOT Bât. Atrium, UCB Lyon 1 Tél : 04.72.44.83.62 secretariat.ediss@univ-lyon1.fr	**Mme Sylvie RICARD-BLUM** Institut de Chimie et Biochimie Moléculaires et Supramoléculaires (ICBMS) - UMR 5246 CNRS - Université Lyon 1 Bâtiment Raulin - 2ème étage Nord 43 Boulevard du 11 novembre 1918 69622 Villeurbanne Cedex Tél : +33(0)4 72 44 82 32 **sylvie.ricard-blum@univ-lyon1.fr**
INFOMATHS	**INFORMATIQUE ET MATHÉMATIQUES** **http://edinfomaths.universite-lyon.fr** Sec. : Renée EL MELHEM Bât. Blaise PASCAL, 3e étage Tél : 04.72.43.80.46 infomaths@univ-lyon1.fr	**M. Hamamache KHEDDOUCI** Université Claude Bernard Lyon 1 Bât. Nautibus 43, Boulevard du 11 novembre 1918 69 622 Villeurbanne Cedex France Tél : 04.72.44.83.69 **hamamache.kheddouci@univ-lyon1.fr**
Matériaux	**MATÉRIAUX DE LYON** **http://ed34.universite-lyon.fr** Sec. : Yann DE ORDENANA Tél : 04.72.18.62.44 yann.de-ordenana@ec-lyon.fr	**M. Stéphane BENAYOUN** Ecole Centrale de Lyon Laboratoire LTDS 36 avenue Guy de Collongue 69134 Ecully CEDEX Tél : 04.72.18.64.37 **stephane.benayoun@ec-lyon.fr**
MEGA	**MÉCANIQUE, ÉNERGÉTIQUE, GÉNIE CIVIL, ACOUSTIQUE** **http://edmega.universite-lyon.fr** Sec. : Stéphanie CAUVIN Tél : 04.72.43.71.70 Bâtiment Direction INSA Lyon mega@insa-lyon.fr	**M. Jocelyn BONJOUR** INSA Lyon Laboratoire CETHIL Bâtiment Sadi-Carnot 9, rue de la Physique 69621 Villeurbanne CEDEX **jocelyn.bonjour@insa-lyon.fr**
ScSo	**ScSo*** **https://edsciencessociales.universite-lyon.fr** Sec. : Mélina FAVETON INSA : J.Y. TOUSSAINT Tél : 04.78.69.77.79 melina.faveton@univ-lyon2.fr	**M. Christian MONTES** Université Lumière Lyon 2 86 Rue Pasteur 69365 Lyon CEDEX 07 **christian.montes@univ-lyon2.fr**

*ScSo : Histoire, Géographie, Aménagement, Urbanisme, Archéologie, Science politique, Sociologie, Anthropologie

INSA LYON

Abstract

Mecanique, energetique, Genie Civil, acoustique
Center for Energy and Thermal Sciences of Lyon (CETHIL)

Doctor of Philosophy

Numerical study on viscoelastic Rayleigh-Bénard Convection

by Xin ZHENG

A direct numerical simulation (DNS) solver based on Fortran language was developed for the viscoelastic laminar Rayleigh-Bénard convection in 2D and 3D rectangular cavity. The solver considers a quasi-linear treatment to hyperbolic terms of the governing equation system to avoid numerical instability at high Weissenberg number. The procedure of DNS solver is based on Finite difference method and includes a variety of temporal discrete schemes (such as 1-order Euler, 2-order backward differential formula), spatial discrete schemes (such as the upwind scheme, central differential scheme, and High Order Upstream Central scheme), and viscoelastic constitutive models (such as Oldroyd-B (OB) and Phan-Thien-Thanner (PTT) models).

Most of the investigation in this thesis focuses on the viscoelastic RBC with the PTT model, because the PTT model is a nonlinear model that is suitable for simulating more complex viscoelastic fluids. The contents of this thesis can be divided into three parts: (a) we focused on the viscoelastic RBC in a $2:1$ cavity and presented a particular regular reverse convection phenomenon in detail. At the same time, we studied the influence of different rheological parameters of viscoelastic fluid (ϵ, ξ, β, and We) on the flow and heat transfer characteristics. We have also discovered, for the first time, the second critical Ra corresponding to the transition from reversal convection to steady convection. (b) We also studied the viscoelastic RBC in the tilted cavity and checked the influence of (β, We) on the convection structure and heat transfer. The results show that flow structure, heat transfer capacity, and critical Rayleigh number of tilted RBC are almost the same for a medium filled with weak elasticity fluids ($\beta = 0.9, We = 0.1$) and Newtonian fluids. However, flow pattern transition process will change dramatically, even if the inclination angle is small ($\alpha < 2$), when the fluid is very elastic ($\beta = 0.1, We > 0.5$). (c) preliminary numerical study about three-dimensional viscoelastic RBC has also started in this thesis, in order to see how the periodic convection with strong elasticity works in 3D cavity.

INSA LYON

Abstract

Mecanique, energetique, Genie Civil, acoustique
Center for Energy and Thermal Sciences of Lyon (CETHIL)

Doctor of Philosophy

Numerical study on viscoelastic Rayleigh-Bénard Convection

by Xin ZHENG

Un solveur de simulation numérique directe (DNS) basé sur le langage Fortran a été développé pour la convection de Rayleigh-Bénard laminaire viscoélastique dans des cavités rectangulaires 2D et 3D. Le solveur considère un traitement quasi-linéaire des termes hyperboliques du système d'équations gouvernant pour éviter l'instabilité numérique à un nombre de Weissenberg élevé. Le solveur DNS développé est basé sur la méthode des différences finies et comprend plusieurs schemas temporels (tels que Euler d'ordre 1, Euler d'ordre 2), des schémas spatiaux (tels que le schéma amont, schéma centré, et HOUC) et deux modèles constitutifs viscoélastiques (les modèles Oldroyd-B (OB) et Phan-Thien-Thanner (PTT)).

La plupart de travaux de recherche realisés dans cette thèse concernent la RBC viscoélastique avec le modèle PTT, car le modèle PTT est un modèle non linéaire qui est plus approprié pour simuler des fluides viscoélastiques complexes. Le contenu de cette thèse peut être divisé en trois parties: (a) nous nous concentrons sur le RBC viscoélastique dans une cavité 2D de rapport de forme 2 : 1 et nous avons présenté en détail le phénomène de convection inverse régulier. En même temps, nous avons étudié l'influence de différents paramètres rhéologiques du fluide viscoélastique (ϵ, ξ, β et We) sur les caractéristiques d'écoulement et de transfert de chaleur. Nous avons également découvert, pour la première fois, le deuxième Ra critique correspondant á la transition de la convection d'inversion à la convection stationnaire. (b) Nous avons également étudié la RBC viscoélastique dans une cavité inclinée et vérifié l'influence de (β, We) sur la structure d'écoulement et le transfert de chaleur. Les résultats montrent que la structure d'écoulement, la capacité de transfert de chaleur et le nombre de Rayleigh critique sont presque les mêmes pour un milieu rempli des fluids á faible élasticité ($\beta = 0,9, We = 0,1$) ou newtoniens. Cependant, le processus de transition d'écoulement changera radicalement, même si l'angle d'inclinaison est petit ($\alpha < 2$), lorsque le fluide est très élastique ($\beta = 0,1, We > 0,5$). (c) Des résultats préliminaires de RBC viscoélastique tridimensionnelle sont également obtenus dans cete thése, afin de voir comment le phénomène d'inversion observé en 2D se comporte dans une cavité tridimensionnelle.

Contents

List of Figures

List of Tables

Chapter 1

Introduction

Contents

The phenomenon of Rayleigh-Bénard convection with viscoelastic fluid is a common and complicated physical phenomenon in industrial processes or daily life. Viscoelastic Rayleigh-Bénard convection, as an important branch of the basic problem of thermal convection, has also received extensive attention in the past few decades. In this chapter, we will separately introduce what is thermal convection driven by bouyancy (especially Rayleigh-Bénard convection) and the effect of viscoelastic characteristics on thermal convection.

1.1 Research background

1.1.1 Rayleigh-Bénard convection

In nature, the local density of a fluid change with its temperature or solute concentration, and the buoyancy caused by the difference in density will drive the fluid to move. This kind of flow is called convection. The convection is one of the most extensive flow in nature, including two mechanisms of heat transfer and mass transfer, and is closely related to people's daily life and production processes. Among convection patterns, Rayleigh-Bénard convection is the most classic thermal convection model abstracted from many natural phenomena, and it is also considered to be one of the most simplified models for studying the mechanism of thermal convection. In 1900, Rayleigh-Bénard convection was first observed by Bénard (1900) in an experiment, in which unstable flow driven by thermal buoyancy is induced by the surface

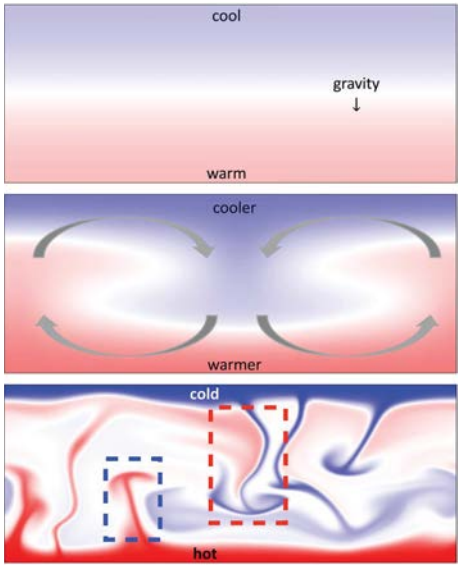

FIGURE 1.1: Three flow regimes of Rayleigh-Bénard convection, including thermal conduction, stable thermal convection and turbulent thermal convection (Doering, 2020).

tension of a fluid changed by temperature. So, above convection can be called Bénard convection. Soon after, Rayleigh (1916) studied a kind of special flow pattern, a thermal buoyancy-driven convection phenomenon was found and caused by the local temperature or density is not uniform in the fluid layer through theoretical analysis. Therefore, nowadays, most common "Rayleigh-Bérnard convection" is used to refer to the effect caused by temperature, and "Bérnard-Maramgoni convection" is used to refer to the effect caused by surface tension.

Physical configuration of a Rayleigh-Bénard convection can be described by, as shown in Fig. 1.1, a closed cavity filled with fluid, heated by the bottom plate and cooled by the top plate. The local density of fluid will increase near the cooling plate and decrease close the heating plate. Due to the effects of buoyancy, cooled (higher density) fluid tends to move down, and heated (lower density) fluid tends to move up. When the temperature difference between the upper and lower plates is small, the fluid in the cavity remains static, and the heat is only transferred through heat conduction, as shown at the top subgraph of Fig. 1.1; when the temperature difference increases into a certain range, the fluid in the cavity will gradually enter a steady flow state, and the heat exchange will be enhanced due to the convection effect, as shown at the middle subgraph of Fig. 1.1; when temperature difference further increases, steady convection will be broken and transformed to regular oscillating convection or quasi-oscillating convection, and heat exchange will be further enhanced; the fluid flow state will change to irregular motion, and finally enter turbulent flow, when the temperature difference is large to a certain extent, as shown at bottom subgraph of Fig. 1.1. Concerning flow pattern evolution in Rayleigh-Bénard convention system, there are three most important flow structures: boundary layer, plume, and large-scale circulation. The boundary layer describes that fluid close to the wall, the flow can still be regarded as laminar flow approximately, and the velocity and temperature maintain a

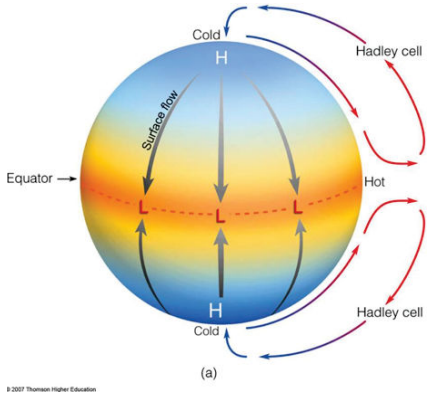

(A) Atmosphere convection (Stevens, 2005)

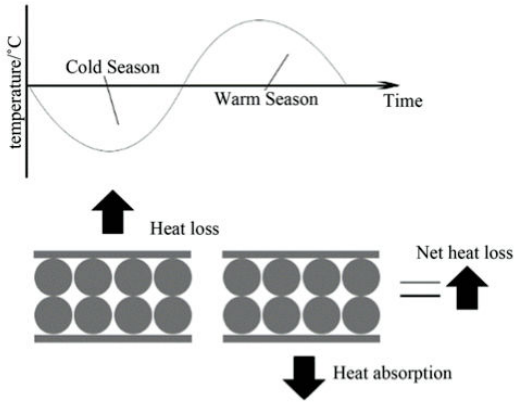

(B) Convection in the crushed rock layer (Qian et al., 2013)

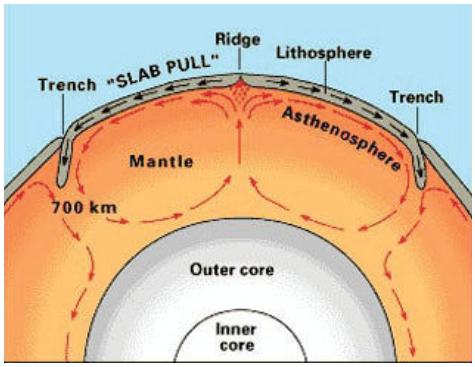

(C) Earth mantle convection (Hilst., Spring 1998)

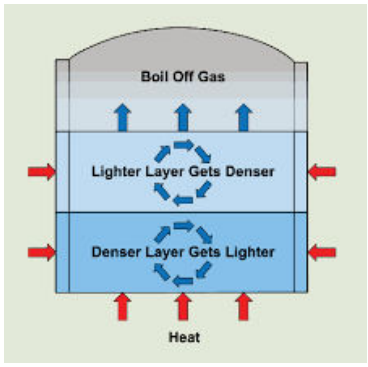

(D) Convection in LNG tank. (Roh et al., 2013)

FIGURE 1.2: Application of Rayleigh-Bénard convection

simple linear distribution. The fluid generated and moved from the upper and lower boundary layers due to buoyancy is called plume, inside the dashed box of the bottom subgraph of Fig. 1.1. During the movement, the hot and cold plumes self-organize to form a circular flow that fills the cavity, which is called large scale circulation (LSC). The development process of Rayleigh-Bénard convection can be described as the flow passing through supercritical bifurcation to reach a steady convective state, and then transitioning to a turbulent state after several consecutive bifurcations.

1.1.2 Application of Rayleigh-Bénard convection

One of the reasons why Rayleigh-Bénard convection is widely studied is its extensive application background. Studying the problem of Rayleigh-Bénard convection can help us deepen our understanding of the nature of convection phenomena and guide human life and production.

Fig. 1.2 shows four examples of the application of the Rayleigh-Bénard convection. Rayleigh-Bénard convection is one of the most practical model for weather prediction (Stevens, 2005), as shown in Fig. 1.2a, because the ground absorbs solar radiation, the air temperature rises and heat is dissipated to the outer space around the earth, also due to the uneven solar radiation and the uneven distribution of the heat of each terrain, leading to the uneven distribution of

the earth's surface temperature causing the fact that the hot air current rises while the cold air drops, leading to different convection phenomena distributed at a different location, further leading to different weather conditions such as winds and rainfall. With season changes, the Rayleigh-Bénard convection phenomenon will appear in the gravel layer of the roadbed (as shown in Fig. 1.2b): in winter, the temperature of frozen soil is higher than the land surface temperature, and due to buoyancy, Rayleigh-Bénard convection is formed with hot air move downward and cold air move upward; in summer, on the contrary, the temperature of frozen soil is lower than the surface temperature, under the effect of gravity, no convection is generated (Qian et al., 2013). The movement of mantle inside the earth is also a good example of Rayleigh-Bénard convection (Hilst., Spring 1998), as shown in Fig. 1.2c, the slow creeping of partially molten magma in shallow regions of the earth due to the difference in density is called mantle convection, which can gradually transfer the heat from the core to the surface of the earth. The sinking or ascending movement of molten magma is the main cause of plate subduction and volcanic eruptions, and it is also one of the driving forces that lead to plate movement. In addition to geophysics, Rayleigh-Bénard convection system is also refluected in all aspects of life, as shown in Fig. 1.2d, in the storage and transportation process of natural liquefied gas, because the external heat flow may cause the liquid in the tank to form turbulent Rayleigh-Bénard convection driven by a very small temperature difference, causing the pressure in the storage tank to surge, it is very easy to cause serious accidents (Roh et al., 2013) .

Rayleigh-Bénard convection system is everywhere, studying the Rayleigh-Bénard convection problem can enable people to deepen the understanding of the phenomenon of thermal convection in life. In-depth research on Rayleigh-Bénard convection has very important theoretical value and practical significance.

1.1.3 Viscoelastic Rayleigh-Bénard convection

Due to the wide range of applications of the Rayleigh-Bénard problem, its flow media are also diverse, by the way of example, egg whites and molten magma are all non-Newtonian fluids. In terms of material properties, fluids can be divided into two categories: Newtonian fluids and non-Newtonian fluids. In the research of fluid mechanics, the fluid that satisfies Newton's internal friction law is called Newtonian fluid; on the contrary, it is called non-Newtonian fluid, which means that its shear stress and shear strain have a nonlinear relationship. For Newtonian fluid, it can be seen everywhere in life, such as air and water. Similarly, non-Newtonian fluids are also very common in engineering and nature and play an important role, mainly including polymer solutions, polymer melts, foam solutions, suspensions, emulsions, pastes and some biological fluids, etc. Examples are shown in Fig. 1.3, such as honey, hot chocolate, toothpaste, magma and blood, etc.

The rheological properties of viscoelastic fluids are greatly different from that of Newtonian fluids, which makes them of great research value in flow and heat transfer. In 1948, Toms (1948) first reported that the addition of polymethyl methacrylate to chlorobenzene can significantly

(A) Honey (B) Hot chocolate (C) Toothpaste

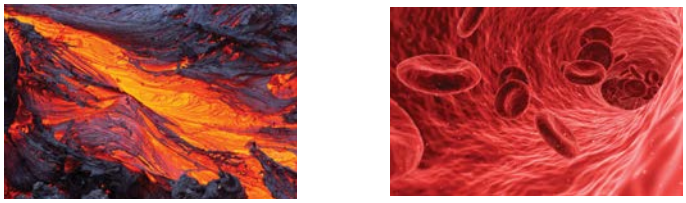

(D) Magma (E) Blood

FIGURE 1.3: Examples of Non-Newtonian fluid

reduce the resistance of turbulent flow at the First International Conference on Rheology. This phenomenon is called the Toms effect. From then on, the study of heat transfer in viscoelastic fluid flow was started. Due to the complexity of polymer drag reduction, research scholars have always paid attention to the research on polymer drag reduction. Using this effect (Toms effect) can effectively reduce friction resistance, thereby improve pipeline transportation efficiency and reduce energy consumption. However, in recent years, a large number of scholars have discovered that while polymer has a drag reduction effect, it has the effect of decreasing heat transfer performance, and this discovery undoubtedly opens the other side of the study of polymers. Existing research results show that additive polymers can increase the heat transfer performance of fluids under certain conditions, but under other conditions, they will weaken the heat transfer of fluids. These indicate that the flow and heat transfer effects of polymer additives on fluid flow are complicated and that the research on heat transfer and flow of polymer additives is still in infancy.

1.2 Objective and contributions of the thesis

From the perspective of engineering background and academic research, this thesis points out the importance of viscoelastic fluid Rayleigh-Bénard convection research, and its complexity of flow and heat transfer against conventional Newtonian Rayleigh-Bénard convection.

The main goal and contribution of this thesis can be described as follows:

- Develop numerical simulation solvers for viscoelastic fluid Rayleigh-Bénard convection system that satisfy the requirements of calculation accuracy and speed.

- Use the developed solver to study the flow pattern transition of viscoelastic Rayleigh-Bénard convection in a closed cavity.

- Use the calculation results to analyze the effect of viscoelastic properties on the flow and heat transfer of Rayleigh-Bénard convection from the energy point of view.
- Investigate the flow and heat transfer of viscoelastic Rayleigh-Bénard convection in an inclined cavity.
- Extand the 2D solver to 3D condition.

1.3 Methodology

The main research methods of fluid mechanics are as follows: theoretical analysis, numerical calculation, and experimental research. In complex situations, measurement is often very difficult or even impossible. Compared with the research method of experiments, computational fluid dynamics has the characteristics of no restrictions on parameters, low cost, and no interference in the flow field. Based on the above reasons, this work adopts numerical simulation research methods and uses Fortran language to develop a set of solvers for calculating viscoelastic Rayleigh-Bénard convection. Then, the self-developed solver is used to numerically simulate the Rayleigh-Bénard convection configuration we concerned with and analyze the results.

1.4 Outline of the thesis

The chapters of this thesis are organised in the following:

- Chapter 1: The context and objective of this thesis.
- Chapter 2: The literature review of viscoelastic Rayleigh-Bénard covnection.
- Chapter 3: The governing equations and numerical shemes used in developed sovler.
- Chapter 4: Numerical study of two dimensional viscoelastic Rayleigh-Bénard convection in a 2:1 enclosure cavity, revealing regular reversal convection phenomenon in certain conditions.
- Chapter 5: Numerical study of two dimensional viscoelastic Rayleigh-Bénard convection in a tilted cavity.
- Chapter 6: Three dimensional viscoelastic Rayleigh-Bénard convection in a cavity.
- Chapter 7: conlustions and perspectives.

Chapter 2

Literature review

Contents

2.1 Newtonian Rayleigh-Bénard convection

For the Rayleigh-Bénard convection, the earliest research began in the early 19th century, Bénard (1900) built a Rayleigh-Bénard-like convection experiment device and observed convection phenomenon driven by surface tension. After that, Rayleigh (1916) used the small disturbance theory for the first time to study the Rayleigh-Bénard convection problem, and established governing equation of convection driven by thermal bouyancy. Their results showed that fluid flow stability is directly related to the Rayleigh number when the fluid is stationary and heated at the bottom: the smaller the Rayleigh number, the more stable the fluid; the greater the Rayleigh number, the worse the fluid stability. The Rayleigh number mentioned is defined as:

$$Ra = \frac{\alpha \Delta T g H^3}{\kappa \nu} \tag{2.1}$$

where g is the gravity acceleration, α is the coefficient of thermal expansion of the fluid, $\Delta T = T_0 - T_1$ $(T_0 > T_1)$ is the temperature difference with T_0 the temperature on the lower boundary and T_1 on the upper boundary, H is the distance between lower and upper boundaries, κ is the thermal diffusivity and ν is the kinematic viscosity.

In a sense, this theory lays the theoretical foundation for the study of thermal convection problems. But it is worth noting that the convection phenomenon observed by Bénard (1900) in the experiment is not caused by surface tension, but caused by its temperature gradient. Therefore, in a fluid configuration with the heated lower part and the cooled upper part, the corresponding convective flow caused by buoyancy is called Rayleigh-Bénard convection.

In the following century, research on Rayleigh-Bénard convection has developed rapidly, and many important results of stability theory and heat exchange efficiency have been obtained (Busse, 1978; Behringer, 1985; Chandrasekhar, 2013). The "Chicago Convection Experiment" hold in the 1980s was an important milestone in the study of modern Rayleigh-Bénard convection systems (Castaing et al., 1989; Sano, Wu, and Libchaber, 1989). The experimental results showed that the fluid flow in the Rayleigh-Bénard system will gradually enter "soft turbulence" and "hard turbulence" regimes when Ra gradually increases. Subsequently, the research focus of the Rayleigh-Bénard convection system includes not only flow stability and heat transfer characteristics but also the statistical characteristics of the physical quantities of the system under the turbulent state (Siggia, 1994).

From the above-mentioned historical evolution of Rayleigh-Bénard convection research, we know that the main issues on Rayleigh-Bénard convection include: a) the onset and transition of Rayleigh-Bénard convection (stability analysis); b) the heat transfer capability of thermal convection; c) the flow structure. Therefore, we will do a literature review of the above three research aspects of Rayleigh-Bernard convection with Newtonian fluids in this section.

2.1.1 Onset of Rayleigh-Bénard convection

As mentioned above, in a Rayleigh-Bénard convection system, when Ra is small enough (for example the temperature difference is sufficiently small), the fluid is completely motionless and the heat transfer entirely depends on thermal diffusion. But, the thermal buoyancy-driven onset of convective instability (transition from conduction to convection) takes place when Ra exceeds a critical value (Drazin and Reid, 2004), and this transition only depends on the aspect ratio of the configuration and boundary conditions (i.e. rough or smooth) but not on the Prandtl number, this results had been summarized by Venturi, Wan, and Karniadakis (2010) and Ma and Wang (2004). By the way of example, for the Rayleigh-Bénard convection in cavity with 1:1 aspect ratio or infinite domain, the critical Rayleigh values of onset have been given by linear or nonlinear stability analysis and experiment in many published work (Davis, 1967; Stork and Möller, 1972; Chandrasekhar, 2013; Gelfgat, 1999; Venturi, Wan, and Karniadakis, 2010; Allgower and Georg, 2012; Asokan and Zabaras, 2005), and are equal to 2858 and 1708, respectively. Prandtl number is a dimensionless parameter and is defined as a ratio of momentum diffusivity to thermal diffusivity:

$$Pr = \frac{kinetic\ viscosity}{thermal\ diffusivity} = \frac{\nu}{\kappa} \tag{2.2}$$

where ν is the kineticc viscosity and κ is the thermal diffusivity. Several Prandtl number commonly used in numerical simulation and experimental research are given at Tab. 2.1.

Fluids	mercury	gases	water	silicon
Pr	0.025	0.7	3-10	5-50

TABLE 2.1: Examples of the Prandtl number of fluids (Miesch, 2005)

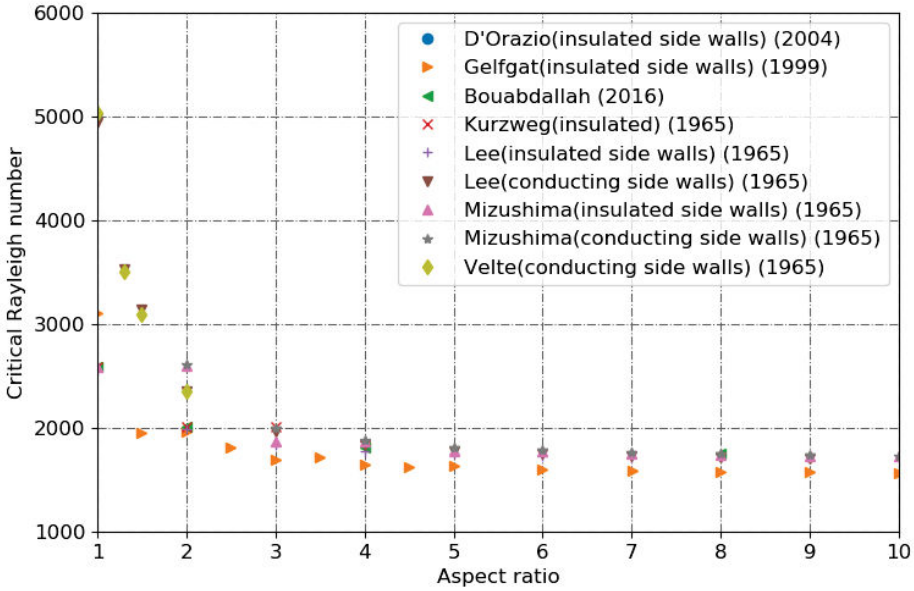

FIGURE 2.1: Effects of the width-to-height aspect ratio on the critical Rayleigh number (D'Orazio, Cianfrini, and Corcione, 2004; Gelfgat, 1999; Bouabdallah et al., 2016; Lee, Schultz, and Boyd, 1989; Mizushima, 1995; Velte, 1964; Kurzweg, 1965).

For the study about the onset of Rayleigh-Bénard convection with Newtonian fluids, regardless of the influence of the fluid property parameter Pr, many attentions had been paid to the effects of the width-to-height aspect ratio on the first critical Rayleigh number (D'Orazio, Cianfrini, and Corcione, 2004; Lee, Schultz, and Boyd, 1989; Gelfgat, 1999; Bouabdallah et al., 2016; Velte, 1964; Mizushima and Adachi, 1997; Kurzweg, 1965). Among them, work of D'Orazio, Cianfrini, and Corcione (2004) and Bouabdallah et al. (2016) about the influence of the width-to-height ratio of the cavity on the critical Rayleigh number almost cover whole aspect ratio scale, D'Orazio, Cianfrini, and Corcione (2004) focused on the small aspect ratio ($A < 1$), and Bouabdallah et al. (2016) focused on the big aspect ratio ($A > 2$), as shown in Fig. 2.1. Gelfgat (1999) considered a more complex Rayleigh-Bénard convection system, in which the temperature boundary conditions are described by Eq. (2.4), and fixed $Bi = 1$, the results are shown in Fig. 2.1. The results show that the critical values of Ra in Gelfgat's cases are smaller than those in Bouabdallah's.

$$y = 0 \quad T = 1 \tag{2.3}$$

$$y = 1 \quad \frac{\partial T}{\partial y} = -BiT \tag{2.4}$$

where Bi is constant.

Lee, Schultz, and Boyd (1989) checked the critical Rayleigh number of Rayleigh-Bénard convection in a cavity with width-to-hight ratio over ($A \in [0.5, 7.0]$). They also considered the conditions with insulated side walls and conducting side walls. For the Rayleigh-Bénard convection with conducting side walls, Velte (1964) also did some work in calculating critical Rayleigh number at different width-to-height ratio ($A = [2/3, 1, 1.3, 1.5, 2]$). Mizushima (1995) studied the Rayleigh-Bénard convection in finite and infinte domain and calculated the critical Rayleigh number for ($A \in [0.1, 10.0]$). These results are also shown in Fig. 2.1.

2.1.2 Routes from laminar to chaos

Once Ra exceeds the critical value for convection onset, as shown in Fig. 2.3, the steady laminar state convection will take place, related numerical and experimental results had been published by Bouabdallah et al. (2016), Venturi, Wan, and Karniadakis (2010), Gelfgat (1999), and Paul et al. (2012). Moreover, past the steady laminar convection stage, there are also many flow patterns and bifurcations in the way of transition from laminar to chaos. These transition routes under different Prandtl number Pr and aspect ratio A have been compared with dynamical systems theories, and have been well studied in numerous simulations and experiments in the past several decades (Gollub and Benson, 1980; Maurer and Libchaber, 1980; Bouabdallah et al., 2016; Venturi, Wan, and Karniadakis, 2010; Mizushima and Adachi, 1997).

We have already known that the onset Rayleigh number of the Rayleigh-Bénard convection is independent of Prandtl number in section 2.1.1, the sequence of bifurcation and evolution process to chaos and turbulence critically depend on the Prandtl number and width-to-height aspect ratio in Rayleigh-Bénard convection system (Yanagita and Kaneko, 1995; Paul et al., 2012). Therefore, in following sections, the flow pattern routes to chaos will be introduced separately by low Prandtl number ($Pr < 1$) and high Prandtl number ($Pr > 1$).

Low Prandtl number ($Pr < 1$)

For Rayleigh-Bénard convection in a cavity with 1:1 aspect ratio and $Pr = 0.7$, Bouabdallah et al. (2016) found that the stable laminar convection will disappear at $Ra = 16Ra_{c1}$, then flow become time-dependent. Their study has been made for Ra in the range $[2.5 * 10^3, 10^6]$, and four flow patterns were obtained, which include single-cell stable convection (1S), two vertical cells stable convection(2S), two vertical cells periodic oscillatory convection(2VC) and two horizontal cells periodic oscillatory convection(2HC), the evolution process and isotherms of flow patterns have been shown in Tab. 2.2 and Fig. 2.2. Venturi, Wan, and Karniadakis (2010)

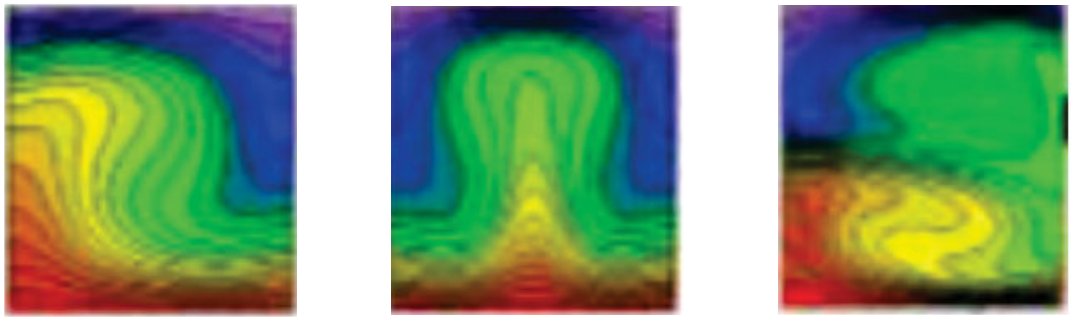

(A) 1S (B) 2S, 2VC (C) 2HC

FIGURE 2.2: Temperature contours at different flow convection patterns in (Bouabdallah et al., 2016)

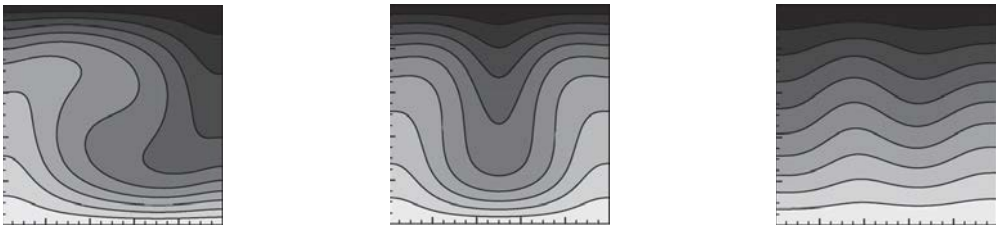

(A) $Ra = 15000$, 1S (B) $Ra = 15000$, 2VC (C) $Ra = 21000$, 3VC

FIGURE 2.3: Temperature contours at different Rayleigh number in (Venturi, Wan, and Karniadakis, 2010)

investigated the instability of the Rayleigh-Bénard convection onset and tested the effects of the initial conditions on the development of the supercritical flow pattern in a 2D closed cavity with the same physical configuration as Bouabdallah et al. (2016), using deterministic linear stability analysis theory and parameter continuation techniques. Venturi showed that there are two kinds of stable convection pattern with one or two cells at the same Rayleigh number, under the different initial flow states, as shown in Fig. 2.3a and Fig. 2.3b. It should be noted that Venturi just tested Ra up to $Ra = 22000$.

High Prandtl number ($Pr > 1$)

Compared to the 'route' in a square configuration, the routes to chaos are always more complex (Kaneko, 1986; Sano and Sawada, 1984), and especially depending on the width-to-height aspect ratio (Γ). Even the route to chaos will change due to changes in the history of the parameters (Yanagita and Kaneko, 1995). These changes are mainly reflected in changes of the cells in the domain, including the number and pattern (Paul et al., 2012; Paul, Wahi, and Verma, 2011).

In previous work with high Prandtl number cases, the most common liquid is water that we can see everywhere, the Prandtl number of water is about 7.56. Therefore, many work on the Rayleigh-Bénard convection are carried out when Pr is equal to around 7.0 (Velte, 1964; Mizushima and Adachi, 1997; Paul et al., 2012; Paul, Wahi, and Verma, 2011).

For $Pr = 6.8$ cases in a box with aspect ratio of $\Gamma = 2\sqrt{2}$, Paul et al. (2012) and Paul, Wahi, and Verma (2011) did lots of work on the flow pattern transition in almost the whole

Source	Ra	Cells	Flow regime
Gelfgat (1999) and Bouabdallah et al. (2016)	2858.01	None	stationary
Venturi, Wan, and Karniadakis (2010)	2858.02	None	stationary
Bouabdallah et al. (2016)	$[2.5 * 10^3, 1.8 * 10^4]$	1-cell (1S)	stable state
Venturi, Wan, and Karniadakis (2010)	$[6742.31, 11279]$	2-cell	unstable
Venturi, Wan, and Karniadakis (2010)	$[11279, 1.8 * 10^4]$	1-cell/2-cell	stable state
Bouabdallah et al. (2016)	$[1.9 * 10^4, 4.57 * 10^4]$	2-cell (2VC)	stable state
Venturi, Wan, and Karniadakis (2010)	$[1.9 * 10^4, 2.2 * 10^4]$	1-cell/2-cell	stable state
Venturi, Wan, and Karniadakis (2010)	$[]19634, 2.1 * 10^4]$	3-cell	stable
Bouabdallah et al. (2016)	$[4.58 * 10^4, 99 * 10^4]$	2-cell (2VC)	periodic oscillatory
Bouabdallah et al. (2016)	$[5 * 10^4, 4.1 * 10^5]$	1-cell (2S)	steady state
Bouabdallah et al. (2016)	$[4.2 * 10^5, 1 * 10^6]$	2-cell (2HC)	periodic oscillatory

TABLE 2.2: Review of flow pattern transition along Rayleigh number in 2D cavity with 1:1 aspect ratio, $Pr = 0.7$.

Rayleigh number range-from conduction state to the developed turbulence. In his study, steady convection is born when Ra exceeds the critical value (Ra_c), after that, time-periodic convection appears through a Hopf bifurcation at $Ra = 80Ra_c$. After this time-periodic convection, a period doubling bifurcation ($Ra = 500Ra_c$) will lead the flow to another time-period state and quasi-periodic state, and eventually chaos ($Ra = 750Ra_c$). For the convection structures that appeared in the investigations (Paul et al., 2012; Paul, Wahi, and Verma, 2011), some earlier experimental and numerically studies also showed the same flow situation (Gollub and Benson, 1980; Maurer and Libchaber, 1979; Curry et al., 1984).

For $Pr = 15.0$ case in a square cavity, Lappa (2011) did lots of work in a domain with strict geometry symmetry. Under their condition, four flow patterns had been obtained at different Rayleigh numbers, they are respectively the antisymmetric–antisymmetric mode with single roll, the symmetric–antisymmetric mode with two vertical rolls, the antisymmetric–symmetric mode with two horizontal rolls, and the symmetric–symmetric mode with four rolls (Fig. 2.4). For a more intuitive understanding, Fig. 2.4 plots a synthesis of flow behaviours at different Rayleigh numbers, and a large-scale-flow Reynolds number as a function of Ra. The Reynolds number used is defined as:

$$Re = \frac{U_c H}{\nu} \tag{2.5}$$

where U_c is characteristic velocity scale of flow and H is a characteristic length scale, that is distance between the heating and cooling plates in our cases.

The flow patterns found in Lappa's simulation (Lappa, 2011) were also observed by Mizushima and Adachi (1997) in a square cavity with $Pr = 7.0$, as shown in Fig. 2.5. They checked the critical Rayeigh numbers for four flow fields types (1S, 2VC, 2HC, 4C) are equal to 5011.3, 7972.4, 28830 and 27933, respectively.

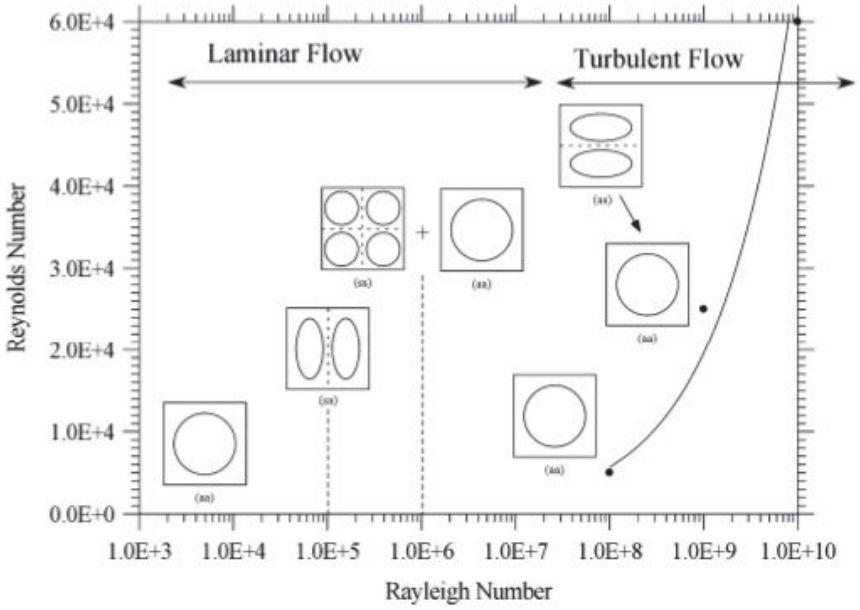

FIGURE 2.4: Reynolds number of the flywheel as a function of Ra, the flow pattern evolves from laminar to chaotic and the range of Rayleigh is $[10^3, 10^{10}]$ (Lappa, 2011). In the cases, $Pr = 15.0$ and width-to-height aspect ration $A = 1.0$.

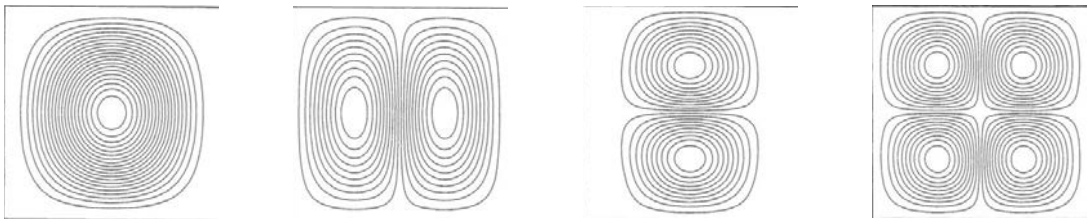

(A) 1S (B) 2VC (C) 2HC (D) 4C

FIGURE 2.5: Streamlines at different flow convection patterns in (Mizushima and Adachi, 1997)

2.1.3 Turbulence regime

After convection flow passes the steady convection and time-periodic oscillating convection, convection flow entered a more disorderly state in time and space. These flow states are called turbulence, which is unstable and random and contrasts with the laminar flow. In fact, most of the flows we meet in natural and industrial processes are turbulent, they all show a complex flow structure, unlike laminar flow which has an obvious main flow or layered structure. The blowing wind, and flowing river, are good examples of the turbulent flow in our life.

The flow transition from laminar flow to turbulence is firstly observed by Hagen (1839), which initiated more than a century of investigation on turbulence. Half a century later, British scientist Reynolds conducted experimental research and showed that there are two kinds of flow regimes with completely different internal structures in liquid flow: laminar flow and turbulent flow (Reynolds, 1883). He revealed an important fluid flow mechanism, that is, according to flow velocity, the fluid flow has two different forms and proposed the famous Reynolds

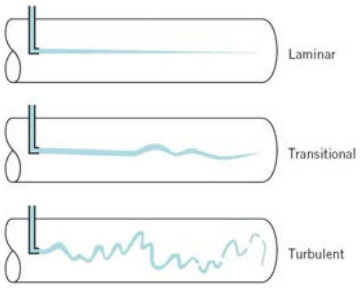

FIGURE 2.6: Laminar, transitional and turbulent flow states in a pipe (Reynolds, 1883).

number for the transition from laminar flow to turbulent flow (including the case of stratified flow). When the fluid velocity is small, the fluid particles only move one-dimensionally along the flow direction, and there is no macroscopic mixing with the surrounding fluid, that is, stratified flow. This flow pattern is called laminar flow or stagnant flow. After the fluid velocity increases to a certain value, the fluid particles move randomly in other directions in addition to the flow in the main direction of the flow, that is, there is an irregular pulsation of the fluid motion.

In the following hundred years of research on turbulence, researchers have put forward many important theories:

- **Energy cascade (1920s)**: Johnson (1922) discovered the cascade process of turbulent kinetic energy. The large-scale vortex pulsation is like a large energy storage pool, which continuously obtains energy from the outside and outputs energy to the small-scale eddies; the small-scale turbulence is like an energy-consuming machine, where all the kinetic energy output from the large-scale turbulence is consumed or dissipated, the inertia of the fluid is like a conveying machine, transmitting large-scale pulsations to small-scale pulsations. The larger the Reynolds number of the flow, the larger the inertial area between the large-scale energy storage and the small-scale energy consumption.

- **Isotropic turbulence theory (1935)**: Taylor (1935) set up one or several rows of regular grids in the uniform airflow of the wind tunnel experiment. When the uniform airflow flows through the grid, irregular disturbances are generated. When this kind of irregular disturbance moves downstream, because there is no external disturbance, it gradually evolves into isotropic turbulence.

- **Kolmogorov scale (1941)**: Moscow mathematician Kolmogorov further developed G.I. Taylor's homogeneous isotropy theory (Taylor, 1935) into a locally uniform isotropy statistical theory, and for the first time in human history derived the law of turbulent microstructure: the structure-function of $-p/3$ law. The spatial distribution characteristics of turbulence are revealed for the first time. Although this theory has some flaws, but it is still known as the greatest turbulence theory achievement in human history so far.

- **Coherent turbulent structure (1967)**: Kline et al. (1967) used hydrogen bubble technology to show the coherent structure of large-scale vortices in the turbulent boundary layer. Robinson (1991) drew the burst pattern of the turbulent boundary layer.

When Ra gradually increases, the fluid flow in the Rayleigh-Bénard system will enter turbulence, therefore, the research focus of the Rayleigh-Bénard system shifted from the stability of the system and the formation of chaotic modes to the statistical characteristics of the physical quantities of the system under the turbulent state (Siggia, 1994).

2.1.4 Efficiency of heat exchange

There are three types of heat transfer: heat conduction, thermal convection, and radiation. The heat transfer efficiency of heat conduction and radiation is highly constrained, caused by their simple and inflexible way of heat exchange (mainly limited by distance and material properties). Therefore, the efficiency of the heat transfer of the convection has always been the focus of convection research. In addition, that is also the focus of study on the Rayleigh-Bénard convection, in the past century.

In order to test the heat transfer capacity of a Rayleigh-Bénard system, a dimensionless number, Nusselt number, should be introduced (Kays, 2011), that is defined as:

$$Nu = \frac{hH}{k} \tag{2.6}$$

where k is the fluid thermal conductivity, and h is the convective heat transfer coefficient ($W/(m^2K)$). In the Rayleigh-Bénard system, convective heat transfer coefficient can be understood as the rate of the heat transfer between solid boundary and the fluid per unit surface area per unit temperature difference:

$$h = \frac{q}{\Delta T} \tag{2.7}$$

where q is the local heat flux density (W/m^2) and ΔT is the temperature difference (K).

The Nusselt number represents the ratio of convective to conductive heat transfer and therefore the averaged temperature gradient at boundaries of the fluid domain. High Nusselt number in Rayleigh-Bénard convection means there is stronger convection. Generally, different values of the Nusselt number correspond to different flow patterns, and Kays (2011) gave a proximate range:

- value of $Nu = 1$ corresponds to heat transfer by pure conduction.
- value of $Nu \in (1, 10)$ corresponds to slug flow or laminar flow.
- value of $Nu \in (10, 1000)$ corresponds to turbulent flow.

Scholars did much work to find the scaling relationship of Nu with Ra and Pr, which can be used to express the energy transmission and heat transfer capacity in the Rayleigh-Bénard

system. The scaling law of Nusselt number with Rayleigh and Prandtl number can be expressed as:

$$Nu = Nu(Ra, Pr) \tag{2.8}$$

This can be written as a common form of power law equation, when Prandtl number is fixed:

$$Nu = CRa^{\alpha} \tag{2.9}$$

where C is a constant and α is the index.

Basic conditions

For flow regime before turbulent flow, the flow pattern always exhibits steady or temporal-spatial periodic or quasi-temporal-spatial periodic characteristics.

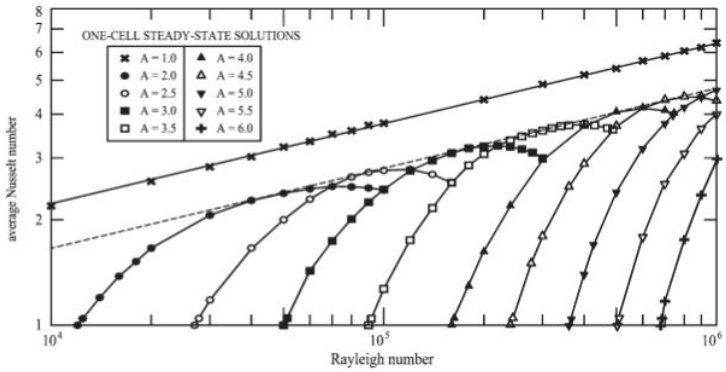

FIGURE 2.7: Nusselt number as a function of Rayleigh number with the one-cell steady state, at fixed Prandtl number $Pr = 0.71$ and different heigh-to-width aspect ratio $A \in [1, 6]$ (D'Orazio, Cianfrini, and Corcione, 2004).

D'Orazio, Cianfrini, and Corcione (2004) numerically studied the scale relationship of Rayleigh number and Nusselt number in an enclosure Rayleigh-Bénard system with various heigh-to-width aspect ratio $A \in [1, 6]$, when Prandtl number is fixed at 0.71, as shown at Fig. 2.7. In his simulation, Ra is controlled within the interval of $Ra \in [10^3, 10^6]$, due to the maintained one-cell flow pattern for different heigh-to-width aspect ratio enclosure domain.

Bouabdallah et al. (2016) numerically investigated the Nusselt number as a function of Ra in Rayleigh-Bénard system at different width-to-height aspect ratio, the results are shown in Fig. 2.8.

In terms of experimental investigation, Castaing et al. (1989) built a Rayleigh-Bénard convection device with aspect ratio 1:1, filled by helium gas. The values of Rayleigh number and Prandtl number in their experiments are $Ra \in [10^6, 6 * 10^{12}]$ and $Pr \in [0.65, 1.5]$, respectively. Fig. 2.9 shows the scaling laws of the Rayleigh and Nusselt numbers in the study of Castaing et al. (1989), where the Nusselt curve is divided into two parts: 'soft turbulence' and 'hard turbulence', and the transition takes place at $Ra = 4 * 10^7$. In addition, their experimental results

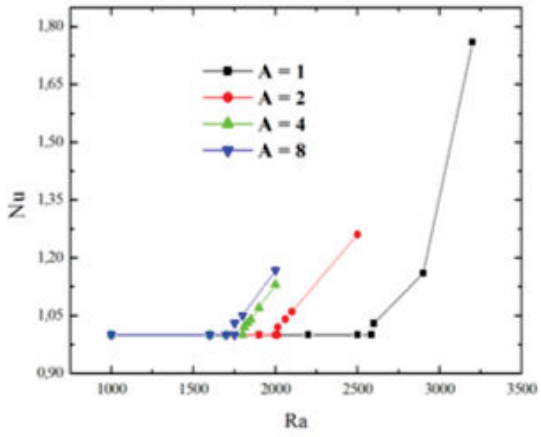

FIGURE 2.8: Nusselt number as a function of Rayleigh number at different width-to-height aspect ratio $A = (1, 2, 4, 8)$ (Bouabdallah et al., 2016).

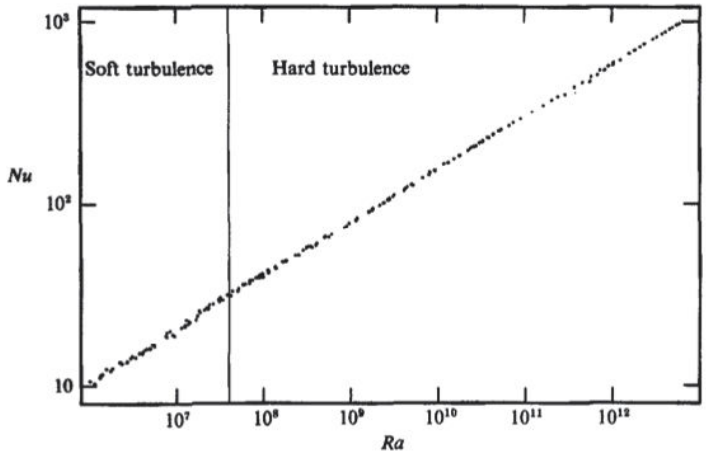

FIGURE 2.9: The scaling law of Nusselt and Rayleigh number. (Castaing et al., 1989)

pointed out that Nusselt number is closely proportional to $Ra^{\frac{2}{7}}$, not to $Ra^{\frac{1}{2}}$ obtained by Kraichnan (1962) and Long (1975). The 'soft turbulence' and 'hard turbulence' are different from the distribution of the temperature in the central vertical line, as shown in Fig. 2.9, specifically the 'soft regime' has a more gaussian character and 'hard regime' has a more exponential character. The similar results (power-law index of Ra equal $\frac{2}{7}$) to the Castaing et al. (1989) have also been observed by subsequent studies (Shraiman and Siggia, 1990; Chavanne et al., 1997; Zaleski, 1998; Cioni, Ciliberto, and Sommeria, 1997).

In addition, many experimental investigations were carried out around the situation with $Pr \in [4.0 - 7.0]$, and gave very significant results (Rossby, 1969; Funfschilling et al., 2005; Sun et al., 2005; He et al., 2012; Cheng et al., 2015), as shown in Fig. 2.10. The dashed lines in the figure are fitted by He et al. (2012). Rayleigh number in these experiments covers the 'soft' and 'hard' turbulent regime, $Ra \in [10^3, 10^{16}]$.

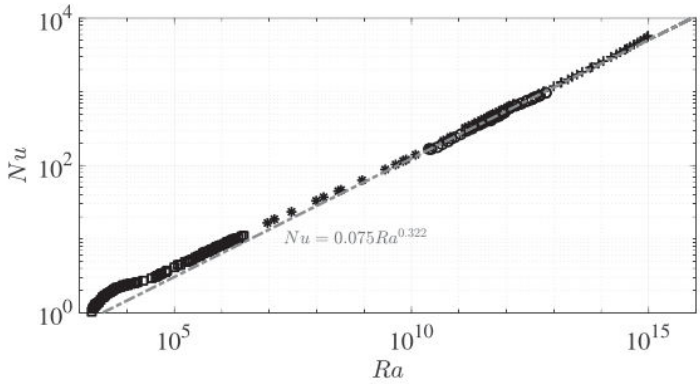

FIGURE 2.10: Scaling law of Nusselt number and Rayleigh number, when $Pr \in [4, 7]$. This results was summarized by Plumley and Julien (2019)

Heat exchange enhancement

The heat transfer capability is a significant indicator of the Rayleigh-Bénard system, especially for evaluating Rayleigh-Bénard systems in industrial production, therefore it is necessary to enhance heat transfer (Bergies, 1999; Kakaç et al., 2013). For Rayleigh-Bénard convection system, the enhanced heat exchange technologies proposed up to now can be divided into passive and active techniques (Bergies, 1999): active techniques require the use of external power, they could be surface vibration or pulse (Raji et al., 2013), application of multiphysics fields (Pallares and Davidson, 2000), etc; passive techniques do not require external power, mainly include treated surfaces (Du and Tong, 1998), additives for liquids (Cheng et al., 2017), etc.

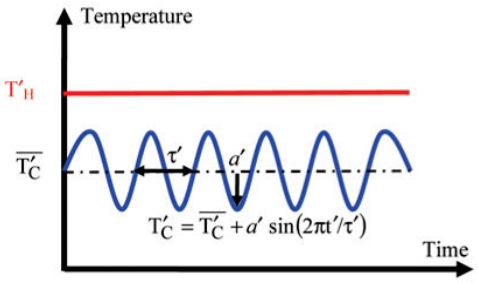

(A) thermal pulse along time

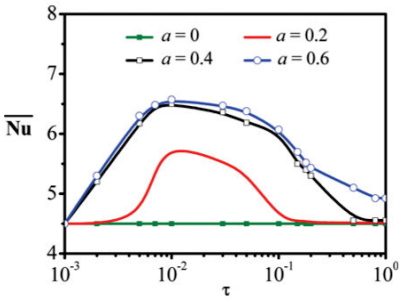

(B) Periodic averaged Nusselt number

FIGURE 2.11: (a) temperature of cooling boundary change over time. (b) Periodic averaged Nusselt number with different amplitudes a and frequency τ. (Raji et al., 2013)

Boundary temperature pulse: Raji et al. (2013) considered the effects of pulse temperature boundary on the heat transfer capacity, applied a pulse cooling bounday condition on a Rayleigh-Bénard system with aspect ratio $A = 1$ and $Pr = 0.71$. In his cases, the temperature of heating is constant $T_H^{'} = 1$ and that of the cooling boundary, as shown in Fig. 2.11a, is set as:

$$T_C^{'} = \overline{T_C^{'}} + a * sin(2\pi t/\tau) \tag{2.10}$$

where $\overline{T_C'} = \frac{1}{L_x}\int_0^{L_x} T|_{y=L_y} dx$ is the averaged temperature of cooling boundary, a is the coefficient of amplitude and τ is the period. When $a = 0$, this physical configuration represents a typical Rayleigh-Bénard convection.

Fig. 2.11b shows the effect of the period τ on the time-averaged Nusselt number for $Ra = 10^6$ with different amplitude a, where $a \in (0, 0.2, 0.4, 0.6)$. In this numerical study, Raji et al. (2013) found that periodic cooling can be used to notably enhance the heat exchange in comparison with the case of constant cooling temperature, and the maximum enhancement is about 46% and takes places when $\tau = 0.01$ and $a = 0.6$. They also tested the cases with $Ra = 10^5$ and observed the heat exchange enhancement with pulse temperature boundary.

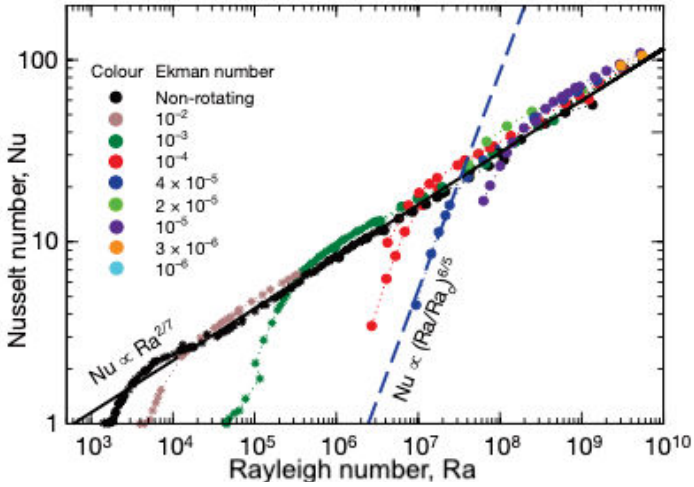

FIGURE 2.12: Nu as a function of Ra. (•) represents the work from King et al. (2009) and (∗) represents the work from Rossby (1969).

Application of multiphysics fields: King et al. (2009) considered rotating convection, which is influenced by the ratio of the relevant global-scale Coriolis force and buoyancy force, the rotation effect changes not only the average motion of the fluid but also the intensity of the turbulence and the pulsation structure. The Prandtl number was fixed at 7 in King's experiments. As shown in Fig. 2.12, we can obviously observe that the rotation conditions may delay the onset of convection, but when Rayleigh number exceeds a certain value, the heat transfer capability will increase.

Rough surface: In fact, most convection phenomena in nature are accompanied by rough surfaces. Shen, Tong, and Xia (1996) and Du and Tong (1998) experimental studied the effects of the rough heating and cooling surface on the convection flow and heat exchange in a cylindrical Rayelgh-Bénard system filled with water. They experimented on two experimental configurations with same the inner diameter $20cm$ and different height $20cm$ and $40cm$, respectively. Fig. 2.13a shows temperature and velocity near the heating rough boundary, and Fig. 2.13b plots the Nusselt number as a function of Rayleigh number in cases with smooth and rough surfaces. 76% increase in heat transfer rate was found in the case with rough surfaces (Du and Tong, 1998).

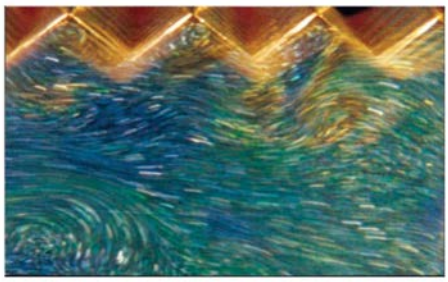

(A) Flow near rough boundary

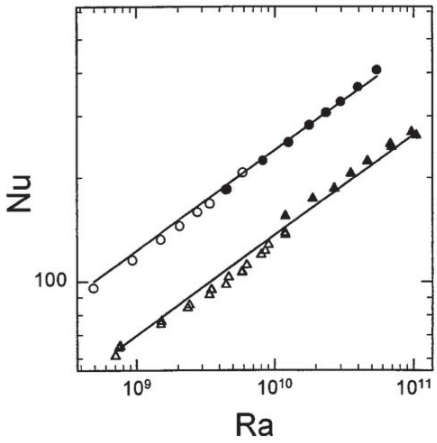

(B) *Nu* vs. *Ra*

FIGURE 2.13: (a) The velocity and temperature distribution near the rough boundary . (b) *Nu* as a function of *Ra* in the smooth (triangles) and rough (circles) cells. The solid symbols are obtained in the cells with height of 20*cm*, and the open symbols are obtained in the cells with height of 40*cm*. (Du and Tong, 1998)

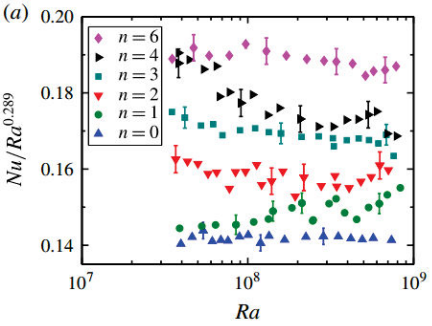

(A) *Nu* vs. *Ra*

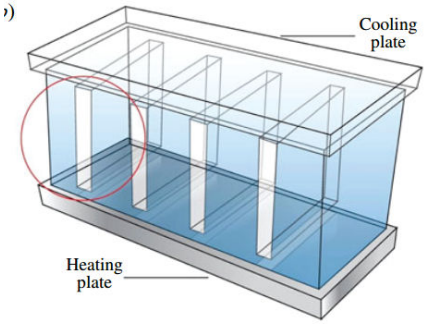

(B) Physical configuration

FIGURE 2.14: Rayleigh-Bénard cell with partition constraint. (Bao et al., 2015)

Partition constraint: In the Rayleigh-Bénard system heat transfer enhancement study (Bao et al., 2015), a new mechanism that will lead to greater heat transfer is revealed: that is, when the vertical partition is inserted vertically into the gap between the cooling and heating plates, convection will become spontaneously organized and more consistent, ultimately leading to an unprecedented increase in heat transfer. Bao et al reported an experimental and numerical study about heat transfer enhancement in Rayleigh-Bénard convection cell with vertical partitions inserted, as shown in Fig. 2.14b. In their cases, Prandtl number equal to 5.3, and Rayleigh number coverage $[3.5 * 10^7, 8.3 * 10^8]$. As shown in Fig. 2.14a, increasing the number of intervals will increase the heat transfer efficiency, and when the interval number is 6, the heat transfer efficiency will increase by nearly 30%.

Additives: Drag reducers are polymer compounds that have the effect of reducing drag. Adding it to the fluid during fluid transportation can reduce resistance and improve heat transfer efficiency. This part of the content will be elaborated in Sec. 2.2.1 and Sec. 2.2.

2.2 Viscoelastic Rayleigh-Bénard convection

For flow system driven by thermal buoyancy, how viscoelastic properties affect flow and heat transfer is a problem worthy of study. Whereas there has been extensive fundamental research of the Rayleigh-Bénard convection in Newtonian fluids, much less progress has been achieved in understanding the convection with viscoelastic fluids. The main reason for this phenomenon comes from the late start of the research on viscoelastic Rayleigh-Bénard convection, the complexity of viscoelastic fluid characteristics, and the nonlinear thermal coupling between viscoelastic fluid properties and flow. The current research status of viscoelastic Rayleigh-Bénard convection will be introduced below.

2.2.1 *Toms effect* and its application

Following the discovery of the British scholar Toms (1948), the Toms effect is used to effectively improve flow efficiency and reduce energy loss. In fact, in the past few decades, experiments using additives to reduce resistance have been launched in various fields, including oil transportation, water transportation, fire protection, heating, etc. In 1970, Paterson and Abernathy (1970) experimentally studied the drag reduction and polymer degradation in turbulent pipe flow with dilute water solutions of unfractionated polyethylene oxide (PEO). They found that when the solute concentration reaches $0.1mg/L$, the additive has already produced a rent reduction effect on the flow. Thereafter, in 1982, Oliver and Bakhtiyarov (1983) found the critical concentration can be reduced to $0.02mg/L$ when the additives are polyacrylamides (PAM). In 1982, Burger, Munk, and Wahl (1982) added polymer additives to Alaska's oil pipeline and increased the ability to transport oil by 25%. This is the first time that additives have been applied to actual business for drag reduction.

However, under the conditions of strong shearing force and high temperature, the polymer chain-like macromolecular structure, which is the main role of drag reduction, will be permanently destroyed, resulting in the loss of turbulent drag reduction effect. After the internal network structure of the surfactant is destroyed, it will be repaired and rebuilt in a very short period of time, so that it has the effect of reducing drag again. Aiming at the characteristics of surfactants, in 2004, Takeuchi (2007) added a 0.5% LSP-01A surfactant to the heating circulation system of the main hall of Sapporo City in Japan. After a year of stable operation, it was found that the energy consumption of the power system was reduced by about 65%.

On the other hand, Groosman and Groisman and Steinberg (2000) discovered for the first time that there is a rotating flow between parallel plates under the conditions of small Reynolds (Re) and large Weissenberg number (We). This phenomena is also called elastic turbulence. Compared with laminar flow, the flow resistance under this condition is greatly increased, and the mixing efficiency is enhanced to a certain extent. Using this effect can effectively strengthen the heat and mass transfer in the microchannel, which has considerable application value in the chemical, pharmaceutical, and medical industries such as heat dissipation chips, microreactors, disease monitoring, and so on. At present, for additive fluid flow, turbulent drag-reductin with

high *Re* and low *We* and mixing enhancement with low *Re* and high *We* (caused by elastic turbulence) has received widespread attention.

As mentioned above, in a flow heat exchange system, flow and heat transfer characteristics are two inseparable considerations. Studies have found that viscoelastic properties will also cause deterioration of heat transfer while reducing drag. As shown in Fig. 2.15, Li, Kawaguchi, and Hishida (2004) experimentally investigated the drag reduction and heat transfer reduction characteristics of a channel flow at different background temperature and Reynolds numbers in 30ppm dilute aqueous solution of a cationic surfactant of cetyltrimethylammonium chloride (CTAC).

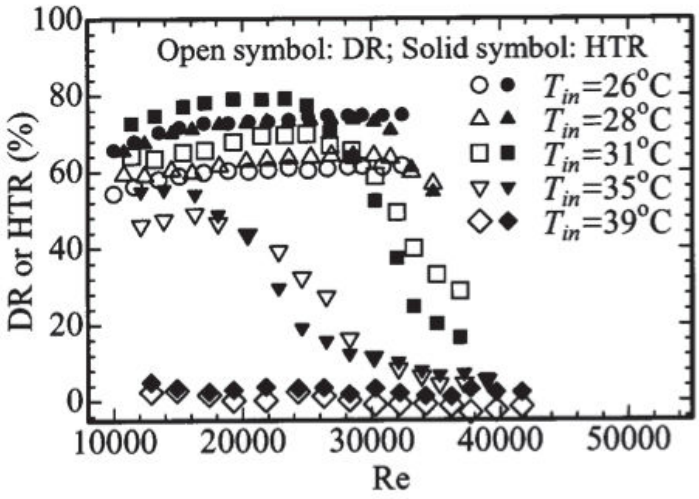

FIGURE 2.15: Drag reduciton (DR) and heat transfer reduction (HTR) as different Reynold number with various temperature (Li, Kawaguchi, and Hishida, 2004).

Fig. 2.15 shows the relationship between drag reduction rate and heat transport reduction with Reynold numbers and temperature. The drag reduction and heat transport reduction are defined as:

$$DR = \frac{f_0 - f}{f_0} \; and \; HTR = \frac{Nu_o - Nu}{Nu_0} \tag{2.11}$$

The result shows that under the same Reynold number and temperature, the heat transfer deterioration rate is always higher than the drag reduction rate; with Reynold number or temperature increase, DR and HTR both increase first and then decrease, in another word, for this kind of drag reduction agent, there is critical value for Reynold number and temperature, once this critical value is exceeded, the drag reduction effect disappears and the heat transfer performance is restored.

Due to the fact that additive drag reduction is accompanied by heat transfer attenuation, in order to achieve a balance between drag and heat transfer reduction, scholars are dedicated to exploring the limits of the flow drag reduction and heat transfer deterioration of viscoelastic fluids (Li et al., 2001; Qi et al., 2003). These methods mainly include pipe diameter effect method (Li, Kawaguchi, and Yabe, 2001), network structure destruction method (Qi et al., 2001), ultrasonic method (Qi, 2002) and ultraviolet irradiation method (Qi, 2002), etc. The basic principle

is to destroy the macromolecular structure in the solution without forming a viscoelastic effect, thereby reducing the deterioration of heat transfer.

2.2.2 Onset and bifurcation of convection

Due to its rich bifurcation sequence and flow structure, Rayleigh-Bénard convection is always used to study the flow state transition of fluid dynamics. The same is true for viscoelastic Rayleigh-Bénard convection. Pattern selection at the start-up of the Rayleigh-Bénard convection with Newtonian fluids has been studied extensively numerically and experimentally. However, viscoelastic Rayleigh-Bénard convection studies are very few compared to Newtonian Rayleigh-Bénard convection. Rayleigh-Bénard convection is complicated enough by its very nature with the further difficulties introduced by the non-linear constitutive model of the viscoelastic fluid with additional material parameters, such as relaxation and retardation times as well as the degree of elasticity embedded in the fluid. Due to the influence of strong nonlinearity, for the start-up of the viscoelastic Rayleigh-Bénard convection, many aspects of this physical phenomenon are still not yet clearly elucidated. Because the viscoelastic Rayleigh-Bénard convection as applications is both present and emerging in industry and nature (some examples are chemical and manufacturing processes and convection in the Earth's mantle), it is absolutly necessary for further in-depth investigation of viscoelastic RBC.

Given the compounded difficulties of observation on experimentally investigation, a numerical approach is best suited to tackle this problem. A major difficulty in numerical simulations of the flow of viscoelastic fluids is the instability caused by the increasing inertia and elasticity of the fluid independently of the discretization chosen called in the literature the High Weissenberg number problem (HWNP). Linear stability analysis predicts the critical Rayleigh number at which thermal convection starts whereas the magnitude of the convection amplitude is determined by the nonlinear stability analysis, Park and Ryu (2002). Linear and non-linear stability analyses in the literature provide evidence that many parameters have a huge impact on the critical Rayleigh number and convection flow pattern.

The earliest linear and non-linear stability analysis of the Newtonian Rayleigh-Bénard convection were conducted by Malkus and Veronis (1958). For viscoelastic Rayleigh-Bénard convection, the first investigation of linear stability analysis was published as early as 1968, Green III (1968), who used an upper convected Maxwell model with a single relaxation time to characterize the fluid, to describe the onset of a thin fluid layer heated from the bottom and to establish the conditions under which an oscillating convection instability may appear. This was followed by Vest and Arpaci (1969) and Sokolov and Tanner (1972) who expanded the investigation of this intriguing phenomenon to the oscillating mode of instability, which appears when the ratio of viscoelastic relaxation time to thermal relaxation time is high. The thermal relaxation time mentioned is defined by d^2/κ, where d is the thickness of the viscoelastic fluid layer and κ is the thermal diffusivity. In the following decades, nonlinear stability analysis of the viscoelastic Rayleigh-Bénard convection has been a focus of attention by several investigators (Eltayeb,

1977; Rosenblat, 1986; Renardy and Renardy, 1992; Martinez-Mardones and Perez-Garcia, 1992; Park and Lee, 1995; Park and Ryu, 2001; Park and Park, 2004; Park, 2018). In their contributions, the relationship between rheology parameters of viscoelastic fluids and the critical Rayleigh number (reflecting the flow mode instability that is flow pattern transition from stationary convection to oscillating convection) was further investigated in-depth and illustrated. A more sophisticated viscoelastic constitutive models were used in their studies as compared to the basic upper-convected Maxwell model usedin the pioneering work of Green III (1968). The heating and cooling boundary conditions used ranged from the rigid-free condition with a free surface to the rigid-rigid (solid wall) condition. Most of the research works outlined above focused on periodic boundary conditions and/or infinite planes, which can be approximated by a one-dimensional instability analysis. Of course, this treatment also limits the application of the stability analysis, as the boundary conditions have a significant effect on the flow and heat transfer in the Rayleigh-Bénard convection.

In many related studies, the first linear and nonlinear instability analysis of the viscoelastic Rayleigh-Bénard convection in an closed cavity with aspect ratio $A \in [1, 10]$ was conducted by Park and Ryu (2001). They used a Chebyshev pseudo-spectral method coupled with a general viscoelastic constitutive model which encompasses Maxwell, Oldroyd, and Phan-Thien-Tanner models. The effects of the Weissenberg number We and β (ratio of solvent viscosity μ_s to total viscosity $\mu_0 = \mu_s + \mu_p$, where μ_p is the viscosity came from polymer addtive) on the critical Rayleigh number for convection start-up and the convection cell structure under different aspect ratios were studied. Park and Ryu (2001) also investigated flow pattern selection mechanisms under different We and β, with aspect ratios $A = 2.0$ and 6.0. They determined that the critical Rayleigh number decreases as Weissenberg number We increases and/or β decreases.

Except the onset of convection, flow pattern selection is also strongly dependent on the parameters We and β. Stability exchange criteria derived is only valid when a new flow pattern grows monotonically without oscillation (Park and Lee, 1995). If the flow pattern grows with oscillation the instability is called overstability. With We increases and/or β decreases enough, the start-up convection flow pattern will transit from stability exhcange steady mode to overstability oscillatory mode (Park and Ryu, 2002). Fig. 2.16 shows the cirtical Rayleigh number and the boundary separating exchange of stabilities and Hopf bifurcation in $\beta - \lambda^0$ plane for viscoelastic Rayleigh-Bénard convection with aspect ratio $2:1$, where $\beta = \mu_{m0}/\mu_0$ is the retardation ratio (where μ_{m0} is the zero-shear rate molecular-contributed viscosity) and λ^0 is the relaxation time (Park and Ryu, 2002). Park and Park (2004) and Park (2018) also numerically simulated the Rayleigh-Bénard convection with a Phan-Thien-Tanner constitutive model and showed that the time period of local vorticity intensity is almost two times larger than that of local momentum with growing values of β.

Khayat (1994), Khayat (1995a), and Khayat (1995b) also conducted numerical studied on the initiation and chaotic dynamics of the viscoelastic Rayleigh-Bénard convection (Oldroyd-B and up-convected Maxwell constitutive model were used) and pointed out that when We exceeds a certain critical value, the convective system will not appear in a steady state (Khayat, 1995a),

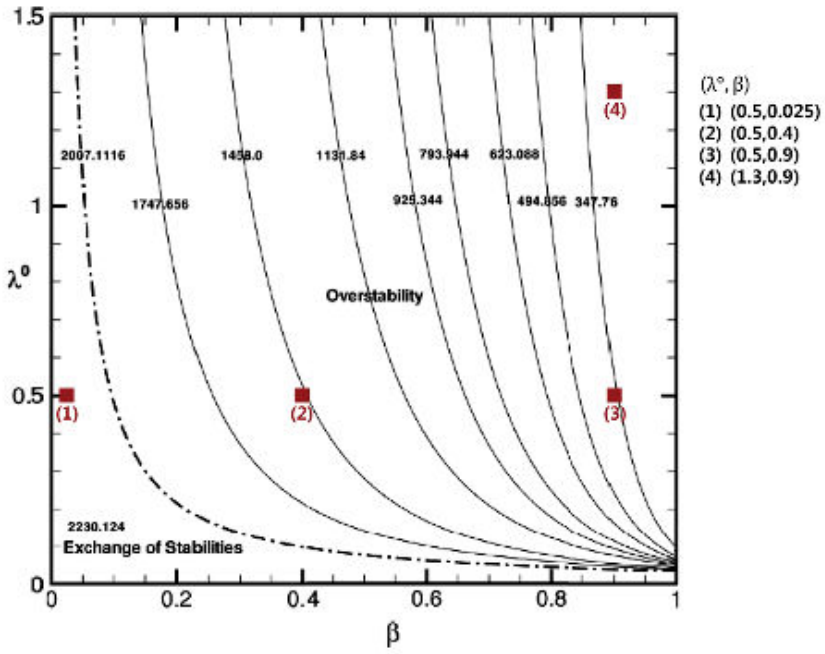

FIGURE 2.16: The cirtical Rayleigh number and the boundary separating exchange of stabilities and Hopf bifurcation in $\beta - \lambda^0$ plane in viscoelastic Rayleigh-Bénard convection with aspect ratio 2 : 1, where $\beta = \mu_{m0}/\mu_0$ is the retardation ratio (where μ_{m0} is the zero-shear rate molecular-contributed viscosity) and λ^0 is the relaxation time (Park and Ryu, 2002).

but the viscoelasticity promotes the initiation of convection and the transition of flow pattern (Khayat, 1995b).

2.2.3 Heat transfer enhancement or suppression

When Rayleigh number is large enough, the Rayleigh-Bénard convection enters a completely chaotic state. In this case, the stability analysis methods can not handle such strong nonlinear problems, so most of the studies currently use experimental research and numerical simulation methods.

Ahlers and Nikolaenko (2010) performed Rayleigh-Bénard convection experiment on a cylindrical container with $\Gamma = 1$, and used a poly-[ethylene oxide] (PEO) aqueous solutio as the experimental medium. With $Ra \in [5 * 10^9, 7 * 10^{10}]$ and different concentration of PEO, they found that as the solute concentration increases, the heat transfer effect becomes worse. Within the range of the test parameters, the heat transfer decay rate reaches a maximum of 10%. This result seems to be contrary to the conclusion of another study (Benzi, Ching, and De Angelis, 2010) about the effect of polymer additives on heat transfer in turbulent Rayleigh-Bénard convection. Benzi, Ching, and De Angelis (2010) numerically (direct numerical simulation) investigated the effects of the polymer additives on the heat transfer in turbulent Rayleigh-Bénard convective flows with $Pr \sim 1$ and $Ra \sim [10^{10}, 10^{13.5}]$. They found that increasing the Weissenberg number will lead to increased heat transfer capacity, and has a relationship $Nu \sim We^{\frac{3}{2}}$. Benzi and

Ahlers firstly proposed that the heat transport of turbulent viscoelastic fluid Rayleigh-Bénard convection should be divided into a central area (Bulk) and a boundary layer area (BL). They speculated that polymer additives can enhance the heat transfer in the central area of Rayleigh-Bénard convection and deteriorate it in the boundary layer area. The overall increase or deterioration depends on which area is the dominant flow.

In order to clarify this issue, researchers (Wei, Ni, and Xia, 2012; Xie et al., 2015; Benzi and Chu, 2011; Benzi et al., 2016) have begun to study the effects of polymers on the heat transfer in the central and boundary layer regions. Wei, Ni, and Xia (2012) conducted experiments in cylindrical cavities with smooth and rough bottom plates with $Ra \sim 10^9$, $Pr \sim 4.3$. Through calculating the dynamic energy dissipation rate and heat dissipation rate, they found that the central area of the convection in the cavity with a rough low plate is dominant rather than the boundary layer region, while the boundary layer region is the dominant flow in the convection with smooth boundary. The experimental results showed that in the smooth bottom plate case, Nu decreases (maximum 12.8%) with increasing polymer concentration, while in the rough bottom plate case, the large-scale circulation velocity (7% and 4% respectively) and Nu increase with polymer concentration.

In order to further reveal the mechanism of heat transfer enhancement caused by the central area, Xie et al. (2015) conducted experiments on a cylindrical square cavity with a rough bottom plate within a certain Ra range $(3.18 * 10^9, 7.43 * 10^9)$, and used thermistor and laser Doppler velocimetry (LDV) to measure temperature and velocity. By calculating the correlation coefficient between velocity and temperature, the results showed that polymer additives can enhance the heat transport of the coherent structure, and inhibit the heat transport of the incoherent structure. These two sets of experiments directly proved that polymer additives can enhance heat transfer in the central area of convection.

Benzi and Chu (2011) numerically investigated the effects of the polymer additives on the heat transfer in a laminar boundary layer, used an Oldroyd-B constitutive model and found that the increase in the viscosity of the boundary layer region leads to an increase in resistance, which slows down the horizontal and vertical flow and weakens heat transfer. Similar conclusions were also observed in the paper by Wei, Ni, and Xia (2012). Subsequent research by Benzi, Ching, and De Angelis (2016) did the same simulation except using a more accurate viscoelastic constitutive model, Finitely Extensible Nonlinear Elastic-Peterlin (FENE-P), and it is found that when the stretched length L is large, the viscoelastic fluid deteriorates heat transfer, and when the length L is small, the heat transport is enhanced. This result is also similar to that of the earlier work of Dubief (2010). Benzi, Ching, and De Angelis (2016) subsequently numerically studied the viscoelastic fluid Rayleigh-Bénard convection in 3D infinitely long parallel plates. They found that Nu showed a non-monotonic change with the Weissenberg number, and the evolute route can be divided into three sections: stable section; enhanced heat transfer section; and a weakened heat transfer section. The effect of viscoelastic on Rayleigh-B'enard convectiveis far from simple, and the mechanism of influence is not single. These issue still needs to be studied more deeply.

2.3 Conclusion

In this chapter, we firstly introduce the basic research status of Newtonian Rayleigh-Bénard convection, such as the critical Ra of convection onset, the transition of flow pattern, and the influence of parameters (Ra, Pr, A) on the flow structure and heat transfer capacity. In addition, some heat transfer enhancement techniques used in Rayleigh-Bénard convection are also introduced. Secondly, the effects of viscoelastic properties on flow and heat transfer in channel flow or in Rayleigh-Bénard convection are introduced, main focuses are on additives for drag-reduction and heat transfer enhancement or suppression. Finally, we summarized the current research status of viscoelastic Rayleigh-Bénard, and proposed the parts that need in-depth research in next stage .

Chapter 3

Flow modeling and numerical approach

Contents

In this chapter, we introduce the governing equations used and the simulation solver developed to numerically simulate the Rayleigh-Bénard convection with Newtonian or viscoelastic fluids. This chapter will be organized as follows. Firstly, the basic nature of fluids is introduced. Secondly, the governing equations will be presented, which include the mass conservation equation, momentum conservation equation, the energy conservation equation, and the

viscoelastic fluid constitutive equation. Thirdly, the numerical schemes applied to solve the governing equations will be illustrated, the solution process will also be shown. Finally, we do code validation by comparing the results obtained to the works of literature on the Newtonian and the viscoelastic Rayleigh-Bénard convection.

3.1 Introduction of non-Newtonian fluids

This part mainly explains the classification of fluids and the material properties of viscoelastic fluids.

3.1.1 Classification of fluids

Rheology is a science about the flow characteristics of matter. In the perspective of rheology, fluids are usually divided into Newtonian fluids and non-Newtonian fluids. The common fluids in our lives, such as water and air, are Newtonian fluids, they all show a simple linear relationship between shear stress and shear deformation, as presented by Eq. (3.1). Unlike the Newtonian fluids, non-Newtonian fluids exhibit a more complex nature between shear stress and shear deformation, not only related to deformation but also time-dependent. Depending on the different properties, non-Newtonian fluids can be divided into time-dependent viscosity fluid, non-Newtonian viscosity fluid, and viscoelastic fluid:

- **Newtonian fluids** is such a fluid: shear stress shows a linear relationship with shear deformation, which can be described as follows:

$$\boldsymbol{\tau} = \mu \frac{\boldsymbol{du}}{\boldsymbol{dy}} \tag{3.1}$$

  where $\boldsymbol{\tau}$ is the shear stress, μ is shear viscosity of the fluid, and $\frac{\boldsymbol{du}}{\boldsymbol{dy}}$ is the derivative of the velocity component which is parallel to the shear direction.

- **Generalized non-Newtonian fluid** The viscosity of generalized non-Newtonian fluid has a more complex relationship with the shear strain rate but has nothing to do with the shear time of the fluid. In view of this, the generalized non-Newtonian fluid is also called non-time-varying non-Newtonian fluid.

- **Time-dependent viscosity fluid** For a time-dependent viscosity fluid, the viscosity is determined by two items instead of one (different from non-Newtonian fluids), namely the shear strain rate and the shearing time.

- **Viscoelastic fluids** The viscoelastic fluid is between viscous fluid and elastic solid. They exhibit both viscous and elastic properties. Under the condition that the yield strength is not exceeded, the deformation energy is partially restored after the shear stress is removed.

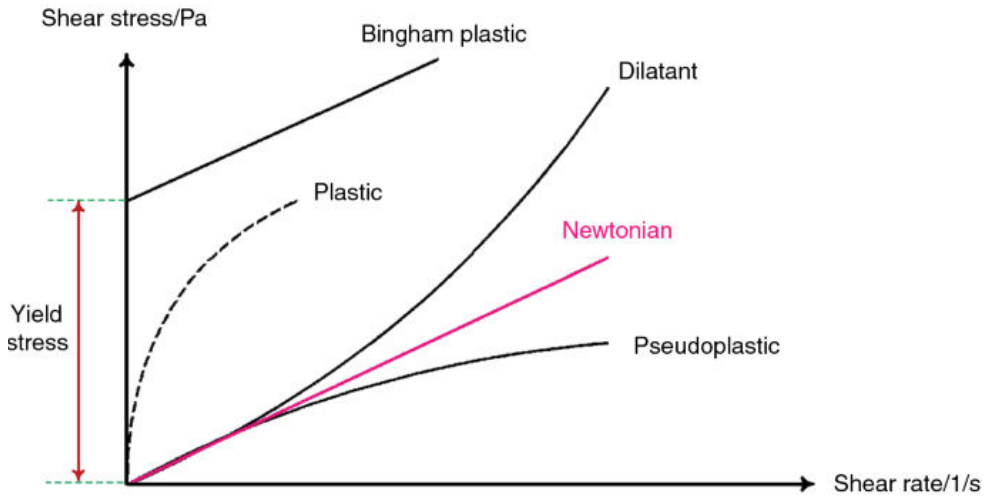

FIGURE 3.1: Flow curves of Newtonian and non-Newtonian fluids: Shear stress σ as functions of the shear rate $\dot{\gamma}$ (Yang and Du, 2019).

Fig. 3.1 shows the relationship between shear rate and shear stress of common non-Newtonian fluids. Most polymer solutions we met show characteristics of shear thinning, they belong to the class of pseudoplastic materials. And an example of common shear-thickening (Dilatant) fluids is cornstarch in water. The viscoelastic fluids we studied in the present work belong to pseudoplastic material.

3.1.2 Microstructure of viscoelastic fluids

We can consider that viscoelastic fluid is understood as a certain concentration of macromolecular structure in Newtonian fluid. Viscoelastic fluid exhibits more complex rheological behavior than Newtonian fluids, due to the existence of macromolecular structures. Therefore, a simple viscous continuous medium model (such as water) is not sufficient to represent the rheological behavior of viscoelastic fluids. Taking into account the contribution of macromolecular in viscoelastic fluids, many excellent constitutive models have been or are derived by modeling the behavior of the polymer macrostructures. Two main macrostructure models are shown below:

- **Spring-dumbbell model**

  This model is the simplest macrostructure model, derived from the Hookean dumbbells model, which treats the molecular structure as spring-dumbbell: chains contain beads connected with elastic springs, as shown in Fig 3.2a. The interaction between the polymer and the fluid is reflected by the interaction force imposed on the dumbbell, and the molecular elasticity changes are reflected by the internal spring. We can understand this model as stochastic spring-dumbbells scattered in a Newtonian fluid. The main representative of this model is the Oldroyd-B model, as shown in Fig 3.2a.

- **Network model**

The network theory was originally extended into viscoelastic study by Phan-Thien and Tanner (1977), who derived the PTT constitutive model (we used in this dissertation) from this network model. This model assumes that the polymer is represented by a network consisting of nodes connected by spring junctions, as shown in Fig. 3.2b. The movement of the nodes represents the effect of the flow on the polymer.

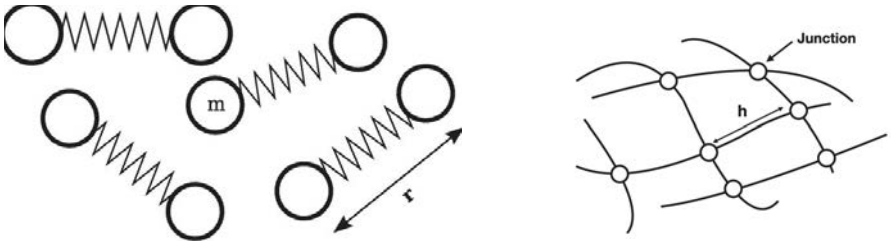

(A) Spring-dumbbell model. (B) Network model.

FIGURE 3.2: Polymer macro-structure models.

3.1.3 Rheology parameters

Due to the existence of viscoelastic effects, viscoelastic fluids have flow characteristics very different from Newtonian fluids, and produce their unique flow phenomena, such as rod climbing, swell, tubeless siphon, Kaye effect, and shear-thinning phenomenon. To describe the characteristics of viscoelastic fluids, several important parameters are introduced here: viscosity ratio, relaxation time, and normal stress difference.

- **Solvent viscosity, solute viscosity and viscosity ratio** (β) In viscoelastic fluids, ν_0 is defined as the viscosity with shear rate equal to zero, and described as:

$$\nu_0 = \nu_s + \nu_p \tag{3.2}$$

where ν_s is solvent viscosity and ν_p is solute viscosity(namely the contribution of polymer). Naturally, a new dimensionless number β is induced, which describes the ratio between viscosity of the solvent ν_s and viscosity with zero shear rate ν_0:

$$\beta = \frac{\nu_s}{\nu_0} = \frac{\nu_s}{\nu_s + \nu_p} \tag{3.3}$$

- **Relaxation time (λ)** As mentioned above, the rheology behavior of viscoelastic fluids have the time-dependent feature, because the stretching and shrinking behaviors of macromolecular structures in viscoelastic fluids at one moment are impacted by flow history. An important physical quantity in a viscoelastic fluid is proposed: λ relaxation time. For Newtonian fluids, the stress on the fluid micelles disappeared immediately when the strain was suddenly removed. However, the stress on the micelles of the viscoelastic fluid

only disappeared after a relaxation time λ and furthermore its time evolution is not linear. In order to describe the rheology behaviour, the dimensionless quantity Weissenberg number We, is induced:

$$We = \frac{\lambda U_c}{H} \tag{3.4}$$

where U_c is the characteristic velocity (m/s) and H is the characteristic length (m). We describes the ratio between the elastic forces to the viscous forces.

- **Normal stress differences** Another important variable defined for viscoelastic is the normal stress difference, which is the main behavior of elascity. The normal stress differences are defined as:

$$N_1 = \tau_{11} - \tau_{22} \tag{3.5}$$

$$N_2 = \tau_{22} - \tau_{33} \tag{3.6}$$

where τ_{11}, τ_{22} and τ_{33} are the normal stresses on $x-$, $y-$ and $z-$ directions, respectively, (Pa). In Newtonian fluid, the normal stress differences all equal zero $N_1 = N_2 = 0$, but in viscoelastic fluid, they exist and are not equal to zero.

3.1.4 Viscoelastic constitutive models

At present, the most commonly used viscoelastic constitutive models are Oldroyd-B, Gieseskus, and Phan-Thien-Tanner models. Gieseskus model can be obtained through the simplification of the Phan-Thien-Tanner model, so this subsection mainly describes Oldroyd-B and Phan-Thien-Tanner constitutive models.

- **Oldroyd-B constitutive model**

  The Oldroyd-B fluid is one of the most simplified constitutive models that can describe the viscosity and elasticity behaviors of the fluids, it is derived by taking into account extra stress in the governing equations of Navier-Stokes equation and Upper-convected Maxwell model (one of the Maxwell models), the latter is the most popular linear viscoelastic model. The model can be written as

$$\overset{\nabla}{\boldsymbol{\tau_p}} = \frac{1}{\lambda}\boldsymbol{\tau_p} + 2\frac{\mu_p}{\lambda}\boldsymbol{D} \tag{3.7}$$

  where:

  - $\boldsymbol{\tau_p}$ is the elastic extra stress tensor
  - $\boldsymbol{D}$ is the deformation rate tensor, strain rate tensor, $\boldsymbol{D} = \frac{1}{2}(\nabla \boldsymbol{u} + \nabla \boldsymbol{u^T})$, $\boldsymbol{u}$ is the fluid velocity

- λ is the relaxation time
- μ_p is the elastic viscosity
- $\overset{\nabla}{\langle \bullet \rangle}$ is an operator that describe upper convected time derivative of the stress tensor:

$$\overset{\nabla}{\boldsymbol{\tau_p}} = \frac{\partial}{\partial t}\boldsymbol{\tau_p} + \boldsymbol{u} \cdot \nabla \boldsymbol{\tau_p} - ((\nabla \boldsymbol{u})^T \cdot \boldsymbol{\tau_p} + \boldsymbol{\tau_p} \cdot (\nabla \boldsymbol{u})) \tag{3.8}$$

- **Phan-Thien-Tanner constitutive model**

  The PTT model is also derived from the Maxwell model, by introducing the elongation behavior of the macromolecular structure and the slip behavior between molecules. The constitutive equation is shown in Eq. (3.9).

$$\overset{\nabla}{\boldsymbol{\tau_p}} = \frac{1}{\lambda}\boldsymbol{\tau_p} + 2\frac{\mu_p}{\lambda}\boldsymbol{D} - \frac{\epsilon}{\mu_p} tr(\boldsymbol{\tau_p})\boldsymbol{\tau_p} - \xi(\boldsymbol{D}\boldsymbol{\tau_p} + \boldsymbol{\tau_p}\boldsymbol{D}) \tag{3.9}$$

  where:

  - ϵ represents the elongation behaviour of the polymer
  - ξ represents the slip behaviour among polymer molecula

There are still many studies aiming at constructing constitutive models that can better describe the flow characteristics of viscoelastic fluids. The methods used are the followings: 1) mechanical comparison, 2) adding nonlinear term, 3) model modification, 4) irreversible thermodynamic.

3.2 Governing equations

The Rayleigh-Bénard convection is one of the most classical physical phenomena, which involve in both fluid flow and heat transfer. All the physical processes in a continuous medium involving fluid flow and heat transfer must conform to three fundamental physical laws: mass conservation; momentum conservation and energy conservation. The definition of the above three physical laws are described as below:

- **Mass conservation**, in any material system isolated from the surroundings (isolated system), no matter what changes or processes occur, its total mass remains unchanged.
- **Momentum conservation**, a system is not subject to external forces or the sum of external forces is zero, the total momentum of this system remains unchanged. More generally the rate of change of momentum in a system is equal to the resultant fore acting on the system.

- **Energy conservation**, energy will neither be produced nor vanished, it will only transform from one form to another, or from one object to another, while the total amount of energy remains the same.

In order to better understand the applicability of the above conservation laws, we should know the scale classification of the materials and the continuous mechanics. We know that the smallest units of the fluids are molecules, molecules consist of things and are separated by space. On the microscopic scale, the fluids are noncontinuous. But we observe objects or phenomena from a macroscopic scale, which is much larger than the molecular scale. On the macroscopic scale, certain objects or physical phenomena can be considered as continuous, meaning the matter is continuously distributed and fills over the space. This continuous matter can be divided into subunit, and each subunit has the same physical properties as the whole.

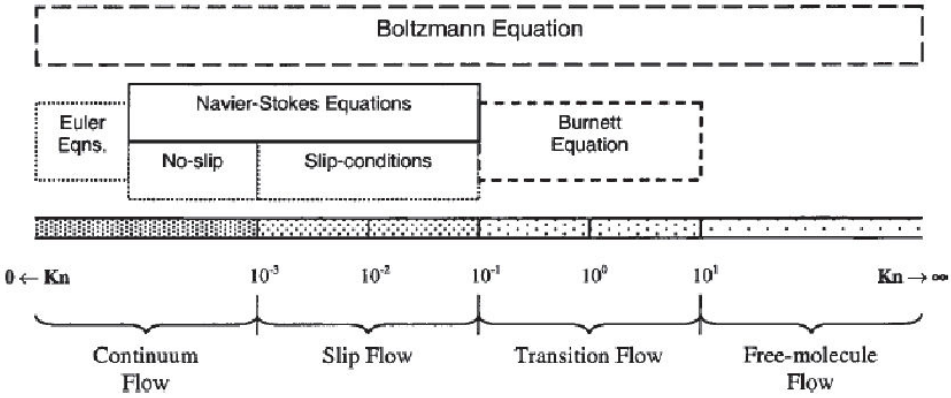

FIGURE 3.3: Applicability range of the numerical model corresponding to the Knudsen number (Ivanov, Bondar, and Markelov, 2007).

Based on the above description, a dimensionless number, the Knudsen number (Kn), has to be introduced to make the analytical method used in this thesis more understandable. Knudsen number ($Kn = \lambda/L$) describes the ratio of the mean free path length of the molecular (λ) to the physical characteristic length scale (L) and helps us determine which mechanical model (statistical mechanics (microscopic scale) or continuous mechanics (macroscopic scale)) to use to discuss physical processes.

The regime classification of fluid flow by Kn is shown in Fig. 3.3. For $Kn > 10$, the flow can be defined as free molecular flow, where the mean free path of the molecular is larger than the length scale of the fluid, the flow is in a transition state between the free molecule and continuous regimes. For $0.001 < Kn < 0.1$, the flow is in a slip flow regime, which means the fluid flow is in a continuous state, but the boundary slip needs to be considered. For $Kn < 0.001$, The flow is in a continuous regime, where the mean free path of the molecular is much smaller than the length scale of the flow. The present work concerns the continuous regime.

3.2.1 Mass conservation

It is assumed that there is an infinitesimal element of fluid in the fluid flow, as mentioned above. The law of mass conservation requires that the mass of the element is constant $\delta m = \rho \delta V$, means that the mass increase of the element within a united time is equal to the mass input at the same time, where δm is mass of the fluid element, ρ is the density of the fluid and the δV is the volume of the element, shown in Fig. 3.4. This can be expressed as:

$$\frac{D(\delta m)}{Dt} = 0 \tag{3.10}$$

where $\frac{D(\cdot)}{Dt} = \frac{\partial(\cdot)}{\partial t} + (\boldsymbol{u} \cdot \nabla)(\cdot)$ is the material derivative, with $\boldsymbol{u} = (u, v, w)$ the velocity vector. Substituting $\delta m = \rho \delta V$ into Eq. (3.10), we obtain:

$$\frac{D\rho}{Dt} + \rho[\frac{1}{\delta V}\frac{D\delta V}{Dt}] = 0 \tag{3.11}$$

The rate of volume change ($\frac{1}{\delta V}\frac{D\delta V}{Dt}$) can be written as the divergence of flow velocity ($\boldsymbol{\nabla} \cdot \boldsymbol{u}$).

$$\frac{D\rho}{Dt} + \rho \boldsymbol{\nabla} \cdot \boldsymbol{u} = 0 \tag{3.12}$$

Under Boussinesq approximation (explained in Sec. 3.2.2), Eq. (3.11) can be presented as:

$$\boldsymbol{\nabla} \cdot \boldsymbol{u} = 0 \tag{3.13}$$

Eq. (3.13) is a divergence form of the continuous equation, it is derived based on the infinitesimal fluid elements move with fluid flow.

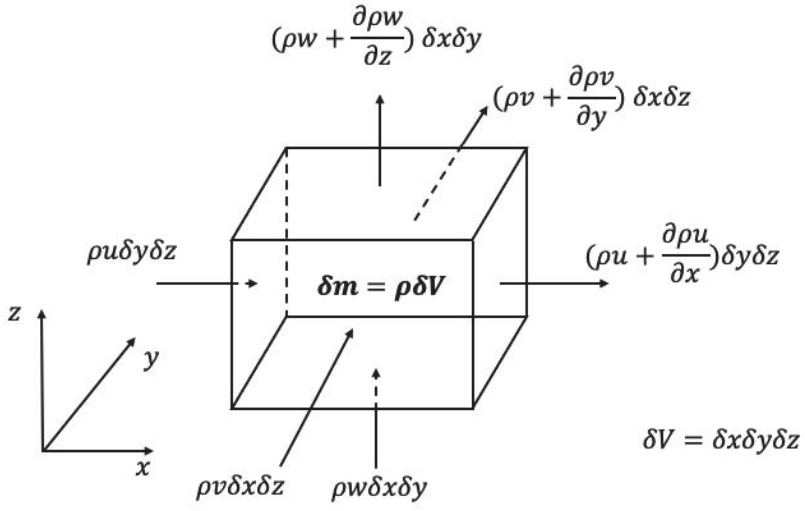

FIGURE 3.4: The conservation of mass in an infinitesimal control volume of fluid.

3.2.2 Momentum equation and Boussinesq approximation

The momentum equation is derived by introducing Newton's second law ($\boldsymbol{F_x} = m\boldsymbol{a_x}$, where m is the mass of the object, $\boldsymbol{F_x}$ and $\boldsymbol{a_x}$ are the force and acceleration of the movement in direction x), which describes the sum of the forces acting on the fluid elements is equal to the mass of the elements multiplied by the acceleration of the movement. The forces acting on the elements mainly are surface force (such as shear and normal stress on the surface) and bulk force (such as gravity). The equation with incompressible restriction can be expressed as:

$$\rho_0 \frac{\partial \boldsymbol{u}}{\partial t} + \boldsymbol{u}\boldsymbol{\nabla}\cdot\boldsymbol{u} = -\boldsymbol{\nabla}\boldsymbol{p} + \boldsymbol{\nabla}\cdot\boldsymbol{\sigma} - \rho g e_z \tag{3.14}$$

where $\boldsymbol{u}$, $\boldsymbol{p}$, g stand for the velocity vector, the pressure, the gravitational acceleration, respectively. e_z is the unit vector in the vertical direction. The last term of Eq. (3.14) will be treated by the Oberbeck-Boussinesq approximation, which will be shown below. The total stress $\boldsymbol{\sigma}$ can be expressed as:

$$\boldsymbol{\sigma} = \begin{cases} \boldsymbol{\tau_s} & \text{Newtonian fluids} \\ \boldsymbol{\tau_s} + \boldsymbol{\tau_p} & \text{Viscoelastic fluids} \end{cases} \tag{3.15}$$

where $\boldsymbol{\tau_s}$ and $\boldsymbol{\tau_p}$ are force contribution of the Newtonian solvent and embedded polymeric long chain molecules, respectively. In Newtonian fluids, $\boldsymbol{\tau_p}$ does not exist, and the solvent contribution $\boldsymbol{\tau_s} = \mu_s \boldsymbol{D}$ is well known.

- **Boussinesq approximation** The Boussinesq approximation is widely used in buoyancy-driven flow, the density differences in the gravity term of momentum equation are considered, while in the other terms,they are neglected. The Boussinesq approximation is valid only when $\Delta\rho << \rho_o$. Under the Boussinesq approximation, we have the relation $\rho = \rho_0[1 - \alpha(T - T_0)]$, where α is coefficient of thermal expansion. Eq. (3.14) can be rewritten as

$$\rho_0 \frac{\partial \boldsymbol{u}}{\partial t} + \boldsymbol{u}\boldsymbol{\nabla}\cdot\boldsymbol{u} = -\boldsymbol{\nabla}\widetilde{\boldsymbol{p}} + \boldsymbol{\nabla}\cdot\boldsymbol{\sigma} + \rho_0\alpha(T - T_0)ge_z \tag{3.16}$$

  where $\widetilde{p} = p - \rho_0 g e_z$

3.2.3 Energy equation and temperature equation

The energy equation also can be derived by the perspective of infinitesimal element of the fluid. For the infinitesimal fluid elements following the flow, the energy conservation law describes that the energy change inside the fluid element is equal the net heat input plus the power of the work done by volume and surface force on the volume:

$$\Delta(U + E^{kin}) = Q - W \tag{3.17}$$

where,

- ΔU: internal energy change in the element
- ΔE^{kin}: kinetic energy change
- Q: heat input
- W: work done by the element

If we expand the terms in Eq. (3.17) from the perspective of interaction between infinitesimal element and the surrounding fluid, we obtain,

$$\frac{\partial}{\partial t}[\rho(e+\frac{1}{2}v^2)]+\nabla\cdot[\rho\boldsymbol{v}(e+\frac{1}{2}v^2)]=\nabla\cdot q+\nabla\cdot(\sigma\cdot\rho\boldsymbol{v})+\rho\boldsymbol{v}\cdot\boldsymbol{F} \tag{3.18}$$

where,

- ρ is the density
- e is the internal energy per unit mass
- $\boldsymbol{v}$ is the velocity vector
- v^2 is the square of the velocity magnitude
- $\boldsymbol{q}$ is the conductive heat flux vector ($q=-k\nabla T$), k is the thermal conductivity and T is the temperature
- σ is the total stress tensor, including pressure and extra stress tensor $\sigma=(-p\boldsymbol{I}+\boldsymbol{\tau_s})+\tau_p$
- $\boldsymbol{F}$ is the body force per unit mass; i.e., the gravity $g\boldsymbol{e_z}$

The terms on the left-hand side of Eq. (3.18) are the rate of energy change per unit element. The terms on the right-hand side of Eq. (3.18) are the net heat conduction input into the element, the work done by the total stress tensor, the work done by body forces, respectively.

By considering that the conduction heat transfer is governed by Fourier's law, the energy equation can also be written with enthalpy, as Eq. (3.19), where enthalpy is related to internal energy as $h=e+p/\rho$.

$$\rho[\frac{\partial h}{\partial t}+\nabla\cdot(h\boldsymbol{u})]=-\frac{Dp}{Dt}+\nabla\cdot(k\nabla T)+\phi \tag{3.19}$$

where ϕ is the dissipation of the element work on the element by the viscous and extra tensor, which is irreversibly converted into internal energy,

$$\phi=\tau_s:\nabla\boldsymbol{u}+(\tau_p:\nabla)\boldsymbol{u} \tag{3.20}$$

The pressure term on the RHS of Eq. (3.19) is usually neglected. If the dissipation can be neglected, the energy conservation equation can be simplified to

$$\rho c_p[\frac{\partial T}{\partial t} + (\boldsymbol{u}\cdot\nabla)T] = k\nabla^2 T + \phi \tag{3.21}$$

where c_p is the specific heat at constant pressure. By using the Boussinesq approximation in Eq. (3.21) and ignoring the dissipation by viscous forces, we can get,

$$\frac{\partial T}{\partial t} + (\boldsymbol{u}\cdot\nabla)T = \frac{k}{\rho_0 c_p}\nabla^2 T \tag{3.22}$$

3.2.4 Viscoelastic constitutive equations

The polymeric contribution to the stress, $\boldsymbol{\tau_p}$, is the molecular extra-stress tensor and can be obtained by a different viscoelastic constitutive equation, as explained in Sec. 3.1.4. These viscoelastic constitutive models can be cast in one general viscoelastic constitutive equation:

$$\frac{\partial \boldsymbol{\tau_p}}{\partial t} + (\boldsymbol{u}\cdot\nabla)\boldsymbol{\tau_p} - \nabla\boldsymbol{u}^T\cdot\boldsymbol{\tau_p} - \boldsymbol{\tau_p}\cdot\nabla\boldsymbol{u} = \frac{1}{\lambda}\boldsymbol{\tau_p} + 2\frac{\mu_p}{\lambda}\boldsymbol{D} + A[-\frac{\epsilon}{\mu_p}tr(\boldsymbol{\tau_p})\boldsymbol{\tau_p} - \xi(\boldsymbol{D}\boldsymbol{\tau_p} + \boldsymbol{\tau_p}\boldsymbol{D})] \tag{3.23}$$

It is called the PTT model. Different values of the model parameters will allow to recover particular viscoelastic constutive models,

- $A = 0$: Oldroyd-B model
- $A \neq 0, \xi = 0, \epsilon \neq 0$: Giesekus model
- $A \neq 0, \xi \neq 0, \epsilon \neq 0$: PTT model

3.2.5 Boundary conditions

According to the physical conditions on the boundary, there are three types boundary conditions:

- First-type boundary condition: A boundary condition which specifies the value of the function itself, is also called Dirichlet boundary condition.
- Second-type boundary condition: A boundary condition which specifies the value of the normal derivative of the function, is also called Neumann boundary condition.
- Third-type boundary condition: A boundary condition which specifies the combination of the two previous is also called the Robin boundary condition.

The problems studied in this thesis concern a cavity filled with a viscoelastic fluid and they are defined on the computational domain Ω: $(x, y) \in [0, L] \times [0, H]$ The velocity boundary conditions are no slip (the first-type boundary condition), the velocity of the fluid at the boundary is

equal to zero. The thermal boundary conditions are adiabatic (the second-type boundary condition) on the vertical walls and isothermal (the first-type boundary condition) on the horizontal walls:

- at $y = 0$: $u_1 = u_2 = 0,\ T = T_0$
- at $y = H$: $u_1 = u_2 = 0,\ T = T_1$
- at $x = 0,\ L$: $u_1 = u_2 = 0,\ \frac{\partial T}{\partial x} = 0$

There is no boundary condition for the pressure (p) and the elastic stress $\boldsymbol{\tau}$.

3.3 Numerical integration

3.3.1 Nondimensionalization

The following scale factors are introduced to non-dimensionalize the governing field equations: H the cavity height for length, $U_c = \frac{\kappa}{H}\sqrt{Ra}$ the reference velocity for velocity, H/U_c for time, $T_0 - T_1$ for temperature difference, $\rho_0 U_c^2$ for pressure and shear tensor. Here Ra is the Rayleigh number defined as $Ra = \alpha g \Delta T H^3/\nu\kappa$, $\kappa = k/\rho_0 C_p$ is the thermal diffusivity and ν is the kinematic viscosity of the working fluid. Using the scaling factors, we can define the folows dimensionless variables:

$$x^* = \frac{x}{H},\ t^* = t\frac{U_c}{H},\ \boldsymbol{u^*} = \frac{\boldsymbol{u}}{U_c},\ T^* = \frac{T - T_1}{T_0 - T_1},\ p^* = \frac{p}{\rho_0 U_c^2} \text{ and } \boldsymbol{\tau_p^*} = \frac{\boldsymbol{\tau_p}}{\rho U_c^2}$$

In order to simplify the notation, we drop hereafter * from all the dimensionless variables and formulas. The dimensionless governing equations are then rewritten as:

$$\nabla \cdot \boldsymbol{u} = 0 \tag{3.24}$$

$$\frac{\partial \boldsymbol{u}}{\partial t} + (\boldsymbol{u}\cdot\nabla)\boldsymbol{u} = -\nabla p + \beta\frac{Pr}{\sqrt{Ra}}\Delta\boldsymbol{u} + \nabla\cdot\boldsymbol{\tau_p} + PrT\boldsymbol{e_j} \tag{3.25}$$

$$\overset{\nabla}{\boldsymbol{\tau}}_{\boldsymbol{p}} + \frac{\boldsymbol{\tau_p}}{We\sqrt{Ra}} - 2\frac{1-\beta}{Ma^2}\boldsymbol{D} = A[-\epsilon\frac{\sqrt{Ra}}{(1-\beta)Pr}tr(\boldsymbol{\tau_p})\boldsymbol{\tau_p} - \xi(\boldsymbol{D}\boldsymbol{\tau_p} + \boldsymbol{\tau_p}\boldsymbol{D})] \tag{3.26}$$

$$\frac{\partial T}{\partial t} + (\boldsymbol{u}\cdot\nabla)T = \frac{1}{\sqrt{Ra}}\triangle T \tag{3.27}$$

where $\beta = \mu_s/\mu_0$ is the ratio of solvent viscosity to total viscosity $\mu_0 = \mu_s + \mu_p$, $Pr = \mu_0 C_p/k$ is the Prandtl number, $We = \lambda\kappa/H^2$ the Weissenberg number and the Mach number $Ma = \sqrt{RaWe/Pr}$ which describes the ratio of the characteristic velocity of the flow to the shear wave speed. Furthermore, we can introduce an elastic number $E = Re/We = \sqrt{Ra}/PrWe$.

We point out that due to the definition of the reference velocity $U_c = \frac{\kappa}{H}\sqrt{Ra}$ in this paper, the natural way to define We is to use U_c as has been done by Cheng et al. (2017). The drawback

Ra	$\alpha g \Delta T H^3/\nu\kappa$	β	μ_s/μ_0	Re	$\sqrt{Ra}/Pr$
Pr	$\mu_0 C_p/k$	We	$\lambda\kappa/H^2$	E	$\sqrt{Ra}/PrWe$

TABLE 3.1: Summary of dimensionless numbers

of using U_c to define We is that the defined We will change with Rayleigh number. In this thesis a definition of We independent of Ra, $We = \lambda\kappa/H^2$, was used: for example for $Ra = 1600$ and $We = 0.1$ in the present work the equivalent Weissenberg number is $We = 10.58$ in the work by Cheng et al. (2017) and Li et al. (2017) (in their work $U_c = \sqrt{\alpha g H \Delta T}$).

3.3.2 Meshing and approximating derivatives

A closed-form mathematical expression, such as a function, or a differential equation, or an integral equation of a function, is regarded as continuous in a certain area and has infinite number of values. The essence of discretization is to approximate it with another similar expression, but this approximate expression only specifies a value on a limited number of discrete points or control bodies in the area. The analytical solution of the partial differential equation is a closed-form expression, which describes the continuous change of the function in the region. On the contrary, the numerical solution can only give results on discrete points in the area, and these discrete points are called grid points.

For better understanding, Fig. 3.5 shows a set of discretized grid points in the $x-y$ of the Cartesian coordinate system. In Fig. 3.5, the intervals of each node in both x and y direction are the same, which are Δx and Δy respectively. In fact, Δx and Δy do not have to be constants. The grid is marked with i in the x direction and j in the y direction. If the mark P point is (i, j), then the points around P point are $(i+1, j)$, $(i-1, j)$, $(i, j+1)$, $(i, j-1)$ respectively. At this time, the physical quantities we need are stored on grid nodes similar to P. In other words, continuous physical quantities in the physical field are represented by discrete physical quantities on grid points.

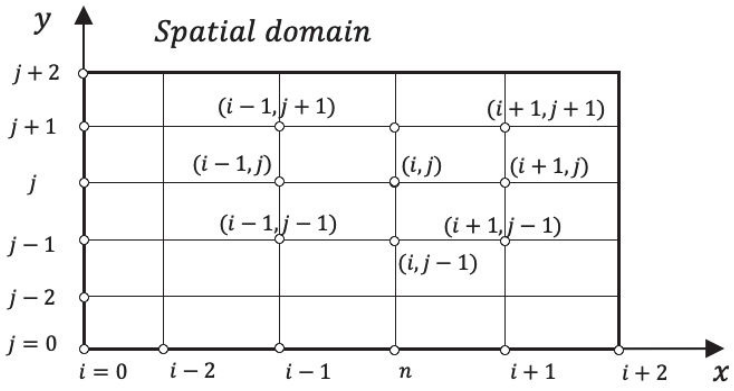

FIGURE 3.5: The finite difference method spatial grid

The finite difference method is a kind of numerical analysis scheme, its purpose is to obtain a numerical solution that is close to the real solution by solving discrete equations. The discrete equations are obtained through approximating derivatives with finite differences. The calculating domain is divided into a finite number of cells, and variables information are stored in the junctions. The calculating time is also discretized into a finite number of steps. The value of the solution at these discrete points is approximately obtained by solving discrete equations including finite differences and values from nearby junctions.

For the finite difference method, the nodes are located on the corner points of the sub-regions, and the clusters of curves dividing the sub-regions are grid lines. In order to determine the control volume of each node, it is necessary to draw a boundary line at the middle position of the adjacent nodes, and these interface lines constitute the control volume of each node. In the process of simulation evolution along the timeline, the discretization in space at each time level is the same as shown in Fig. 3.6 for a uniform grid.

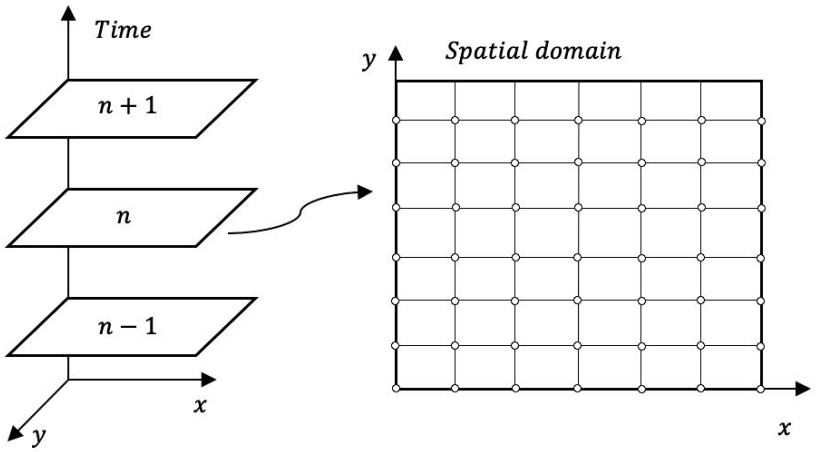

FIGURE 3.6: time evolution

The general form of the reciprocal finite difference can be derived using Taylor series expansion. As shown in Fig. 3.5, the first order partial derivative velocity at position (i, j) can be expressed as

$$f_{i+1,j} = f_{i,j} + \frac{\partial f}{\partial x}|_{i,j}(x_{i+1,j} - x_{i,j}) + \frac{\partial^2 f}{\partial x^2}|_{i,j}\frac{(x_{i+1,j} - x_{i,j})^2}{2} + \frac{\partial^3 f}{\partial x^3}|_{i,j}\frac{(x_{i+1,j} - x_{i,j})^3}{6} + \cdots \tag{3.28}$$

after considering the uniform grid, Eq. (3.28) can be write as

$$f_{i+1,j} = f_{i,j} + \frac{\partial f}{\partial x}|_{i,j}(\Delta x) + \frac{\partial^2 f}{\partial x^2}|_{i,j}\frac{\Delta x^2}{2} + \frac{\partial^3 f}{\partial x^3}|_{i,j}\frac{\Delta x^3}{6} + \cdots \tag{3.29}$$

If the above algebraic difference is used as an approximation of the partial derivative, we have

$$\frac{\partial f_{i,j}}{\partial x} = \frac{f_{i+1,j} - f_{i,j}}{\Delta x} + \frac{\partial^2 f_{i,j}}{\partial x^2}\frac{\Delta x}{2} + \frac{\partial^3 f_{i,j}}{\partial x^3}\frac{\Delta x^2}{6} + \cdots \tag{3.30}$$

and the truncation error is order of $O(\Delta x)$,

$$\frac{\partial f}{\partial x}|_{i,j} = \frac{f_{i+1,j} - f_{i,j}}{\Delta x} + O(\Delta x) \tag{3.31}$$

where the symbol $O(\Delta x)$ is mathematically representing "a term of the same order as Δx". Eq. (3.31) is called the first order forward difference of the derivate $(\frac{\partial f_{i,j}}{\partial x})$. Here, we display several common and used in this thesis discrete schemes:

1st order upwind scheme (Δx):

$$\frac{\partial f_{i,j}}{\partial x} = \begin{cases} \frac{f_{i+1,j}-f_{i,j}}{\Delta x} \\ \frac{f_{i,j}-f_{i-1,j}}{\Delta x} \end{cases} \tag{3.32}$$

2nd order central difference scheme (Δx^2):

$$\frac{\partial f_{i,j}}{\partial x} = \frac{f_{i+1,j}-f_{i-1,j}}{2\Delta x} \tag{3.33}$$

$$\frac{\partial f^2_{i,j}}{\partial x^2} = \frac{f_{i+1,j}-2f_{i,j}+f_{i-1,j}}{\Delta x^2} \tag{3.34}$$

2nd order upwind scheme (Δx^2):

$$\frac{\partial f_{i,j}}{\partial x} = \begin{cases} \frac{-3f_{i,j}+4f_{i+1,j}-f_{i+2,j}}{2\Delta x} \\ \frac{3f_{i,j}-4f_{i-1,j}+f_{i-2,j}}{2\Delta x} \end{cases} \tag{3.35}$$

3rd order high order upstream central scheme (Δx^3):

$$\frac{\partial f_{i,j}}{\partial x} = \begin{cases} \lambda\frac{f_{i-2,j}-6f_{i-1,j}+3f_{i,j}+2f_{i+1,j}}{6\Delta x_1} & \text{if} \quad \lambda > 0 \\ \lambda\frac{-2f_{i-1,j}-3f_{i,j}+6f_{i+1,j}-f_{i+2,j}}{6\Delta x_1} & \text{if} \quad \lambda < 0 \\ 0 \quad \text{otherwise} \end{cases} \tag{3.36}$$

3.3.3 Quasi-linear treatment

For viscoelastic fluid flow, the complexity is not only reflected by the fact that it is different from Newtonian fluid in the flow and heat transfer, but also in the process of numerical simulation. The numerical difficulties lie mainly in (a) the constitutive equation of viscoelastic fluids that can accurately reflect the actual elastic response; (b) the sufficient numerical stability of coupling the Navier-Stokes equation and constitutive equation of viscoelastic fluids.

So far, the numerical simulation methods for viscoelastic fluid flow mainly include molecular dynamics method (Jin, 2007), Monte Carlo method (Xu, Ding, and Yang, 1997; Xu, Ding,

and Yang, 2000), Brownian dynamics method (Somasi et al., 2002), Smoothed Particle Hydrodynamics method (Ye et al., 2019) and direct numerical simulation method (Tsukahara et al., 2011). Apart from direct numerical simulation methods, the other numerical methods are all from a microscopic perspective, considering the interaction of viscoelastic particles to describe the state of viscoelastic fluid molecules in the flow, and they need huge computer resources.

In the process of solving the viscoelastic fluid flow by direct numerical simulation, because the constitutive equation of the viscoelastic fluid is a hyperbolic equation and lacks a viscous dissipation term, there will be physical discontinuities in the elastic stress tensor, which may cause great elastic deformation. This problem will cause calculation instability when simulating the cases with high Weissenberg number (Keunings, 1987). In order to avoid this problem, some scholars added an artificial viscosity term into the viscoelastic constitutive equation (Sureshkumar and Beris, 1995; Zhang et al., 2016). This operation increases the elastic dissipation and reduces the elastic stress gradient, but it also makes the calculation result untrue. It is found that using a suitable discrete scheme for the convection term in the viscoelastic constitutive equation can effectively improve the stability of the calculation.

MINMOD method: Min, Yoo, and Choi (2001) proposed that the use of a third-order compact welcome style and the introduction of local artificial viscosity can ensure the stability and accuracy of the calculation. Yu and Kawaguchi (2004) tried to solve the problem by a MINMOD (Zhu and Rodi, 1991) discrete scheme, but it is found that this method cannot guarantee the symmetric positive definite nature of the conformation tensor, and it still cannot carry the large We situation. In order to ensure the symmetrical positive definite nature of the conformation tensor, Kurganov and Tadmor (2000) proposed the K-T format of the central difference, which was further improved by Vaithianathan et al. (2006), so that the conformation tensor can always be positive and symmetric.

Log-conformation reformulation: Fattal and Kupferman (2004) and Fattal and Kupferman (2005) believe that the fundamental reason for the emergence of the High Weissenberg Number Problem (HWNP) is that the direct polynomial fitting solution to the conformation tensor transport equation is only valid when We is small. When We increases to a certain value, the growth of the conformation tensor is of exponential type, the polynomial fitting method is no longer applicable, resulting in an increased error and unstable calculation. As any symmetric positive definite matrix can be decomposed into the form of $A = D\Lambda D^T$, therefore a logarithmic reconstruction method is proposed. First, a simple logarithmic transformation is performed on the conformation tensor, and then the output of the transformed conformation tensor index is solved. In this way, the solution of tensor multiplication is transformed into the form of a solution of tensor exponent addition, which greatly reduces the error caused by the polynomial fitting. The logarithmic reconstruction method of conformation has become the most effective method to solve High Weissenberg Number Problem at present. In the process of solving the constitutive equation, it can not only ensure the symmetric positive definiteness of the conformation tensor but also calculation error of eliminate the conformation tensor under high We (Hulsen, Fattal, and Kupferman, 2005; Afonso et al., 2009; Balci et al., 2011).

Quasi-linear treatment: This treatment has been developed by Hagani (2021) and is used in the present work.

To simplify the numerical process, we firstly reorganized for 2D cases Eq. (3.25) and Eq. (3.26) into a quasi-linear system by separating the homogeneous part and the source term:

$$\frac{\partial W}{\partial t} + \sum_{i=1}^{2} A_i \frac{\partial W}{\partial x_i} = S_{ql} \tag{3.37}$$

where $W = [u_1, u_2, \tau_{11}, \tau_{12}, \tau_{22}]$ is the vector of variables including velocity components u_i and extra-stress components τ_{ij}. S_{ql}, the source term, includes pressure, buoyancy and viscous terms of the momentum equation and feature terms of the PTT constitutive equation and is written as

$$S_{ql} = \begin{bmatrix} -\nabla p + \beta \frac{Pr}{\sqrt{Ra}} \Delta \boldsymbol{u} + PrT\boldsymbol{e_j} \\ \frac{-\boldsymbol{\tau_p}}{We\sqrt{Ra}} - A[\frac{\epsilon\sqrt{Ra}}{(1-\beta)Pr} tr(\boldsymbol{\tau_p})\boldsymbol{\tau_p} + \xi(\boldsymbol{D\tau_p} + \boldsymbol{\tau_p D})] \end{bmatrix} \tag{3.38}$$

A_i is the matrix acting on the first derivative of W in the flow direction i. For example A_1 is expressed in Eq. (3.39), and more detail will be shown in Appendix. A.

$$A_1 = \begin{bmatrix} u_1 & 0 & -1 & 0 & 0 \\ 0 & u_1 & 0 & -1 & 0 \\ -2(\frac{1-\beta}{Ma^2} + \tau_{11}) & 0 & u_1 & 0 & 0 \\ -\tau_{12} & -(\frac{1-\beta}{Ma^2} + \tau_{11}) & 0 & u_1 & 0 \\ 0 & -2\tau_{12} & 0 & 0 & u_1 \end{bmatrix} \tag{3.39}$$

In simple shear flow with an Oldroyd-B constitutive model, the system is hyperbolic only when $\tau_{ii} + \frac{1-\beta}{Ma^2}$ is positive for each i, Crochet, Davies, and Walters (2012) and Trebotich, Colella, and Miller (2005). To reveal the hyperbolic feature of our quasi-linear governing system, the spectra of A_i need to be real. Symbolic computation of the eigenvalues and eigenvectors of A_i shows that the eigenvalues of A_i depend on $\sqrt{\tau_{ii} + \frac{1-\beta}{Ma^2}}$ for each i, which means that the eigenvalues are real only when

$$\tau_{ii} + \frac{1-\beta}{Ma^2} \geq 0. \tag{3.40}$$

Following Tsai and Miller (2014) for the Giesekus model, we get for the PTT model:

$$\begin{aligned} \boldsymbol{G}(\boldsymbol{\tau_p} + \frac{1-\beta}{Ma^2})\boldsymbol{G^T} = \int_{-\infty}^{t} e^{\frac{t-s}{\sqrt{Ra}We}} [\frac{1-\beta}{\sqrt{Ra}WeMa^2}\boldsymbol{GG^T} - \epsilon\frac{\sqrt{Ra}}{(1-\beta)Pr}\boldsymbol{G}tr(\boldsymbol{\tau_p})\boldsymbol{\tau_p}\boldsymbol{G^T} \\ - \xi\boldsymbol{G}(\boldsymbol{D\tau_p} + \boldsymbol{\tau_p D})\boldsymbol{G^T}]ds \end{aligned} \tag{3.41}$$

where $\boldsymbol{G}$ is decomposition transformation gradient. The hyperbolicity of the PTT model requires that the RHS of Eq. (3.41) is positive,

$$\frac{1-\beta}{\sqrt{Ra}WeMa^2}\boldsymbol{G}\boldsymbol{G}^{\boldsymbol{T}} - \epsilon\frac{\sqrt{Ra}}{(1-\beta)Pr}\boldsymbol{G}tr(\boldsymbol{\tau_p})\boldsymbol{\tau_p}\boldsymbol{G}^{\boldsymbol{T}} - \xi\boldsymbol{G}(\boldsymbol{D}\boldsymbol{\tau_p}+\boldsymbol{\tau_p}\boldsymbol{D})\boldsymbol{G}^{\boldsymbol{T}} > 0. \tag{3.42}$$

This should be verified a posteriori.

If Eq. (3.42) holds true, we can rewrite A_i as $A_i = L_i\Lambda_i R_i$, where Λ_i is a diagonal matrix containing the eigenvalues of A_i. L_i is the matrix formed by the eigenvectors of A_i and R_i is the inverse of L_i. The convective terms of Eq. (3.37) can then be transformed into

$$A_i\frac{\partial W}{\partial x_i} = L_i\Lambda_i\frac{\partial R_i W}{\partial x_i} \tag{3.43}$$

This transformation allows to calculate first $\Lambda_i\frac{\partial R_i W}{\partial x_i}$ by using suitable numerical schemes and to compute explicitly the convective terms $A_i\frac{\partial W}{\partial x_i}$ as can be seen hereafter.

After introducing the quasi-linear treated, the governing system can be written as follows:

$$\begin{cases} \dfrac{\partial T}{\partial t} + (\boldsymbol{u}\cdot\nabla)T &= \frac{1}{\sqrt{Ra}}\triangle T \\ \dfrac{\partial W}{\partial t} + \displaystyle\sum_{i=1}^{2} A_i\frac{\partial W}{\partial x_i} &= S_{ql} \\ \nabla\cdot\boldsymbol{u} &= 0 \end{cases} \tag{3.44}$$

3.3.4 Temporal discretisation

For a time-related physical problem described by the governing equation, the calculation of the time term in the differential form promotes the evolution of the variables in each governing equation. The general governing equation with variable Φ can be write as:

$$\frac{\partial\Phi}{\partial t} = F(t,\Phi(t)) \tag{3.45}$$

Here, we define the difference of two time levels $[t, t+\Delta t]$ is one time step size Δt. The time-related term, left side term, can be discretised to first-order backward difference form:

$$\frac{\Phi_{n+1}-\Phi_n}{\Delta t} = F(\Phi^{n+1}) \tag{3.46}$$

or second-order discretised backward difference form:

$$\frac{3\Phi_{n+1}-4\Phi_n+\Phi_{n-1}}{2\Delta t} = F(\Phi^{n+1}) \tag{3.47}$$

where $n-1$, n and $n+1$ denote the last time level, present time level, and next level.

Implementation of backward differential fomula

For governing Eqs. (3.44) used in our work, it is discretized in time by a semi-implicit second-order scheme: partial derivatives in time are treated by a second-order backward differential formulation (BDF2). The Backward Differential Formula is a kind of linear multi-step method and firstly proposed by Curtiss and Hirschfelder (1952), which approximate the derivative of the time term of the governing equation by known information from already computed time points.

The quasi-linear terms, PTT related nonlinear terms, and the convective term in the energy equation is treated explicitly by a second-order extrapolation in time. The diffusion terms, relaxation terms, mass conservation, and pressure gradients are treated implicitly.

Application of BDF2 to the governing system is shown as follows:

$$\begin{cases} \dfrac{3T^{n+1}-4T^{n}+T^{n-1}}{2\Delta t}+2\left((\boldsymbol{u}\cdot\nabla)T\right)^{n}-\left((\boldsymbol{u}\cdot\nabla)T\right)^{n-1} &= \frac{1}{\sqrt{Ra}}\triangle T^{n+1} \\ \dfrac{3W^{n+1}-4W^{n}+W^{n-1}}{2\Delta t}+2\left(\sum_{i=1}^{2}A_i\dfrac{\partial W}{\partial x_i}\right)^{n}-\left(\sum_{i=1}^{2}A_i\dfrac{\partial W}{\partial x_i}\right)^{n-1} &= S_{ql}^{n+1} \\ \nabla\cdot\boldsymbol{u}^{n+1} &= 0 \end{cases} \tag{3.48}$$

with

$$S_{ql}^{n+1}=\begin{bmatrix} -\nabla p^{n+1}+\beta\frac{Pr}{\sqrt{Ra}}\Delta\boldsymbol{u}^{n+1}+PrT^{n+1}e_j \\ \frac{-\boldsymbol{\tau_p}^{n+1}}{We\sqrt{Ra}}-2A[\frac{\epsilon\sqrt{Ra}}{(1-\beta)Pr}tr(\boldsymbol{\tau_p})\boldsymbol{\tau_p}+\xi(\boldsymbol{D\tau_p}+\boldsymbol{\tau_p D})]^{n}+A[\frac{\epsilon\sqrt{Ra}}{(1-\beta)Pr}tr(\boldsymbol{\tau_p})\boldsymbol{\tau_p}+\xi(\boldsymbol{D\tau_p}+\boldsymbol{\tau_p D})]^{n-1} \end{bmatrix} \tag{3.49}$$

Alternative direction implicit method

Eqs. (3.48-3.49), apart from the velocity-pressure coupling, lead to Helmholtz equations for the unknowns T^{n+1}, u_1^{n+1} and u_2^{n+1} and simple scalar equations for τ_{11}^{n+1}, τ_{12}^{n+1}, and τ_{22}^{n+1},

$$(1+\frac{2\Delta t}{3We\sqrt{Ra}})\tau_{ij}^{n+1}=\text{RHS} \tag{3.50}$$

that can be easily solved at any grid point. We use the energy equation to illustrate the approach used to solve the Helmholtz equations. The method is similar to the alternative direction method. The Helmholtz equation for T^{n+1} is written as

$$\left(1-\frac{2\Delta t}{3\sqrt{Ra}}\triangle\right)T^{n+1}=\frac{4}{3}T^{n}-\frac{1}{3}T^{n-1}-\frac{4\Delta t}{3}\left((\boldsymbol{u}\cdot\boldsymbol{\nabla})T\right)^{n}+\frac{2\Delta t}{3}\left((\boldsymbol{u}\cdot\boldsymbol{\nabla})T\right)^{n-1} \tag{3.51}$$

The 2D Helmholtz operator can be factorized into a product of two 1D operators:

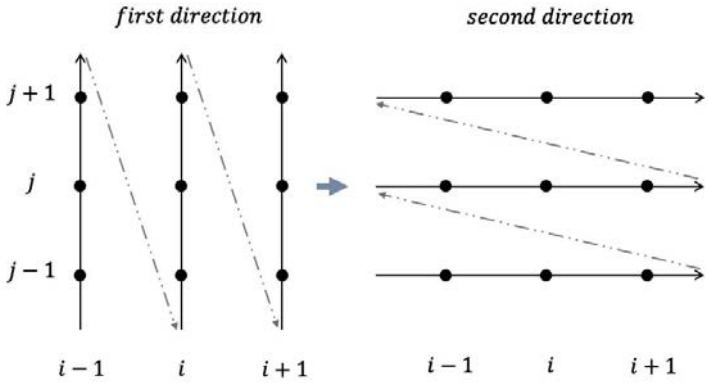

FIGURE 3.7: Solving process for a 2D ADI scheme.

$$1-\frac{2\Delta t}{3\sqrt{Ra}}\triangle=(1-\frac{2\Delta t}{3\sqrt{Ra}}\frac{\partial^2}{\partial x_1^2})(1-\frac{2\Delta t}{3\sqrt{Ra}}\frac{\partial^2}{\partial x_2^2})-\frac{4\Delta t^2}{9Ra}\frac{\partial^2}{\partial x_1^2}\frac{\partial^2}{\partial x_2^2} \tag{3.52}$$

The cross term is of the order of Δt^2 and neglecting it results in a first-order time scheme. The factorized operator is only applied to temperature increment $(T^{n+1}-T^n)$ to keep a second order time scheme, which is of the order of Δt. In this way

$$\frac{4\Delta t^2}{9Ra}\frac{\partial^2}{\partial x_1^2}\frac{\partial^2}{\partial x_2^2}(T^{n+1}-T^n) \tag{3.53}$$

becomes of the order of Δt^3 and can be neglected without decreasing the accuracy of the second-order time scheme. The final equation of temperature to be solved is the following:

$$\begin{aligned}(1-\frac{2\Delta t}{3\sqrt{Ra}}\frac{\partial^2}{\partial x_1^2})(1-\frac{2\Delta t}{3\sqrt{Ra}}\frac{\partial^2}{\partial x_2^2})(T^{n+1}-T^n)=\frac{2\Delta t}{3\sqrt{Ra}}\triangle T^n+\frac{1}{3}(T^n-T^{n-1})\\ -\frac{4\Delta t}{3}\left((\boldsymbol{u}\cdot\nabla)T\right)^n+\frac{2\Delta t}{3}\left((\boldsymbol{u}\cdot\nabla)T\right)^{n-1}\end{aligned} \tag{3.54}$$

In this way, solving the 2D temperature Helmholtz equation can be done by solving only 1D problems (first in the x_1 direction and then in the x_2 direction). Fig. 3.7 shows a solve process of a 2D ADI. The same method is also used to solve the Helmholtz equations for the velocity.

3.3.5 Spatial discretisation

We use the finite differential method to discretize the governing equations in space. The finite differential method had briefly introduced above, Sec. 3.3.2.

Velocity- pressure staggered grid

For the velocity-pressure coupling problem, if the velocity and pressure components are placed on the same nodes, a common pressure chessboard problem will arise. The checkerboard problem describes that the pressure gradient using the central difference method Eq. (3.55) will get an unreasonable solution in the case of a regular grid, as described in Fig. 3.8.

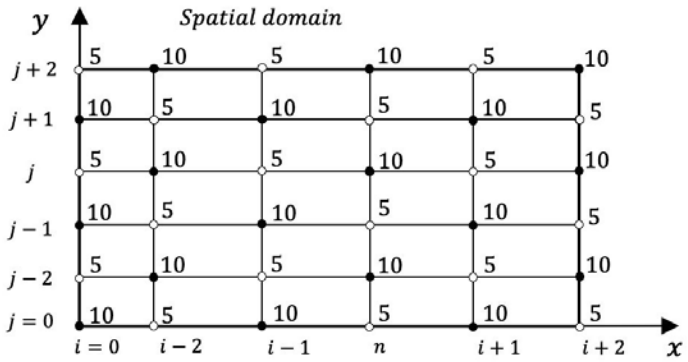

FIGURE 3.8: Checkerboard pressure problem on a normal grid.

$$\frac{\partial p_{i,j}}{\partial x} = \frac{p_{i+1,j} - p_{i-1,j}}{2\Delta x} \tag{3.55}$$

In order to avoid this problem, Harlow and Welch (1965) proposed the staggered grid technique. A staggered grid is a manner of spatial discretization, in which the variables are not allocated at the same position. For the present problem, the main nodes (nodes made by the original grid) are marked with temperature, velocity components, and elastic stress components. We define the new nodes obtained by moving the original grid by half the grid distance in the x direction and y direction as the secondary grid nodes, which are marked by a scalar of pressure. The above description is shown in Fig. 3.9. This technique not only retains the central difference discrete scheme for pressure but also effectively avoids numerical errors caused by the pressure chessboard problem.

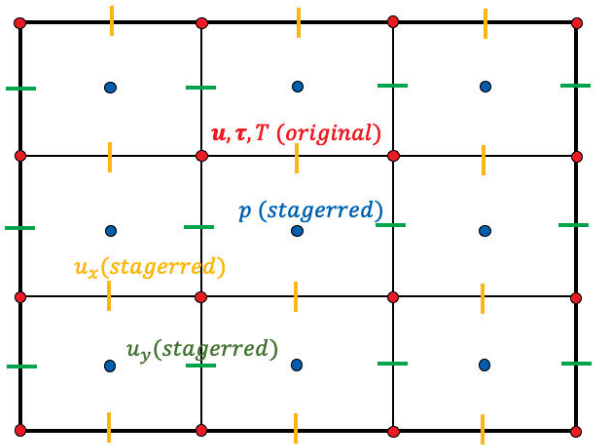

FIGURE 3.9: Stagerred grid.

Projection method

The velocity-pressure coupling is treated by the projection method: enforcing the incompressibility constraint at time step $(n+1)$ in the momentum equation results in a Poisson equation for the pressure p^{n+1} or its increment $(p^{n+1}-p^n)$. Pressure increment is used in the present study. In the prediction step, momentum equations are solved using the gradients of p^n. The resulting velocity field is not divergence-free; in the correction step this velocity field is projected onto a divergence-free space by using the gradients of $(p^{n+1}-p^n)$ and the resulting Poisson equation is solved by a partial diagonalization method. The calculation process is as follows:

- Prediction step

$$\frac{3u^* - 4u^{n+1} + u^n}{\Delta t} = 2HP_u^{n+1} - HP_u^n - \nabla p^{n+1} + \beta\frac{Pr}{\sqrt{Ra}}\Delta u^* + PrT^{n+2}e_z \tag{3.56}$$

$$u^*\big|_{\partial\Omega} = u_b \cdot n \tag{3.57}$$

  where u_b and n are the velocity and normal vectors at the domain boundaries $\partial\Omega$, HP_u includes all the contributions of the hyerbolic terms in the momentum equation.

- correction step: $\phi = p^{n+1} - p^n$

$$\frac{u^{n+1} - u^*}{\Delta t} = -\nabla\phi \tag{3.58}$$

$$\nabla \cdot u^{n+1} = 0 \tag{3.59}$$

$$\Longrightarrow \quad \nabla^2\phi = -\frac{\nabla \cdot u^*}{\Delta t} \tag{3.60}$$

  the correction step is used to project the velocity onto a divergence-free vector space and get ultimate pressure and velocity. Then update pressure with $p^{n+1} = p^n + \phi$ and velocity.

High order upstream central scheme

Concerning Eqs.(3.49 -3.50), a second-order central differencing is applied to all the terms except for the quasi-linear terms which are expressed by Eq (3.43). A High-Order (third order) Upstream Central (HOUC-3) scheme (Nourgaliev and Theofanous, 2007) is applied to $\frac{\partial R_i W}{\partial x_i}$ according to the sign of the eigenvalues in Λ_i. For example for $i = 1$, the matrix of coefficient A_1 shown at Eq. (3.39) has five eigenvalues:

$$\mathbf{\Lambda_1} = \begin{bmatrix} \lambda_1, & \lambda_2, & \lambda_3, & \lambda_4, & \lambda_5 \end{bmatrix}$$

and the five corresponding eigenvectors $\boldsymbol{R_1}$. $\boldsymbol{R_1 W}$ have five columns:

$$\boldsymbol{R_1 W} = \left[(R_1W)^1,\ \ (R_1W)^2,\ \ (R_1W)^3,\ \ (R_1W)^4,\ \ (R_1W)^5\right]$$

Note that R_1 like λ_1, λ_2, ..., λ_5 contains only information related to A_1 at the grid point (l, m). By the way of example, in order to calculate $\lambda_2 \frac{\partial (R_1W)^2}{\partial x_1}$ at grid point (l, m), the following HOUC-3 scheme is applied (the nodes used shown in Fig. 3.10):

$$\lambda_2 \frac{\partial (R_1W)^2}{\partial x_1}\bigg|_{l,m} = \begin{cases} \lambda_2 \frac{(R_1W)^2_{l-2,m} - 6(R_1W)^2_{l-1,m} + 3(R_1W)^2_{l,m} + 2(R_1W)^2_{l+1,m}}{6\Delta x_1} & \text{if} \quad \lambda_2 > 0 \\ \lambda_2 \frac{-2(R_1W)^2_{l-1,m} - 3(R_1W)^2_{l,m} + 6(R_1W)^2_{l+1,m} - (R_1W)^2_{l+2,m}}{6\Delta x_1} & \text{if } \lambda_2 < 0 \\ 0 \qquad \text{otherwise} \end{cases} \tag{3.61}$$

At any grid point (l, m) application of HOUC-3 scheme to the five eigenvalues allows to calculate explicitly $A_i \frac{\partial \boldsymbol{W}}{\partial x_i}$. Second-order schemes are used for grid points near the domain boundaries.

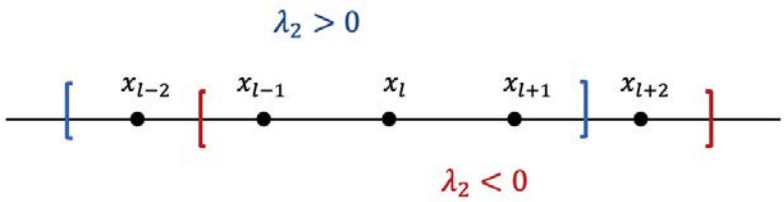

FIGURE 3.10: Nodes used of the HOUC-3 scheme on a one-dimensional with uniform grid for different eigenvalue λ_2.

3.3.6 Tridiagonal matrix algorithm (TDMA)

Second-order central differencing is applied to Eq. (3.54), the obtained algebraic equations are tridiagonal and can be solved by the tridiagonal matrix algorithm (TDMA) (Patankar, 2018). Tridiagonal matrix algorithm is a one-dimension simplified form of Gaussian elimination, and also able to solve multi-dimension problems through the line-by-line way. Its advantage is to save storage and computing resources.

The process of the TDMA mainly consists of two stages: a forward elimination phase and a backward substitution phase.

$$a_i x_{i-1} + b_i x_i + c_i x_{i+1} = y_i, \quad i = 1, 2, 3, ..., n \tag{3.62}$$

By the way of example, the process of the TDMS for 1D problem, as Eq. (3.62), with n unknowns as follows:

- matrix form of Eq. (3.62) with ($a_1 = 0, c_n = 0$)

$$\begin{pmatrix} b_1 & c_1 & & & & & & 0 \\ a_2 & b_2 & c_2 & & & & & \\ & a_3 & b_3 & c_3 & & & & \\ & & \cdot & \cdot & \cdot & & & \\ & & & \cdot & \cdot & \cdot & & \\ & & & & \cdot & \cdot & \cdot & \\ & & & & & a_{n-1} & b_{n-1} & c_{n-1} \\ 0 & & & & & & a_n & b_n \end{pmatrix} \begin{pmatrix} x_1 \\ x_2 \\ x_3 \\ \cdot \\ \cdot \\ \cdot \\ x_{n-1} \\ x_n \end{pmatrix} = \begin{pmatrix} y_1 \\ y_2 \\ y_3 \\ \cdot \\ \cdot \\ \cdot \\ y_{n-1} \\ y_n \end{pmatrix} \tag{3.63}$$

- **Step 1:** forward elimination phase:

$$b_1 x_1 + c_1 x_2 = y1 \implies x_1 + \frac{c_1}{b_1} x_2 = \frac{y_1}{b_1} \text{ (new row 1)} \tag{3.64}$$

with new $c_1^* = \frac{c_1}{b_1}$ and $y_1^* = \frac{y_1}{b_1}$. We use Eq. (3.64) to eliminate $a_2 x_1$ on row two:

$$(b_2 - \frac{c_1}{b_1}) x_2 + c_2 x_3 = y_2 - \frac{y_1}{b_1} \text{ (new row 2)} \tag{3.65}$$

with new $c_2^* = b_2 - \frac{c_1}{b_1}$ and $y_2^* = y_2 - \frac{y_1}{b_1}$. The following rows are processed like Eq. (3.65). Finally, a new matrix was obtained:

$$\begin{pmatrix} 1 & c_1^* & & & & & & 0 \\ & 1 & c_2^* & & & & & \\ & & 1 & c_3^* & & & & \\ & & & \cdot & \cdot & & & \\ & & & & \cdot & \cdot & & \\ & & & & & \cdot & \cdot & \\ & & & & & & 1 & c_{n-1}^* \\ 0 & & & & & & & 1 \end{pmatrix} \begin{pmatrix} x_1 \\ x_2 \\ x_3 \\ \cdot \\ \cdot \\ \cdot \\ x_{n-1} \\ x_n \end{pmatrix} = \begin{pmatrix} y_1^* \\ y_2^* \\ y_3^* \\ \cdot \\ \cdot \\ \cdot \\ y_{n-1}^* \\ y_n^* \end{pmatrix} \tag{3.66}$$

- **Step 2:** backward institution phase:

  In backward institution phase, we start from last row and step backward,

$$x_n = y_n^* \text{ (row n)} \tag{3.67}$$

$$x_i = y_i^* - c_i^* y_{i+1}^* \text{ (for } i = n-1 \cdots 1) \tag{3.68}$$

The following rows are also processed like Eq. (3.68), and a tridiagonal matrix is solved.

3.4 Code validation

The purpose of this section is to verify the calculation capabilities of the solver we developed, including the ability to calculate flow and heat transfer in viscoelastic fluid flow. We will verify the accuracy of the solver in temporal and space and examine the convergence by comparing it with the results of published publications. Part of this chapter had been published in the *The American Society of Mechanical Engineers* conference paper, and the title is 'A new approach to the numerical modeling of the viscoelastic Rayliehg-Bénard convection'.

3.4.1 Overview of solving process

So far, the introduction of the solver for viscoelastic RBC is finished and Fig. 3.11 shows the calculation flow chart of the solver.

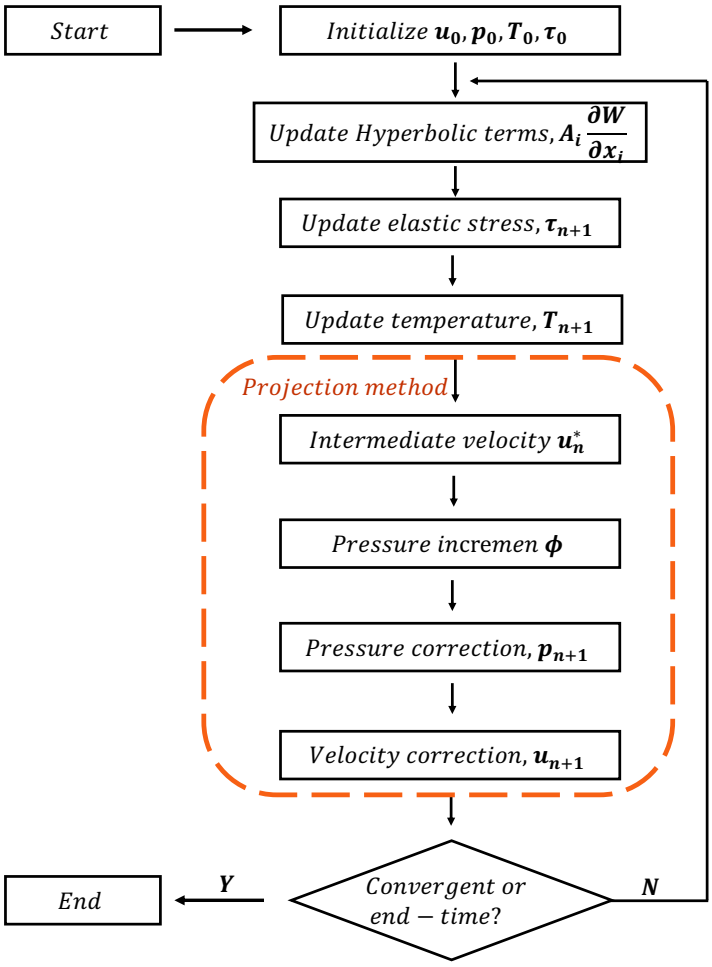

FIGURE 3.11: Flow chart of the numerical solve progress.

3.4.2 Newtonian Rayleigh-Bénard convection in square cavity

Firstly, we tested the spatial and temporal convergence of the solver in Newtonian Rayleigh-Bénard convection in enclusure square cavity. In order to be consistent with the references, the Prandtl number is fixed at $Pr = 0.71$ and the Rayleigh number at $Ra = 10^5$ in this physical configuration. The test computations have been carried out for four time steps ($\Delta t = 0.01, 0.005, 0.001, 0.0005$) and four grids ($Nx * Ny = 32 * 32, 64 * 64, 128 * 128, 256 * 256$). And in order to check the heat transfer capacity, here, we define two Nusselt numbers at the bottom and the up boundaries of the cavity. They present the dimensionless mean temperature gradient averaged over the heating and cooling boundaries at steady state.

$$Nu_H = -\int_0^1 \frac{\partial T^*}{\partial y^*}|_{y^*=0} dx^*, \qquad Nu_U = -\int_0^1 \frac{\partial T^*}{\partial y^*}|_{y^*=1} dx^*$$

The results are shown in Tab. 3.2 and Tab. 3.3, where $umax$ and $vmax$ are the maxima of velocity at $x-$ and $y-$ directions in the flow domain. The convergence in space and time is well observed.

grid	u_{max}	v_{max}	Nu_H
$32 * 32$	0.2867	0.315335	3.9931
$64 * 64$	0.2893	0.316230	3.9198
$128 * 128$	0.2898	0.316303	3.9113
$256 * 256$	0.2898	0.316312	3.9108

TABLE 3.2: Convergence of u_{max}, v_{max} and Nu_H with grid refinement for cases with $Pr = 0.71$ and $Ra = 10^5$. The time step is set at $\Delta t = 0.001$.

Time step	0.01	0.005	0.001	0.0005
Nu_H	1.000158	1.000175	1.000182	1.000182
Nu_U	1.000152	1.000171	1.000178	1.000178

TABLE 3.3: Average Nu number at upper and bottom boundary with different time step for cases with $Pr = 0.71$ and $Ra = 10^5$, when dimensionless time is equal to $t = 10$. The grid setting $128 * 128$ was chosen.

After checking the temporal and spatial convergence of the solver, a validation the numerical scheme capability so constructed through a comparison with the case of Newtonian fluids, for which a benchmark is available in the literature. It consists of Newtonian RBC flow in a square cavity with Prandtl number equal to 7.0 and $Ra = 10^5$ and 10^6 (Ouertatani et al., 2008). The comparisons concern the hot wall Nusselt number Nu_H and the maximum velocity components.

As shown in Table 3.4, our results (Pre.) are in real agreement with those from the published benchmark (Ref.), in terms of maximum velocity and Nusselt number at two different Rayleigh numbers. Fig. 3.12 show the comparison of u velocity distribution on the central vertical line of the flow domain from our simulated results and reference (Ouertatani et al., 2008). The intrinsic

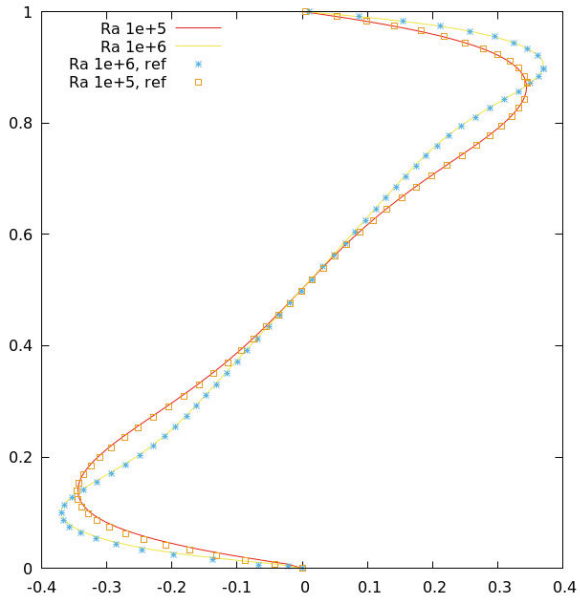

FIGURE 3.12: comparison of the u velocity distribution on the central vertical line of the flow domain from our simulated results and reference (Ouertatani et al., 2008).

behavior of the code developed was first tested. The results of the numerical tests have all confirmed that the code is second-order accurate both in time and space in agreement with the theoretical behavior of the numerical schemes used (Hagani et al., 2018).

	$u_{max} * 10$		$v_{max} * 10$		Nu_H	
Ra	Pre.	Ref.	Pre.	Ref.	Pre.	Ref.
10^5	3.457	3.443	3.757	3.757	3.889	3.910
10^6	3.699	3.709	4.051	4.060	6.277	6.309

TABLE 3.4: Numerical results of a RBC benchmark in a square cavity filled with a Newtonian fluid of $Pr = 7.0$ (Ouertatani et al., 2008).

3.4.3 Viscoelastic Rayleigh-Bénard convection

The second validation consists of a comparison with the results presented in Park and Ryu (2001) for a viscoelastic RBC in a closed cavity of aspect ration 2 : 1. The authors investigated the stability of a viscoelastic fluid of $Pr = 7.0$ described by an Oldroyd-B model and determined the critical value Ra_c corresponding to the convection set-up for various parameters (aspect ratios, Weissenberg number, β).

For a polymer solution of $\beta = 0.6$ with an important contribution of the solvent, the convection set-up is almost the same as a Newtonian fluid ($\beta = 1$): the same Ra_c, steady flow and the same cell number at a fixed aspect ratio. For example in a cavity of aspect ratio 2 : 1 the unstable mode is steady and has two flow cells and the critical Rayleigh number is approximately equal to 2000 at $We = 0.0075$. We performed numerical simulations for several Ra above 2000

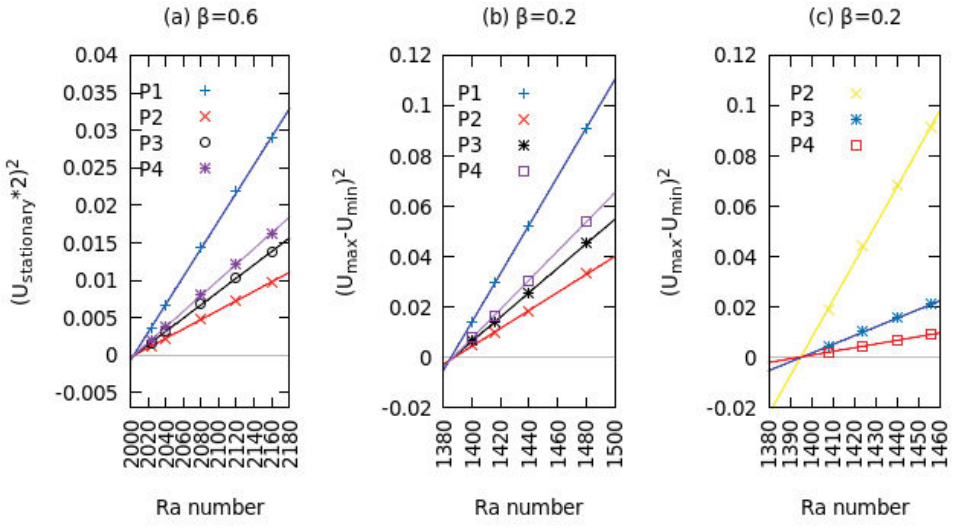

FIGURE 3.13: Square of vertical velocity ($\beta = 0.6$) and amplitude of vertical velocity ($\beta = 0.2$) at four monitoring points versus Ra in a $2:1$ cavity filled with an Oldroyd-B fluid. (a) $\beta = 0.6$, $We = 0.0075$, 2-cell steady flow, (b) $\beta = 0.2$, $We = 0.1$, 2-cell time-periodic flow, (c) $\beta = 0.2$, $We = 0.1$, 3-cell time-periodic flow. The monitoring points are P1 (H, H/2), P2 (3H/4, H/2), P3 (H/4, H/2) and P4 (H/2, H/4). The solid lines are linear fitting curves of the numerical results and the linear relationship indicates that the corresponding bifurcation (pitchfork for $\beta = 0.6$ and Hopf for $\beta = 0.2$) is supercritical. The estimated Ra_c is equal to respectively 2008($\beta = 0.6$), 1387 ($\beta = 0.2$ and 2-cell flow) and 1395 ($\beta = 0.2$ and 3-cell flow).

and obtained steady-state solutions of two-cell flow. Fig. 3.13 (a) shows a linear relationship between Ra and velocity squared at four monitored points, confirms that the convection set-up corresponds to a supercritical pitchfork bifurcation and indicates that the $Ra_c = 2008$ is located slightly above 2000 according to the extrapolation.

For a polymer solution of $\beta = 0.2$ with an important contribution of polymer, Park and Ryu (2001) reported an overstability or Hopf bifurcation leading to time-dependant flows. Also, the authors showed that for the aspect ratio of $2:1$ two different modes with two and three cells respectively are unstable at almost the same Rayleigh number (about 1380). Simulations performed for the aspect ratio $2:1$ yielded only a time-periodic flow of two cells and a three-cell flow was first obtained by using an aspect ratio of $2.2:1$ and then stabilized for the aspect ratio $2:1$. For both flow structures, time-periodic flows were obtained for several Rayleigh numbers and the squares of velocity amplitude displayed a linear relationship with Rayleigh number (Fig. 3.13 (b) and (c)). This confirms that the convection set-up takes place through a supercritical Hopf bifurcation. Extrapolation yielded $Ra_c = 1387$ for the flow structure of two cells and $Ra_c = 1395$ for three flow cells. An instantaneous stream function of each flow structure is depicted in Fig. 3.14. In terms of flow structure (two or three cells), the flow feature (steady-state or time-dependent) and the critical Rayleigh number, the present results agree well with the previous study of viscoelastic RBC in the literature (Park and Ryu, 2001).

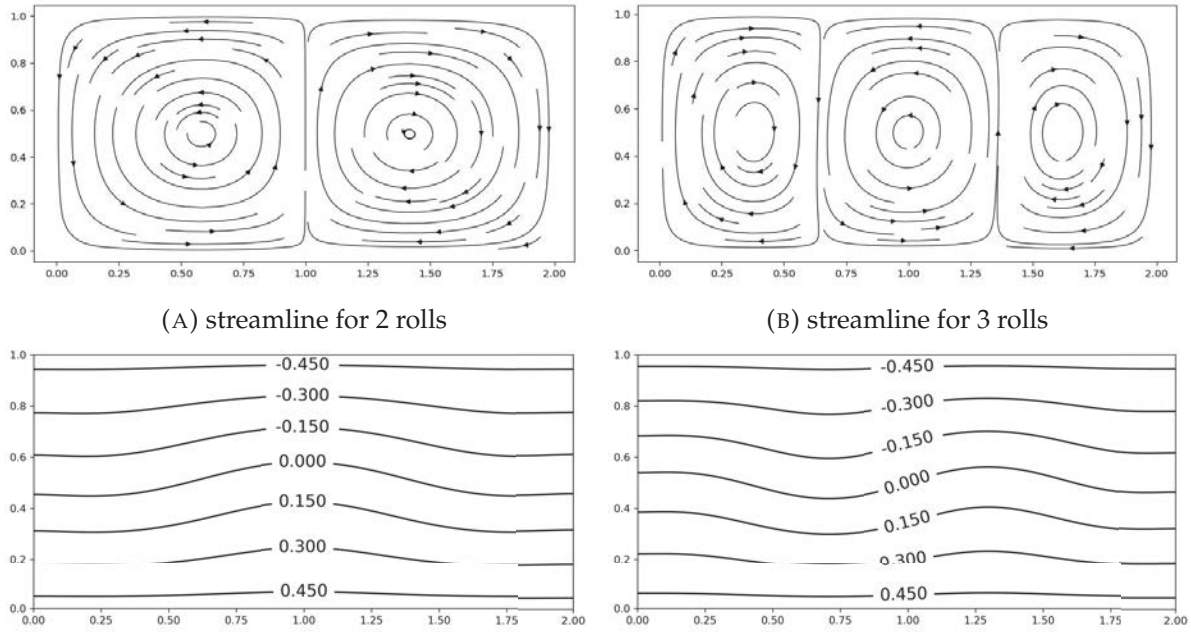

(A) streamline for 2 rolls

(B) streamline for 3 rolls

(C) isothermal for 2 rolls

(D) isothermal for 3 rolls

FIGURE 3.14: Instantaneous streamlines and isothermal of two convective flow structures ($Pr = 7.0$, $\beta = 0.2$, $We = 0.1$ and $Ra = 1480$. (A, C) 2-cell time-periodic flow is observed after a supercritical Hopf bifurcation. (B, D) 3-cell time-periodic flow is also observed.

It is thus concluded that a numerical solver of the governing equations of incompressible viscoelastic fluids in Rayleigh-Bénard configuration was developed, where viscoelastic fluids were described by the Oldroyd-B and Phan-Thien-Tanner models. To ensure numerical stability, a quasi-linear treatment was adopted to calculate the hyperbolic part. To validate the solver, Newtonian and viscoelastic Rayleigh-Bénard convection cases were simulated: the results showed a good match with the published data in the literature. Especially in a 2 : 1 cavity filled with viscoelastic fluid, the results obtained in terms of flow structure (number of cells), flow feature (steady or not) and critical Rayleigh number are in good agreement with the results of Park and Ryu (2001). This suggests that the numerical solver developed can be used to study viscoelastic Rayleigh-Bénard convection with confidence.

3.5 Conclusion

In this chapter, we have introduced the numerical scheme used to solve Newtonian or viscoelastic Rayleigh-Béanrd convection problems in detail and summarised the process of the solver in Sec. 3.4.1. We checked the temporal and spatial convergence of the solver for simulating the Newtonian or viscoelastic Rayleigh-Bénard.Through comparing the results of our solver with those in the published literature, it is shown that our solver has the ability to solve Newtonian or viscoelastic Rayleigh-Bénard convection.

It should be noted that time-dependent convection onset in an enclosure of aspect ratio 2:1 is chosen to validate the code developed using the parameters $(\beta, We) = (0.6, 0.0075)$ and $(0.2, 0.1)$ and $Pr = 7.0$. The critical Rayleigh numbers are obtained and compared with those in the literature for these values of the parameters for both two-cell and three-cell convection flow configurations thus validating the code developed.

Chapter 4

Regular reversal convection in 2D rectangular cavity

Contents

4.1 Introduction

At present, the understanding of viscoelastic Rayleigh-Bénard convection has been very rich, especially for the onset of Rayleigh-Bénard convection and the corresponding bifurcation. In non-linear dynamic systems, the influence of fluid rheology and physical properties on the transition and heat transfer of thermal convection has also attracted more attention, especially viscoelasticity, which may lead to a new flow structure of thermal convection, further affecting the heat transfer efficiency.

Regarding the start-up and bifurcation problems of Rayleigh-Bénard convection, linear and non-linear stability analysis is traditionally used for research, but due to the over idealization, the results are still insufficient. Many researchers have shown that the constitutive equations of most viscoelastic fluids are hyperbolic-elliptic equations in the steady state and hyperbolic-parabolic equations in the transient state. As a result, stability analysis can only be limited to some basic constitutive models (such as the Maxwell model, etc.), and cannot reveal the influence of complex rheological properties on thermal convection, such as shear thinning and elastic nonlinearity. After entering the oscillation interval, even if it is a non-linear stability analysis, the error of the result will gradually expand. Therefore, it is necessary to study the instability of more real viscoelastic fluid thermal convection.

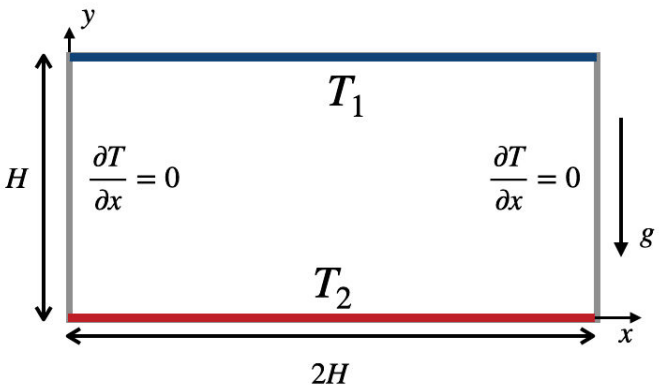

FIGURE 4.1: Physical configuration: A rectangular cavity with an aspect ratio 2 : 1 filled by the viscoelastic fluid, heated at (T_2) by the bottom and cooled at (T_1) by the top. Both vertical boundaries are adiabatic and all boundaries are no-slip for velocity. We use H as the reference length, in dimensionless form the cavity is defined by $x \in [0, 2]$ and $y \in [0, 1]$.

In this chapter, we present the numerical results of the viscoelastic Rayleigh-Béarnd convection in a 2:1 cavity shown in Fig.4.1, where the viscoelastic constitutive models include the Oldroyd-B model and the Phan-Thien-Tanner model. The main contents include: the influence of the rheology parameters of viscoelastic fluids on the onset critical Rayleigh number Rac_1 and the critical Rayleigh number Rac_2, which induce flow pattern transition; the mechanism of the flow and heat transfer in viscoelastic Rayleigh-Bénard convection; analysis of the reversal convection process from perspective of the energy budget, and summary of the general laws of reversal convection.

4.2 Onset of the viscoelastic RBC

4.2.1 Supercritical Hopf bifurcation

As mentioned in the last chapter, there is a critical Rayleigh number for the onset of Rayleigh-Bénard convection, and we call this critical Rayleigh number as Rac_1. When Rayleigh number exceeds this critical value, a convection will occur in the cavity. Below Rac_1, the fluid in the

cavity was in a state of pure heat conduction. From the perspective of the direct numerical simulation, if a small temperature perturbation is given to the flow field at the initial moment, and if $Ra < Rac_1$, the temperature perturbation will be gradually damped until the entire cavity returns to a pure heat conduction state. On the contrary, if $Ra > Rac_1$, the perturbation will be continuously amplified, and cause convective flow throughout the cavity.

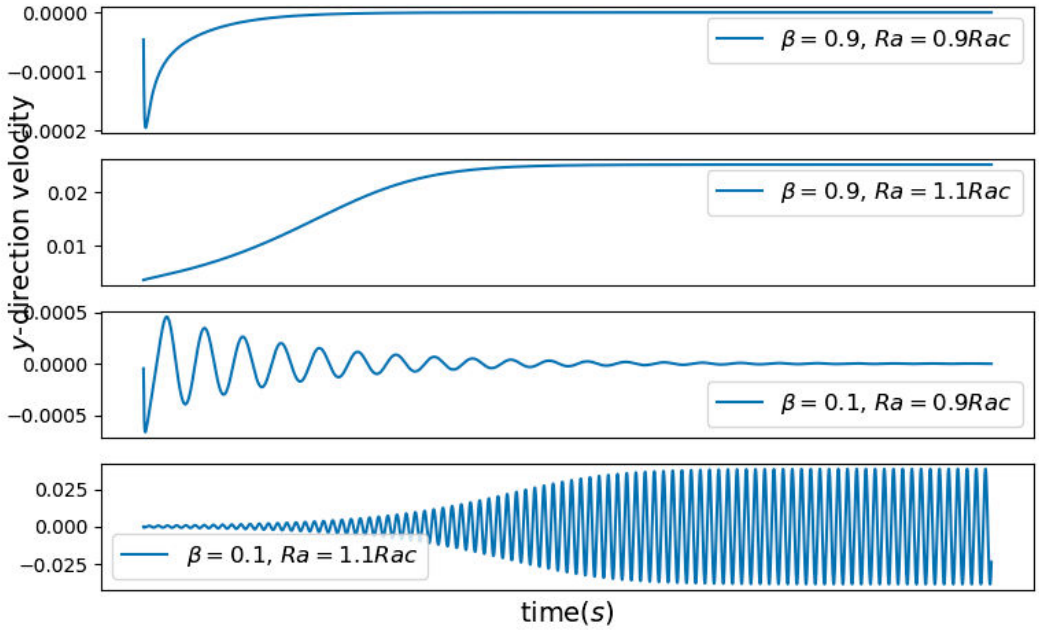

FIGURE 4.2: y-direction velocity time evolution at the central point of the domain for viscoelastic Rayleigh-Bénard convection (Oldroyd-B constitutive model was used) with two concentration ($\beta = (0.1, 0.9)$), when Ra equal to $0.9Rac$ and $1.1Rac$. In simulations, we set $Pr = 7.0$ and $We = 0.1$ and the corresponding RBC is of two cells.

By the way of example, a geometry configuration like Fig. 4.1 was adopted, and a monitor point was fixed at the centre of the fluid domain $P(1, 1/2)$. Fig. 4.2 shows the y-direction velocity at point P evolves along time at different Rayleigh numbers ($Ra = 0.9Rac_1$ and $1.1Rac_1$) and for two polymer concentration $\beta = (0.1, 0.9)$ with Oldroyd-B model. The initial condition of the simulations used is a random temperature disturbance. It can be found that the initial disturbance is damped and that the $y-$ velocity evolves slowly to zero at $Ra = 0.9Rac_1$. Note that for the case with $\beta = 0.9$ the fluid velocity evolves monotonically to zero while for the case with $\beta = 0.1$ it is oscillatorilly damped to zero. At $Ra = 1.1Ra$, the velocity of the case with $\beta = 0.9$ increases monotonically to steady-state, however, it is periodically amplified to reach a constant amplitude for case with $\beta = 0.1$. Not all the onsets of viscoelastic R-B convection are oscillating as is shown in Fig. 4.2: for large β and small We the convection onset will take place through a pitchfork bifurcation and a steady-state convection will be observed as is the case for the Newtonian fluids. The mechanism of flow pattern selection of time dependent viscoelastic RBC onset will be analyzed in Sec. 4.3.

4.2.2 Effect of (ϵ, ξ) on Rac_1

In fact, the viscoelastic constitutive model used in Sec. 4.2.1 is the Oldroyd-B constitutive model, which corresponds to a PTT fluid with $\xi = 0$ and $\epsilon = 0$. The investigation about effect of the rheology parameters of the Oldroyd-B constitutive fluids on the first critical Rayleigh number has been presented by Park and Ryu (2001) through linear instability analysis, shown in Fig. 2.16. However, the existing work has not studied the rheological parameters in more complex viscoelastic models, such as ϵ and ξ in PTT constitutive model. From this starting point, viscoelastic RBC flows with the PTT model were simulated for various values of ξ with $\epsilon = 0.1$ and various values of ϵ with $\xi = 0$, respectively. ϵ and ξ are two important rheological parameters of the PTT model, they characterize elongational behavior of the polymer molecules and slip between the long chain molecules and the surrounding continuum. These simulations aim to understand their effects on the convection onset and heat transfer. In order to determine the influence of the parameters, in the following simulations we fixed $Pr = 7.0$, $\beta = 0.2$ and $We = 0.1$ and the corresponding result concern mainly the two-cell R-B flows.

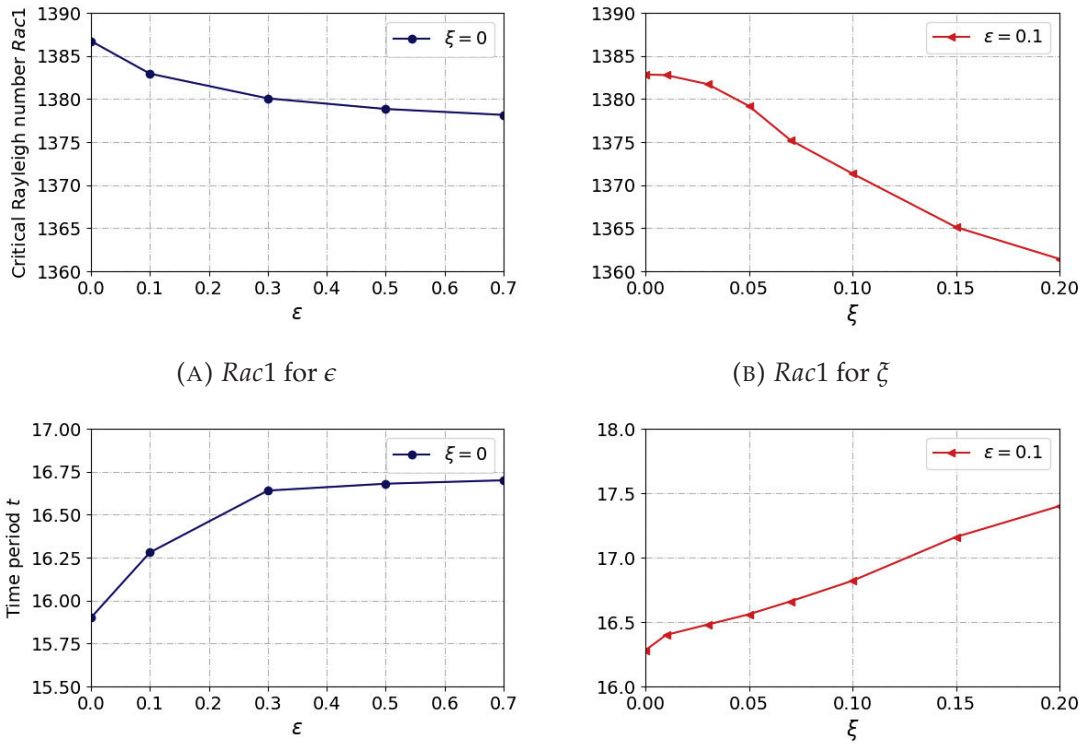

(A) $Rac1$ for ϵ

(B) $Rac1$ for ξ

(C) Time period for ϵ

(D) Time period for ξ

FIGURE 4.3: Effects of ϵ and ξ on the critical Rayleigh number and oscillating time period of the 2-cell flow pattern at $Pr = 7.0$, $\beta = 0.2$, and $We = 0.1$. The effects of ϵ are studied for fixed $\xi = 0$ while those of ξ are investigated for $\epsilon = 0.1$.

For each pair of ξ and ϵ, several Rayleigh numbers are investigated. We found that the convection onset takes place also with time-dependent flows. At supercritical Rayleigh numbers, the relationship between Ra and the square of the velocity amplitude is linear. This means

that the corresponding Hopf bifurcation is supercritical. Through an extrapolation approach illustrated in Fig. 3.13, the corresponding critical Rayleigh number, Ra_{c1}, is determined and presented in Fig. 4.3.

We observe that ξ and ϵ have a very weak influence on the convection onset and the critical Rayleigh number. With $\xi = 0$ and ϵ in the range of $[0, 0.7]$ the critical Rayleigh number, Ra_{c1}, decreases very slightly and remains almost constant. With $\epsilon = 0.1$ and ξ in the range of $[0, 0.2]$ the decrease in Ra_{c1} is slightly more important but less than 2%. This means that enhanced slip between polymer molecules and the surrounding continuum can make the onset of the oscillating convection occur slightly earlier. The first critical Rayleigh numbers (Rac_1) obtained for viscoelastic Rayleigh-Bénard convection mentioned above are smaller than that in the Newtonian case in the same physical configuration.

4.2.3 Effect of We and β on Rac_1

In addition to ϵ and ξ, the viscosity ratio β representing the solution concentration and the Weissenberg number We representing the elsticity of viscoelastic fluids will also affect the occurrence of convection. Fig. 4.4 shows the influence of solution concentration ($\beta \in (0.1, 0.2)$) at different Weissenberg numbers ($We \in [0.075, 0.25]$) on Rac_1 for $\epsilon = 0.1$ and $\xi = 0.05$. It can be observed that as β decreases, the elastic effect (We) increases, which promotes the occurrence of viscoelastic convection, resulting in a decrease in Rac_1. These results show that during the start-up phase of convection, even for small We flow conditions, the elastic force generated by the action of the elastic fluid molecules is still very strong, so that the effect of the properties of the viscoelastic fluid on Rac_1 is relatively big. But with the continuous increase of We, the influence of the viscoelastic effect gradually decreases. This trend is also proved by Li and Khayat (2005).

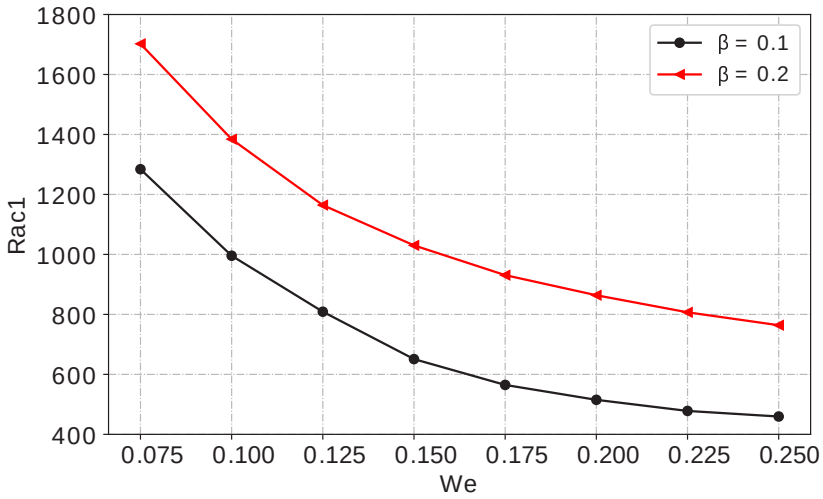

FIGURE 4.4: Effects of (We, β) on the first critical Rayegih number Rac_1 at $Pr = 7.0$, $\epsilon = 0.1$ and $\xi = 0.05$ in a $2:1$ cavity.

4.3 Time-dependent viscoelastic RBC

As said above, when Ra passes Rac_1, a regular reverse convection takes place for viscoelastic RBC, which is different from the frequent turbulent random reversal phenomenon and rarely reported. We briefly introduce the reverse Rayleigh-Bénard convection in a cavity of aspect ratio 2:1 filled with PTT viscoelastic fluids. The previous values of the parameters $\beta = 0.2$, $We = 0.1$ and $Pr = 7.0$ are kept. In fact, for the parameters $\epsilon = 0.1$, $\xi = 0.05$ and $Ra = 1480$, depending on the initial conditons two reversal convection patterns are found, regular reverse with 2 and 3 cells, as shown in Fig. 4.5 and Fig. 4.6. Both figures describe the half period, $\lambda/2$, of the regular reverse. It can be easily found that 2-cell reverse convection is strictly symmetric with respect to $x = 1$, while 3-cells are center-symmetric.

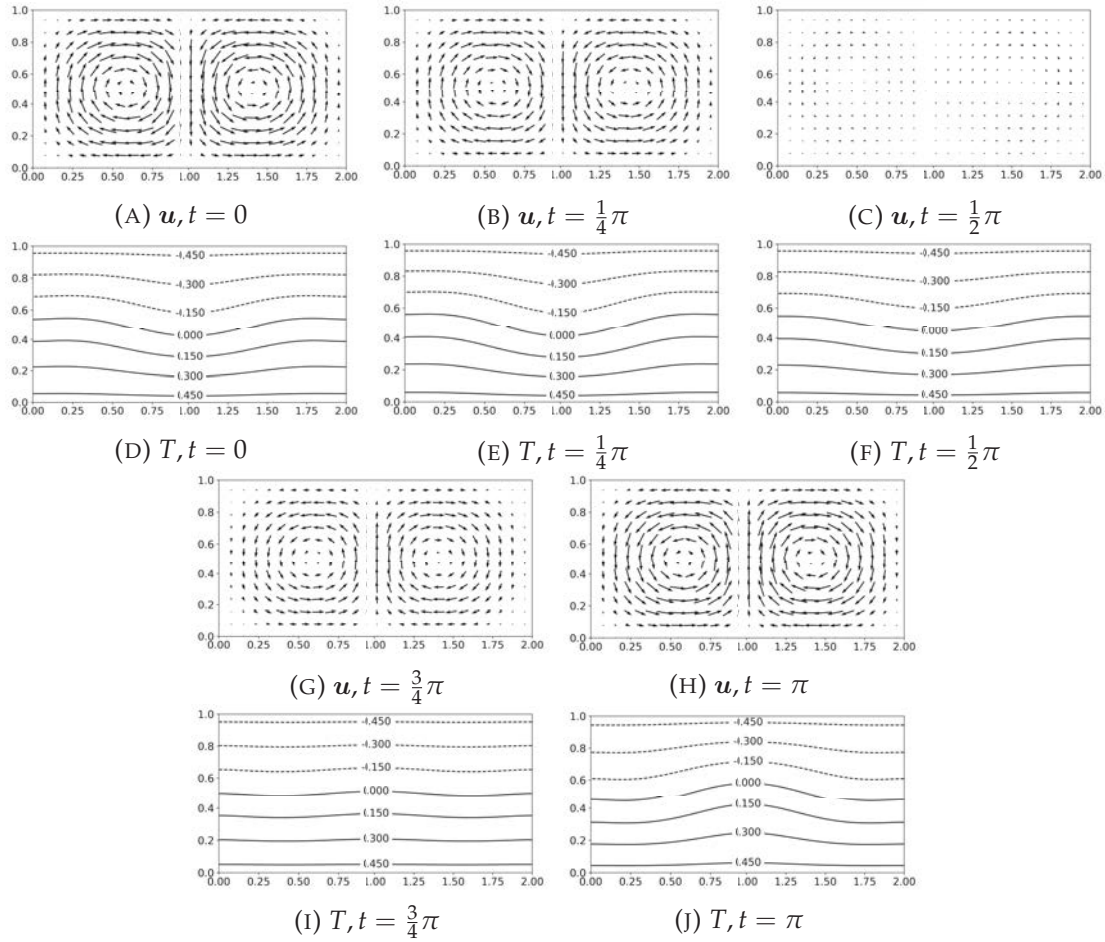

(A) $\boldsymbol{u}, t = 0$ (B) $\boldsymbol{u}, t = \frac{1}{4}\pi$ (C) $\boldsymbol{u}, t = \frac{1}{2}\pi$

(D) $T, t = 0$ (E) $T, t = \frac{1}{4}\pi$ (F) $T, t = \frac{1}{2}\pi$

(G) $\boldsymbol{u}, t = \frac{3}{4}\pi$ (H) $\boldsymbol{u}, t = \pi$

(I) $T, t = \frac{3}{4}\pi$ (J) $T, t = \pi$

FIGURE 4.5: Velocity vector and isothermal lines of the reverse convection with 2 cells at five time points of the half period. We fixed $Ra = 1480$, $Pr = 7.0$, $\beta = 0.2$, $We = 0.1$, $\epsilon = 0.1$ and $\xi = 0.05$.

In order to better understand the flow pattern transition related to the convection onset, we use hereafter time evolution of the total kinetic energy defined by

$$E_{Total} = \int_{\Omega} \frac{1}{2}(u^2 + v^2) d\Omega \tag{4.1}$$

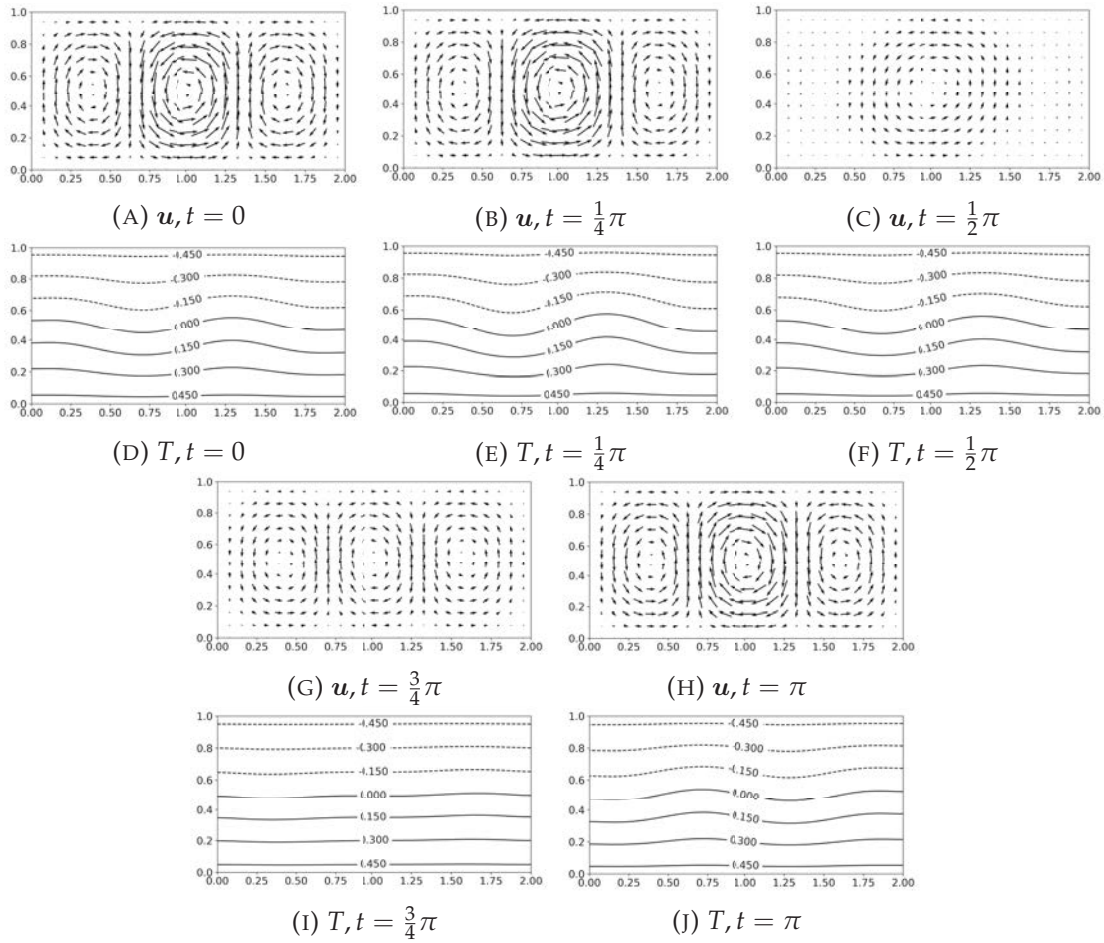

(A) $\boldsymbol{u}, t = 0$ (B) $\boldsymbol{u}, t = \frac{1}{4}\pi$ (C) $\boldsymbol{u}, t = \frac{1}{2}\pi$

(D) $T, t = 0$ (E) $T, t = \frac{1}{4}\pi$ (F) $T, t = \frac{1}{2}\pi$

(G) $\boldsymbol{u}, t = \frac{3}{4}\pi$ (H) $\boldsymbol{u}, t = \pi$

(I) $T, t = \frac{3}{4}\pi$ (J) $T, t = \pi$

FIGURE 4.6: Velocity vector and insotermal lines of the reverse convection with 3 cells at five time points of the half period. We fixed $Ra = 1480$, $Pr = 7.0$, $\beta = 0.2$, $We = 0.1$, $\epsilon = 0.1$ and $\xi = 0.05$.

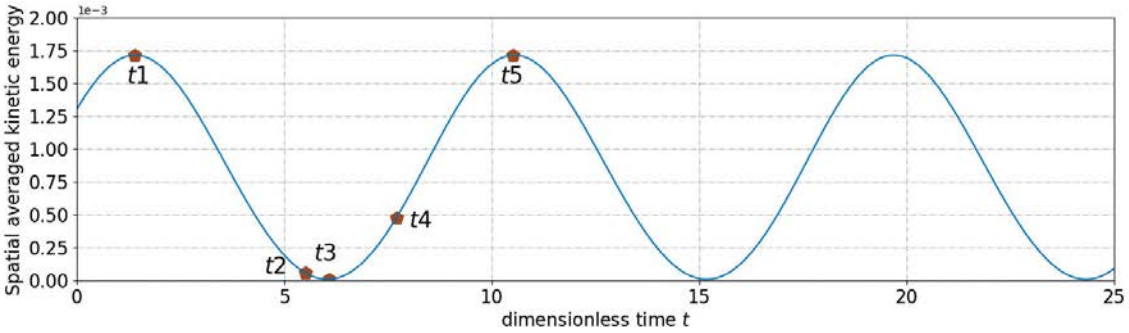

FIGURE 4.7: Time evolution of total kinetic energy E_{total} and five particular time points studied in detail in order to show the flow pattern transition of 2-cell convection.

where Ω is the computational domain.

4.3.1 Two-cell reverse convection

Fig.4.7 plots the total kinetic energy E_{total} as a function of time and shows a regular periodic behavior. On this figure are marked five particular time points for one kinetic energy period, $\lambda/2$, from t_1 to t_5: t_1 and t_5 are at the maximum kinetic energy while t_3 is at the minimum kinetic energy (about zero). Note that one time period of kinetic energy is only one half of time period of velocity, i.e. the convection reverse. The flow fields corresponding to these five time points are displayed in Fig. 4.8 and Fig. 4.9.

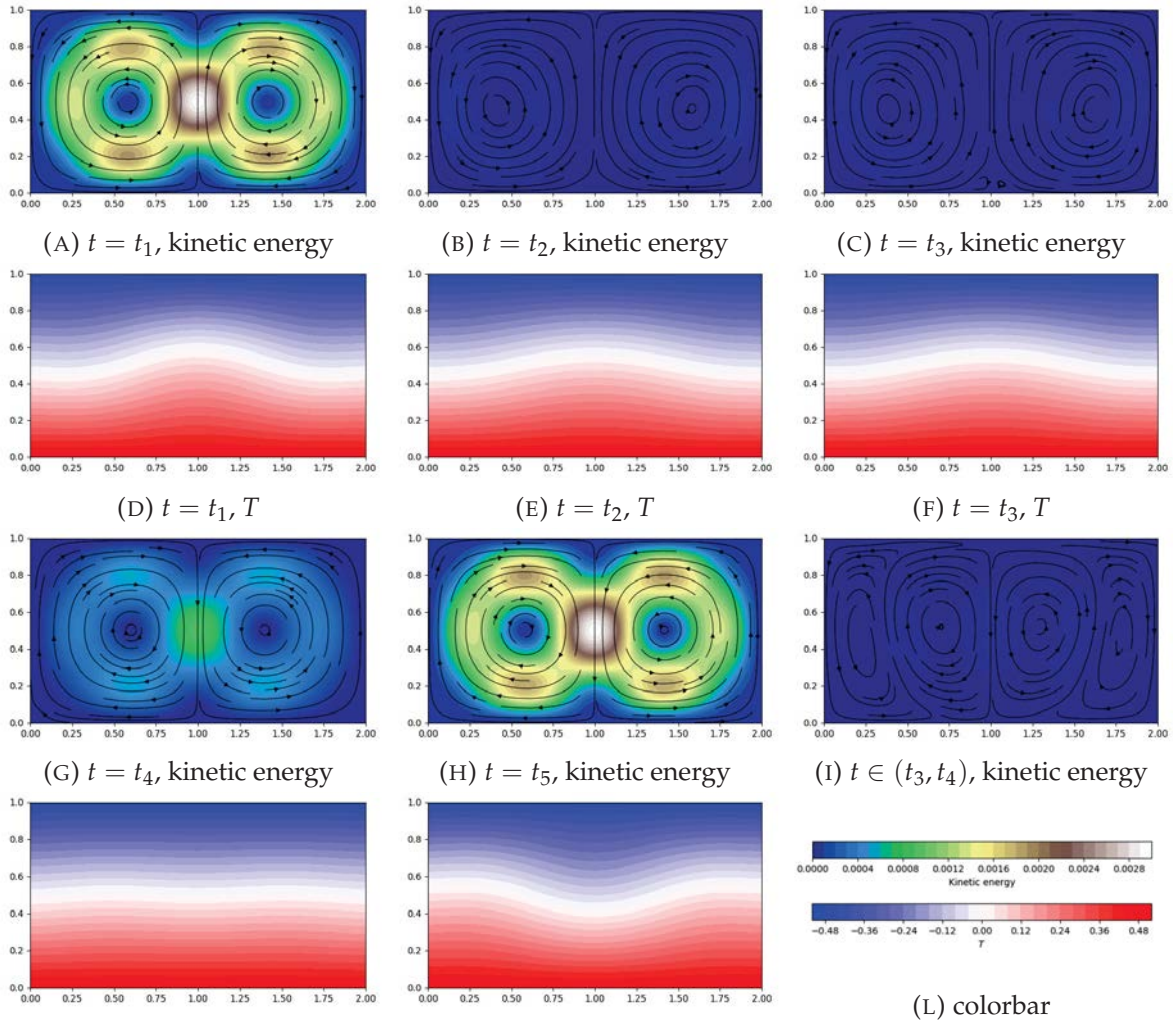

(A) $t = t_1$, kinetic energy (B) $t = t_2$, kinetic energy (C) $t = t_3$, kinetic energy

(D) $t = t_1$, T (E) $t = t_2$, T (F) $t = t_3$, T

(G) $t = t_4$, kinetic energy (H) $t = t_5$, kinetic energy (I) $t \in (t_3, t_4)$, kinetic energy

(L) colorbar

(J) $t = t_4$, T (K) $t = t_5$, T

FIGURE 4.8: Kinetic energy (streamline) and temperature snapshots of convection reversal in a 2:1 cavity filled with a PTT fluid ($\beta = 0.2$, $We = 0.1$, $Pr = 7.0$ $\epsilon = 0.1$, $\xi = 0.05$ and $Ra = 1440$) at the five particular time points indicated in Fig. 4.7. Fig. 4.8i shows the streamline when t is between t_3 and t_4.

At t_1, E_{total} is maximum and flow is upward along the cavity centerline. Velocity gradient also reaches its extreme values. The extrema of the velocity gradient amplify and continue to amplify τ_{ij}.

At t_2, the extrema of τ_{11} and τ_{22} happen at about $(x, y) = (1, 0.9)$ and $(x, y) = (1, 0.3)$,

respectively. These extrema are much larger than those in the same regions at t_1. From t_1 to t_2, the amplification of τ_{ij} also increases its divergence, for example u_1 and u_2 are amplified due to $\frac{\partial \tau_{11}}{\partial x_1}$ and $\frac{\partial \tau_{22}}{\partial x_2}$, respectively. The increase in $\frac{\partial \tau_{11}}{\partial x_1}$ about $(x, y) = (0, 75, 0.9)$ increases therefore u_1 there, this makes u_1 (< 0) evolve toward 0. The decrease in $\frac{\partial \tau_{22}}{\partial x_2}$ (< 0) about $(x, y) = (1, 0.4)$ decreases u_2 there as well. The amplification of τ_{ii} weakens considerably the velocity field as the maximum velocity changes from approximately 0.09 at t_1 to approximately 0.015 at t_2. During the same period no significant change is observed on the temperature field. The weakening of the velocity field continues from t_2 to t_3 and t_4.

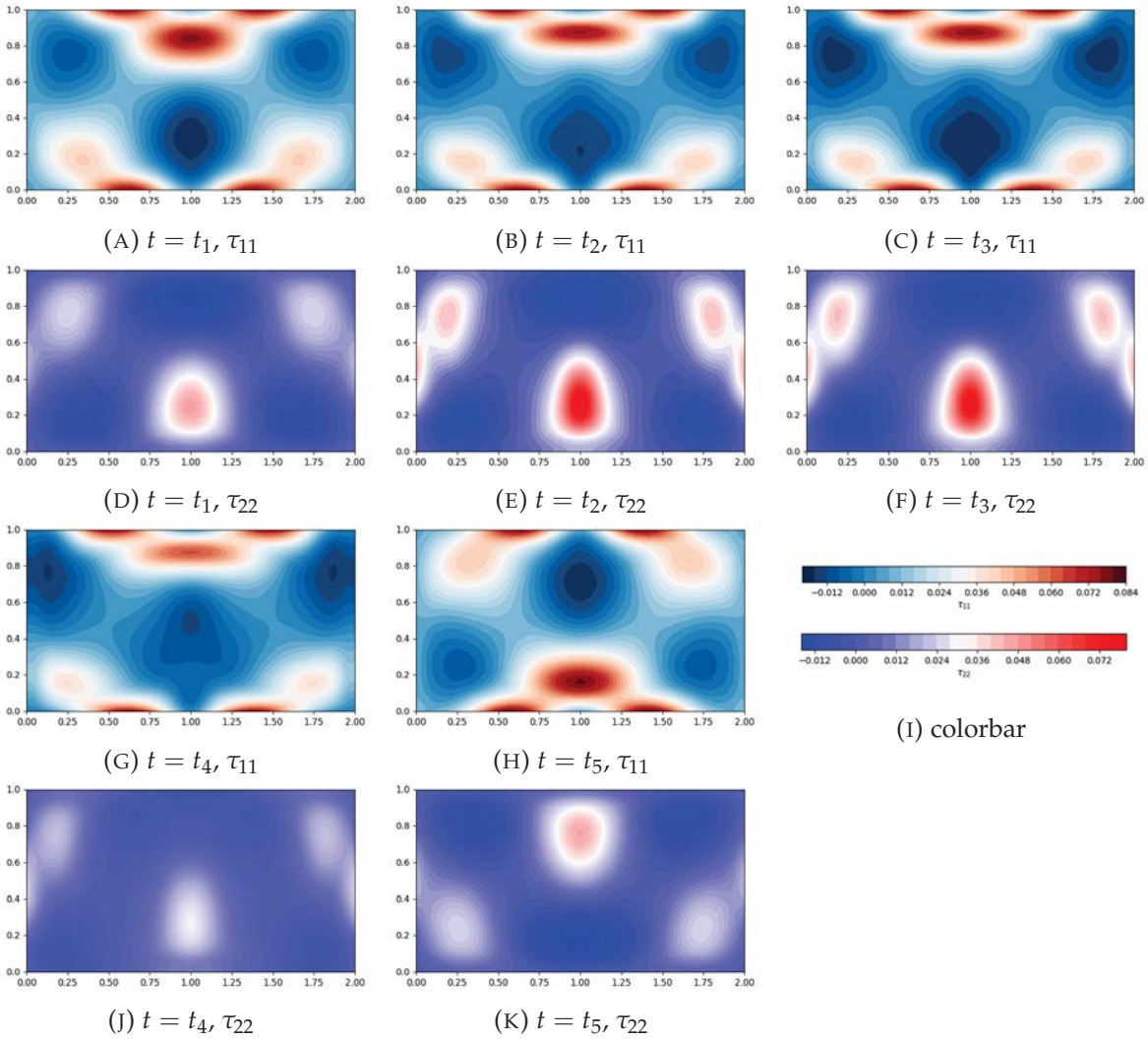

(A) $t = t_1$, τ_{11} (B) $t = t_2$, τ_{11} (C) $t = t_3$, τ_{11}

(D) $t = t_1$, τ_{22} (E) $t = t_2$, τ_{22} (F) $t = t_3$, τ_{22}

(G) $t = t_4$, τ_{11} (H) $t = t_5$, τ_{11} (I) colorbar

(J) $t = t_4$, τ_{22} (K) $t = t_5$, τ_{22}

FIGURE 4.9: Normal stresses τ_{11} and τ_{22} snapshots of convection reversal in a 2:1 cavity filled with a PTT fluid ($\beta = 0.2$, $We = 0.1$, $Pr = 7.0$ $\epsilon = 0.1$, $\xi = 0.05$ and $Ra = 1440$) at the five particular time points indicated in Fig. 4.7.

When time passes t_2, two small vortices appear near the bottom wall about the cavity vertical centerline (see Fig. 4.8c), then grow rapidly up and invade completely the cavity at t_4. It is in the interval from t_3 to t_4 that temperature field undergoes an important evolution.

At t_4 temperature distribution is almost completely conductive. Note also that at t_4 velocity field remains very weak and is downward along the cavity centerline. A weak velocity field

means also a weak source term of $\boldsymbol{\tau_p}$. As $\boldsymbol{\tau_p}$ is governed approximately by

$$\frac{\partial \boldsymbol{\tau_p}}{\partial t} + \boldsymbol{\tau_p}/We + \frac{\epsilon\sqrt{Ra}}{(1-\beta)Pr} tr(\boldsymbol{\tau_p})\boldsymbol{\tau_p} = 0 \tag{4.2}$$

τ_{ii} is damped slightly from t_2 to t_3 and damped strongly from t_3 to t_4. The signs of τ_{11} and τ_{22} change along the vertical centerline on the way from t_4 to t_5. When t_4 is reached τ_{11} is negative at $(x, y) = (1, 0.2)$ and positive at $(x, y) = (1, 0.8)$, while they are getting to change sign. At t_5 τ_{11} is positive at $(x, y) = (1, 0.2)$ and negative at $(x, y) = (1, 0.8)$. From t_4 to t_5 velocity field is amplified to reach an extremum at t_5 and temperature field also evolves from conductive distribution to convective distribution. Again the amplified velocity gradient amplifies $\boldsymbol{\tau_p}$ and the amplified extrema of $\boldsymbol{\tau_p}$'s divergence weaken the velocity field; weak velocity field damps $\boldsymbol{\tau_p}$ in turn, small vortices appear near the top wall about the vertical centerline, grow rapidly and invade the cavity, flow direction is reversed and convective temperature distribution switches to a conductive distribution; the damping of $\boldsymbol{\tau_p}$ continues, τ_{ii} change signs along the cavity vertical centerline, velocity is amplified again to reach the extremum and temperature field becomes again convective.

The above observations indicate that there is a phase shift between the amplification and damping cycles of the velocity (see Fig. 4.10) and the extra-stress. This phase shift is responsible for the time-dependent flow regime.

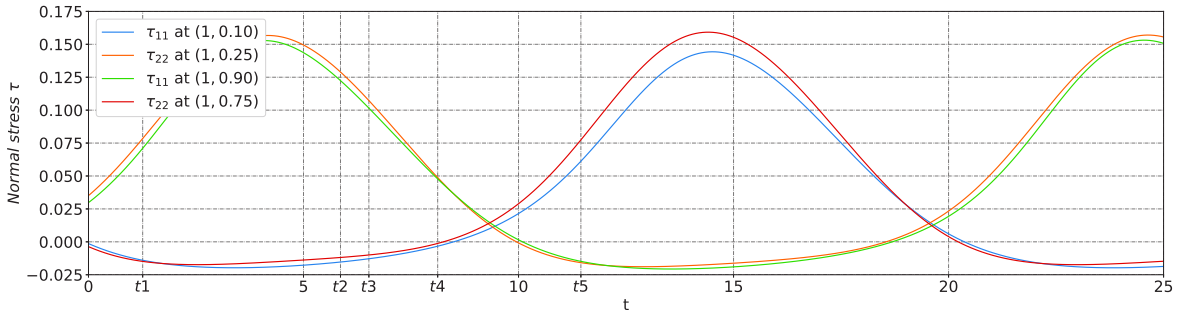

FIGURE 4.10: Time evolution of the extra-stresses τ_{ii} at positions on the vertical centerline . It is clear from the time evolution of these entities from t_1 to t_5 that the extrema of τ_{ii} occur later in time than the maximum of kinetic energy and therefore than the velocity extrema.

Energy transport equation

In order to have a deeper understanding of reverse convection, a simple idea is to follow Cheng et al. (2017) and Li et al. (2017) who give a new insight into reversal mechanic by considering the turbulent kinetic energy budget (TKE). An understanding of the reversal evolution, and the effects of the viscoelastic feature on it, can be obtained by considering the global and local energy transport between flow structure and polymer.

From Eq. (3.13) (mass conservation equation) and Eq. (3.16) (momentum equation), we can establish the kinetic energy equation of the instantaneous fluid flow:

$$\frac{dE}{dt} = \Phi_D + \Phi_V + \Phi_G + \Phi_F \tag{4.3}$$

where

- $E = \frac{1}{2}u_i u_i$ denotes the kinetic energy;
- $\Phi_D = -\frac{\partial(pu_j)}{\partial x_j} + \beta\frac{Pr}{\sqrt{Ra}}\frac{\partial^2 E_{ij}}{\partial x_j^2}$ represents the pressure diffusion and molecular viscous transport;
- $\Phi_V = -\beta\frac{Pr}{\sqrt{Ra}}\frac{\partial u_i}{\partial x_j}\frac{\partial u_i}{\partial x_j}$ represents the viscous dissipation, which describes the work done by a fluid on adjacent layers because the action of shear forces is transformed into heat;
- $\Phi_G = -u_i\frac{\partial \tau_{ij}}{\partial x_j} = -(\frac{\partial(u_i\tau_{ij})}{\partial x_j} - \tau_{ij}\frac{\partial u_i}{\partial x_j})$ denotes the energy transition between flow structures and polymer microstructures due to the stretching and relaxation behaviour of polymer chains.
- $\Phi_F = PrTe_j u_j$ is buoyancy flux which describes the work done by the density difference according to the Boussinesq approximation.

In the term Φ_G, $\frac{\partial(u_i\tau_{ij})}{\partial x_j}$ and $\tau_{ij}\frac{\partial u_i}{\partial x_j}$ denote the elastic dissipation and interactive impact between flow and polymers respectively. In RHS of Eq. (4.3), Φ_G only offers the intensity of energy transfer between flow and polymer structures, doesn't directly represent the magnitude of the elastic potential energy. For a flow with the viscoelastic fluid of the PTT model, we can think of the component C_{ij} of the conformation tensor C as the end-to-end moment ($\langle r_i r_j \rangle$) of the extension of the polymers, modelled as linear spring-dumbbell. In this scaling, the equilibrium conformation corresponds to an isotropic distribution with unit end-to-end displacements. When C is a unit vector, it means that the polymer structure is in a natural state, without force. We know that the relationship between the elastic stress and conformation tensor can be expressed by

$$\tau_p = \frac{1-\beta}{We}(C - I) \tag{4.4}$$

where C is the polymer conformation tensor and I is the unit matrix . The elastic energy stored in the polymers is proportional by

$$tr(\tau_p) \sim \frac{1-\beta}{We}(tr(C) + constant) \tag{4.5}$$

In the following, we will use the total normal elastic stress (τ_{ii}) to represent the stretching and shrinking energy of the macromolecular structure of polymer in the viscoelastic flow. Eq. (4.5) is important for the convection flow with the PTT model in our simulation, as shown the third term of LHS of Eq. (4.2).

Eq. (4.3) describes the relationship among different energy contributions, it can be used in either the current local form or the global-integrated form (with operator $\langle\cdot\rangle_\Omega$). The energy convection framework described by Eq. (4.3) is pictured in Fig. 4.11.

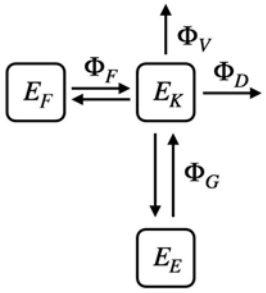

FIGURE 4.11: Energy convertion framework for viscoelastic Rayleigh-Bénard convection. Three energy reservoirs, the kinetic energy reservoir, the elastic energy reservoir and the buoyancy potential energy reservoir are E_K, E_E and E_F respectively in the RBC system. Energy transport between E_K and E_E is performed by Φ_G. Energy transport between E_F and E_E is performed by buoyancy flux Φ_F.

Process of kinetic energy transport

To discuss the influence of We and β on the energy transport mechanism in reverse regime, and depcit the energy transfer process, we fixed the following parameters $Ra = 1200$, $Pr = 7.0$, $\epsilon = 0.1$ and $\xi = 0.05$.

Firstly, we checked the effect of the (We, β) on the energy evolution, We and β adopted are in $We \in (0.1, 0.15, 0.2)$ and $\beta \in (0.1, 0.2)$ respectively. Fig. 4.12 shows each type of the integrated energy ($\langle\cdot\rangle_\Omega$) evolution corresponding to the dimensionless time in one completed reversal period with various β and We. In order to facilitate the comparison, the time period in each case is rescaled graphically into the same x-coordinate range, and the real time period is texted in the right-down of the figure. $\langle\Phi_V\rangle_\Omega$ is negative or almost zero during the reversal process, this agrees with its definition. $\langle\Phi_D\rangle_\Omega$ is almost zero all the time and can be neglected in the process of kinetic energy transport. $\langle\Phi_F\rangle_\Omega$ is globally generating term during the process because it is most of the time positive, this agrees with the fact that RBC is a buoyancy-driven flow. $\langle\Phi_G\rangle_\Omega$ is globally dissipation term because it is most of the time negative.

According to the instantaneous flow structure and potential energy state of the reverse convection, we tend to divide a half-period of the reversal process (from the time-point with peak kinetic energy value to next maximum kinetic energy time-point with opposite velocity direction) into two phases, including the phase *kinetic-decrease* ($a - b$) and the phase *kinetic-increase* ($b - a^*$): in phase *kinetic-decrease*, the kinetic energy $\langle E\rangle_\Omega$ decrease from the peak value (a) to zero (b). As $\langle E\rangle_\Omega$ gets to almost zero, each term in left of Eq. (4.3) is equal to almost zero as well; in phase *kinetic-increase*, the flow structure is reorganized, the kinetic energy gradually increases and gets to peak value again (a^*). Actually, the phase *kinetic-increase* is a complex process that the flow structure is driven by multi contributions from elastic stress and thermal buoyancy

in the different time range. The elastic stress does work to increase kinetic energy in phase $(b-d)$ and the buoyancy flux does work to increase kinetic energy in phase $(c-a^*)$. In order to explain the reversal process clearly, we prefer to divide the *kinetic-increase* phase into three sub-phases by distinguishing the contributions that drive the flow,: phase *elastic-contribution* $(b-c)$, in which only elastic stress does positive work on flow structure; phase *elastic-buoyancy-contribution* $(c-d)$, in which elastic stress and thermal buoyancy do positive work on flow structure together; and phase *buoyancy-contribution* $(d-a^*)$, in which only thermal buoyancy do positive work on flow structure. Note that a complete reverse period has two kinetic energy periods, which differ only in the evolution of velocity direction (from $u_2 > 0$ to $u_2 < 0$ or from $u_2 < 0$ to $u_2 > 0$).

As shown in Fig. 4.12, the phase *kinetic-decrease* starts at time-point (a) and ends at time-point (b), in which the global kinetic energy decreases from peak value (a) to zero (b). in the same phase, the term of elastic energy exchange $\langle\Phi_G\rangle_\Omega$ remains negative, which means the system energy was transformed from the kinetic energy into elastic potential energy, in another word, the kinetic energy was stored into polymer macromolecular structure. In addition, the buoyancy flux $\langle\Phi_F\rangle_\Omega$ which is the only generating term also decreases to zero, resulting in the gradually vanishing of the velocity field. At the end of the phase *kinetic-decrease*, the high values of normal stress (τ_{11}, τ_{22}) appeared in the near-wall areas and along the vertical central line as shown in Fig. 4.9b and Fig. 4.9e. Two symmetric small vortices are born and grow near the horizontal wall about the vertical centerline of the cavity when time pass time-point (b), shown in Fig. 4.8b and Fig. 4.8c.

The *elastic-contribution* and *elastic-buoyancy-contribution* phases are in time range $(b-c)$ and $(c-d)$. At the start of the *elastic-contribution* the velocity field almost stays stationary and buoyancy flux is also almost zero, but, elastic stress field has important value (shown in Fig. 4.9b and Fig. 4.9e). At the the beginning of phase *elastic-contribution*, $\langle\Phi_G\rangle_\Omega$ changes from negative to positive, kinetic energy slightly increases but buoyancy flux keeps going down to negative values $\langle\Phi_F\rangle_\Omega < 0$, which means that polymer structure starts to do positive work (contribution) on the flow structure, however, buoyancy distribution plays an inhibiting role in flow convection. In this phase, an important question was raised: *what supports the reverse occurrence and its growth?* The only positive energy input (for flow structure) to drive the birth of opposite convection is the release of the elastic stress ($\langle\Phi_G\rangle_\Omega > 0$), especially normal stress τ_{22} (in the central region of the domain) and τ_{11} (in the near-horizontal wall) which offer enormous tensile force, the elastic energy of polymer macrostructure is transformed into the kinetic energy of flow structure, it even cancels out the dissipation effect of the negative buoyancy flux (shown in Fig. 4.8f and Fig. 4.8j).

At the phase *elastic-buoyancy-contribution*, $\langle\Phi_F\rangle_\Omega$ changes its sign to be positive, both $\langle\Phi_F\rangle_\Omega$ and $\langle\Phi_G\rangle_\Omega$ contribute and accelerate the growth of the new vortices. Because both $\langle\Phi_F\rangle_\Omega$ and $\langle\Phi_G\rangle_\Omega$ are positive, the growth rate of kinetic energy is significantly improved and a more

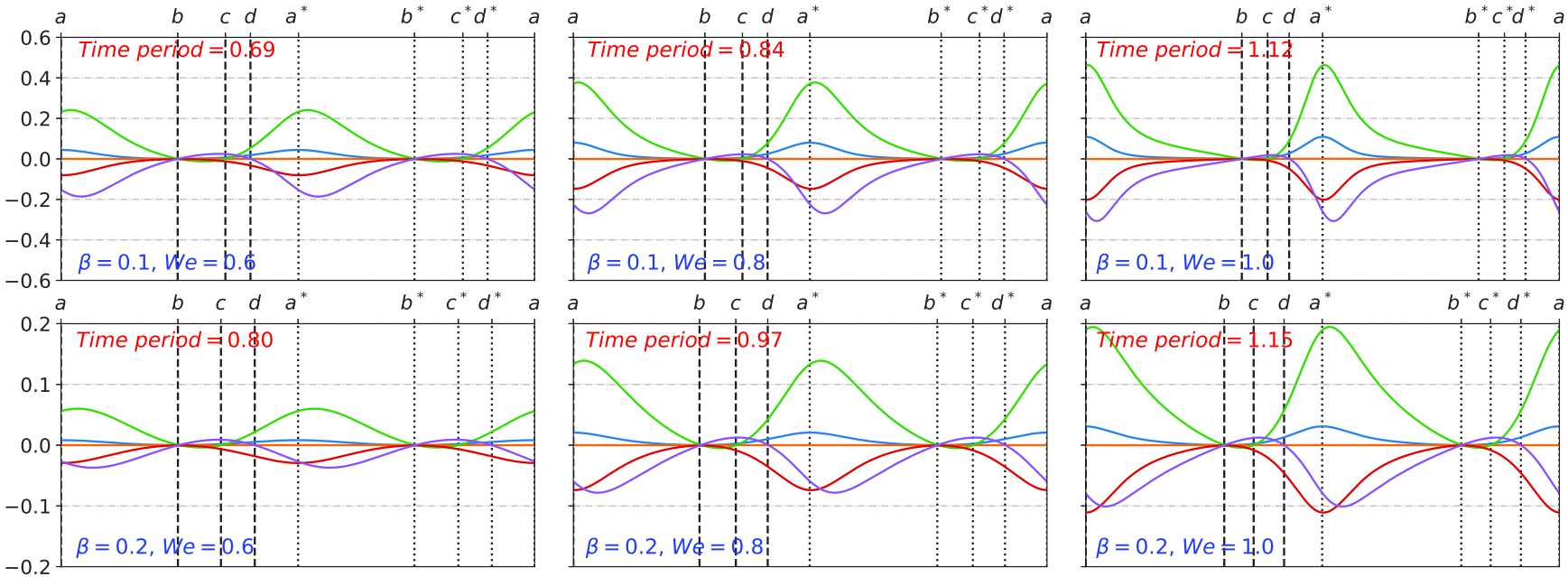

FIGURE 4.12: Different energy evolution in one period corresponding to a complete reversal for $\beta = 0.1$ (top) and $\beta = 0.2$ (bottom) and $We = (0.150, 0.200, 0.250)$ (from left to right), where the time period was normalized graphically. The (——) corresponding to buoyancy flux ($\langle\Phi_F\rangle_\Omega$), the (——) corresponding to kinetic diffusion ($\langle\Phi_D\rangle_\Omega$), the (——) corresponding to energy exchange between flow structures and polymer microstructures due to the stretching and relaxation of polymer chains ($\langle\Phi_G\rangle_\Omega$), the (——) corresponding to bulk viscous dissipation of kinetic energy ($\langle\Phi_V\rangle_\Omega$), the (——) corresponding to global kinetic energy ($\langle E\rangle_\Omega$). We fixed $Ra = 1200$, $Pr = 7.0$, $\epsilon = 0.1$ and $\xi = 0.05$.

important dissipating $\langle \Phi_V \rangle_\Omega$ is also found in this phase. For flow structure, in *elastic-buoyancy-contribution* phase, the original vortices completely vanish and new vortices with opposite rotation take up all the domain, as shown in Fig. 4.8g.

The *buoyancy-contribution* phase depicts the rapid increase of kinetic energy to the maximum value because the new large-scale circulations are formed and the flow structure is more efficiently driven by the buoyancy. In phase *buoyancy-contribution* ($b - a^*$), the elastic potential energy finishes its mission in the former two phases (initiate and accelerate reversals) and turns to absorb energy from flow structure in this phase, as shown in Fig. 4.12. The contours of the normal stresses (τ_{11}, τ_{22}) at key time points can be observed at Fig. 4.9g (Fig. 4.9h) and Fig. 4.9j (Fig. 4.9k): they are amplified again. Comparatively speaking, the increase in viscosity ratio (β) will reduce the time period while the increase in elastic strength (We) is opposite.

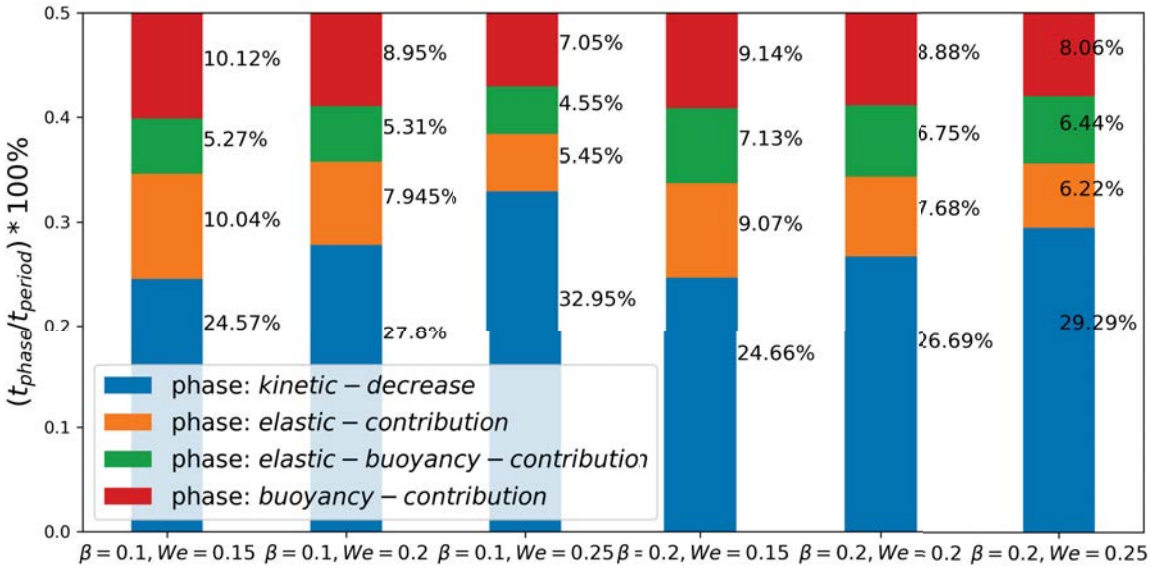

FIGURE 4.13: Time proportion of each phase in one kinetic energy period for cases with $We = (0.1, 0.15, 0.2)$ and $\beta = (0.1, 0.2)$. Other parameters are fixed $Ra = 1200$, $Pr = 7.0$, $\epsilon = 0.1$ and $\xi = 0.05$. As a kinetic energy period is only the half period of the convection reversal, the time ratio is based on the convection reversal period and the sum of the ratios is equal to 0.5. The time period for ech cases are shown in Fig. 4.12 and remarked by red text.

Fig. 4.13 summarizes the time ratio proportion of the each phase in one whole reverse period for cases with $We = (0.1, 0.15, 0.2)$ and $\beta = (0.1, 0.2)$. We define time ratio proportion of the each phase by:

$$\frac{t_{phase}}{t_{period}} * 100\% \tag{4.6}$$

where t_{phase} is the time of each phase, t_{period} is the reversal time period of one flow reversal, which is shown in Fig. 4.12 and remarked in red text. Half period ($a - b - c - d - a^*$) is shown in the figure, as the time proportion of each phase in two half periods is the same. It can be clearly found that time proportion changes of each phase are almost monotonic relative to We and β. As

We increases and β decreases, the time proportion of the phase *kinetic-decrease* was is extended. This can be explained by the fact that, as the elastic effect increases in the reversal process, the macromolecular structure of the polymer can absorb and store more potential energy, and that it takes longer time for the energy to transfer from the flow structure to the elastic structure. For large *We* and small β the stronger elastic effect means that elastic energy will be released more quickly and strongly into the flow structure when the average kinetic energy of the velocity field is almost zero. The reversal process takes place at the beginning of the *elastic-contribution* phase, in this phase elastic stress does positive work alone on flow structure, and drives reverse to occur. As *We* increases and β decreases, the time proportion of *elastic-contribution* and *elastic-buoyancy-contribution* phases is compressed. In fact, elastic energy release takes less time to bring buoyancy flux to be positive and buoyancy flux increases rapidly and makes $\langle \Phi_G \rangle_\Omega$ to be begative rapidly. The time proportion of phase $(d - a^*)$ also decrease with increasing *We* and decreasing β. It leads to a decrease in phase *kinetic-increase* for large *We* and small β.

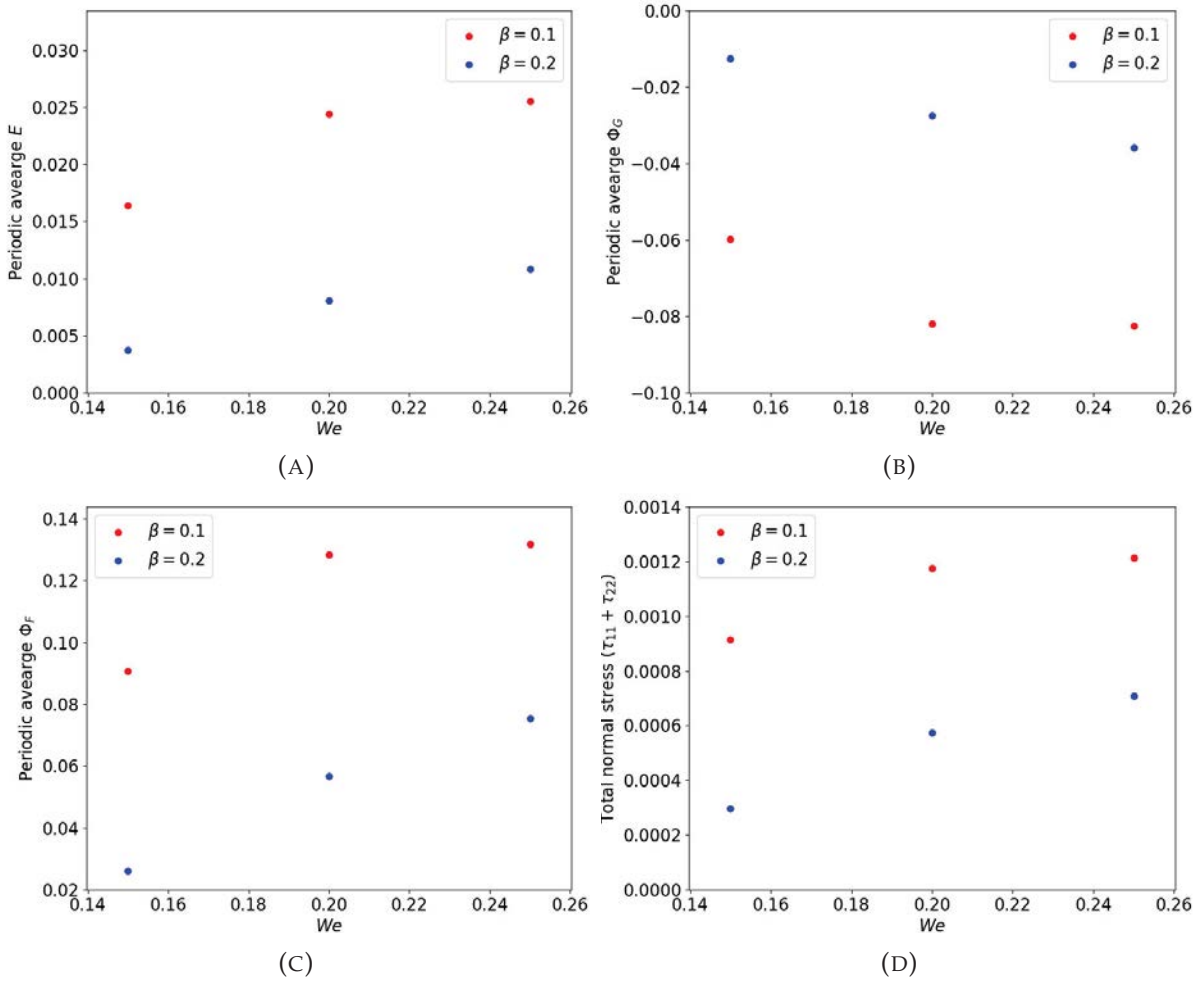

FIGURE 4.14: (a) Averaged kinetic energy $\frac{1}{\lambda}\int_0^\lambda \langle E \rangle_\Omega dt$, (b) averaged energy exchange rate between flow structure and polymer $(\frac{1}{\lambda}\int_0^\lambda \langle \Phi_G \rangle_\Omega dt)$, (c) averaged buoyancy flux $(\frac{1}{\lambda}\int_0^\lambda \langle \Phi_F \rangle_\Omega dt)$, and (d) averaged elastic potential power intensity $(\frac{1}{\lambda}\int_0^\lambda \langle (\tau_{11} + \tau_{22}) \rangle_\Omega dt)$ as a function of *We* with $\beta = (0.1, 0.2)$.

In addition, temporally-spatially averaged energies are also studied. Fig. 4.14 shows the temporally-spatially averaged values of kinetic energy (E), energy exchange rate (Φ_G), buoyancy flux (Φ_F) and total normal elastic stress (τ_{ii}) as functions of We with different β. Under the same conditions, it is easy to find that these quantities increase with We increasing and β decreasing. Bigger We and smaller β make higher the kinetic energy and changes the convective flow.

Spatial distribution of energies

In this part, we shift our attention from spatially integrated variables to local distribution to see how each type of energy evolves in the reverse process, that allows us to know more about reverse process. Fig. 4.15 gives the detail of spatial distribution of the potential energies, including E, Φ_G and Φ_F, for $Ra = 1200$, $Pr = 7.0$, $\beta = 0.1$, $We = 0.150$, $\epsilon = 0.1$ and $\xi = 0.05$. Following Fig. 4.12, potential energy contours corresponding to five key time-points ($a - b - c - d - a^*$) are presented. The streamline is drawn in E figures, and the isoheight with zero value is drawn in Φ_G and Φ_F figures.

From Fig. 4.15 we can see that, at the beginning of the *kinetic-decrease* phase ($t = a$), two symmetrical large circulations completely fill up the domain and are shown in Fig. 4.15a. At $t = a$ the elastic-kinetic energy exchange term $\langle\Phi_G\rangle_\Omega$ is negative, but Φ_G is not negative everywhere in the cavity: the local maximum and minimum values take place about the vertical central line, as shown in Fig. 4.15d. This indicates that kinetic energy is globally being either stored or dissipated in polymer structure and that the negative area fills most of the cavity as indicated by Fig. 4.15d, but, at some places the kinetic energy is released into the flow. At the same time, the buoyancy flux ($\langle\Phi_F\rangle_\Omega > 0$) does the positive work on flow structure, but note that Φ_F is not positive everywhere in the cavity as shown in Fig. 4.15g). We distiguish positive and negatie zones seperated by $u_2 = 0$ and $T = 0$ as $\Phi_F = Tu_2$. Obviously the positive zones are larger the the negative ones: The central part near the bottom and the top parts near the cavity corners are negative zones and Φ_F is dissipating kinetic energy there. From $t = a$ to $t = b$, the kinetic energy $\langle E\rangle_\Omega$ is reduced to almost zero. At $t = b$, $\langle E\rangle_\Omega = 0$ and the velocity field is zero everywhere in the cavity. $\langle\Phi_G\rangle_\Omega = 0$ and $\langle\Phi_F\rangle_\Omega = 0$ because u_2 is very weak and almost zero everywhere in the cavity. It is at this moment that positive zones of Φ_G appear and behave as the source term of the kinetic energy: the kinetic energy increases very slowly from $t = b$ to $t = c$. This confirms that from $t = b$ to $t = c$ $\langle\Phi_G\rangle_\Omega$ is the only positive source term to amplify the kinetic energy and hence the velocity field. At $t = c$, $\langle\Phi_G\rangle_\Omega > 0$ and $\Phi_G = -u_{ij}\frac{\partial\tau_{ij}}{x_j} > 0$ takes place in most of the cavity because of $\tau_{ij}\frac{\partial u_i}{x_j}$ in the term Φ_G while $\langle\Phi_F\rangle_\Omega = 0$ is due to the symmetries observed in T (T is almost fully conductive) and u_2. From $t = c$ the positive zones of Φ_F are growing and $\langle\Phi_F\rangle_\Omega$ becomes a positive source term of the kinetic energy and both $\langle\Phi_F\rangle_\Omega$ and $\langle\Phi_G\rangle_\Omega$ contribute to increasing the kinetic energy. At $t = d$, $\langle\Phi_G\rangle_\Omega$ is back to zero again and the positive zones of Φ_F become larger than the negative ones. From $t = d$, $\langle\Phi_F\rangle_\Omega$ is the only positive source term which increases the kinetic energy.

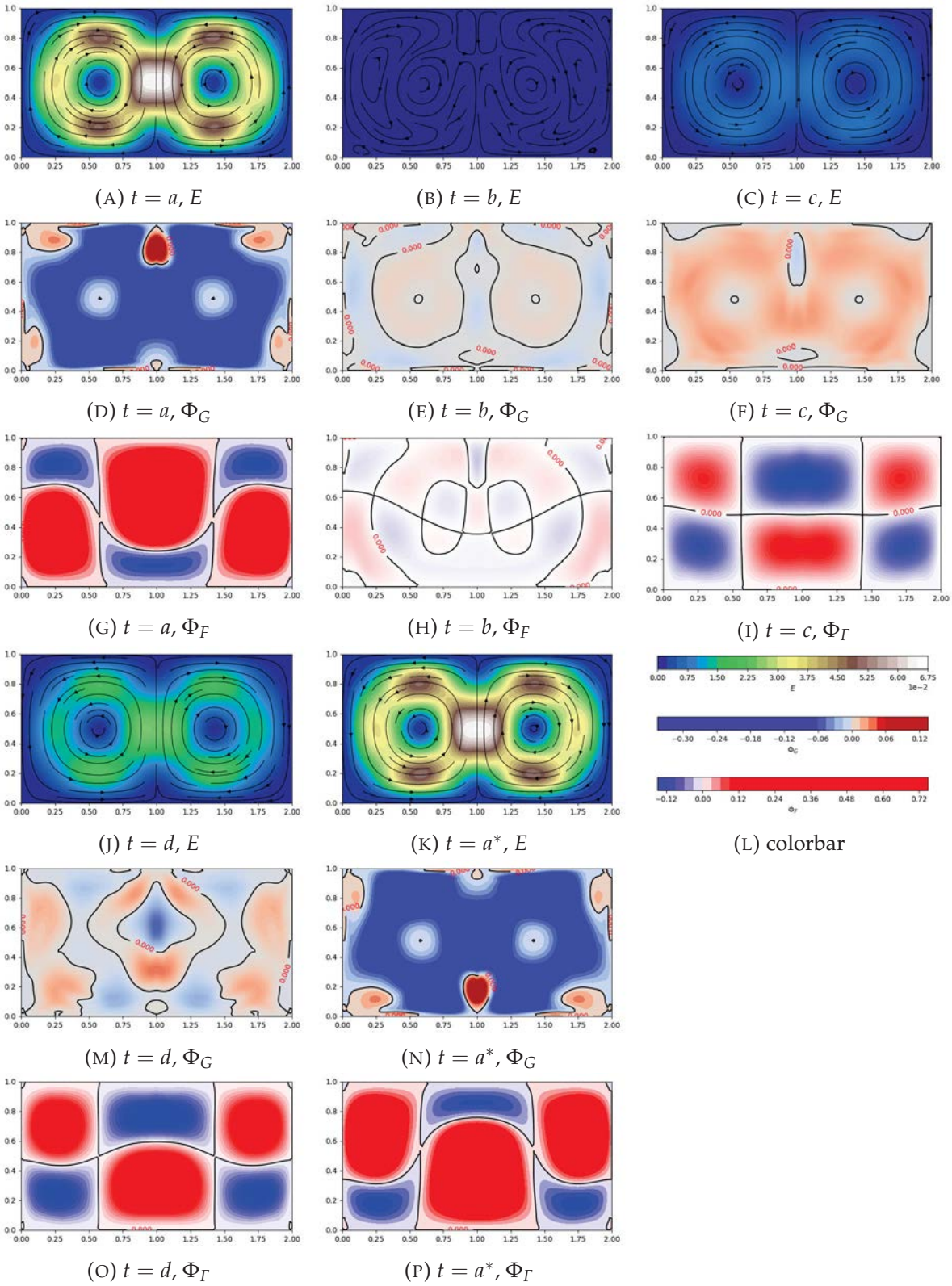

(A) $t = a$, E (B) $t = b$, E (C) $t = c$, E

(D) $t = a$, Φ_G (E) $t = b$, Φ_G (F) $t = c$, Φ_G

(G) $t = a$, Φ_F (H) $t = b$, Φ_F (I) $t = c$, Φ_F

(J) $t = d$, E (K) $t = a^*$, E (L) colorbar

(M) $t = d$, Φ_G (N) $t = a^*$, Φ_G

(O) $t = d$, Φ_F (P) $t = a^*$, Φ_F

FIGURE 4.15: The contours of E, Φ_G, Φ_F at five key time-points ($a - b - c - d - a^*$). The streamline is drawn in E figures, and the isoheight with zero value is drawn in Φ_G and Φ_F figures. In the case we fixed $Ra = 1200$, $Pr = 7.0$, $\beta = 0.1$, $We = 0.150$, $\epsilon = 0.1$ and $\xi = 0.05$.

Total normal elastic stress $(\tau_{11} + \tau_{22})$

Regarding the mechanism of the viscoelastic reverse convection, in order to make it more intuitive, the mechanism can be explained from the perspective of the movement of the long molecular chain of polymer in the convection. The spatial distribution of the total normal elastic stress $(\tau_{11} + \tau_{22})$ at key time-point (corresponding to the Fig. 4.13) are shown in Fig. 4.16. In the figure, the red region represents high value of the $(\tau_{11} + \tau_{22})$ and white region represents low value of the $(\tau_{11} + \tau_{22})$, and the elastic stress in the central vertical region mainly is contributed by τ_{22}, the elastic stress in the horizontal regions near top and bottom walls are mainly contributed by τ_{11}.

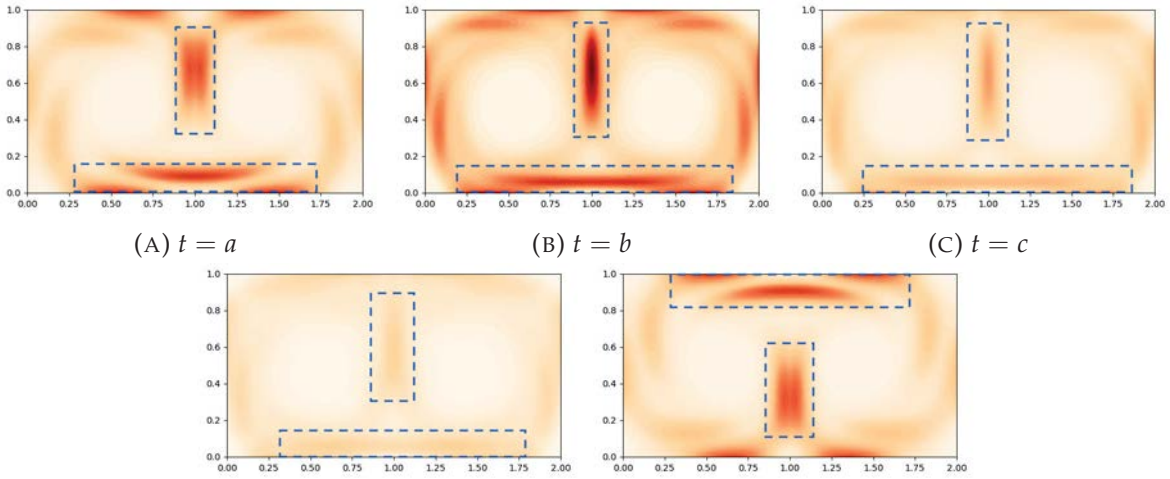

(A) $t = a$ (B) $t = b$ (C) $t = c$

(D) $t = d$ (E) $t = a^*$

FIGURE 4.16: Total normal elastic stress $((\tau_{11} + \tau_{22})|_{(i,j)})$ distribution and evolution in half period. The red region means maximum value and white region means minimum value.

In phase *kinetic-decrease* $(a - b)$, the long molecular chains of polymer (in the blue box region) are in a state of continuous extension, as shown in Figs. (4.16a-4.16b). In this process, the energy stored by the long-chain tension. In phase *elastic-contribution* $(b - c)$, the flow velocity is small enough and the elastic potential energy is large enough, the long-chain of polymer starts to shrink and rebound, as shown in Figs. (4.16b-4.16c). During this process, the polymer releases energy into the flow, meanwhile, the flow reverses. Finally, under the action of the thermal buoyancy and the elasticity, the large-scale circulation in the domain gradually increases in velocity in the opposite direction, as shown in Figs. (4.16c-4.16d).

4.3.2 Three-cell reverse convection

In order to fully explain the mechanism of the viscoelastic property which drives the reversal convection, we also checked the kinetic energy transport in the reversal convection system with 3 cells. To facilitate comparison with the 2-cell situation, in the 3-cell case, we picked up the same fixed parameters $Ra = 1200$, $Pr = 7.0$, $\beta = 0.1$, $We = 0.150$, $\epsilon = 0.1$ and $\xi = 0.05$.

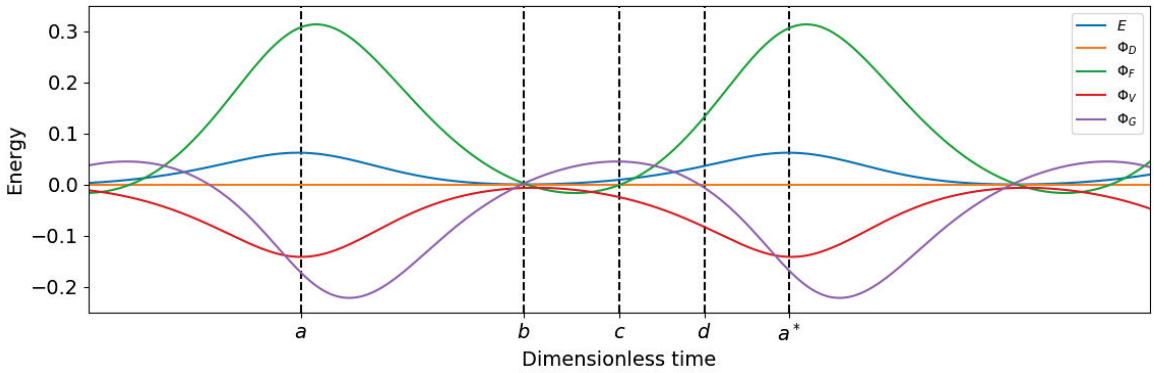

FIGURE 4.17: Different averaged quantities as function of dimensionless time in regular reversal convection system with 3 cells, where the rheology parameters are $\beta = 0.1$, $We = 0.15$, $Ra = 1200$, $\epsilon = 0.1$ and $\xi = 0.05$.

Fig. 4.17 plots the different averaged terms (appearing in the kinetic energy) transport equation in the 3-roll regular reversal convection along dimensionless time. The time period for this case is $\lambda = 0.92$, which is longer than that in the 2-roll situation ($\lambda = 0.69$). Compared with the 2-roll reversal convection, the time evolutions show similar behaviour as that in Fig. 4.12. Fig. 4.17 displays also the five key time-points (a, b, c, d, a^*). Time point a marks the maximum of the kinetic energy and the minimum of the viscous dissipation, the maximum of the buoyancy flux $\langle\Phi_F\rangle_\Omega$ and the minimum of $\langle\Phi_G\rangle_\Omega$ occur later, but note that there is a slight delay between the extrema of $\langle\Phi_F\rangle_\Omega$ and $\langle\Phi_G\rangle_\Omega$. Time-point b corresponds to the moment where $\langle E\rangle_\Omega$, $\langle\Phi_F\rangle_\Omega$ and $\langle\Phi_G\rangle_\Omega$ are equal to almost zero. At this particular time, $\langle\Phi_G\rangle_\Omega$ becomes possitive and therefore becomes a production term, while $\langle\Phi_F\rangle_\Omega$ becomes negative and becomes dissipation term. Time-point c is the moment where $\langle\Phi_F\rangle_\Omega$ crosses zero again. Between b and c, $\langle\Phi_F\rangle_\Omega$ behaves as a dissipation term and after c both $\langle\Phi_F\rangle_\Omega$ and $\langle\Phi_G\rangle_\Omega$ are preduction terms. At time-point d, $\langle\Phi_F\rangle_\Omega$ crosses zero again and retakes its role of a dissipation term. Between d and a^* $\langle\Phi_F\rangle_\Omega$ is the only driving force to amplify to kinetic energy and hence the velocity field.

The mechanism of the convection reversal is the following: before the time point a, the buoyancy flux $\langle\Phi_F\rangle_\Omega$ increase in time, amlifies the kinetic energy and adds energy in the elastic reservoir; $\langle\Phi_F\rangle_\Omega$ reachs its maximum after the time-point a and continues to decrease $\langle\Phi_G\rangle_\Omega$ which reaches its minimum later. This delay in time leads that the kinetic energy $\langle\Phi_F\rangle_\Omega + \langle\Phi_G\rangle_\Omega + \langle\Phi_V\rangle_\Omega + \langle\Phi_D\rangle_\Omega$ is negative and that the kinetic energy $\langle E\rangle_\Omega$ is decreased, and reduced to almost zero at time point b. The elastic potential plays then the leading role as a producton term after b and makes $\langle\Phi_G\rangle_\Omega$ to become positive again before retaking the dissipation role at time point d.

As observed in the 2-cell case, at $t = a$ $\langle\Phi_F\rangle_\Omega$ is a positive term, but Φ_F displays local negative zones and at $t = b$ and c $\langle\Phi_F\rangle_\Omega$ is equal to zero because of $u_2 \sim 0$ at $t = b$ and the symmetries of T and u_2 at $t = c$. In the same way $\langle\Phi_G\rangle_\Omega$ is a dissipation term at $t = a$ but Φ_G displays local positive zones. In terms of the total nomal stress, it remains globally positive: it is amplified from $t = a$ to b, and decreased from $t = b$ to $t = c$ and d. From $t = d$ to a^* it is

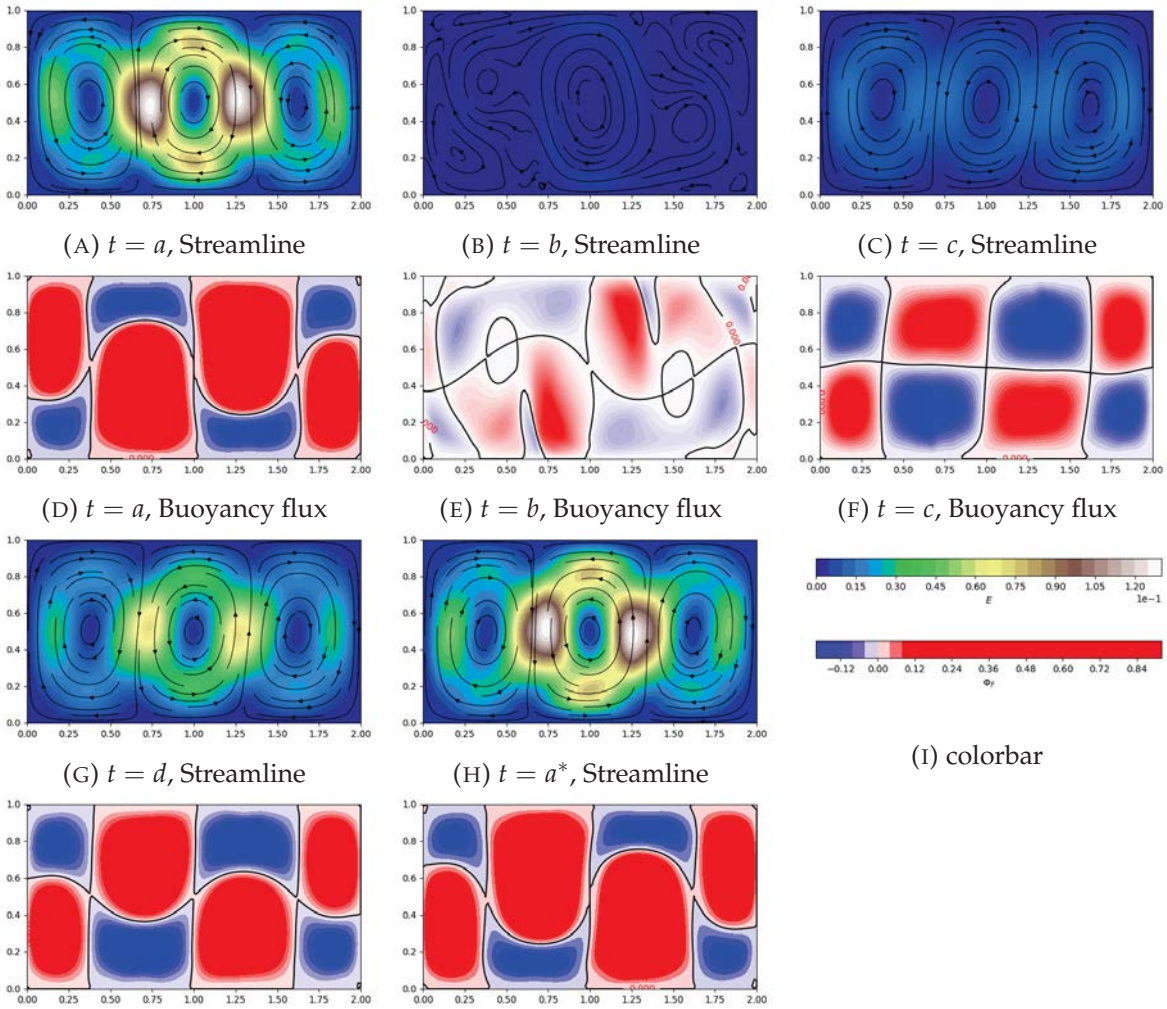

(A) $t = a$, Streamline (B) $t = b$, Streamline (C) $t = c$, Streamline

(D) $t = a$, Buoyancy flux (E) $t = b$, Buoyancy flux (F) $t = c$, Buoyancy flux

(G) $t = d$, Streamline (H) $t = a^*$, Streamline (I) colorbar

(J) $t = d$, Buoyancy flux (K) $t = a^*$, Buoyancy flux

FIGURE 4.18: The contours of the kinetic energy E, buoyancy flux Φ_F at five key time-points ($a - b - c - d - a^*$). In the case we fixed parameters $Ra = 1200$, $Pr = 7.0$, $\beta = 0.1$, $We = 0.150$, $\epsilon = 0.1$ and $\xi = 0.05$.

increased again.

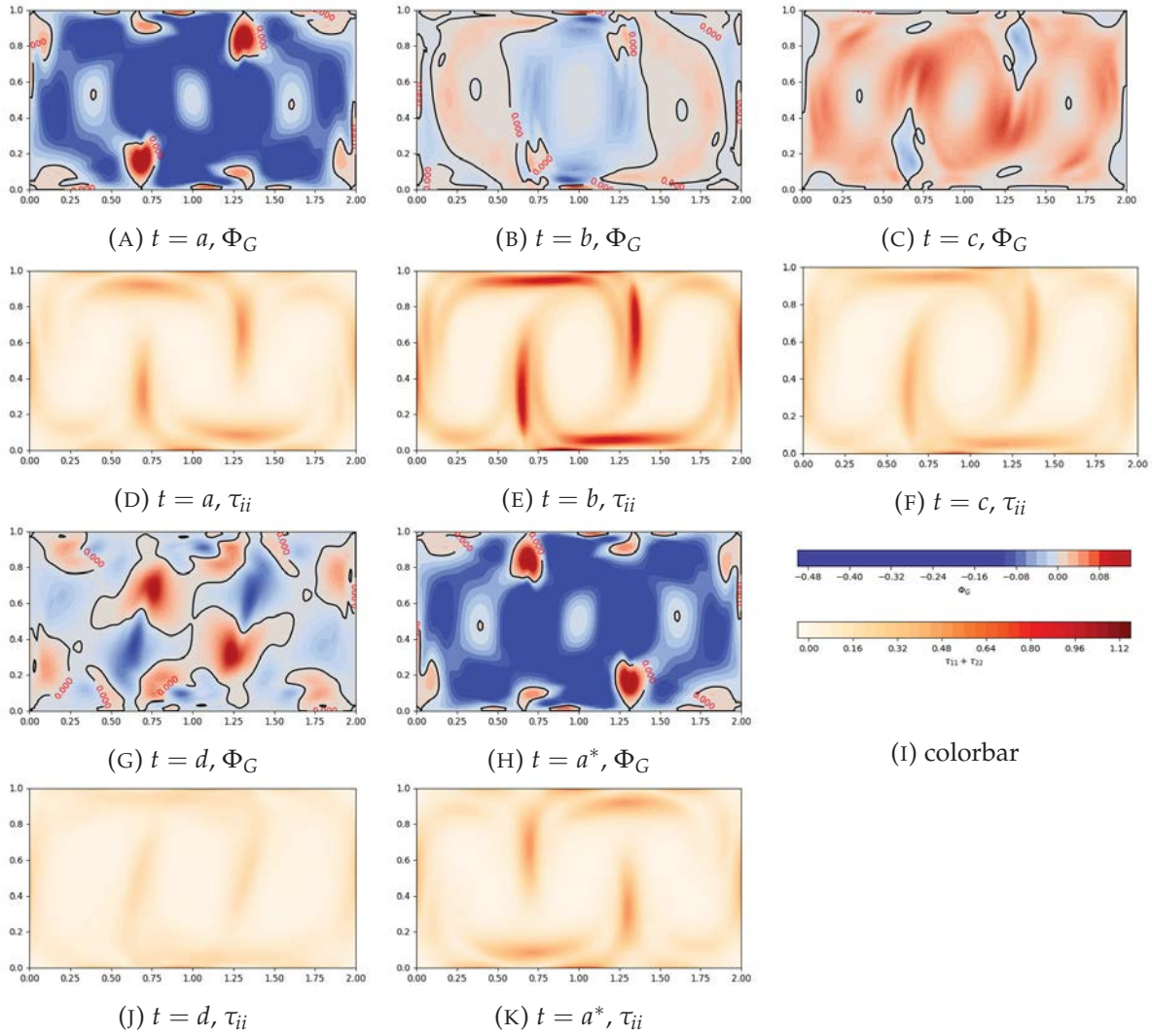

(A) $t = a$, Φ_G (B) $t = b$, Φ_G (C) $t = c$, Φ_G

(D) $t = a$, τ_{ii} (E) $t = b$, τ_{ii} (F) $t = c$, τ_{ii}

(G) $t = d$, Φ_G (H) $t = a^*$, Φ_G (I) colorbar

(J) $t = d$, τ_{ii} (K) $t = a^*$, τ_{ii}

FIGURE 4.19: The contours of Φ_G, total normal stress τ_{ii} at five key time-points ($a - b - c - d - a^*$). In the case we fixed parameters $Ra = 1200$, $Pr = 7.0$, $\beta = 0.1$, $We = 0.150$, $\epsilon = 0.1$ and $\xi = 0.05$.

4.4 Second transition at critical Rayleigh number Rac_2

In this part we will discuss another important parameter in 2-cell periodic reversal convection, reversal frequency, and its behavior with increasing Rayleigh number. This further leads to another key phenomenon, the transition to 2-cell steady-state flows, and the definition of the second critical number $Rac2$. At the same time, we will also study the influence of different rheological parameters on $Rac2$.

Fig. 4.20 shows the time period of reverse at different (ϵ, ξ) and Rayleigh numbers for viscoelastic RBC in 2:1 cavity with fixed $Pr = 7.0$, $\beta = 0.2$, and $We = 0.1$. The overall observation is that increase in both ϵ and ξ increases the periods of time-dependant flows, but near the critical points, at $Ra = 1400$ for example, ϵ and ξ have limited effects on the period increase while at higher Rayleigh number the increase in time period is more important. For a fixed pair of (ϵ, ξ) the period of time-dependant flow increases with Rayleigh number except for $(\epsilon, \xi) = (0, 0)$

(Oldroyd-B fluid). In fact for Oldroyd-B fluid the time period decreases slightly with Ra increasing, that means the flow frequency becomes greater; For the PTT model cases, the time period becomes longer.

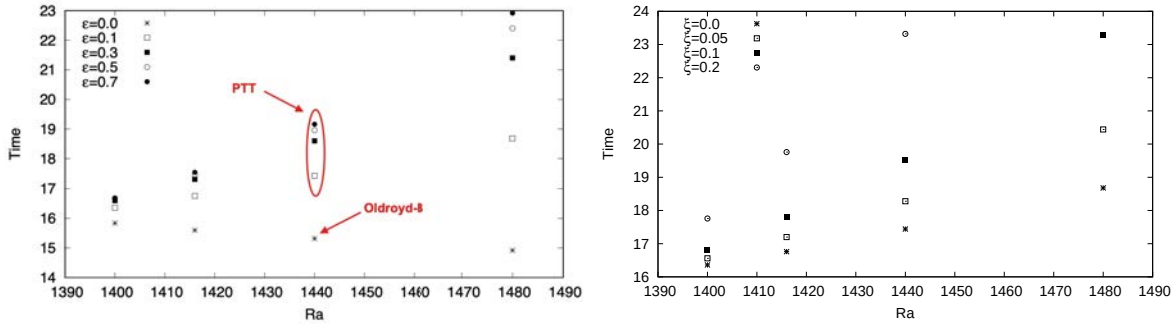

(A) $\epsilon \in [0.0, 0.7]$ and $\xi = 0$ (B) $\epsilon = 0.1$ and $\xi \in [0.0, 0.2]$

FIGURE 4.20: Effects of ϵ and ξ on the time period of the two-cell flows with $Pr = 7.0$, $\beta = 0.2$, and $We = 0.1$. (a) Time period versus Ra at different ϵ and $\xi = 0$ ($\xi = 0.0$ and $\epsilon = 0.0$ denotes Oldroyd-B model) . (b) Time period versus Ra at different ξ and $\epsilon = 0.1$. Increasing ϵ and ξ leads to increase in time period and it is more pronounced at higher Rayleigh number.

For a fixed pair of ϵ and ξ, when increasing further Rayleigh number, a particular phenomenon is observed. Both the convection reversal period and the reversal amplitude increase with Rayleigh number, for PPT constitutive model, as is shown in Fig. 4.20 and Fig. 4.21. The effects of Rayleigh number on the period is stronger than on the amplitude. Beyond a certain limit there is no more time-dependent flow and a steady-state flow is observed. This transition from time-periodic flow to steady-state flow corresponds to another type of bifurcation which is a drift pitchfork bifurcation instead of a Hopf bifurcation.

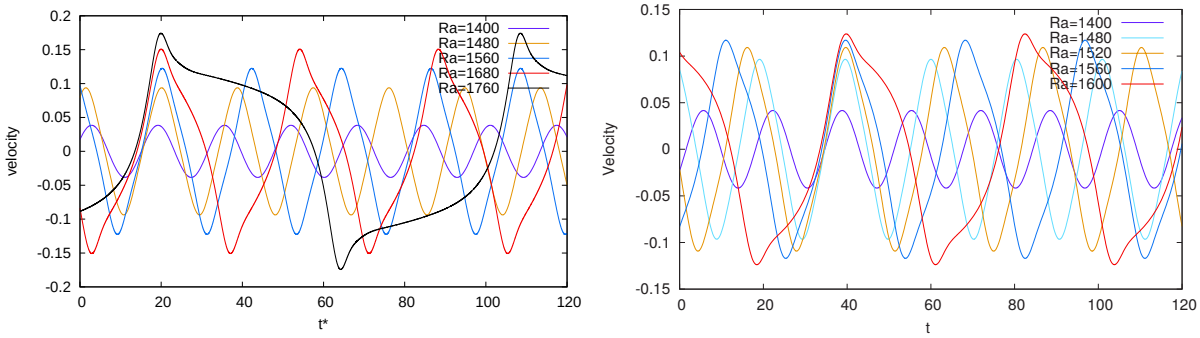

(A) $\epsilon = 0.1, \xi = 0$ (B) $\epsilon = 0.1, \xi = 0.05$

FIGURE 4.21: Time evolution of u_2 at the cavity center $(x, y) = (1, 0.5)$. For both PTT cases the increase in amplitude and the decrease in frequency are observed with increasing Rayleigh number. In the cases, $\beta = 0.2$, $We = 0.1$ and $Pr = 7.0$.

In fact, the control parameter controls the frequency of the reversal flows which is equal to zero at the critical point. The oscillation frequency ω of the reversal convection flow is defined as $\omega = 1/\lambda$ where λ is the oscillation period. Fig. 4.22 displays the relationship between ω^2, square of the oscillation frequency of the reversal convection flow, and Rayleigh number, a

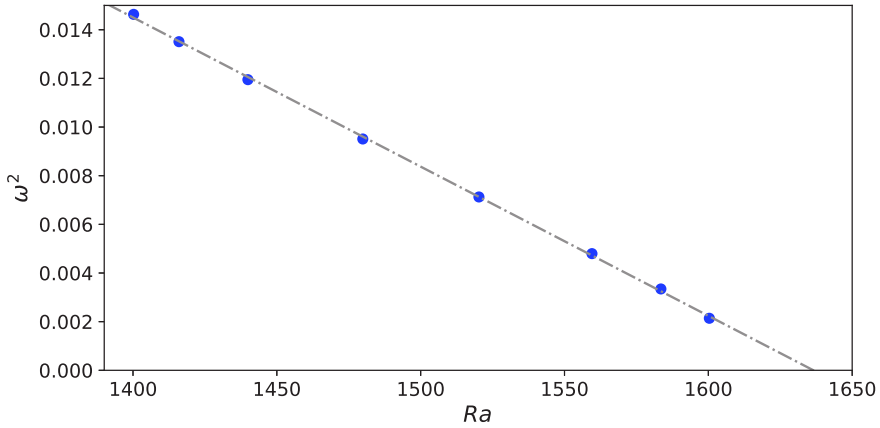

FIGURE 4.22: Square of the oscillation frequency of reversal convection flow versus Rayleigh number ($\beta = 0.2$, $We = 0.1$, $Pr = 7.0$, $\epsilon = 0.1$ and $\xi = 0.05$). A linear relationship is observed and the extrapolation of the linear fitting curve yields $Ra_{c2} = 1635$.

trivial linear relationship is obvious: the drift pitchfork bifurcation is supercritical. The linear curve has a cross-over point with $\omega^2 = 0$, which is the second bifurcation point, Ra_{c2}. An extrapolation of the linear fitting curve can be used again to obtain Ra_{c2}, the second critical Rayleigh number. Above Ra_{c2}, viscoelastic Rayleigh-Bénard convection flow is steady.

4.4.1 Effects of (ϵ, ξ) on Rac_2

The same methodology is applied to $\epsilon \in [0.1, 0.7]$ with $\xi = 0$ and $\xi \in [0.01, 0.2]$ with $\epsilon = 0.1$ and Ra_{c2} was obtained. Fig. 4.23 plots two critical Rayleigh numbers Ra_{c1} and Ra_{c2} against different values of ϵ and ξ used to illustrate the effect of ϵ and ξ on the critical Rayleigh numbers. Ra_{c2} decreases with increasing ϵ (with $\xi = 0$) and ξ (with $\epsilon = 0.1$). The decrease in Ra_{c2} is more pronounced than that in Ra_{c1}: Ra_{c2} decreases from 1762 at $\epsilon = 0.1$ to 1585 at $\epsilon = 0.7$ for $\xi = 0$ and from 1732 at $\xi = 0.01$ to 1500 at $\xi = 0.2$.

The two critical Rayleigh numbers separate the domain of Rayleigh numbers studied into three regions in terms of flow and heat transfer: (i) pure heat conduction without convection flow, $Ra < Ra_{c1}$ (Region 1); (ii) time-periodic oscillating flow, $Ra_{c1} < Ra < Ra_{c2}$ (Region 2); (iii) steady-state convective flow and heat transfer, $Ra > Ra_{c2}$ (Region 3). Region 2 decreases with increasing ϵ and ξ due to the decrease of Ra_{c2}. Flow regime above Ra_{c2} is not studied in the present thesis.

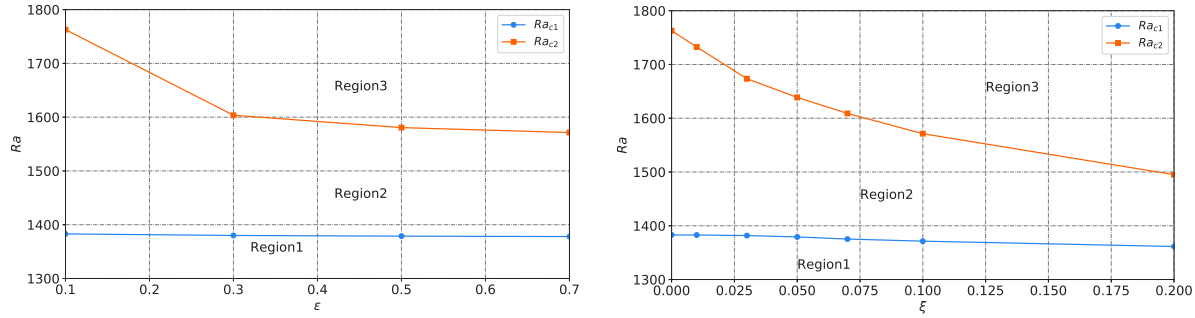

(A) $\epsilon \in [0.1, 0.7], \xi = 0$ (B) $\epsilon = 0.1, \xi \in [0, 0.2]$

FIGURE 4.23: Critical Rayleigh numbers Ra_{c1} and Ra_{c2} versus ϵ and ξ. (a) Effect of ϵ on Ra_c with $\xi = 0$. (b) Effect of ξ on Ra_c with $\epsilon = 0.1$. The critical Rayleigh numbers Ra_{c1} and Ra_{c2} divide the flow regime into three regions: pure conduction without convective flow (Region 1), time-periodic convective flow limited by Rac_1 and Rac_2 (Region 2) and steady-state convective flow for $Ra > Ra_{c2}$ (Region 3). In the cases, $\beta = 0.2$, $We = 0.1$ and $Pr = 7.0$.

4.4.2 Effects of We and β on Rac_2

For PPT constutive model, except (ϵ, ξ), there are other important rheological parameters (β, We) that have an important influence on the second critical Rayleigh number $Rac2$. Fig. 4.24 shows the effects of the Weissenberg number on the two critical Rayleigh numbers when β is fixed at $(0,1,\ 0.2)$, where the coverage range of We is $[0.075, 0.25]$. We can observe that the Weissenberg number has an important influence on the two critical Rayleigh number, reducing the values of two critical Rayleigh numbers. At the same time, a threshold of the Weissenberg number also was found. For example, when $\beta = 0.2$ and the threshold of Weissenberg number is around 0.067. This means that the reverse convection phenomenon will disappear, no matter what Rayleigh number is, when Weissenberg number is less than 0.067.

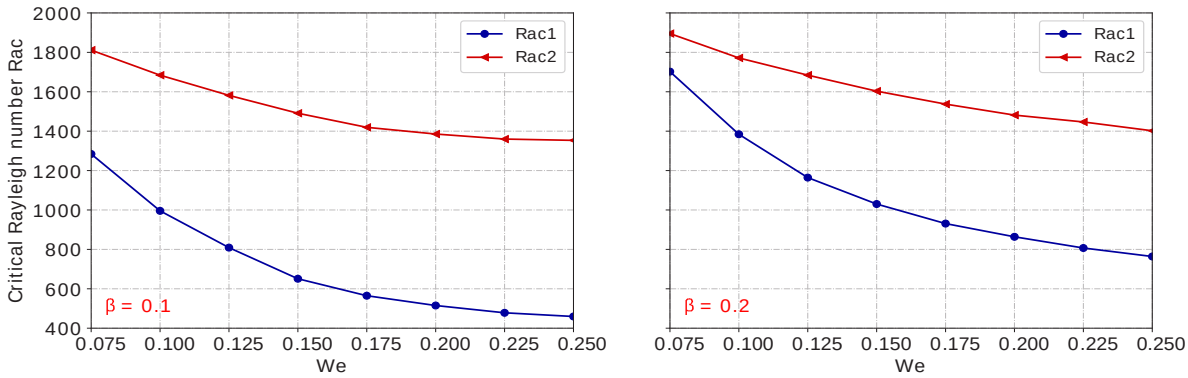

FIGURE 4.24: Critical Rayleigh numbers Ra_{c1} and Ra_{c2} as a function of We with $\beta = 0.1, 0.2$. The definition of Region 1, Region 2 and Region 3 are same as that in Fig. 4.23. The other rheology parameters are fixed at $Pr = 7.0$, $\epsilon = 0.1$ and $\xi = 0.05$.

4.4.3 Summary of the studied cases

In this part, we summarized the cases simulated, Tab. 4.1 gives the viscoelastic convection condition with different Ra and We. In this table, (S) represents the steady convection and (R) represents the reversal convection. $\beta = 0.2$, $\epsilon = 0.1$ and $\xi = 0.05$ were fixed in simulations. When $We = 0.07125$, only three cell reversal convection was observed. For $We = 0.225$ and $We = 0.25$ cases, we did not calculate 2-cell steady convection, because the corresponding comprehensive elastic coefficient is too large under this rheology parameter, especially when β is small ($= 0.2$), which exceeds the solving ability of this solver. In fact, when β is relatively small, the proportion of elasticity in the fluid is particularly large, and the convection is dominated by the elastic part.

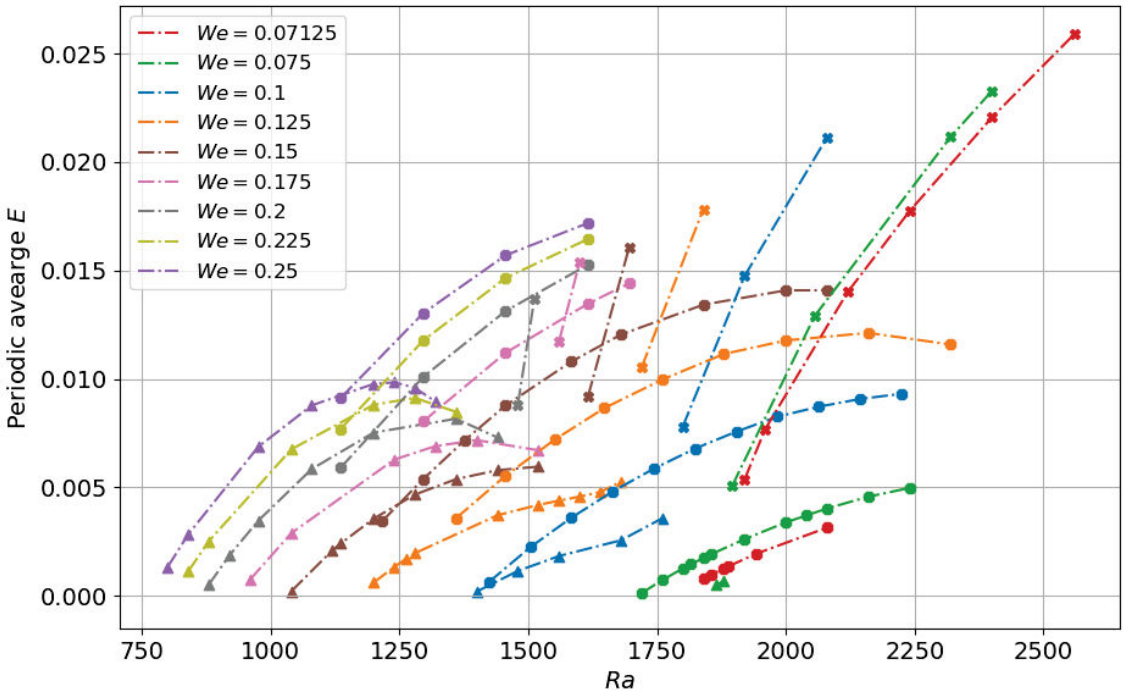

FIGURE 4.25: Mean kinetic energy $E = \frac{1}{\lambda}\frac{1}{\Omega}\int_0^{\lambda}\int_0^{\Omega}(u_i u_i)dtdV$ as a function of Ra in viscoelastic Rayleigh-Bénard convection, where the viscoelastic constitutive model is Phan-Thien-Tanner (PTT) model with $We \in [0.07125, 0.250]$ and $\beta = 0.2$. In the figure, ($\bullet$) means 3-cell reversal flow, ($\triangle$) means 2-cell reversal flow and ($\times$) means 2-cell steady convection flow.

Fig. 4.25 shows the temporally-spatially averaged E as a function of Ra with different We. It can be found that We increases will cause an increase in E, which was explained in the previous section (Sec. 4.3.1). From Fig. 4.25, the following results are obtained:

- The different flow structures have different increase rate of kinetic energy (as Ra). Among them, the steady-state flow has the highest increase rate of kinetic energy.
- As Ra closes the second critical Rayleigh number (flow changes from 2R to 2S), the average kinetic energy will decrease slightly.

We	Ra	Cells number	Flow regime
0.07125	–	2	R
	[1920, 1960, 2120, 2240, 2400, 2560]	2	S
	[1400, 1856, 1880, 1944, 2080]	3	R
0.075	[1864, 1880]	2	R
	[1896, 2056, 2320, 2400]	2	S
	[1720, 1760, 1800, 1816, 1840, 1856, 1920, 2000, 2040, 2080, 2160, 2240]	3	R
0.1	[1400, 1480, 1560, 1680, 1760]	2	R
	[1800, 1920, 2080]	2	S
	[1424, 1504, 1584, 1664, 1744, 1824, 1904, 1984, 2064, 2144, 2224]	3	R
0.125	[1200, 1240, 1264, 1280, 1440, 1520, 1560, 1600, 1640, 1680]	2	R
	[1720, 1840]	2	S
	[1360, 1456, 1552, 1648, 1760, 1880, 2000, 2160, 2320]	3	R
0.150	[1040, 1120, 1136, 1200, 1280, 1360, 1440, 1520]	2	R
	[1616, 1696]	2	S
	[1216, 1296, 1376, 1456, 1584, 1680, 1840, 2000, 2080]	3	R
0.175	[960, 1040, 1240, 1320, 1400, 1520]	2	R
	[1560, 1600]	2	S
	[1296, 1456, 1616, 1696]	3	R
0.2	[880, 920, 976, 1080, 1200, 1360, 1440]	2	R
	[1480, 1512]	2	S
	[1136, 1296, 1456, 1616]	3	R
0.225	[840, 880, 1040, 1200, 1280, 1360]	2	R
	–	2	S
	[1136, 1296, 1456, 1616]	3	R
0.250	[800, 840, 976, 1080, 1200, 1240, 1280, 1320]	2	R
	–	2	S
	[1136, 1296, 1456, 1616]	3	R

TABLE 4.1: The flow condition with different Weissenberg numbers and Rayleigh numbers. In tested cases, $Pr = 7.0$, $\beta = 0.2$, $\epsilon = 0.1$ and $\xi = 0.05$

- There is a overlap range of Rayleigh number for 2-cell and 3-cell reversal flows. Note that 3-cell reversal flow overlaps both 2-cell reversal and 2-cell steady-state flows. Under a certain Ra, the same convection system can have different flow states, reverse convection or stable convection. Such as when $We = 0.125$ and $Ra = 1750$, the flow state can be 3-cell reverse convection or 2-cell steady-state convection, depending on the previous flow mode. For the reversed convection state, the 3-cell situation is more stable than the 2-cell reversal convection.

- No matter which the initial flow state (2-cell or 3-cell reverse convection) is, the steady-state convection obtained always has only two circulations.

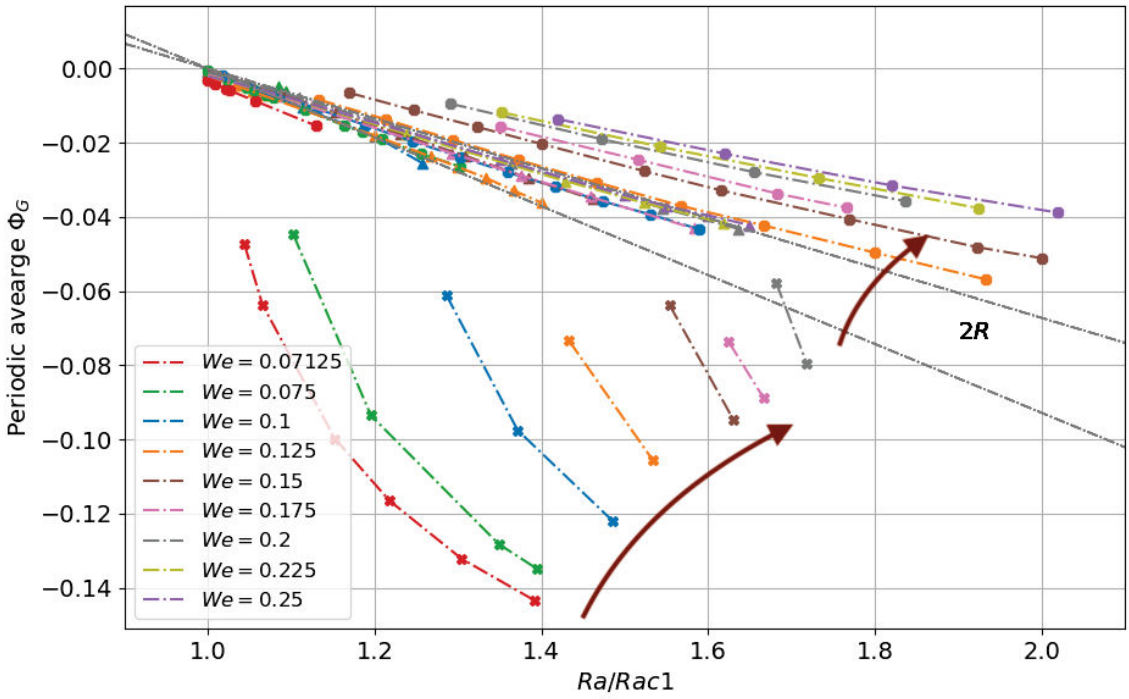

FIGURE 4.26: Averaged energy exchange rate Φ_G as a function of Ra in viscoelastic Rayleigh-Bénard convection, where the viscoelastic constitutive model is Phan-Thien-Tanner (PTT) model with $We \in [0.07125 - 0.250]$ and $\beta = 0.2$. In the figure, ($\bullet$) means 3-cell reversal flow, ($\triangle$) means 2-cell reversal flow and ($\times$) means 2-cell steady convection flow.

Fig. 4.26 shows the capacity of the energy exchange between flow structure and polymer macro-molecular structure at different We, Ra, and flow condition. From Fig. 4.26, we can find that the overall energy exchange capacity of steady-state convection is stronger than that in reversed convection. The existence of the reversal phenomenon has a huge impact on the energy dissipation of the system. We can found a threshold of the energy exchange rate of Φ_G (in range of $(-0.05, -0.06)$ for this simulation series) between reversal and steady convection, regular reversal convection only takes place when Φ_G is above this value, and the flow pattern will change to steady convection once Φ_G is under this value. Φ_G shows a more linear relationship with Ra in the reverse region, compared with that in the steady convection region.

Fig. 4.27 shows the time shift (delay) of peak value of (E, Φ_F) and (Φ_F, Φ_G) as a function of Ra. The time shift proportion is defined by:

$$R_{(E,\Phi_F)} = (t_{\Phi_F \text{ peak value}} - t_{E_{peak\ value}})/t_{period} \tag{4.7}$$

$$R_{(\Phi_F,\Phi_G)} = (t_{\Phi_G \text{ peak value}} - t_{\Phi_F \text{ peak value}})/t_{period} \tag{4.8}$$

where $t_{E_{peak\ value}}$, $t_{\Phi_F \text{ peak value}}$ and $t_{\Phi_G \text{ peak value}}$ are the time points when the peak values of E, Φ_F and Φ_G take place in one period. It can be easily found that the time shift $R_{(E,\Phi_F)}$ and $R_{(\Phi_F,\Phi_G)}$ almost show the same decrease trend as Ra increases, and when Ra is close to the second critical

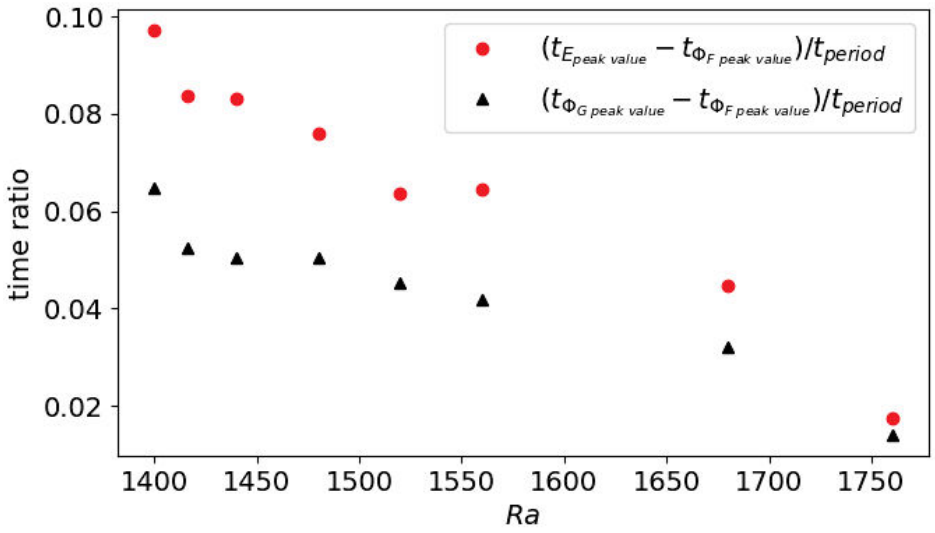

FIGURE 4.27: The time shift (delay) of peak value of (E, Φ_F) and (Φ_F, Φ_G) as a function of Ra is shwon. In the figure, $t_{E_{peak\ value}}$, $t_{\Phi_{F\ peak\ value}}$, $t_{\Phi_{G\ peak\ value}}$ are the time point when the peak value of E, Φ_F and Φ_G take place in one period. Here, we fixed $Pr = 7.0$, $\beta = 0.2$, $We = 0.1$, $\epsilon = 0.1$ and $\xi = 0.05$.

Rayleigh number $Rac2$, $R_{(E,\Phi_F)}$ and $R_{(\Phi_F,\Phi_G)}$ are almost equal to zero. This fact also supports our proposition that the formation of viscoelastic periodic reversal convection is due to the alternating transition of system energy in kinetic energy, elastic energy, and buoyancy potential energy.

4.5 Heat transfer characteristic

Different from steady-state convection, the periodic behavior of the distribution of velocity and temperature in regular oscillating convection will have a huge impact on the heat transfer capacity of the system. Therefore, this section directly studies the influence of different rheological parameters on heat transfer efficiency. Here we use a nondimensional parameter Nu (Nusselt number) to scale the heat transfer capacity of the system, Nu is defined as the nondimensional temperature gradient at the bottom boundary of the cavity, and the spatially averaged Nusselt number Nu_s and the spatially-temporally averaged Nusselt number Nu_{ts} can be described as:

$$Nu_s = \frac{1}{2}\int_0^2 \frac{\partial T}{\partial y}|_{y=0} dx \tag{4.9}$$

$$Nu_{ts} = \frac{1}{\lambda}\frac{1}{2}\int_0^{\lambda}\int_0^2 \frac{\partial T}{\partial y}|_{y=0} dxdt \tag{4.10}$$

4.5.1 Viscous and elastic dissipation

If we consider the viscous and elastic dissipation in the viscoelastic Rayleigh-Bénard convection system, the temperature equation should be writen as:

$$\rho c_p(\frac{\partial T}{\partial t} + (\boldsymbol{u}\cdot\nabla)T) = k\nabla^2 T + 2\mu_s \boldsymbol{D} : \nabla\boldsymbol{u} + \boldsymbol{\tau_p} : \boldsymbol{\nabla u} \tag{4.11}$$

where the second term on the right-hand side is the viscous dissipation term causing temperature rise in the flow and the third term is called elastic dissipation. After introducing dimensionless quantities, Eq. (4.11) is organized as

$$\frac{\partial T}{\partial t} + (\boldsymbol{u}\cdot\nabla)T = \frac{1}{\sqrt{Ra}}\nabla^2 T + 2\beta\frac{EcPr}{\sqrt{Ra}}\boldsymbol{D} : \nabla\boldsymbol{u} + Ec\boldsymbol{\tau_p} : \boldsymbol{\nabla u} \tag{4.12}$$

where Eckert number Ec, expressing the relationship between kinetic energy and the enhalpy, is used to characterize the influence of the dissipations :

$$Ec = \frac{U_c^2}{c_p\Delta T} = \frac{\left(\frac{\alpha}{H}\sqrt{Ra}\right)^2}{c_p\Delta T} = \frac{\alpha^2 Ra}{H^2 c_p \Delta T} \tag{4.13}$$

where α is the fluid thermal diffusivity, c_p is the specific heat capacity, H is the cavity height and ΔT is the temperature difference between the upper and lower horizontal boundaries. When Ec is very small ($\ll 1$), the effects of the viscous dissipation can be neglected.

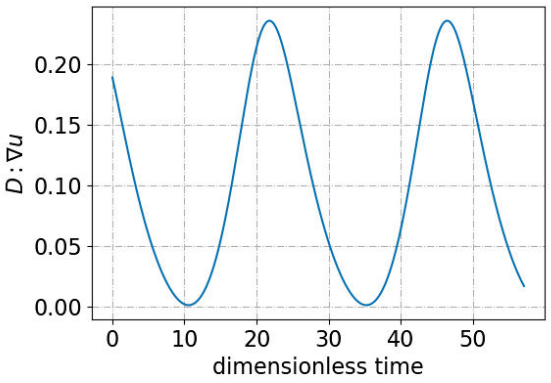

(A) $(\boldsymbol{D} : \nabla\boldsymbol{u})$, viscous dissipation without the coefficient $(2\beta\frac{EcPr}{\sqrt{Ra}})$

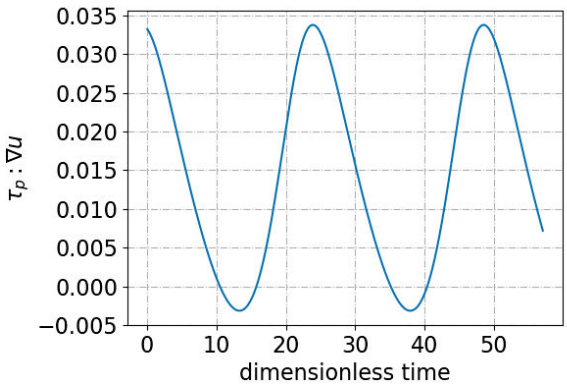

(B) $(\boldsymbol{\tau_p} : \boldsymbol{\nabla u})$, elastic dissipation without the coefficient (Ec).

FIGURE 4.28: Viscous and elastic dissipaitons in case with $Pr = 7.0$, $Ra = 1600$, $\beta = 0.2$, $We = 0.1$.

Fig. 4.28 shows the spatially averaged dimensionless viscous and elastic dissipations for the case with $Pr = 7.0$, $Ra = 1600$, $\beta = 0.2$, $We = 0.1$. As is indicated by the figure, the viscous dissipation is always positive and thus a positive source term for temperature. While the elastic disspation is positive for most of the time and negative for a short time during one period. Therefore the elastic dissipation could also lead to decreasing temperature. For all the cases investigated in this work, Ec takes on values of $O(10^{-10})$, and the magnitude of $2\beta\frac{EcPr}{\sqrt{Ra}}$

corresponds to $O(10^{-11})$. Il means that the viscous and elastic disspitions are very small in magnitude and do not play any role on temperature. Therefore, the viscous and elastic dispersions can be neglected in the numerical simulations and this justifies completely the equation used in the present study.

4.5.2 Nu changes with non-dimentional time

To understand the effects of ϵ and ξ on heat transfer, two pairs of (ϵ, ξ), $(0.1, 0)$ and $(0.1, 0.05)$, are chosen and the corresponding Nusselt numbers are displayed in Fig. 4.29.

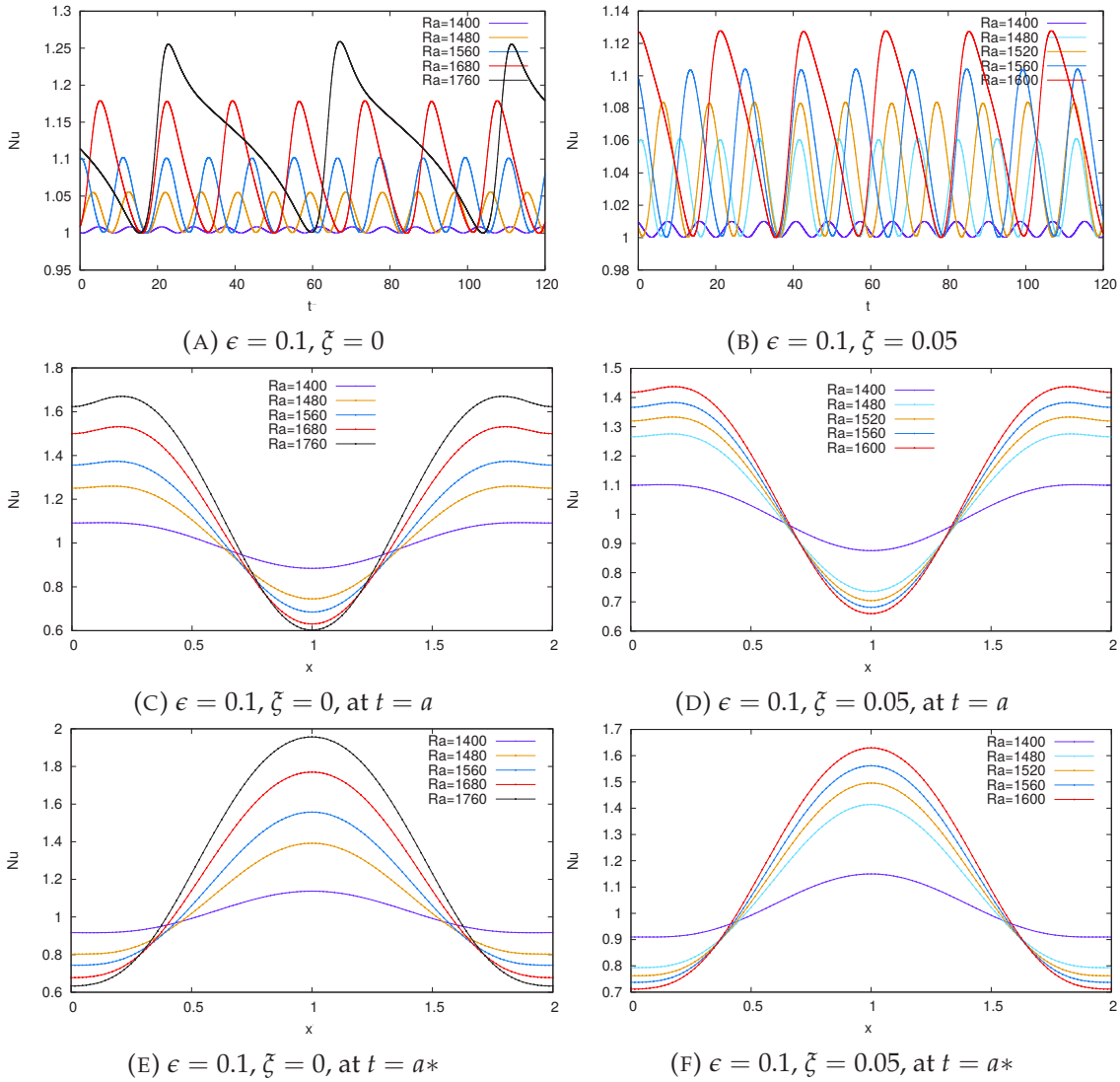

(A) $\epsilon = 0.1, \xi = 0$ (B) $\epsilon = 0.1, \xi = 0.05$

(C) $\epsilon = 0.1, \xi = 0$, at $t = a$ (D) $\epsilon = 0.1, \xi = 0.05$, at $t = a$

(E) $\epsilon = 0.1, \xi = 0$, at $t = a*$ (F) $\epsilon = 0.1, \xi = 0.05$, at $t = a*$

FIGURE 4.29: Time evolution of Nu_s ((a) and (b)) and instantaneous local Nu on the bottom wall ((c), (d), (e) and (f)) at different Ra for 2-cell convective flow. (c) and (d) correspond to the time point t_1 while (e) and (f) to the time point t_5. Both t_1 and t_5 concern the maximum of the total kinetic energy: at t_1 upward convective flow near the cavity center is at its maximum and the minimum of Nu on the bottom wall is located at $x = 1$; at t_5 downward convective flow near the cavity center is at its maximum and the maximum of Nu on the bottom wall is located at $x = 1$.

The time evolutions of the spatially averaged Nusselt number Nu_s are shown for several Rayleigh numbers in Figs. 4.29a and 4.29b. For a fixed pair of (ϵ, ξ), both the amplitude and the period of Nu_s increase with increasing Rayleigh number the same as the velocity. It is worth mentioning that the frequency of Nu_s is two times that of the velocity: one time period of velocity is two times that of Nu_s and there are two maximum values and two minimum values of Nu_s in one velocity period. When the velocity gets to its maximum value (see Fig. 4.21), Nu_s reaches the first maximum value (local Nu distribution is shown in Figs. 4.29c and 4.29d); then convection reversal occurs, velocity drops from maximum to zero, Nu_s moves from the first maximum to the first minimum value of about one. Subsequently, velocity increases to reach its maximum value in the opposite direction at the same time, Nu_s reaches the second maximum value (local Nu on the bottom wall is depicted in Figs. 4.29e and 4.29f).

For the influence of We on heat transfer capacity Nu, Fig. 4.30 illustrated the influence of Weissenberg number for the time evolution of Nusselt number. The results show that the amplitude and time period of Nu gradually increases with the increase of We, and the peak is sharper. In contrast, when We is small, the change of Nu within one period is more symmetrical. The similar results were also given by Li and Khayat (2005).

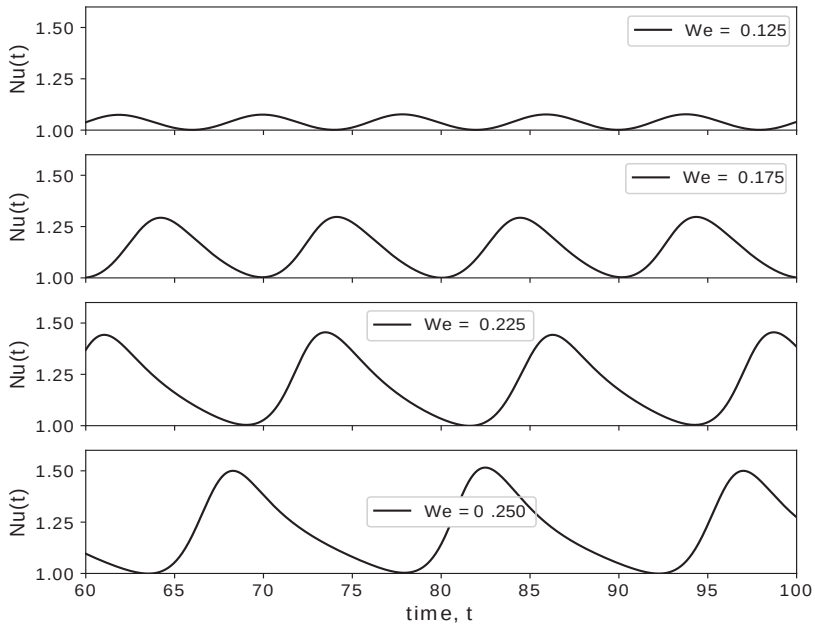

FIGURE 4.30: Time signature for the Nusselt number, Nu, and effect of Weissenberg number for $We \in [0.125, 0.250]$ with $Ra = 1280$, $Pr = 7.0$ and $\beta = 0.2$.

4.5.3 Effect of (ϵ, ξ) and We on averaged Nu

For the influence of rheology parameters on the heat transfer capacity, we first consider the two parameters, ϵ and ξ. Fig. 4.31 illustrates the variation of the Nusselt number averaged in time

and space Nu_{ts} versus Ra for different values of (ϵ, ξ). Note that the reduction of Ra interval in the figure is due to the reduction of Ra_{c2} with increasing ϵ or ξ.

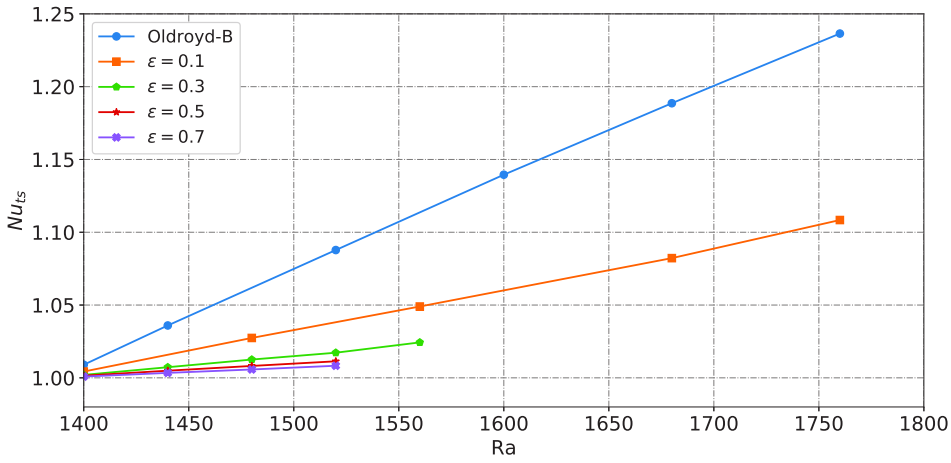

(A) $\epsilon \in [0.1, 0.7]$, $\xi = 0$

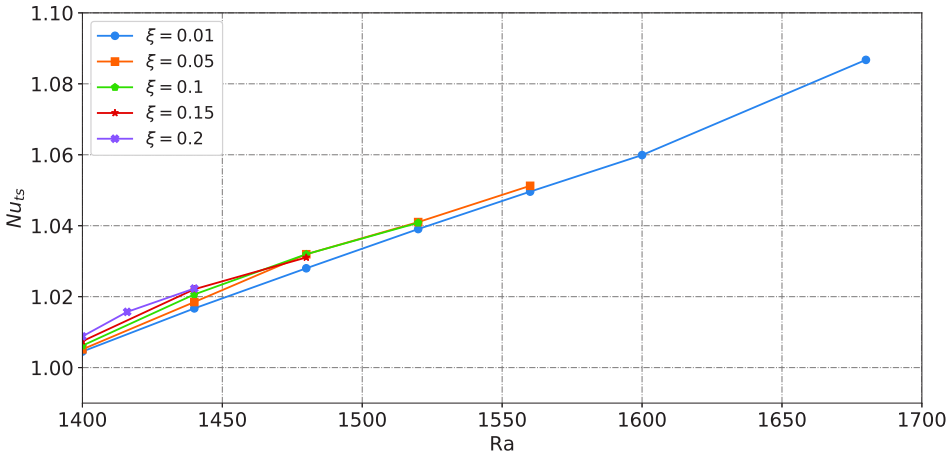

(B) $\epsilon = 0.1$, $\xi \in [0.01, 0.2]$

FIGURE 4.31: Effects of (ϵ, ξ) on the Nusselt number averaged in time and space Nu_{ts} of 2-cell convection flow at $Pr = 7.0$, $\beta = 0.2$ and $We = 0.1$. With $\xi = 0$ increasing ϵ decreases Nu_{ts} whereas with $\epsilon = 0.1$ increasing ξ only slightly increases Nu_{ts}. The reduced range of Ra at higher ϵ or ξ corresponds to the fact that Ra_{c2} is reduced and that Ra range of the time-dependent flow is reduced.

Fig. 4.31a shows the time-averaged Nusselt number changes with Rayleigh nubmer at different ϵ, for $\xi = 0$ increasing ϵ decreases Nu_{ts} and the relationship between Nu_{ts} and Ra is almost linear. It should be noted that the general viscoelastic constitutive model with $\xi = 0$ represents the Giesekus model. Fig. 4.31b shows the time-averaged Nusselt number changes with Rayleigh nubmer at diferent ϵ, the results show that for $\epsilon = 0.1$ increasing ξ increases Nu_{ts} slightly. However the curves of Nu_{ts} show more non-linear characteristic than that in cases with $\xi = 0$. Butϵ and ξ have opposite and limited effects on heat transfer. Increasing elongational behavior of polymer molecules decreases slightly heat transfer in the time-dependent flow regime.

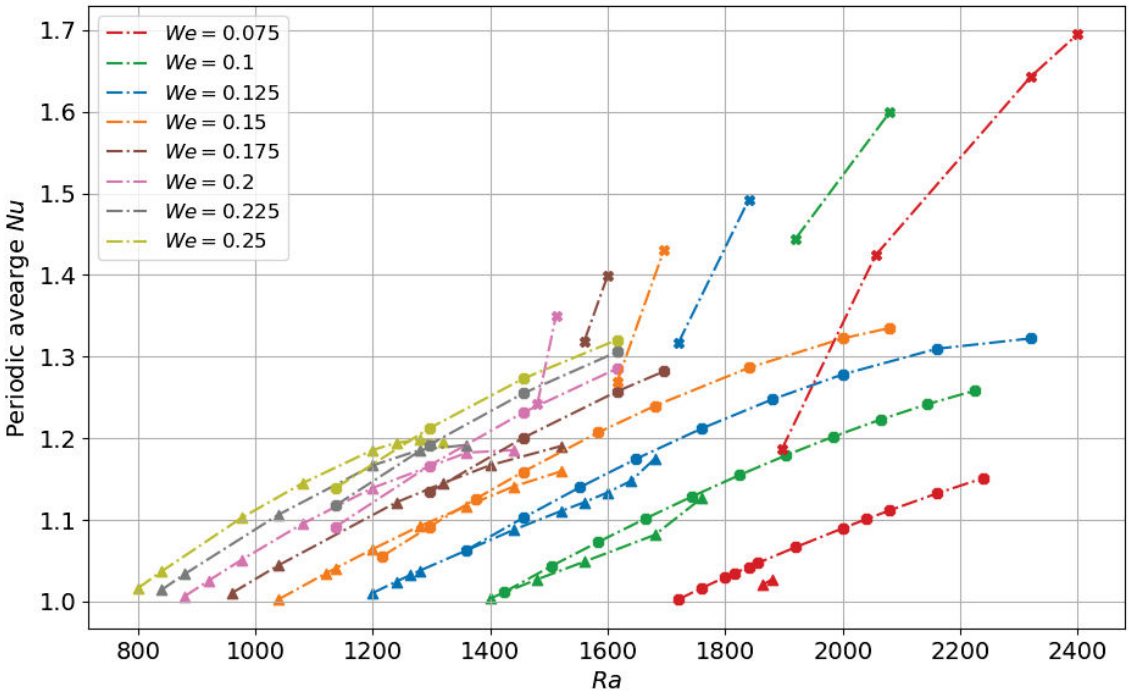

FIGURE 4.32: Averaged Nusselt number Nu_{ts} as a function of Ra in viscoelastic Rayleigh-Bénard convection, where the viscoelastic constitutive model is Phan-Thien-Tanner (PTT) model with $We \in [0.07125 - 0.250]$ and $\beta = 0.2$. In the figure, ($\bullet$) means 3-cell reversal flow, ($\triangle$) means 2-cell reversal flow and ($\times$) means 2-cell stable convection flow.

From the perspective of heat transfer capacity, the Nu increase rate in 2-cell steady-state convections is much greater than that of reverse convection, as described in Fig. 4.32. The reason probably is in the flow process of reverse convection, the continuous stretching and contraction of the polymer structure in the system play an intermittent obstructive effect on the flow.

4.6 Conclusion

For viscoelastic R-B convecton with We increasing and β decreasing, time-dependent flow instead of steady flow, sets up at the convection onset. The main results we obtained are the following:

- For convection with PTT model, critical Rayleigh numbers corresponding to the onset of time-dependent convection are determined for various values of the constitutive parameter ϵ with $\xi = 0$ and various values of the constitutive parameter ξ with fixed $\epsilon = 0.1$. There is only a slight dependency of the critical Rayleigh number on these parameters.

- For time-dependent reversal convection, 2-cell and 3-cell flow structures evolute was investigated in detail. We revealed the energy relationship in the regular reversal convection, and determined the elasticity effect on the promotion of reversal formation. The

potential energy in the convection system is periodically transported between the flow structure and by elastic force and thermal buoyancy. There seems to be a critical value of energy exchange rate Φ_G between periodically reversed convection and steady-state convection.

- At higher Rayleigh numbers, time-dependent flow is replaced by a steady-state flow, here, we found another critical Rayleigh number $Rac2$. This flow transition corresponds to a drift pitchfork bifurcation. The critical Rayleigh number $Rac2$ is also determined for various values of ϵ with $\xi = 0$ and various values of ξ with $\epsilon = 0.1$ in our simulations. For the parameters investigated, increasing We will make $Rac1$ and $Rac2$ both decrease, and will make the range of Ra for the regular reversal will enlarge. A smaller β will induce smaller $Rac1$ and $Rac2$.

- The influence of ϵ, ξ, and We on heat transfer is investigated for the time-dependent flow regime. The results show that ϵ and ξ have opposite but limited effects on heat transfer. Increasing ϵ decreases Nu whereas Nusselt number increases slightly with increasing ξ. Increasing We improve the capacity of heat exchange.

The onset of the time-dependent reverse convection in the Rayleigh-Bénard convection with nonlinear viscoelastic fluids is a novel flow feature because of the particular flow patterns. These flow reversal characteristics should be distinguished from a random reversal in turbulent Rayleigh-Bénard convection.

Chapter 5

Convection in 2D tilted cavity

Contents

5.1 Introduction

In the previous chapter, we introduced some special phenomena of viscoelastic Rayleigh-Bénard convection (RBC) in a horizontal rectangular cavity, i.e. the reversal phenomena and special flow pattern transition, etc. In fact, in actual life or industrial production, most of the occurrence of RBC will not run in an horizontal space, horizontal RBC is an ideal situation. Through a simple mechanical analysis, for a tilted RBC system, we can know that the gravity is not only applied in the direction perpendicular to the bottom heating wall, but part of that is placed in the direction paralleled to the heating wall. Many pieces of research showed that the existence of the inclination in RBC will make a huge impact on the flow and heat transfer characteristics.

For tilted Newtonian RBC, lots of experiments and numerical simulation studies had given us an in-depth understanding of it in past decades (Catton, Ayyaswamy, and Clever, 1974; Arnold, Catton, and Edwards, 1976; Soong et al., 1996; Corcione, 2003; Torres et al., 2015; Wang et al., 2018). The steady convection in tilt cell with different aspect ratios and Ra was experimentally investigated by Arnold, Catton, and Edwards (1976). They investigated the effects of tilt angle (from 0° to 90°) on heat transfer capacity in rectangular cavity for a wide range $Ra \in [10^3, 10^6]$ and several aspect ratios ($\Gamma \in (1, 2, 6, 12)$). Their results gave a simple scaling law between heat transfer capacity and Ra. Acharya and Goldstein (1985) did similar work about 2D RBC of air in tilted ($\alpha \in (0^\circ, 30^\circ, 60^\circ, 90^\circ)$) square cavity for $Ra \in [10^3, 10^5]$ by DNS,

and mainly studied the heat transfer characteristics of the convection system. For tilted convection patterns transiton, Torres et al. (2015) showed flow patterns evolute for physical configurations changing from the RBC (heated and cooled by horizontal walls) to the natural convection (heated and cooled by side walls) in 3D cubical cavity with $Pr = 0.71$. Wang et al. (2018) investigated the effect of tilt angle on turbulent RBC in the caivty with two aspect ratio $\Gamma = (1,\ 2)$ by 2D direct numerical simulation. They mapped out the flow states in $\alpha - Pr$ space for $Ra = 10^7$ and $\Gamma = (1,\ 2)$, and $\alpha - Ra$ space for $Pr = 0.3$ and $\Gamma = (1,\ 2)$. In the cases with $\Gamma = 1$, the turbulent flow reversals are detected at small α, and that will vanish once $\alpha > 7°$. For $\Gamma = 2$ cases, three flow structures are found in $\alpha - Pr$ space with $Ra = 10^7$ and $\alpha - Ra$ space with $Pr = 0.3$, they are 2-roll flows without flow reversals and with flow reversals, and the single-roll flow without flow reversals.

For tilted non-Newtonian RBC, only Khezzar, Siginer, and Vinogradov (2012) did relevant research. Their studies are based on a steady 2D RBC in rectangular cavities filled by power-law fluids, a comprehensive study of the influence of tilt angle, Rayleigh number, Prandtl number, and aspect ratio on Nusselt number was given.

At the present stage, we didn't found any numerical investigation of the inclined RBC with the nonlinear viscoelastic fluid constitutive model. Given the interesting reversal phenomenon and the complex flow bifurcation of viscoelastic RBC described in Chapter 4, an investigation about tilted viscoelastic RBC is necessary. In this chapter, we will study numerically the viscoelastic RBC in an inclined cavity. Firstly, we introduce flow and heat transfer in typical Newtonian RBC for a moderate Rayleigh number $Ra = 5000$. It will help to compare with viscoelastic RBC in the present work. Then, we study the tilted viscoelastic RBC under two viscosity ratios $\beta = (0.1,\ 0.9)$, and discuss the influence of the inclination angle on critical Rayleigh number Rac for convection onset, heat transfer capacity, etc.

Physical model

A two-dimensional inclined rectangular cavity filled with Newtonian or viscoelastic fluids is adopted, as described in Fig. 5.1. The temperature and velocity boundary conditions are set as the same as that in Chapter 4. In the figure, α represents the inclined angle, and g is the gravity. The tilt angle α in this chapter is fixed in the range of $[0°, 90°]$. The aspect ratio is $A = L/H = 2:1$ with $L = 2$ and $H = 1$.

In the tilted physical configuration, the gravity acceleration can be decomposed into two parts: one perpendicular to the bottom (heating boundary), another parallel to the bottom, that can be described by:

$$g\boldsymbol{e_g} = -(sin(\alpha)g\boldsymbol{e_1} + cos(\alpha)g\boldsymbol{e_2}) \tag{5.1}$$

where $\boldsymbol{e_g}$ is the unit vector in the gravity direction, $\boldsymbol{e_1}$ and $\boldsymbol{e_2}$ are the unit vectors in x and y directions, respectively. $gsin(\alpha)\boldsymbol{e_1}$ and $gcos(\alpha)\boldsymbol{e_2}$ are the components of the gravity contribution

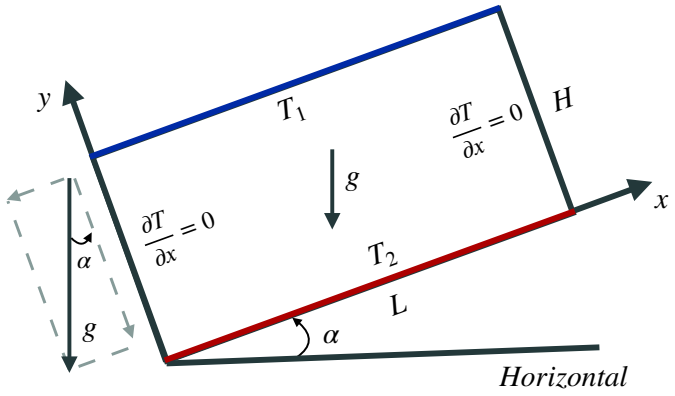

FIGURE 5.1: Physical configuration with inclination.

in the parallel and perpendicular directions of the bottom. Substitute Eq. (5.1) into Eq. (3.16), the dimentionless momentum equation for tilted viscoelastic RBC can be written as:

$$\frac{\partial \boldsymbol{u}}{\partial t} + (\boldsymbol{u}\cdot\nabla)\boldsymbol{u} = -\nabla p + \beta\frac{Pr}{\sqrt{Ra}}\Delta\boldsymbol{u} + \nabla\cdot\boldsymbol{\tau_p} - (sin(\alpha)PrT\boldsymbol{e_1} + cos(\alpha)PrT\boldsymbol{e_2}) \tag{5.2}$$

To facilitate the description, we choose the coordinate axes that are consistent with the cavity walls, as is shown in Fig. 5.1. Concerning the number of nodes we follow the setting of the previous chapter, namely $N_x \times N_y = 128 \times 64$ for cases with aspect ratio $2:1$ and $N_x \times N_y = 64 \times 64$ for cases with aspect ratio $1:1$.

5.2 Newtonian RBC in tilted cavity

We start by studying the Newtonian RBC in tilted closed cavity. In the simulated cases, the Prandtl number and Rayleigh number are fixed at $Pr = 7.0$ and $Ra = 5000$, respectively. The rotation angle is in range of $[0°, 45°]$.

5.2.1 Flow patterns

The isolines of the dimensionless velocity and temperature for $\alpha = (0°, 5°, 10°, 15°, 30°, 45°)$ are shown in Fig. 5.2 and Fig. 5.3. From the figures, we can find that, except the situation (Fig. 5.2a and Fig. 5.3a) without inclination, the distribution of the velocity all shows a similar profile. The velocity value in the domain first increases with α increasing (Fig. 5.2b to Fig. 5.2f). The flow directions in the simulated cases are all counterclockwise (Fig. 5.2b to 5.2f), which is consistent with the rotation direction of the configuration. These flows are obtained by the initial conditon like Fig. 5.5a. When the initial state is like Fig. 5.5a, flow will quickly change to single-roll convection as α appears. In the work of Shishkina and Horn (2016), this transition angle is in $\alpha \in [0.45°, 0.9°]$ under tilted RBC for fixed parameters $Pr = 100$ and $Ra = 10^6$.

In fact, when the inclined angle is in certain range for $Ra = 5000$, the flow can also keep two-cell sturcture with counterclockwise-clockwise directions. In order to obtain two-cell structure,

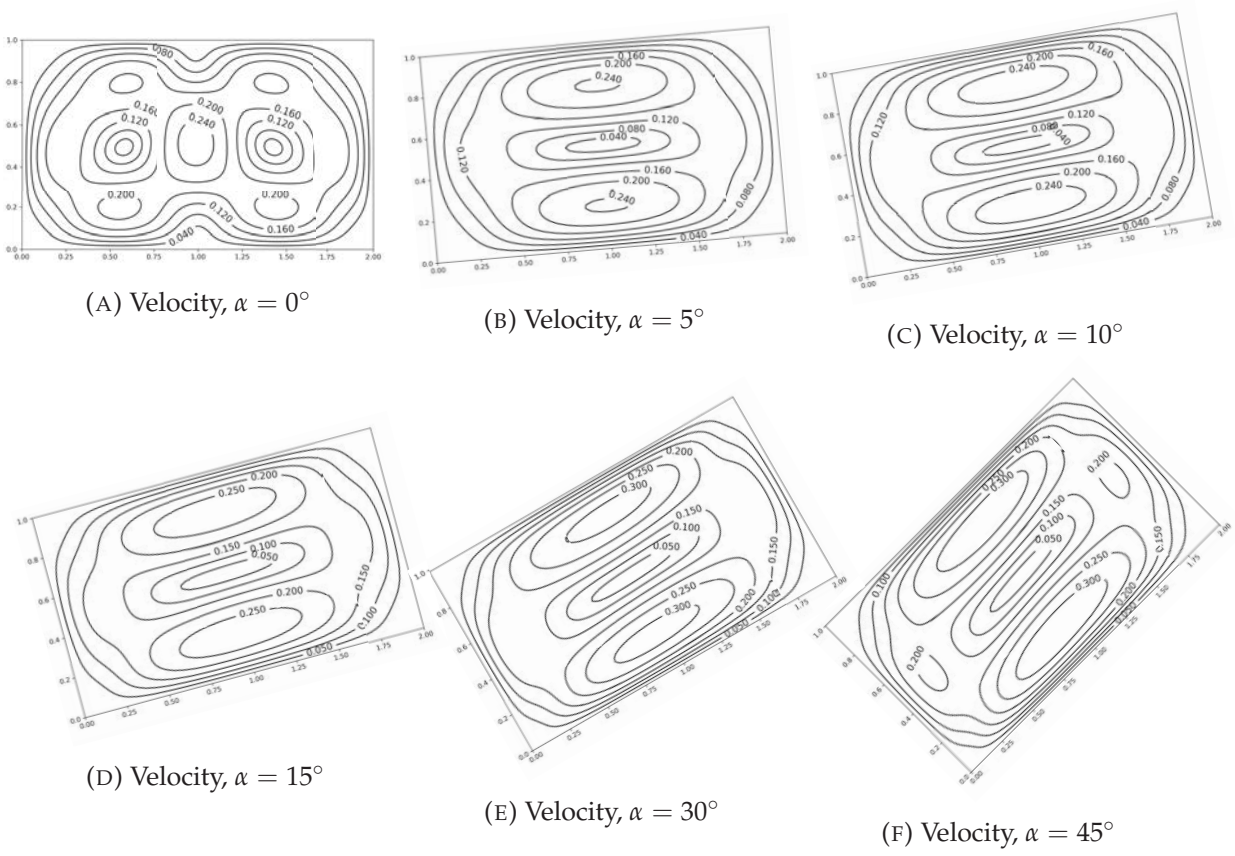

(A) Velocity, $\alpha = 0°$

(B) Velocity, $\alpha = 5°$

(C) Velocity, $\alpha = 10°$

(D) Velocity, $\alpha = 15°$

(E) Velocity, $\alpha = 30°$

(F) Velocity, $\alpha = 45°$

FIGURE 5.2: Isolines of the dimensionless velocity with $\alpha = (0°, 5°, 10°, 15°, 30°, 45°)$ in cases with $Pr = 7.0$ and $Ra = 5000$. The circulations are in the counterclockwise direction.

we transform the stable solution shown in Fig. 5.2a and Fig. 5.3a. We rewrite the temperature solution as following:

$$T(x,y) = T_L(x,y) + T_P(x,y) \tag{5.3}$$

where $T_L(x,y) = T_2 - \frac{y}{H}(T_2 - T_1)$ is the basic conductive temperature distribution. We transform temperature and velocity as follows:

$$\widetilde{T}(x,y) = T_L(x,y) - T_P(x,y) \tag{5.4}$$

$$(\widetilde{u},\widetilde{v})(x,y) = -(u,v)(x,y) \tag{5.5}$$

where $\widetilde{T}(x,y)$ and $(\widetilde{u},\widetilde{v})(x,y)$ are the new intial condition.

We also tested the cases with $\alpha = (0°, 5°, 10°, 15°, 30°, 45°)$, and we got the same solutions shown in Fig. 5.3 for $\alpha = (15°, 30°, 45°)$. But, for the cases with $\alpha = (5°, 10°)$, the results show different flow structures, as shown in Fig. 5.4, the counterclockwise-clockwise circulations filled the flow space. As α increasing, the counterclockwise circulation gradually becomes bigger and fills up the domain evently, and the clockwise circulation gradually disappears. When α exceeds 12°, the flow becomes a single large-scale circulation, as shown in the (Fig. 5.2b to Fig. 5.2f).

The reason that the two different flow conditions both exist at a certain inclination can be

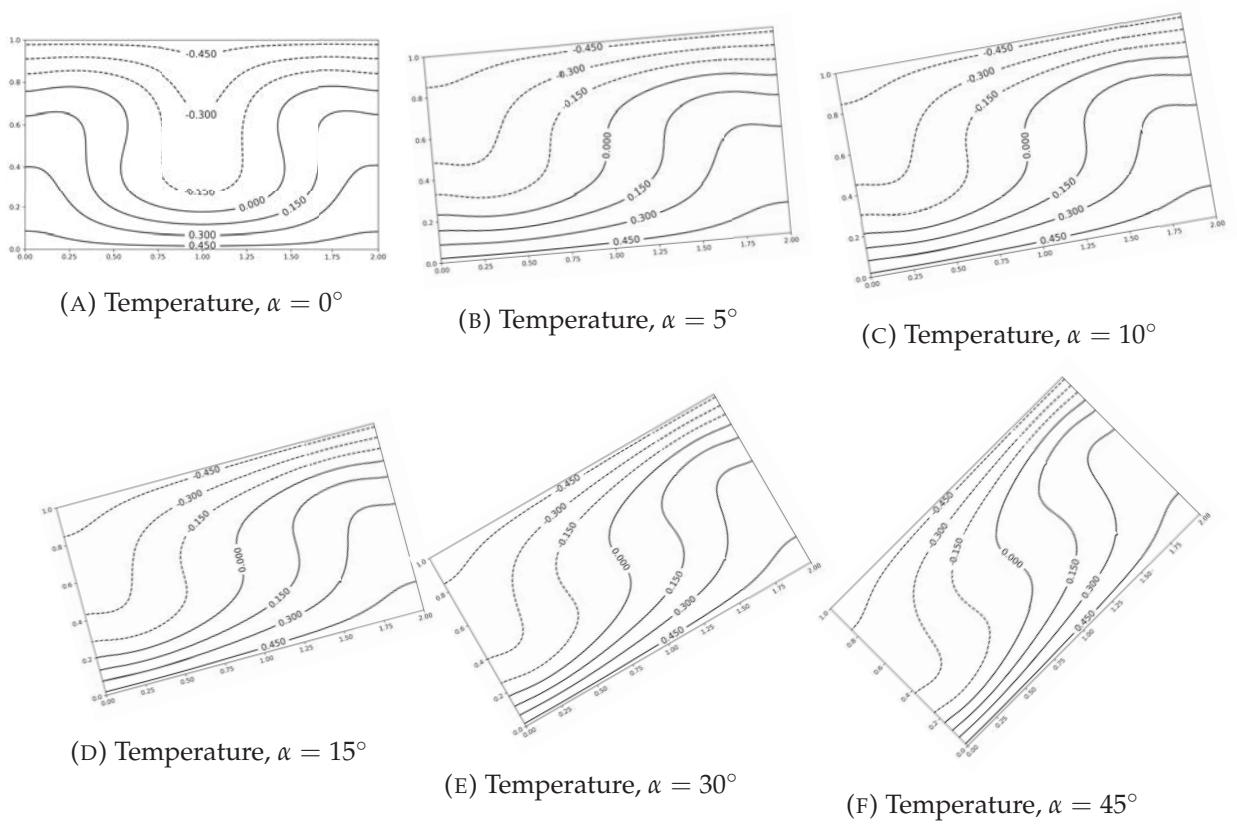

(A) Temperature, $\alpha = 0°$

(B) Temperature, $\alpha = 5°$

(C) Temperature, $\alpha = 10°$

(D) Temperature, $\alpha = 15°$

(E) Temperature, $\alpha = 30°$

(F) Temperature, $\alpha = 45°$

FIGURE 5.3: Isoheight of the dimensionless velocity with $\alpha = (0°, 5°, 10°, 15°, 30°, 45°)$ in cases with $Pr = 7.0$ and $Ra = 5000$. The circulations are in the counterclockwise direction.

briefly explained as follows. Fig. 5.5 shows the relationship between the flow structures direction and the buoyancy at four different situations. $F_{thermal\ buoyancy}$ is caused by the gravity, F_x and F_y denote the horizontal (parallel to the heating wall) and vertical (perpendicular to the heating wall) components. Figs. 5.5a and 5.5b show that in the normal RBC, directions of Bénard cells are random (counterclockwise-clockwise or clockwise-counterclockwise). Once the inclination exists, the inclination will make an opposite influence on counterclockwise and clockwise circulations, respectively. The buoyancy force along with heating and cooling walls (F_x) will have a positive impact on the counterclockwise circulation (because it is in the flow direction) and a negative effect for the clockwise one(because it is in the opposite direction of the flow). If the initial flow situation is like Fig. 5.5a, the counterclockwise circulation will quickly fill up the domain and the flow transition to the single counterclockwise roll convection is observed, as shown in Fig. 5.5c. If the initial flow situation is like Fig. 5.5b, as α increases, counterclockwise-clockwise circulations will keep the original situation for small α firstly (as shown in Fig. 5.5d) and then transit to the single clockwise circulation convection, as shown in Fig. 5.5c. For this situation, the threshold value (α_c) of the tilted angle in the present work ($Pr = 7.0$ and $Ra = 5000$) is between $\alpha_c \in (10°, 12°)$ for the transition from two-roll counterclockwise-clockwise convection to single roll clockwise circulation convection.

For further understanding, Fig. 5.6 shows the bifurcation diagram for tilted Newtonian RBC

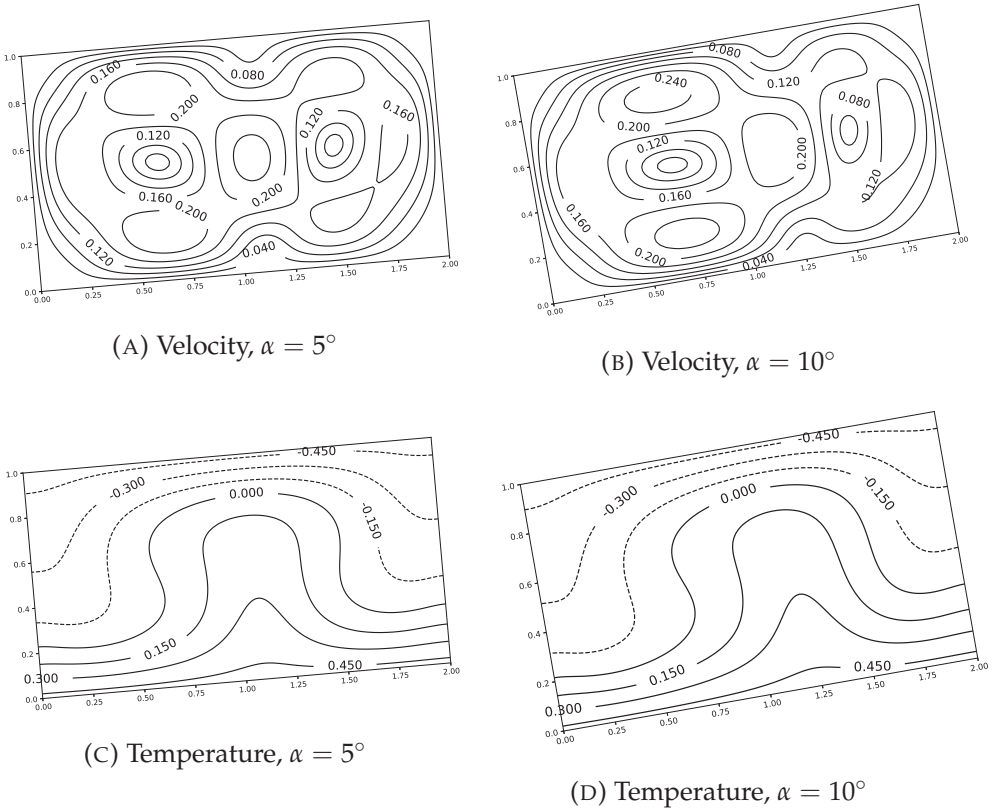

(A) Velocity, $\alpha = 5^\circ$

(B) Velocity, $\alpha = 10^\circ$

(C) Temperature, $\alpha = 5^\circ$

(D) Temperature, $\alpha = 10^\circ$

FIGURE 5.4: Velocity and temperature porfiles at steady-state convection with 2 large-scale circulation (counterclockwise-clockwise) in cases with $Pr = 7.0$ and $Ra = 5000$, when $\alpha = 5^\circ$ and $\alpha = 10^\circ$.

with $\alpha = 2^\circ$. In the figure, the velocity u_2 at the monitor point $(x, y) = (7/8, 1/2)$ is used as the solution representative to describe the flow evolution with Ra. From Fig. 5.6, it can be seen that two flow pattern branches exist, 1-roll –> 2-roll and 2-roll. For branch 1-roll –> 2-roll, the appearance of the inclination breaks the pure thermal conduction of the horizontal RBC and single-roll convection takes place in the same direction as the cavity rotation (counterclockwise) at relative small Ra. As Ra further increases, the flow pattern naturally develops a 2-roll convection with clockwise-counterclockwise circulations. We can call Ra range of the flow pattern transition as the imperfect pitchfork bifurcation. Another flow branch with two counterclockwise-clockwise rolls starts approximatively at $P1$ (about $Ra = 2100$). An unstable flow branch is connected with it, but can not be obtained by our solver. This bifurcation diagram is a deformed diagram of a pitchfork bifurcation and it is called imperfect pitchfork bifurcation. As α increases, this imperfect pitchfork bifurcation takes place at higher Ra, for example, the imperfect pitchfork bifurcation occurs at $Ra = 5000$ when α is around 12°. In order to clearly shows the flow pattern transition when Ra passes the imperfect pitchfork bifurcation, i.e. the transition from the 1-roll steady convection to 2-roll steady convection, Fig. 5.7 shows the streamlines at several Rayleigh numbers. It is clear that the center of the large circulation moves to the right as Ra increases, and then a new circulation is generated when Ra cross the imperfect pitchfork bifurcation.

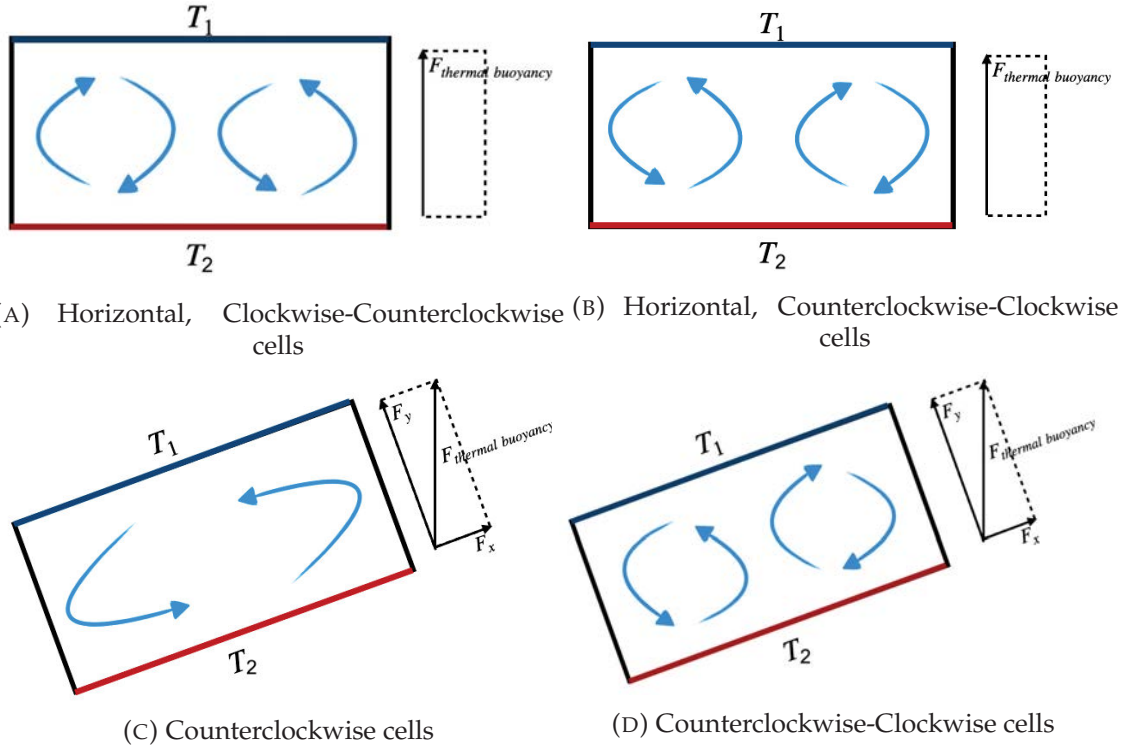

(A) Horizontal, Clockwise-Counterclockwise cells (B) Horizontal, Counterclockwise-Clockwise cells

(C) Counterclockwise cells (D) Counterclockwise-Clockwise cells

FIGURE 5.5: The relationship between the flow direction near heating wall and the thermal buoyancy.

5.2.2 Heat transfer

Fig. 5.8 shows Nu distribution along the bottom boundary for the cases with $\Gamma = (1:1, 2:1)$ for $Ra = 5000$ and $Pr = 7.0$, where Fig. 5.8a concerns the $1:1$ cavity and Fig. 5.8b plots the $2:1$ cavity. (Cc) and (c) in Fig. 5.8a represent circulation directions, i.e. counterclockwise direction and clockwise direction, respectively. In Fig. 5.8b (1cell) and (2cell) mean that one or two circulations take place in the cavity.

Fig. 5.9 shows the averaged Nu with different α for $\Gamma = (1:1,\ 2:1)$, $Pr = 7.0$ and $Ra = 5000$. The black curves are for the $\Gamma = 1:1$ cases and the red curves are for the $\Gamma = 2:1$ cases. For the $\Gamma = 1:1$ cases, two paths of Nu along α exist when tilted angle under $12°$. For the decreasing one, the circulation is in clockwise direction, we can explain that the increase in α weakens the flow circulation, and the minimum value of Nu can reach $Nu = 1.33$ at $\alpha = 10°$. For the gradually increasing one, the circulation is in the counterclockwise direction, the increase in α means that the buoyancy force strengthens the flow circulation. This coupling effect reaches its maximum when the angle is equal to $45°$, the corresponding averaged Nu reaches about 2.

Similar explanations as above can also be applied to the cases with $2:1$ cavity. For the red curves in Fig. 5.9, the red filled circles ($\bullet$) represent the flow patterns with two rolls, and the red filled stars ($\star$) represent the flow patterns with a single roll. Compared with the single-roll cases, the two-roll cases have a larger averaged Nu under the same tilt angle (when $\alpha < 10°$).

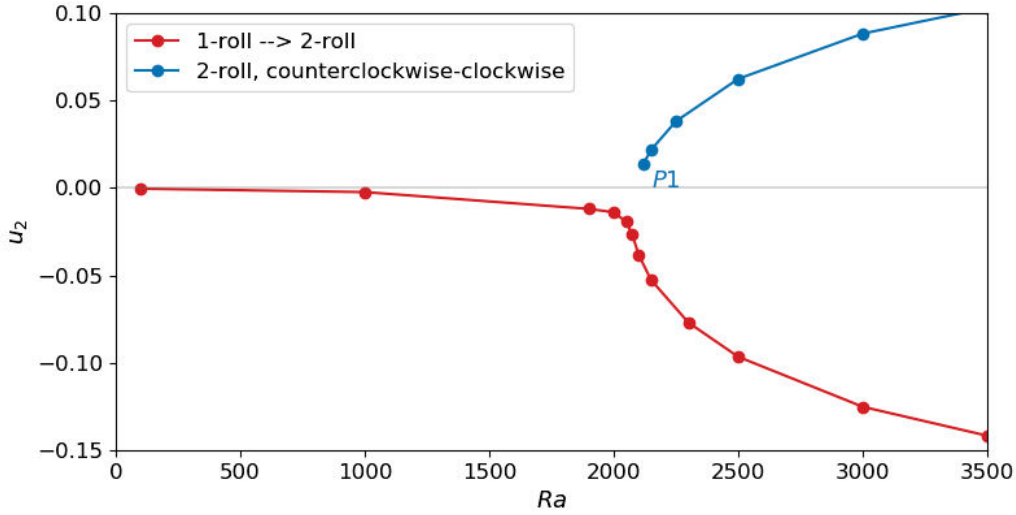

FIGURE 5.6: Bifurcation diagram for tilted Newtonian RBC with fixed $Pr = 7.0$ under inclination $\alpha = 2°$. u_2 represents the 'y-' velocity at the monitor point $(x, y) = (7/8, 1/2)$. Colored curves represent different flow patterns: (——) corresponding to stable convection with flow pattern transition from 1-roll (counterclockwise) to 2-roll (clockwise-counterclockwise); (——) corresponding to stable convection with 2-roll with counterclockwise-clockwise direction. $P1$ is the saddle node.

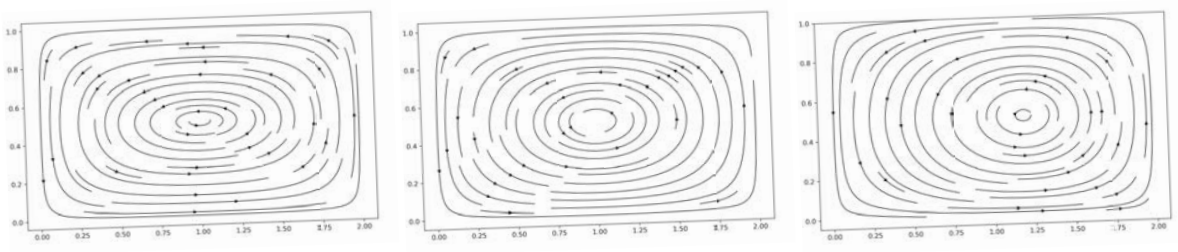

(A) $Ra = 1000, \alpha = 2°$ (B) $Ra = 2050, \alpha = 2°$ (C) $Ra = 2075, \alpha = 2°$

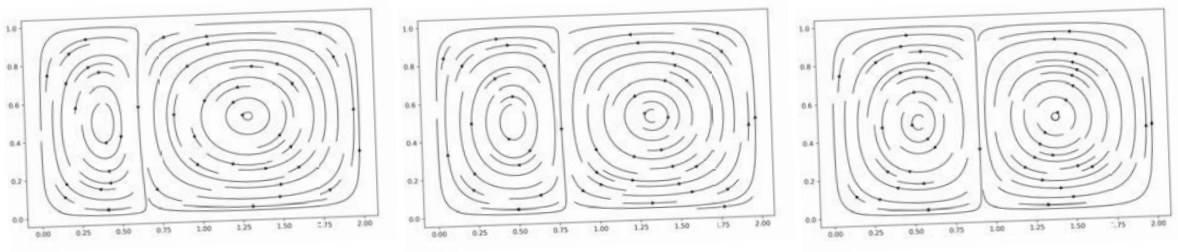

(D) $Ra = 2100, \alpha = 2°$ (E) $Ra = 2150, \alpha = 2°$ (F) $Ra = 2500, \alpha = 2°$

FIGURE 5.7: Streamlines evolution along with Rayleigh number for Newtonian cases with $\alpha = 2°$ for the branch of 1-roll –> 2-roll.

The reason is there are two peak values in the profile of the local Nu distribution for 2-roll convection compared with the 1-roll convection, as shown in Fig. 5.8b, and the trough values of the local Nu are almost the same for 1-roll and 2-roll conditions. Similar to the cases of the configuration with $1:1$ aspect ratio, for the single roll branch in the $2:1$ cases, Nu increases with tilt angle α. The peak value of Nu occurs at $\alpha = 60°$. A similar result also was given

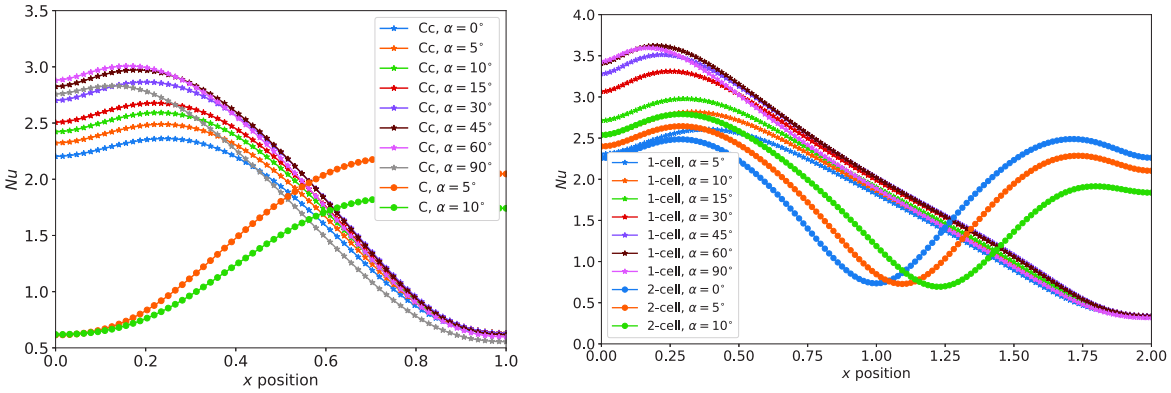

(A) 1 : 1 (B) 2 : 1

FIGURE 5.8: Nu distribution along with x positon for $Ra = 5000$ and $Pr = 7.0$. (Cc) and (c) represent circulation directions, i.e. counterclockwise direction and clockwise direction.

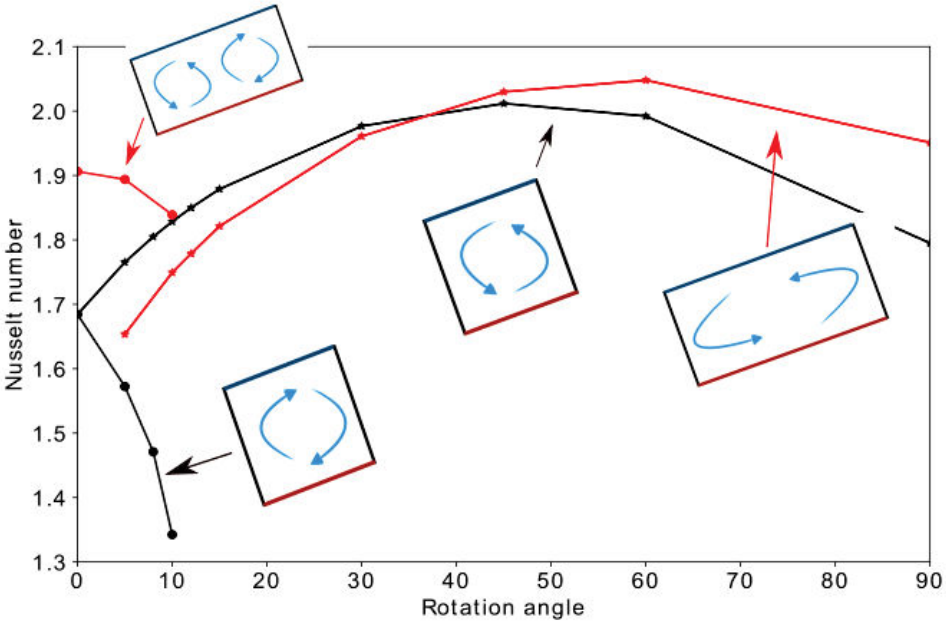

FIGURE 5.9: Nu for different tilted angle at 1 : 1 and 2 : 1 cavity. The black curves represent the cases with aspect ratio 1 : 1 and the red curves represent the cases with aspect ratio 2 : 1.

by Bairi, Laraqi, and Maria (2007), who experimentally investigated the RBC at a moderate Rayleigh number ($Ra < 10^6$) in the cavity with an aspect ratio of 1.5 : 1.

5.3 Viscoelastic RBC in tilted cavity

We pay attention to the tilted viscoelastic RBC in cavity with aspect ratio of 2 : 1, and present the results obtained in two parts: (a) the results about the tilted viscoelastic RBC with high β and small We (weak elasticity) will be given to illustrate the effect of viscoelasticity, through

comparison with the Newtonian cases; (b) the temporal and spatial evolution of the reversal convection under the action of a small α for small β and large We (strong elasticity) will be given to describe the effect of α on the viscoelastic reversal.

5.3.1 Steady convection in dilute solutions ($\beta = 0.9$)

A series of tilted RBC filled with weak elasticity viscoelastic fluids was simulated to obtain the effect of viscoelastic properties on the convection. $Pr = 7.0$, $\epsilon = 0.1$, $\xi = 0.05$ and $Ra = 5000$ are used in simulations. The overlapping velocity isolines for stable Newtonian and viscoelastic convections in tilted cavity with different α are shown in Fig. 5.10. In the figure, colored curves represent isolines of dimensionless velocity for the cases with the Newtonian fluid (black line) and viscoelastic fluids $(\beta = 0.9, We = 0.0025, 0.01, 0.02)$ (red, blue and green) at $\alpha = (0°, 30°, 45°, 60°, 90°)$. The results show that the increasing We has slightly enhencement effect on the velocity field. Fluids with low We are almost Newtonian.

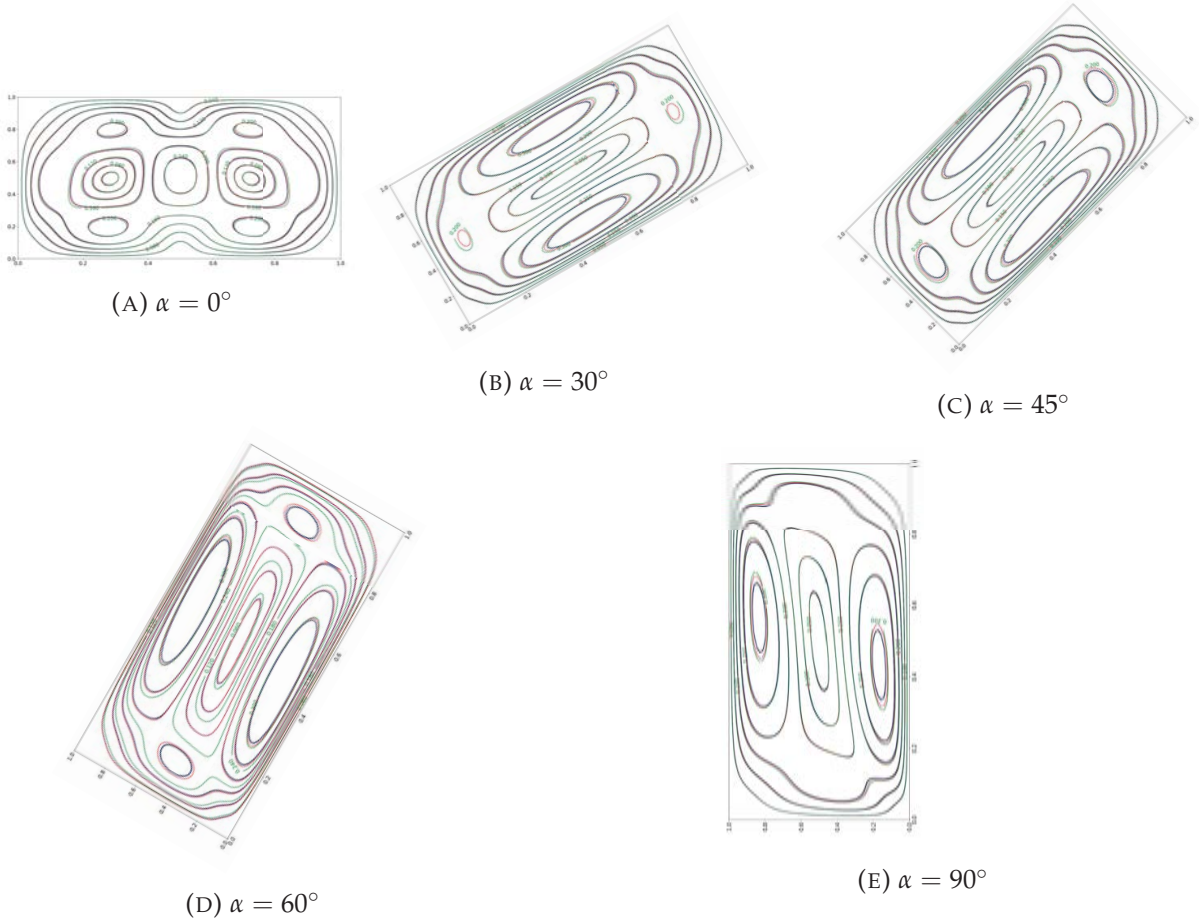

(A) $\alpha = 0°$ (B) $\alpha = 30°$ (C) $\alpha = 45°$ (D) $\alpha = 60°$ (E) $\alpha = 90°$

FIGURE 5.10: The overlapping dimensionless velocity isolines for Newtonian fluid $((\beta = 1, We = 0))$ (black line) and viscoelastic fluid with $(\beta = 0.9, We = 0.0025)$ (red line), $(\beta = 0.9, We = 0.01)$ (blue line), and $(\beta = 0.9, We = 0.02)$ (green line) at $\alpha = (0°, 30°, 45°, 60°, 90°)$.

Meanwhile, except the $\alpha = 0°$ case, the velocity fields are similar for other α. The temperature and $y-$ velocity distribution along the $y = 0.5$ center line for the cases with $We = 0.01$ at different α are presented in Fig. 5.11. Compared with the velocity distribution, α has less impact on the temperature distribution for the viscoelastic cases, as shown in Fig. 5.11a. In terms of velocity, α influences only the biggest velocity value which occurs at about 45°, 60°.

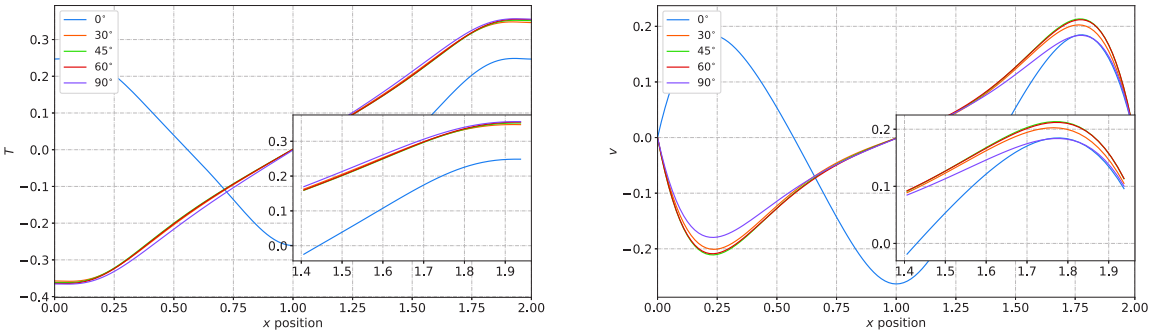

(A) T. (B) v.

FIGURE 5.11: Temperature and v-velocity distribution along the central horizontal line of the cavity for tilted viscoelastic RBC with fixed parameters $Ra = 5000$, $Pr = 7.0$, $\beta = 0.9$, $We = 0.01$, $\epsilon = 0.1$ and $\xi = 0.05$.

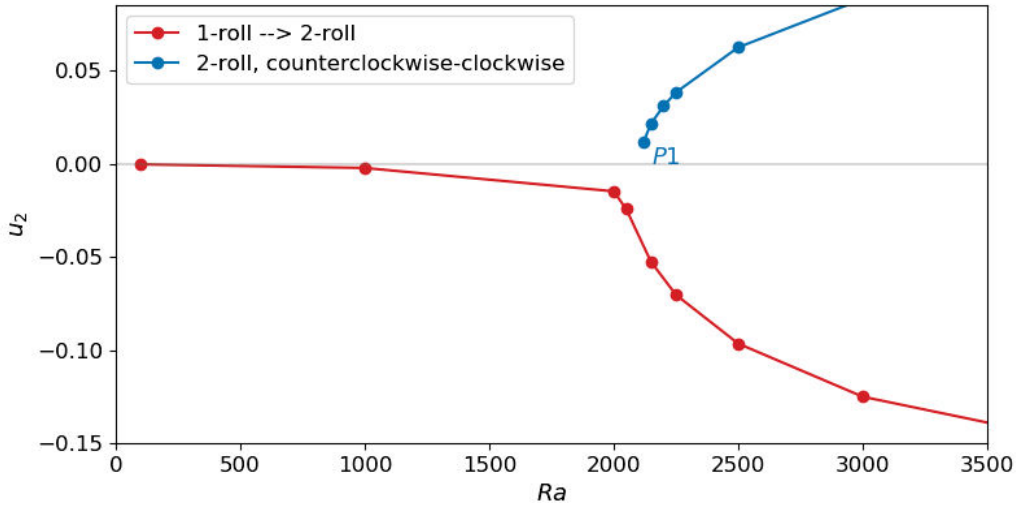

FIGURE 5.12: Bifurcation diagram for tilted weak viscoelastic RBC at inclination $\alpha = 2°$ under fixed parameters $Pr = 7.0$, $\beta = 0.9$, $We = 0.01$, $\epsilon = 0.1$ and $\xi = 0.05$. y-axis represents the 'y-' velocity at the monitor point $(x, y) = (7/8, 1/2)$. The flow structure profile of the branch of 1-roll –> 2-roll is similar to that shown in Fig. 5.7.

We also checked the flow bifurcation for weak viscoelastic RBC with fixed parameters $Pr = 7.0$, $\beta = 0.9$, $We = 0.01$, $\epsilon = 0.1$ and $\xi = 0.05$ (Fig. 5.12). The results are almost the same compared with the Newtonian cases, excepts the bifurcation points $P1$ is slightly lagging (see Fig. 5.7 for the details).

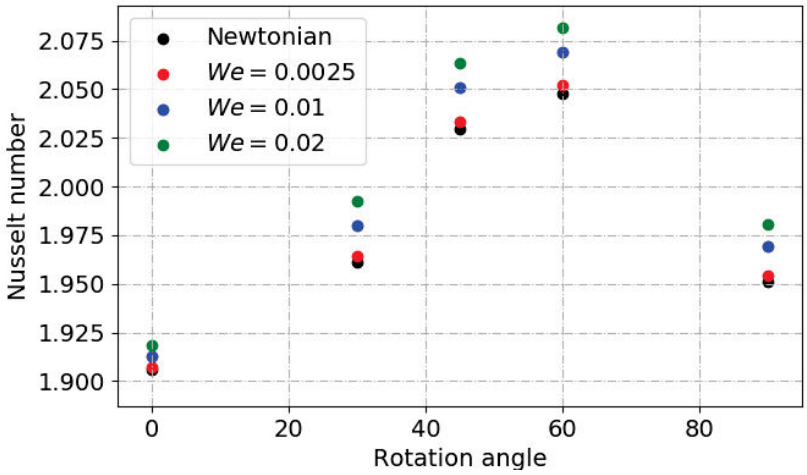

FIGURE 5.13: Averaged Nu as a function of the inclined angle ($\alpha = (0°, 30°, 45°, 60°, 90°)$) for Newtonian fluid and viscoelastic fluid with different We. In simulated viscoelastic cases, parameters are fixed at $Ra = 5000$, $Pr = 7.0$, $\beta = 0.9$, $\epsilon = 0.1$ and $\xi = 0.05$.

Fig. 5.13 plots the averaged Nu in tilted Newtonian and viscoelastic RBC as a function of α at different We. It can be found that the properties of viscoelastic fluids do not change the influence of α on Nu, and the peak value of the averaged Nu for viscoelastic RBC also takes place at α about 60°. The maximum value Nu ($\alpha = 60°$) is almost 10% higher than the minimum value ($\alpha = 0°$), whether it is Newtonian fluid or viscoelastic fluid. The enhancement of the heat transfer brought by the increasing We gets to peak when $\alpha = 60°$.

5.3.2 Reversal convection in concentrated solutions ($\beta = 0.2$)

In the last chapter, we found that a special regular reverse convection phenomenon takes place for viscoelastic RBC in the certain range of β and We. In this part, we extend that investigation to the effect of α on this viscoelastic reversal convection. Following the parameters setting of Chapter 4, the PTT constitutive model is still used in the following cases, where $We = (0.1, 0.15, 0.2)$, $\beta = 0.2$, $\epsilon = 0.1$ and $\xi = 0.05$. The calculation parameters and the corresponding flow structures of the tested cases in Tab. 5.1, where $1S$ and $2S$ represent the steady convection with a single roll and two rolls, respectively; $2R$ and $3R$ represent time-dependent reversal convection with two rolls and three rolls, respectively.

From Tab. 5.1, we find that once the inclination takes place ($\alpha \neq 0$), the original flow state (conduction state in horizontal cases) under the same parameters setting is broken (see the flow transition from ($\alpha = 0°$, $We = 0.1$, $Ra = 640$) to ($\alpha = 2°$, $We = 0.1$, $Ra = 640$)). For tilted cases, there is no more pure conduction state, and the flow transition path is different from $\alpha = 0°$ cases. By the way of example at $We = 0.1$ and $\alpha = 2°$, as increasing Ra, the flow state first quickly gets to the region of steady laminar convection with a single roll, and then changes to the time-dependent reversal convection with three rolls ($3R$) as we have known in Chapter 4. At the same time, another branch of time-dependent convection with left-right movement ($2R$) also

α	We	640	800	960	1120	1280	1360	1440	1600	1920	2080	2160
				1040					1760			
	0.1	–	–	–	–	–	–	2R,3R	2R,3R	3R,2S	3R,2S	3R,2S
0°	0.15	–	–	–	–	2R,3R	2R,3R	2R,3R	2R,3R	3R,2S	3R,2S	3R,2S
	0.2	–	–	2R,3R	2R,3R	2R,3R	2R,3R	2R,3R	3R,2S	2S	2S	2S
	0.1	1S	1S	1S	1S	1S	1S	1S	2R, 3R	2R, 3R	2R, 3R	2R, 3R
2°	0.15	1S	1S	1S	2R	2R	2R	2R	2R	2R	2R	
	0.2	1S	1S	2R	2R	2R	2R					
	0.1	1S	1S	1S	1S	1S	1S	1S	1S	2R		
3°	0.15	1S	1S	1S	1S	2R	2R	2R	2R			
	0.2	1S	1S	2R	2R	2R	2R					
	0.1	1S	1S	1S	1S	1S	1S	1S	1S			
5°	0.15	1S	1S	1S	1S	1S	1S	1S	1S			
	0.2	1S	1S	1S	1S	1S	1S					

TABLE 5.1: The flow patterns at different Rayleigh numbers with various tilted angle $\alpha = (0°, 2°, 3°, 5°)$ and different Weissenberg number $We = (0.1, 0.15, 0.2)$.

takes place for Ra big enough and α small enough. At the same tilt angle $\alpha = 2°$, as We further increases, the flow pattern $3R$ does not take place, only $2R$ takes place. The same situation is also observed for $\alpha = 3°$. As α increases to 3°, for $We = 0.1$, only the flow patterns $1S$ and $2R$ are observed. One can find that increasing We will reduce the critical Rayleigh number for flow transition from steady-state to reversal. When α exceeds a certain value α_c (in present cases α_c is in range of $[3°, 5°]$), the periodic reversal convection (tilted $2R$ and $3R$) totally disappears, only $1S$ exists. Note that for high Ra the critical α for Newtonian reversal RBC with $Ra = 4 * 10^7$, $Pr = 2$ is about 7° (Wang et al., 2018).

In order to understand the flow pattern transition in the tilted viscoelastic RBC more intuitively, we simulated cases with fixed inclination $\alpha = (0°, 2°)$ and studied the relationship between the velocity and Ra. In the studied cases, fluid parameters are $Pr = 7.0$, $\beta = 0.2$, $We = 0.1$, $\epsilon = 0.1$ and $\xi = 0.05$. Fig. 5.14 shows the bifurcation diagrams in range of $(0 < Ra < 2500)$ for the horizontal ($\alpha = 0°$) and tilted ($\alpha = 2°$) viscoelastic RBC. Fig. 5.14a plots the $y-$ velocity at monitor point $(x, y) = (7/8, 1/2)$ as a function of Ra for a normal horizontal viscoelastic RBC. There are two (positive and negative) solution branches for convection pattern of $2R$ and $3R$, the positive and negative values of branches are maximum and minimum velocities in one reversal period, respectively. For $\alpha = 0°$ both $2R$ and $3R$ time-dependent reversal convection set from pure conduction state and possess two slighty different Hopf bifurcation points $P1$ and $P2$. With increasing Ra, the secondary bifurcation $P3$, the drift pitchfork bifurcation, takes place and induces the flow transition from $2R$ to $2S$.

Fig. 5.14b plots the $y-$ velocity at monitor point $(x, y) = (7/8, 1/2)$ as function of Ra for tilted viscoelastic RBC with $\alpha = 2°$ and fixed parameters $Pr = 7.0$, $\beta = 0.2$, $We = 0.1$, $\epsilon = 0.1$ and $\xi = 0.05$. The bifurcation diagram of $\alpha = 0°$ viscoelastic RBC was also drawn in the figure by transparent grey curves. The curve (——) corresponds to the steady convection with counterclockwise single roll ($1S$), the curve (——) corresponds to the time-dependent reversal

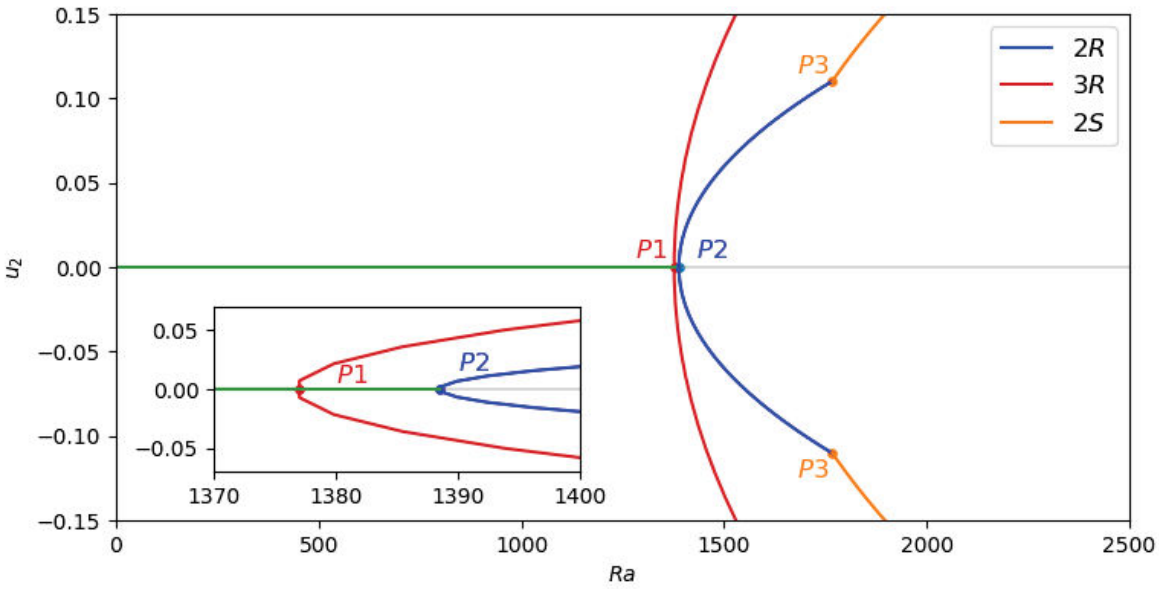

(A) Horizontal cases, $\alpha = 0°$.

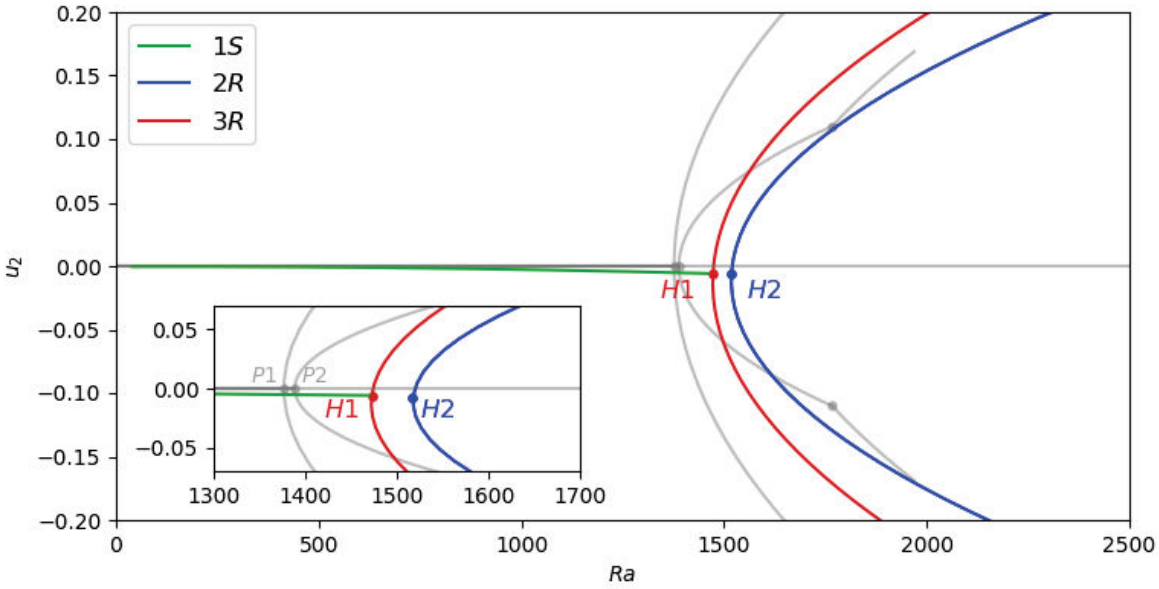

(B) Tilted cases, $\alpha = 2°$.

FIGURE 5.14: Bifurcation diagrams showing the multiple flow patterns found in horizontal viscoelastic RBC and tilted viscoelastic RBC. y-axis represents the 'y-' velocity at the monitor point $(x, y) = (7/8, 1/2)$. The simulated cases correspond to $Pr = 7.0$, $\beta = 0.2$, $We = 0.1$, $\epsilon = 0.1$ and $\xi = 0.05$.

convection with three rolls ($3R$), and the curve (——) corresponds to the time-dependent reversal convection with two rolls with horizontal movement ($2R$). The branch of $3R$ develop from the bifurcation $H1$. Considering the reversal in $\alpha = 0°$ viscoelastic RBC, there is a certain Ra range for coexistence of $2R$ and $3R$ (shown in Fig. 5.14a). In order to find $2R$ reversal convection at $\alpha = 2°$, we read $2R$ solution of $\alpha = 0°$ viscoelastic RBC as the initial value, and changed the inclination to $\alpha = 2°$. The branch of tilted $2R$, that develop from the bifurcation $H2$. Due to the

inclination, the rolls in tilted $2R$ has the characteristics of periodic horizontal oscillation (flow reversal process can be found in Fig. 5.15), instead of standing wave in horizontal $2R$. However, this time-dependent reversal convection also disappears with the further increase of α and we observe only steady-state single roll convection (Tab. 5.1). Compared to the bifurcation points $P1$ and $P2$ in the horizontal cases, $H1$ and $H2$ are slightly higher. It should be noted that due to the inclination, the branches of tilted $2R$ and $3R$ are not symmetric about the x-axis, and the maximum value of the downward velocity will be slightly larger than the maximum value of the upward velocity.

Flow transition in tilted cavity

Figs. 5.15-5.17 depict two kinds of velocity vector evolution of tilted $2R$ and tilted $3R$ listed in Tab. 5.1. Obviously, they both have the special characteristics brought by the inclination.

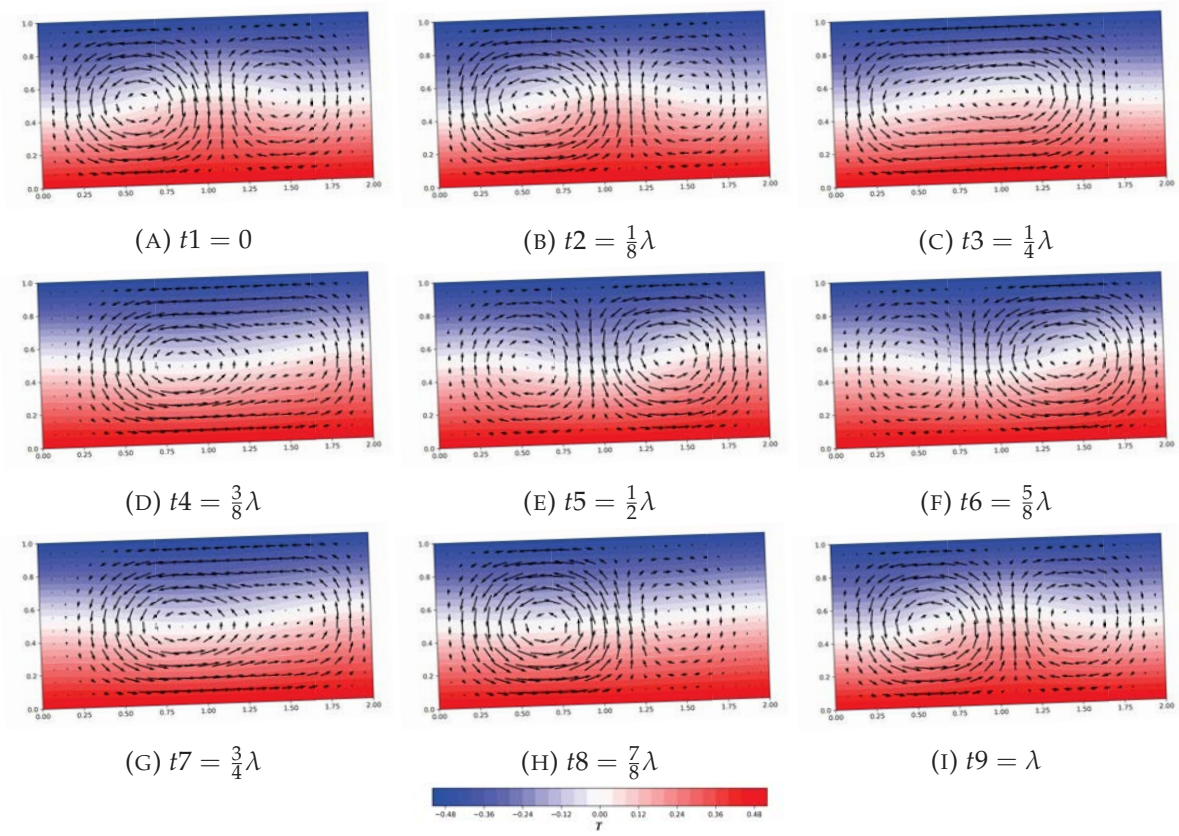

(A) $t1 = 0$ (B) $t2 = \frac{1}{8}\lambda$ (C) $t3 = \frac{1}{4}\lambda$

(D) $t4 = \frac{3}{8}\lambda$ (E) $t5 = \frac{1}{2}\lambda$ (F) $t6 = \frac{5}{8}\lambda$

(G) $t7 = \frac{3}{4}\lambda$ (H) $t8 = \frac{7}{8}\lambda$ (I) $t9 = \lambda$

(J) colorbar

FIGURE 5.15: Evolution of the velocity vector of the periodic flow with $\alpha = 2°$ and $Ra = 1760$. In simulated case, $\Pr = 7.0$, $\beta = 0.2$, $We = 0.1$, $\epsilon = 0.1$ and $\xi = 0.05$. The time period is $\lambda = 88.29$. The time range $t1 - t9$ covers one period.

The main reason for periodic reversal convection is the alternating growth of the velocity field and the elastic stress field, generation and growth of the new vortex are driven by elastic dissipation and buoyancy flux, which are described in Sec. 4.3. The convection consists of two circulations with the clockwise and counterclockwise flow directions, and each circulation is of

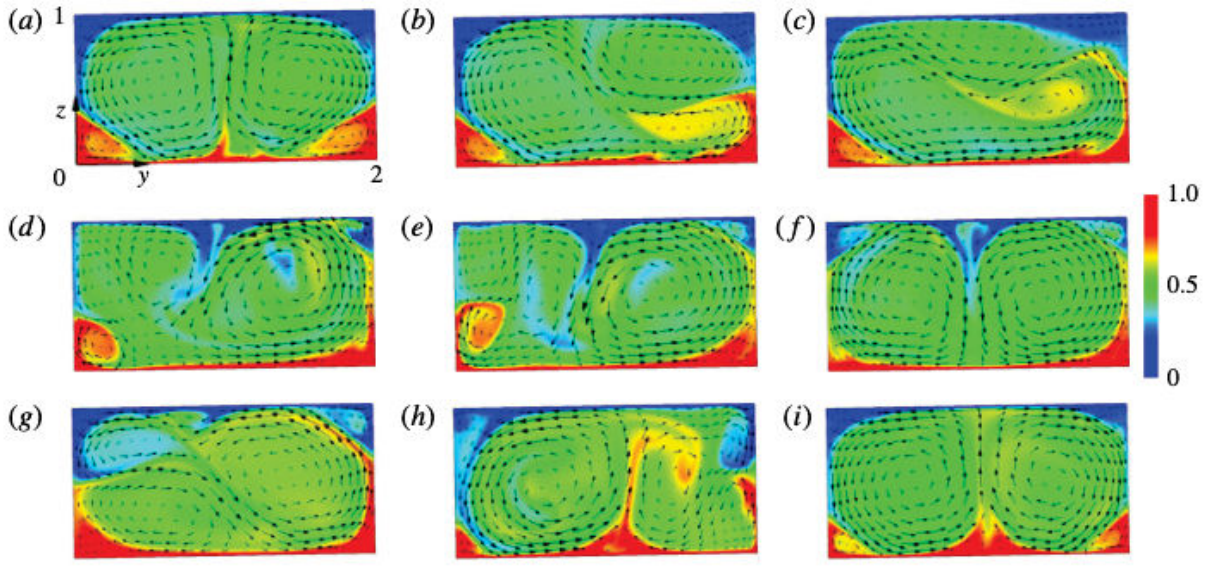

FIGURE 5.16: Nine snapshots of the temperature field superimposed with velocity vectors during two of the flow reversals for $Ra = 10^7$, $Pr = 0.71$, $\alpha = 1^\circ$ in cavity with aspect ratio 2 (Wang et al., 2018).

equal status in the whole process for $\alpha = 0^\circ$. However, when the flow space is tilted, from the convection patterns of tilted $2R$ and tilted $3R$ (shown in Fig. 5.4), it can be easily observed that the counterclockwise circle (with the same direction to the inclination of space) is stronger than the clockwise one, and that this trend is enhanced with α increase, as shown in Fig. 5.4. We call the circulation with counterclockwise rotating the main circulation and the clockwise rotating one the secondary circulation.

The periodic reversal is mainly reflected in the continuous absorption of the secondary circulation energy by the main circulation, driven by elastic energy releasing and buoyancy flux(the process has been explained in Sec. 4.3.1). Take the tilted $2R$ as an example, as shown in Fig. 5.15, in this process the continuous energy obsorption of the macromolecular structure makes the secondary circulation (right part in Fig. 5.15a) smaller and due to the energy release of the macromolecular structure the main circulation (Fig. 5.15b) keeps getting bigger. From Fig. 5.15a to Fig. 5.15c we see this evolution: the main circulation grows and occupies almost the whole cavity. From Fig. 5.15c to Fig. 5.15d it moves from left to right and frees the left part for another secondary circulation which is formed completely in Fig. 5.15e. Then the secondary circulation is weakened again (Fig. 5.15f) and the main circulation grows and moves from right (Fig. 5.15g) to left (Fig. 5.15h). Finally the secondary circulation is formed again (Fig. 5.15h) and amplified (Fig. 5.15i). The repeated occurrence of the above process alternately forms this time-dependent reversal convection (tilted $2R$). In the above reversal procedure, the strict symmetry of geometry is broken by the small-angle tilt. As α increases, the critical Ra of tilted $2R$ appears to increase slightly, and then when α is large enough, tilted $2R$ disappears and only $1S$ appears. This tilted reversal phenomenon, the main circulation absorbs the secondary circulation and then reverses, also exists in the Newtonian fluid RBC at high Rayleigh number ($Ra \sim 10^7$) (Wang et al., 2018),

as shown in Fig. 5.16. Fig. 5.16 depicts a turbulent Newtonian RBC reversal process, we can clearly observe that the main circulation is strengthened and that the secondary circulation is weakened (from Fig. 5.16a to 5.16b), and then the main circulation takes up space and generates the secondary circulation (from Fig. 5.16c to 5.16f) to form a reversal.

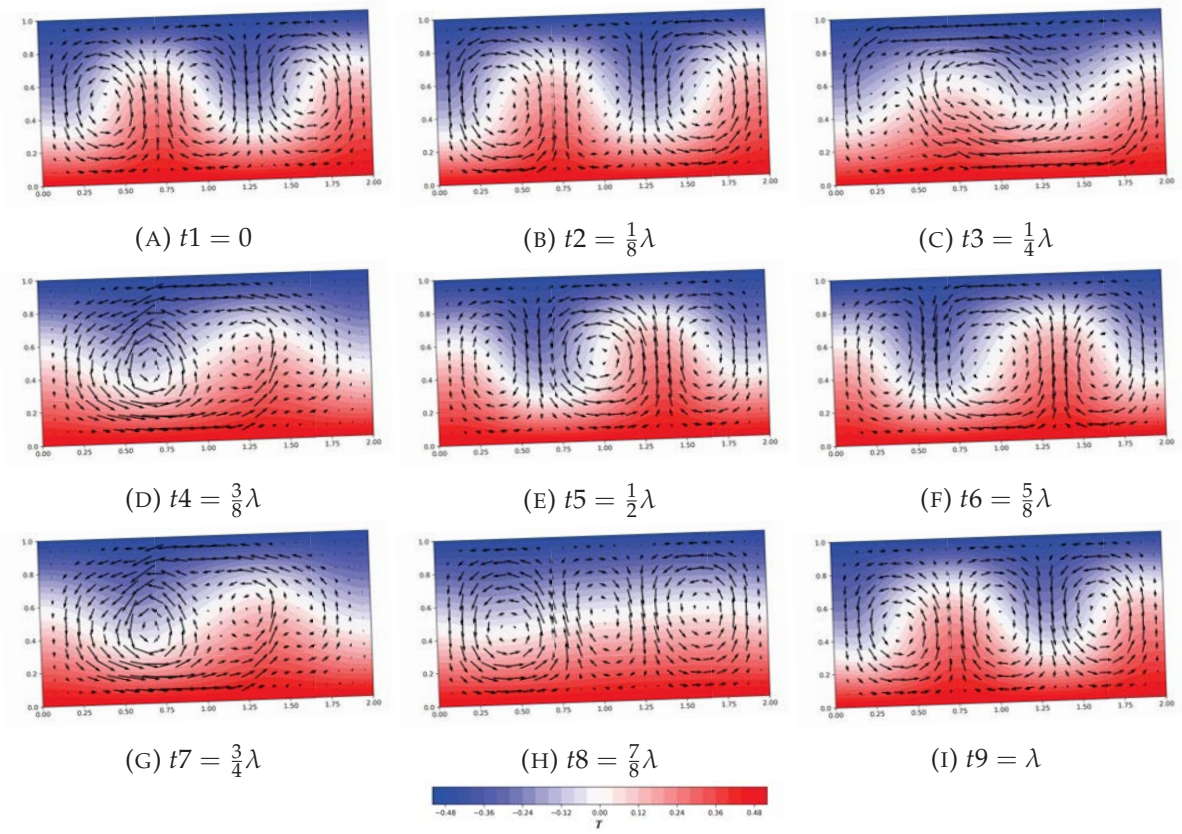

(A) $t1 = 0$ (B) $t2 = \frac{1}{8}\lambda$ (C) $t3 = \frac{1}{4}\lambda$

(D) $t4 = \frac{3}{8}\lambda$ (E) $t5 = \frac{1}{2}\lambda$ (F) $t6 = \frac{5}{8}\lambda$

(G) $t7 = \frac{3}{4}\lambda$ (H) $t8 = \frac{7}{8}\lambda$ (I) $t9 = \lambda$

(J) colorbar

FIGURE 5.17: Evolution of the velocity vector of the periodic flow with $\alpha = 2°$ and $Ra = 1760$. In simulated case, $\Pr = 7.0$, $\beta = 0.2$, $We = 0.1$, $\epsilon = 0.1$ and $\xi = 0.05$. The time period is $\lambda = 23.15$. The time range ($t1 - t9$) cover one period.

Fig. 5.17 shows the reversal evolution process of $3R$. In Fig. 5.17a, the main circulations are located on the left and the right and the secondary circulation in the center is then weakened and obsorbed (Fig. 5.17b and Fig. 5.17c). The main circulations take the cavity center (after Fig. 5.17d) and the secondary circulations are formed (Fig. 5.17e). The main circulation grows (Fig. 5.17f) and the secondary circulations are weakened (Fig. 5.17g). The main circulation is broken to fill the left and right parts of the cavity (Fig. 5.17h).

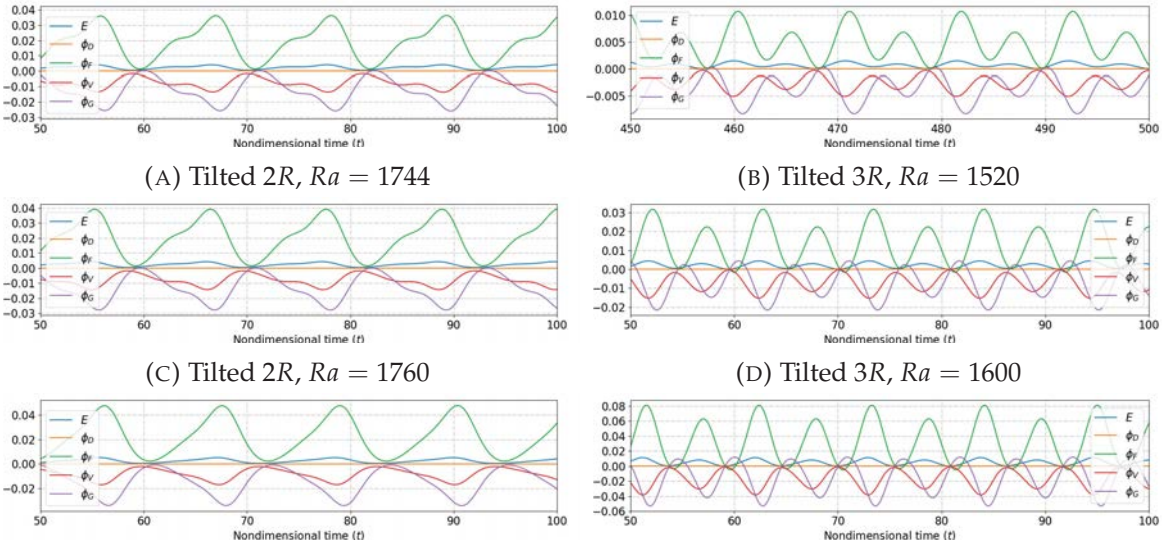

(A) Tilted $2R$, $Ra = 1744$

(B) Tilted $3R$, $Ra = 1520$

(C) Tilted $2R$, $Ra = 1760$

(D) Tilted $3R$, $Ra = 1600$

(E) Tilted $2R$, $Ra = 1800$

(F) Tilted $3R$, $Ra = 1840$

FIGURE 5.18: Different averaged quantities as function of dimensionless time in regular tilted reversal convection system for tilted $2R$ and tilted $3R$ patterns, where the rheology parameters are $\beta = 0.2$, $We = 0.1$, $Pr = 7.0$, $\epsilon = 0.1$ and $\xi = 0.05$.

Fig. 5.18 plots the different energy transports in tilted $2R$ and $3R$ reverse convection system with fixed rheology parameters $\beta = 0.2$, $We = 0.1$, $Pr = 7.0$, $\epsilon = 0.1$ and $\xi = 0.05$. Figs. 5.18a, 5.18c and 5.18e are for tilted $2R$ pattern, and Figs. 5.18b, 5.18d and 5.18f are for tilted $3R$ pattern. Note that a velocity reversal period consists of two half periods, and each half period can be expressed as kinetic energy from one maximum to another maximum, but the direction of velocity is opposite. The kinetic energy evolution in the two half-periods is equivalence in magnitude, in horizontal $3R$ and $2R$ reversals. This situation also occurs in tilted $2R$ reversal (shown at Fig. 5.18a, 5.18c and 5.18e) because there is only one primary circulation and one secondary during the entire reversal process, and the evolution process is only an exchange between these two circulations (shown in Fig. 5.15). But that is completely broken in tilted $3R$ because in one half period two main circulations absorb the secondary circulation and in another half period the main circulation absorbs two secondary circulations. The explanation for this phenomenon in $3R$ pattern can be traced back to the fact (in Sec. 5.2.1) that the counterclockwise flow circulation is the primary flow, that clockwise flow circulation is the secondary flow, the counterclockwise circulation is always stronger than clockwise one, which is obviously affected by the inclination and explained in Sec. 5.2.1.

Heat transfer

Here, we discuss the heat transfer properties, the heat transport in strong elasticity RBC at different β, α, We, and Ra was studied. For periodic convections, the periodically and spatially averaged Nusselt number Nu_{ts} has been defined in Eq. (4.10). Fig. 5.19 shows Nu_{ts} as a function of Ra for $\alpha = (2^\circ, 3^\circ, 5^\circ)$, $Pr = 7.0$, $\beta = 0.2$, $\epsilon = 0.1$ and $\xi = 0.05$.

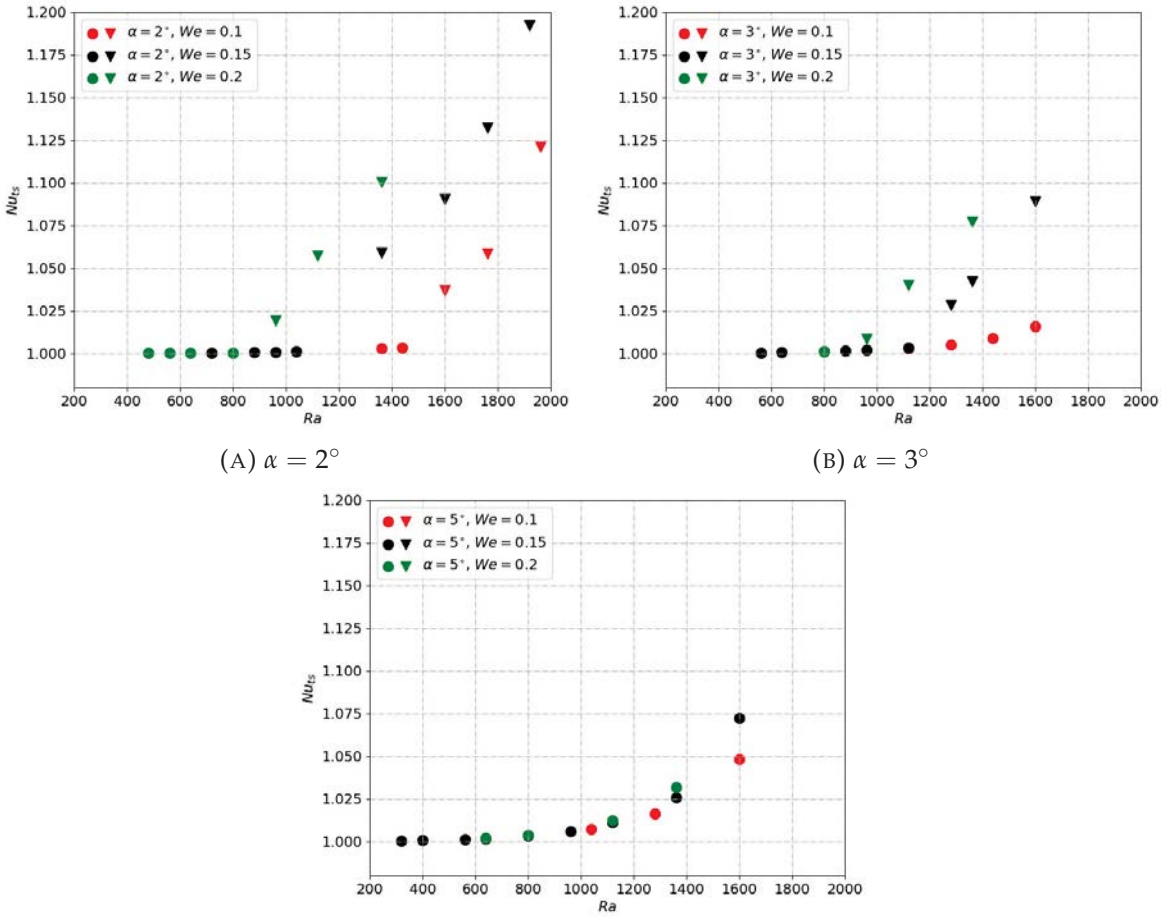

(A) $\alpha = 2^\circ$

(B) $\alpha = 3^\circ$

(C) $\alpha = 5^\circ$

FIGURE 5.19: Nu_{ts} as a function of Ra for $\alpha = (2^\circ, 3^\circ, 5^\circ)$ and $We = (0, 1, 0.15, 0.2)$. In the figure, • and ▼ represent $1S$ and tilted $2R$ convection conditions, respectively.

We distinguish the two kinds of flow pattern by • ($1S$) and ▼ (tilted $2R$), it can be easily found that heat exchange capacity will increase with α increasing for flow pattern tilted $1S$, it is the same as in weak elastic RBC. However this rule is opposite for tilted $2R$ pattern, one can see case groups ($We = 0.15$, $\alpha = (2^\circ, 3^\circ)$) and ($We = 0.2$, $\alpha = (2^\circ, 3^\circ)$). Compared with the weak elastic RBC, Nu_{ts} is also enhanced by increasing We, we can see that from the cases with $\alpha = 2^\circ$ and $We = 0.1, 0.15, 0.2$. The reason is that the strong elasticity breaks at smaller Ra the steady single roll convection, and increases the tilted $2R$ convection intensity.

Fig. 5.20 shows the local Nu distribution for cases when temporally-spatially averaged Nu gets to maximum. Fig 5.20a displays the local Nu distributions in steady flow condition under strong elasticity cases ($We = 0.2$ and $\beta = 0.2$), with different inclined angles ($2^\circ, 3^\circ, 5^\circ$). We can clearly find that increasing slightly the inclined angle will greatly change the local Nu distribution. Fig. 5.20b shows the local Nu distribution with diffrent Ra, under fixed inclined angle $\alpha = 5^\circ$, $\beta = 0.2$ and $We = 0.2$.

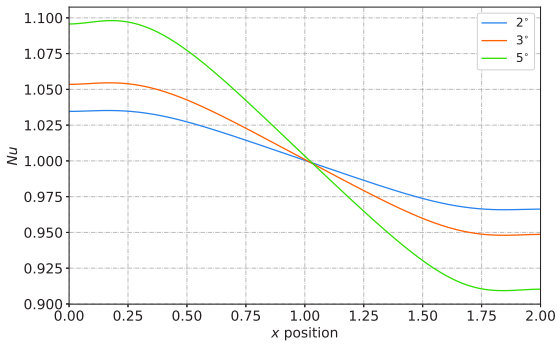

(A) Local Nusselt number at heating boundary with different inclined angle, under $We = 0.2$, $\beta = 0.2$ and $Ra = 800$.

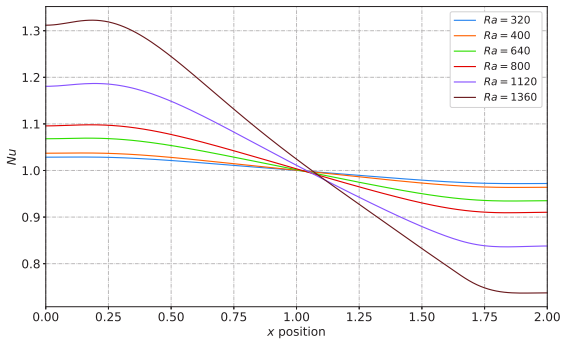

(B) Local Nusselt number at heating boundary with different Rayleigh number, under $We = 0.2$, $\beta = 0.2$ and $\alpha = 5°$.

FIGURE 5.20: Local Nu distributions.

5.4 Conclusion

In this chapter, the Newtonian and viscoelastic RBC in a 2D inclined closed cavity with aspect ratio 2 : 1 is numerically studied, and we can observe that:

- For tilted Newtonian RBC, three types of flow structures take place in Ra range about the onset of convection, effects of α on flow patterns was investigated in 2 : 1 cavities. For a moderate Rayleigh number ($Ra = 5000$ in our cases), when α remains small (about 12°), two convection patterns (1S and 2S) take place, and with α increasing, one (2S) disappears. Nu shows a trend of first increasing and then decreasing with α increasing. For weak elasticity cases, viscoelasticity has a very limited effect, compared with the Newtonian cases. We shows an improvement effect on Nu.

- For strong elasticity tilted viscoelastic RBC, the periodic reversal convection also takes place, for example in the cases with $\beta = 0.2$, $\alpha = 2°$, bifurcation diagram (Fig. 5.14) shows that there are three flow patterns: one steady single roll convection and two time-dependent reversals take place. The inclination delays the occurrence of the reversal, and when the inclination is big enough, the periodic reversal will vanish. Compared with typical horizontal viscoelastic RBC, any small α will also have a huge impact on flow pattern and Nu. For steady flow, increasing α will bring enhancement of heat transfer. For reversal flow, increasing α will bring weaken of heat transfer.

Chapter 6

Three-dimensional viscoelastic laminar Rayleigh-Bénard covnection

Contents

In this chapter, the 3D viscoelastic Rayleigh-Bénard convection problem was studied through our developed solver. First, we will introduce the governing equations and the essential numerical scheme. Second, we will validate the solver for Newtonian and viscoelastic 3D Rayelgih-Bénard convection. Finally, the flow structure in 3D viscoelastic RBC cavities with different aspect ratio will be shown.

6.1 Introduction

As we know, few previous numerical studies of the Rayleigh-Bénard convection have focussed on the viscoelastic fluid convection, and fewer researches focus on numerical simulation of three-dimensional viscoelastic Rayleigh-Bénard convection. A main reason is that huge computing resources are required for three-dimensional problems.

For 3D viscoelastic Rayleigh-Bénard problem, Park and Ryu (2001) and Park and Ryu (2001) first numerically investigated the effects of the aspect ratio and elasticity intensity (β, We) on the convection onset for the cases with either two periodic horizontal directions or one periodic horizontal direction. They gave for the first time Rac as functions of aspect ratio A and elastic intensity (β, We). Lappa and Boaro (2020) for the first time numerically examined the dynamics of viscoelastic RBC with the FENE-CR model in a 3D cylindrical geometries and showed the transition of more complex and diverse flow patterns under strong elasticity and different aspect

ratio. The rheology parameters in the examined cases are set as Prandtl number $Pr = 8.0$, aspect ratio $0.7 < A = (height/diameter) < 1$ and different elasticity $0 < We < 0.2$. Benzi, Ching, and De Angelis (2010) and Benzi, Ching, and De Angelis (2016) also did relative work about the three-dimentional Rayleigh-Bénard convection between parallel plates filled with polymer solution through direct numerical simulation. Cai et al. (2016) numerically investigated the effect of the viscoelatic Rayleigh-Bénard convection in 3D unbounded system and found that the viscoelastic fluid will delay the onset of the Rayleigh-Bénard convection under a certain condition.

From the above review, it can be found that most of the existing studies have been produced for the case of laterally unbounded geometries (mainly in infinite horizontal layers with periodic boundary conditions), so we will focus on the three-dimensional Rayleigh-Bénard convection in a finite domain in this chapter.

6.2 Physical configuration and numerical scheme

6.2.1 Governing equations and boundary conditions

The physical model is shown in Fig. 6.1, we consider a three dimensional cell of height H, width L_x and depth L_y containing a viscoelasitc fluid. The cell is heated at the bottom boundary and cooled at the top boundary, which induce a temperature difference $\Delta T = T_2 - T_1$. Boussinesq approximation is used to simplify the Navier-Stokes equation to describe the buoyancy-driven flow.

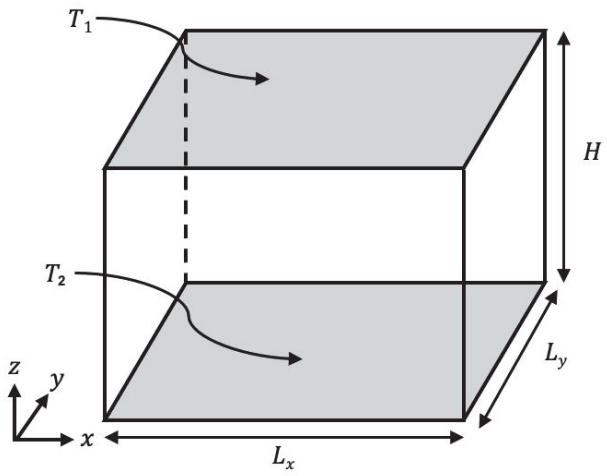

FIGURE 6.1: A schematic diagram of the 3D viscoealstic Rayleigh-Bénard convection cell.

The governing equations for 3D cases, similar to those in 2D introduced in Chapter 3, include mass conservation equation Eq. (6.1), momentum equation Eq. (6.2), viscoelastic constitutive equation Eq. (6.3) and temperature equation Eq. (6.4). In dimensionless form, they read:

$$\nabla \cdot \boldsymbol{u} = 0 \tag{6.1}$$

$$\frac{\partial \boldsymbol{u}}{\partial t} + (\boldsymbol{u} \cdot \nabla)\boldsymbol{u} = -\nabla p + \beta \frac{Pr}{\sqrt{Ra}} \Delta \boldsymbol{u} + \nabla \cdot \boldsymbol{\tau_p} + PrT\boldsymbol{e_z} \tag{6.2}$$

$$\overset{\nabla}{\boldsymbol{\tau_p}} + \frac{\boldsymbol{\tau_p}}{We\sqrt{Ra}} - 2\frac{1-\beta}{Ma^2}\boldsymbol{D} = -\epsilon \frac{\sqrt{Ra}}{(1-\beta)Pr} tr(\boldsymbol{\tau_p})\boldsymbol{\tau_p} - \xi(\boldsymbol{D}\boldsymbol{\tau_p} + \boldsymbol{\tau_p}\boldsymbol{D}) \tag{6.3}$$

$$\frac{\partial T}{\partial t} + (\boldsymbol{u} \cdot \nabla)T = \frac{1}{\sqrt{Ra}} \triangle T \tag{6.4}$$

where the velocity vector becomes $\boldsymbol{u} = (u_1, u_2, u_3)$ and the elastic stress tensor becomes

$$\boldsymbol{\tau_p} = \begin{pmatrix} \tau_{11} & \tau_{12} & \tau_{13} \\ \tau_{21} & \tau_{22} & \tau_{23} \\ \tau_{31} & \tau_{32} & \tau_{33} \end{pmatrix} \tag{6.5}$$

Concerning the boundary conditions, the upper and lower boundaries are isothermal, and the other walls are adiabatic. All the boundaries are no-slip for velocity. The length, width and height of the cell are respectively $L_x = 2$, $L_y = 1$ and $H = 1$. The boundary conditions are set as follows:

- at $z = 0$: $u_1 = u_2 = u_3 = 0,\ T = 1$
- at $z = 1$: $u_1 = u_2 = u_3 = 0,\ T = 0$
- at $x = 0,\ 2$: $u_1 = u_2 = u_3 = 0,\ \frac{\partial T}{\partial x} = 0$
- at $y = 0,\ 1$: $u_1 = u_2 = u_3 = 0,\ \frac{\partial T}{\partial x} = 0$

The local and averaged Nusselt numbers at the bottom in 3D are, respectively, given by the following:

$$Nu = -\frac{\partial T}{\partial z}|_{z=0} \tag{6.6}$$

$$Nu_s = \frac{1}{A}\int_0^{L_x}\int_0^{L_y} (-\frac{\partial T}{\partial z}|_{z=0})\, dxdy \tag{6.7}$$

where $A = L_x L_y$ is the area of the bottom boundary.

6.2.2 Numerical schemes

Here we just briefly introduce the numerical schemes used in the three-dimensional situation. For three-dimensional cases, a second-order semi-implicit time scheme is used: the implicit

terms are mass conservation, pressure gradient, molecular diffusion, relaxation term, and thermal diffusion; other terms including the quasi-linear forms are explicit. Time evolution implemented makes use of the 2-order backward differential formula (BDF2) for time integration and a 3D Alternative Direction Implicit (ADI). This can decompose a 3D problem into three groups of one-dimensional problems and solve them in dimensional order. Take the temperature equation as an example, as described in Eq. (3.54), the time discretised partial differential equation is:

$$\begin{aligned}\frac{3T^{n+1}-4T^{n}+T^{n-1}}{2\Delta t} &= -(2\left((\boldsymbol{u}\cdot\boldsymbol{\nabla})T\right)^{n}-\left((\boldsymbol{u}\cdot\boldsymbol{\nabla})T\right)^{n-1}) \\ &+\frac{1}{\sqrt{Ra}}(\frac{\partial^2 T}{\partial x_1^2}+\frac{\partial^2 T}{\partial x_2^2}+\frac{\partial^2 T}{\partial x_3^2})^{n+1}+O(\Delta t^2)\end{aligned} \tag{6.8}$$

After reorganization, it can be writen:

$$\begin{aligned}\left(1-\frac{2\Delta t}{3\sqrt{Ra}}(\frac{\partial^2}{\partial x_1^2}+\frac{\partial^2}{\partial x_2^2}+\frac{\partial^2}{\partial x_3^2})\right)T^{n+1} &= \frac{4T^{n}-T^{n-1}}{3}-\frac{4\Delta t}{3}\left((\boldsymbol{u}\cdot\boldsymbol{\nabla})T\right)^{n} \\ &+\frac{2\Delta t}{3}\left((\boldsymbol{u}\cdot\boldsymbol{\nabla})T\right)^{n-1}+O(\Delta t^2)\end{aligned} \tag{6.9}$$

Solving this 3D system by the ADI method amounts to approaching the 3D Helmholtz operator by factorizing it into three 1D operators. In fact, factorization of the 3D Helmholtz operator for temperature will destroy the order 2 of the time scheme. In order to maintain the order 2 of the time scheme, temperature increment $\delta T = T^{n+1} - T^{n}$ was brought in, where $\delta T^{n+1} \approx O(\Delta t)$, and then the equation becomes:

$$\begin{aligned}(1-\frac{2\Delta t}{3\sqrt{Ra}}\frac{\partial^2}{\partial x_1^2})(1-\frac{2\Delta t}{3\sqrt{Ra}}\frac{\partial^2}{\partial x_2^2})(1-\frac{2\Delta t}{3\sqrt{Ra}}\frac{\partial^2}{\partial x_3^2})\delta T &= \frac{2\Delta t}{3\sqrt{Ra}}\triangle T^{n}+\frac{1}{3}(T^{n}-T^{n-1}) \\ &-\frac{4\Delta t}{3}\left((\boldsymbol{u}\cdot\nabla)T\right)^{n}+\frac{2\Delta t}{3}\left((\boldsymbol{u}\cdot\nabla)T\right)^{n-1}+O(\Delta t^3)\end{aligned} \tag{6.10}$$

In space, second-order central differencing is applied to most of the terms except for the quasi-linear parts which are treated in the eigenspace of A_i by a High-Order (3-order) Upstream Central (HOUC) scheme according to the sign of each eigenvalue. Finally, the velocity-pressure coupling is assured by the projection method.

6.2.3 Code validation

At present, there are no published papers investigating the three-dimensional laminar viscoelastic RBC in a rectangular closed cavity. The validation work will start with the steady Newtonian RBC.

Newtonian RBC

A pure thermally conductive temperature field is initially distrubed at a certain positon to get the target final convective structure. Fig. 6.2 shows two kinds of convection structure and local Nusselt number distribution at the bottom heating boundary. The flow structure is represented by isothermal surfaces, and the color on the isothermal surface is marked as the velocity in the $x-$ direction.

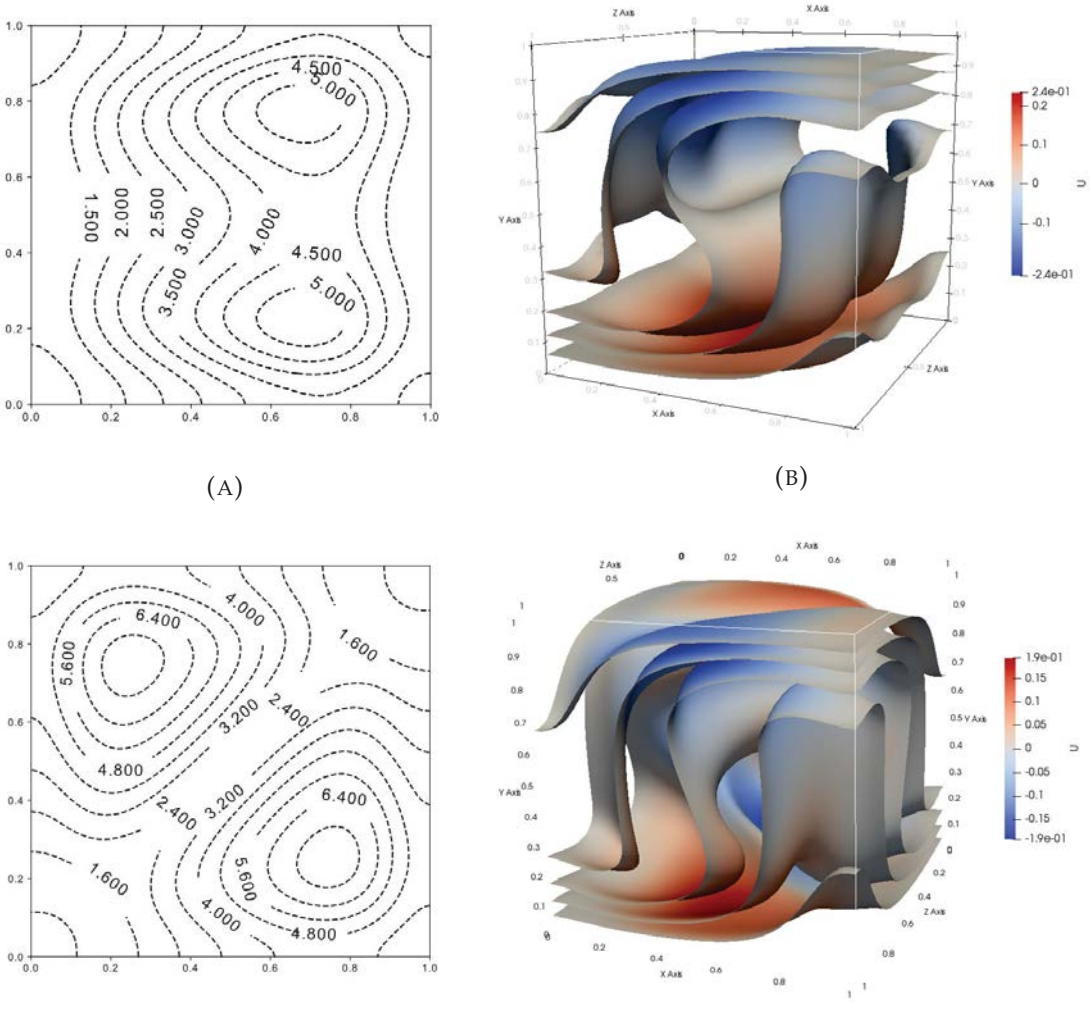

FIGURE 6.2: Structure $S3$ and $S5$ mentioned in (Pallares, Grau, and Giralt, 1999) at $Pr = 0.71$, $Ra = 6 \times 10^4$. (A) and (B) are local Nusselt number distribution at heating boundary and isosurfaces of temperature for flow structure of $S3$ (Single roll elongated towards two opposite horizontal edges). (C) and (D) are local Nusselt number distribution at heating boundary and isosurface of temperature for flow structure of $S5$ (Four roll structure, each one with its axis perpendicular to one sidewall).

Fig. 6.3 shows the grid independence verification carried out for two kinds of convection structure at $Pr = 0.71$ and $Ra = 6 \times 10^4$ with uniform grids of $N = N_x N_y N_z$ nodes ($N = 32^3$,

42^3, 52^3 and 64^3). A sufficiently small time step is fixed at $\Delta t = 0.001$, in order to avoid errors caused by the size of the time step. The values of dotted line in Fig. 6.3 are Nu_s at the heating bottom boundary for the two convection structures obtained by Pallares et al (Pallares, Grau, and Giralt, 1999). In fact, we can find that the averaged Nu obtained by each grid number is very close to the result of Pallares et al (Pallares, Grau, and Giralt, 1999), especially when the grid number is big enough ($N = 64^3$). That also means that the node number $N = 64^3$ is sufficient to calculate the Newtonian Rayelgih-Bénard convection at this Rayleigh number.

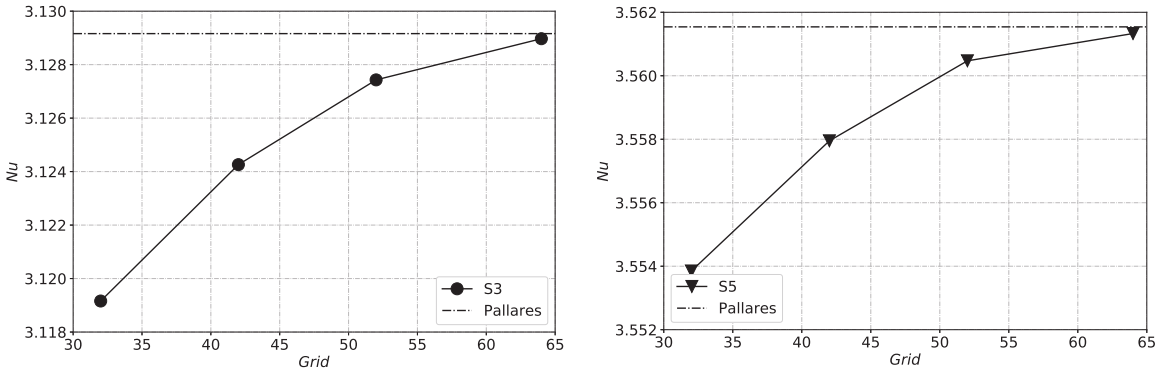

(A) $S3$ (B) $S5$

FIGURE 6.3: Nu_s at the bottom boundary according to the mesh refinement. The dashlines in the figure are the results of Pallares, Grau, and Giralt (1999). The numbers on the x-axis indicate the number of nodes in one direction of the cube, and the number of nodes in the three directions is the same. (A) Nu_s with flow structure of $S3$. (B) Nu_s with flow structure of $S5$.

6.3 Results

We are interested in viscoelastic RBC taking place in a 3D rectangular cavity with aspect ratio of $2:1:1$ and the PTT viscoealstic fluids with $Pr = 7.0$, $\beta = 0.2, We = 0.1$, $\epsilon = 0.1$ and $\xi = 0.05$. For the 3D cases studied, we give a perturbed initial condition simaliar to 2D for 3D viscoelastic RBC. Specifically, the initial zero field for velocity and elastic stress, vertical direction gradient change for temperature field ($\overline{T}_{i,j,k} = \Delta T(1 - z_k)$) with a perturbition $T_{(1,1/2,1/2)} = \overline{T}_{(1,1/2,1/2)} + 0.01T_0$, $T_{(1/4,1/2,1/2)} = \overline{T}_{(1/4,1/2,1/2)} - 0.01T_0$ and $T_{(7/4,1/2,1/2)} = \overline{T}_{(7/4,1/2,1/2)} - 0.01T_0$, where T_0 is the average of $T_0 = (T_1 + T_2)/2$.

Under such a parameters setting condition, the regular reversal convction that has been obtained in 2D viscoelastic RBC also takes place in 3D. The first time-dependent solution has been obtained at $Ra = 1600$ and two other solutions have been obtained at respectively $Ra = 1616$ and 1632. In a similar way used in 2D cases, the solution amplitudes squared can be plotted against Ra (Fig. 6.4a) and the least square method allows to determine the critial Rayleigh number: $Rac1 = 1591.7$. The critical Rayleigh number equals to $Rac1 = 1384.3$ in 2D cases with parameters $Pr = 7.0$, $\beta = 0.2, We = 0.1$, $\epsilon = 0.1$ and $\xi = 0.05$. Fig. 6.4b plots u_2 at $P1(\frac{1}{2}, \frac{1}{2}, \frac{1}{2})$

along dimensionless time with different Ra. Due to the computation cost the highest Ra studied is equal to 1720 and the convective flow obtained is still periodic.

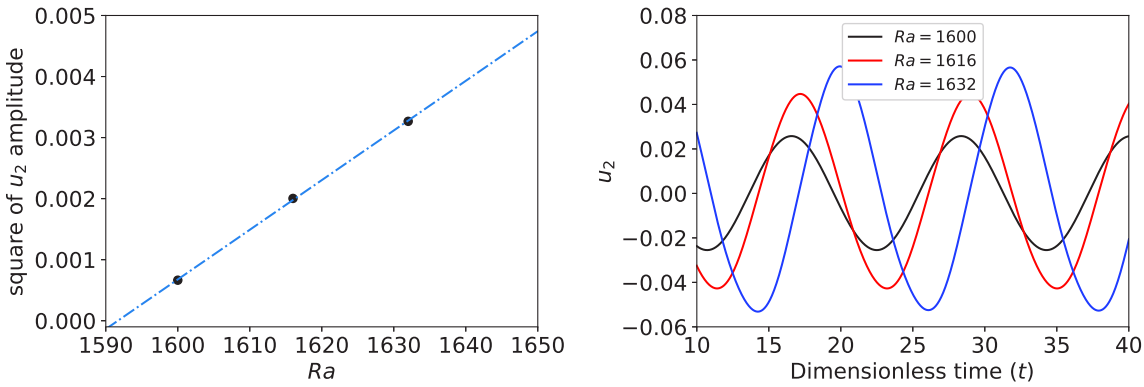

(A) (B)

FIGURE 6.4: (A) The square of u_2 amplitude at monitoring point $P1(\frac{1}{2}, \frac{1}{2}, \frac{1}{2})$ as a function of Ra. (B) time evolution of u_2 at $P1(\frac{1}{2}, \frac{1}{2}, \frac{1}{2})$ at three different Ra.

In order to assess the effects of the mesh size and timestep size on the results, the time step and grid independence for viscoelastic Rayleigh-Bénard convection have been investigated based on a careful analysis of three time steps ($\Delta t = 0.5E-3, 0.1E-2, 0.2E-2$) and four uniform mehses ($N_x \times N_y \times N_z = 64 \times 32 \times 32, 96 \times 48 \times 48, 128 \times 64 \times 64, 160 \times 80 \times 80$). The Rayleigh number are fixed at $Ra = 1600$. The detailed settings of $(\Delta t, \Delta x)$ and the results obtained are given in Tab. 6.1.

Num.	Δt	$N_x \times N_y \times N_z$	Nu_s	λ	v_{max}	$\tau_{22\ max}$	T_{max}
t1m1	0.002	$64 \times 32 \times 32$	1.00234	11.702	0.02444	0.00448	0.02116
$\phi_{(\%)}$			0.05	0.47	4.82	3.44	2.03
t2m1	0.001	$64 \times 32 \times 32$	1.00280	11.750	0.02560	0.00462	0.02152
$\phi_{(\%)}$			0.004	0.068	0.311	0.431	0.370
t3m1	0.0005	$64 \times 32 \times 32$	1.00284	11.758	0.02568	0.00472	0.02160
$\phi_{(\%)}$			–	–	–	–	–
t2m2	0.001	$96 \times 48 \times 48$	1.00286	11.754	0.02566	0.00466	0.02156
$\phi_{(\%)}$			0.006	0.033	0.310	1.271	0.185
t2m3	0.001	$128 \times 64 \times 64$	1.00290	11.762	0.02570	0.00468	0.02158
$\phi_{(\%)}$			0.00199	0.0169	0.155	0.8474	0.0925
t2m4	0.001	$160 \times 80 \times 80$	1.00292	11.762	0.02574	0.00472	0.02160
$\phi_{(\%)}$			–	–	–	–	–

TABLE 6.1: Simulation cases for time step and mesh independence. N_x, N_y and N_z are the number of grid points in x, y, and z directions, respectively. The rheology parameters in test cases are $Ra = 1600$, $Pr = 7.0$, $\beta = 0.2$, $We = 0.1$, $\epsilon = 0.1$ and $\xi = 0.05$. λ is the time period of reversal convection. The monitor point is fixed at $P(\frac{1}{2}, \frac{1}{2}, \frac{1}{2})$.

The monitoring variables in the Tab. 6.1 are averaged Nusselt number at the heating boundary Nu_s, time period λ, peak value of the velocity, normal stress and temperature (v, τ_{22}, T) at

monitoring point ($P(\frac{1}{2}, \frac{1}{2}, \frac{1}{2})$), respectively. The cases (t1m1, t2m1, t3m1) are used to examine the time step independence by comparing the relative error with the reference case (t4m1), the relative error is calculated by, for example, $\phi_{Nu_{t1m1}} = (Nu_{t1m1} - Nu_{t3m1})/Nu_{t3m1}$. The cases (t3m1, t3m2, t3m3, t3m4) are used to examine the mesh independence by compare the relative error with the reference case (t2m4). It is easy to find that when the number of grids exceeds $128 \times 64 \times 64$ and the time step is smaller than $\Delta t = 0.001$, the relative error of the result is extremely small (less than 0.43% for time step and 0.85% for mesh), so the further simulations performed still use this setting.

A comparison of 2D and 3D results of visocelastic RBC with PTT model will be presented in this part. Due to the time-consuming of 3D calculation, the 3D results obtained are limited. For the test case, the relevant parameters are as follows: $Pr = 7.0$, $Ra = 1600$, $\beta = 0.2$, $We = 0.1$ and $\epsilon = 0.1$. The aspect ratios of 2D and 3D configurations are $((L_x : H) = 2 : 1)$ and $(L_x : L_y : H = 2 : 1 : 1)$, respectively.

spatio-temporal evolution of velocity and temperature

As mentioned earlier, there are two different flow states within the parameters studied in a 2D horizontal cavity, namely: steady convection and oscillating reversal convection. In these flows, the convective cell is closed, the fluid can only circulate in its own cell, and the cell will not move in the horizontal direction, as described in Fig. 4.5 and Fig. 4.6.

However, when the same parameters are set in 3D cases, a new and interesting phenomenon appears: Travelling wave. In Newtonian fluid 3D RBC and cylindrical liquid bridge viscoelastic 3D RBC system (Lappa, 2011), the bifurcation of the critical mode will also lead to similar phenomena. For intuitive understanding, Fig. 6.5 plots the isosurface of velocity scale colored by $y-$ velocity at key time-points for the 3D cases in one period. The minimum E take place at $t = (b, b*)$, when they are two rolls in the domain.

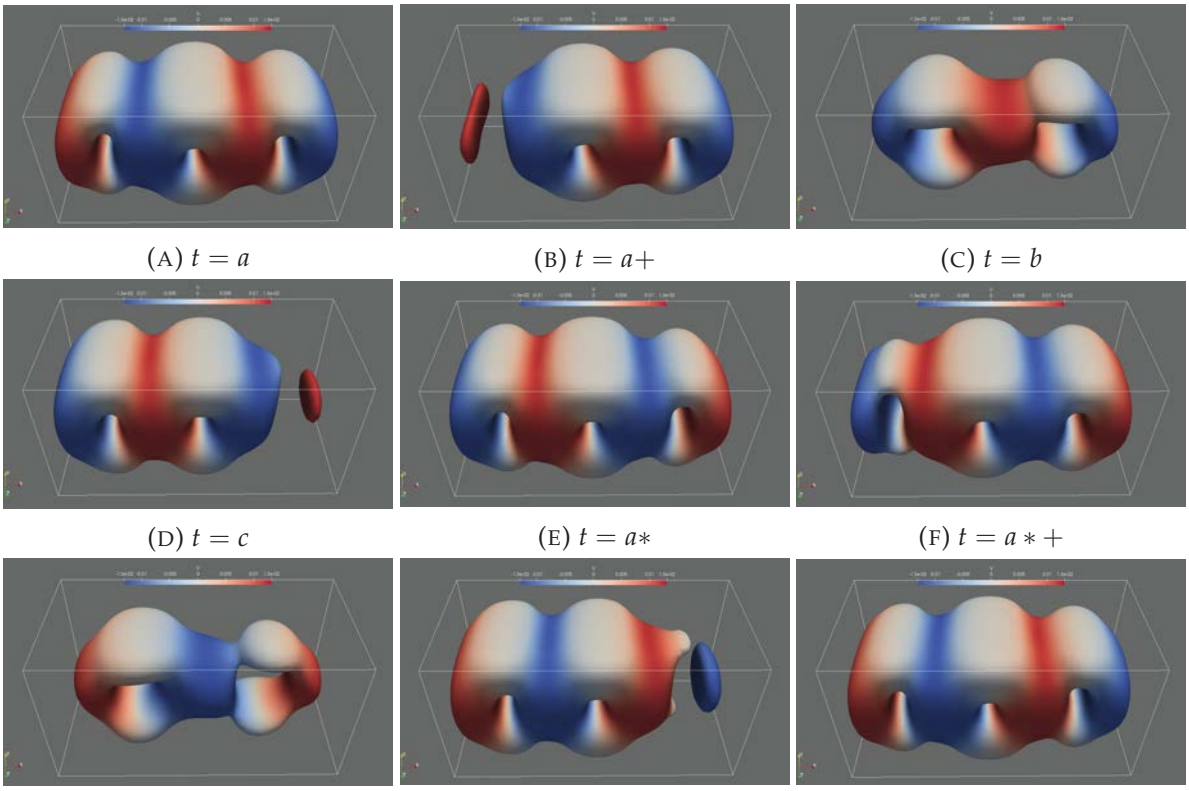

(A) $t = a$ (B) $t = a+$ (C) $t = b$

(D) $t = c$ (E) $t = a*$ (F) $t = a* +$

(G) $t = b*$ (H) $t = c*$ (I) $t = a$

FIGURE 6.5: The isosurfaces of velocity $\sqrt{u^2 + v^2 + w^2} = 0.012$ colored by $y-$ velocity at key time-points in one period. The parameters are $Ra = 1600$, $Pr = 7.0$, $We = 0.1$, $\beta = 0.2$, $\epsilon = 0.1$ and $\xi = 0.05$.

Fig. 6.6 plots the components of the velocity $\boldsymbol{U}$ at the clip planes yz and xz, when $t = a$. Fig. 6.6a-6.6f show the (u, v) contours in the yz planes at $x = 0.5, 1.0, 1.5$. w contours are not shown because it is really weak. Combining with Fig. 6.5, we can find that w is almost zero in the domian, and the reverse is a kind of qusi-2D flow. By monitoring the evolution of a variable with time to draw its spatio-temporal contour, it is possible to clearly distinguish the difference between the oscillating reversal convection and the traveling convection, Fig. 6.7 displays the time evolution of the vertical velocity v and the temperature T on the horizontal section $y = 1/2$ for 2D case and $(y, z) = (y = 1/2, z = 1/2)$ for 3D case.

When the flow is 2D periodic reversal convection, as shown in Fig. 6.7a-6.7b, the spatio-temporal contours of temperature and velocity are regular periodic structures, the peaks and troughs of the detection variables appear alternately. It is especially important to note that the phase of temperature and velocity has not moved in the space evolution: the spatial position between the main convective cells has not changed.

However, when looking at 3D viscoelastic RBC, a completely different spatio-temporal evolution is discovered, it is in a traveling wave state, as shown in Fig.6.7c and 6.7d. The pattern is some inclined wave-like periodic curves, which indicates that the position of the convective cell in the horizontal direction has changed over time. The moving speed can be obtained by calculating the slope of the curve ($u_t = \Delta x/\Delta t$, Δx is the distance moved within Δt). From Fig. 6.7d,

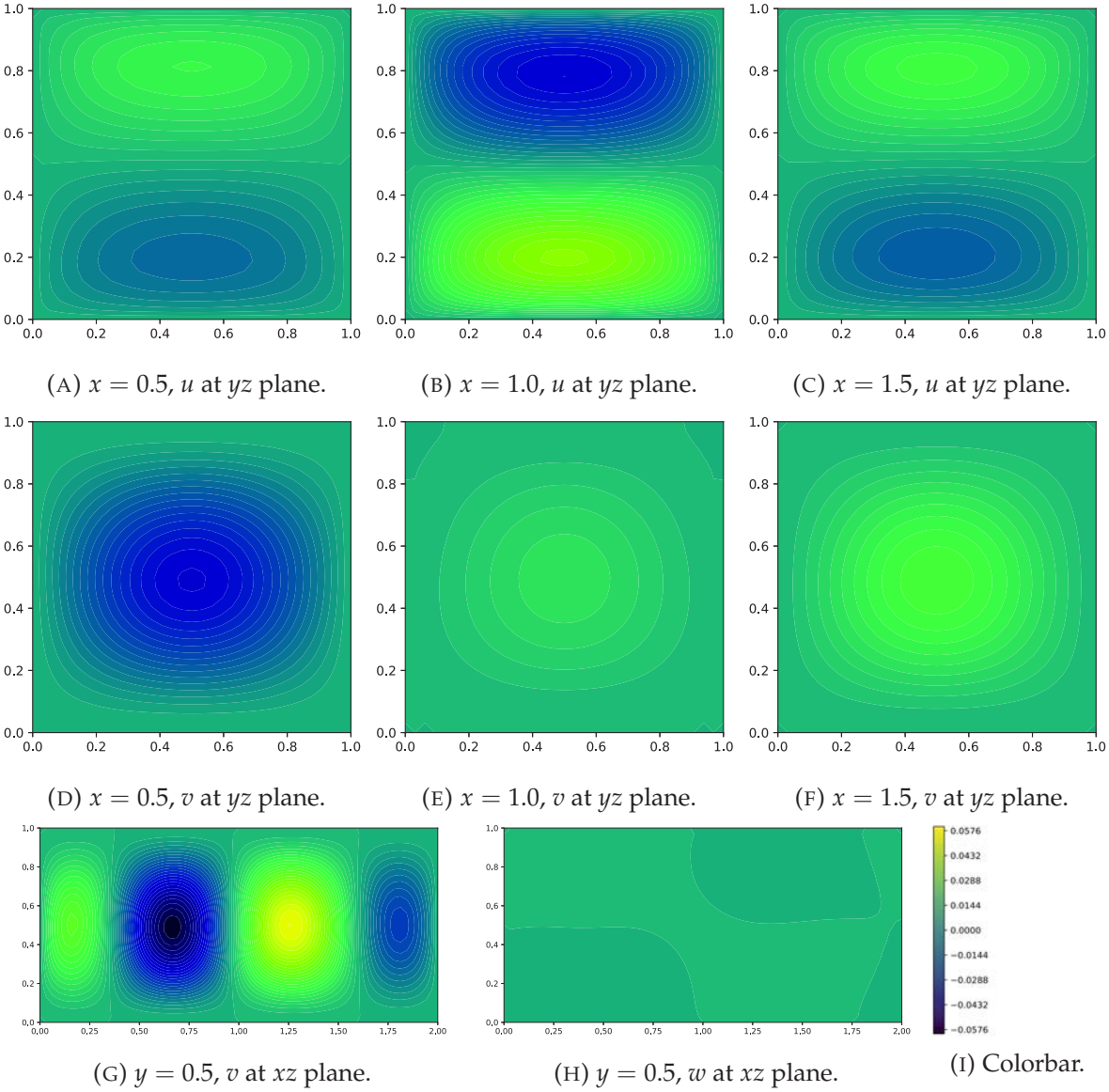

(A) $x = 0.5$, u at yz plane. (B) $x = 1.0$, u at yz plane. (C) $x = 1.5$, u at yz plane.

(D) $x = 0.5$, v at yz plane. (E) $x = 1.0$, v at yz plane. (F) $x = 1.5$, v at yz plane.

(G) $y = 0.5$, v at xz plane. (H) $y = 0.5$, w at xz plane. (I) Colorbar.

FIGURE 6.6: The components of the velocity $\boldsymbol{U}$ at the clip planes yz and xz, when $t = a$.

we found that the moving direction of the travelling vortex is leftward, the new vortex is generated from right side wall and the older vortex is annihilated at left side. In fact, in the study of Lappa (2011), it was discovered that traveling wave convection could change the direction of traveling. Experimentally, Metivier et al. (2020) gave an impressed results for the oscillating viscoelastic RBC with Carbopol gel (the maxwell model). A very intuitive velocity vector diagram of reversal convection are given for different yield stress cases, and they discussed the effect of elasticity on reverse.

Fig. 6.8 shows the Nusselt number changes along time for 2D standing vortices and 3D travelling vortices. We can find that there is a huge difference in the values of Nu amplitude between 2D standing vortices and 3D travelling vortices, and the time period of the traveling vortices is smaller than that in 2D case. Furthermore, Figs. (6.9a-6.9d) depict the y-velocity and

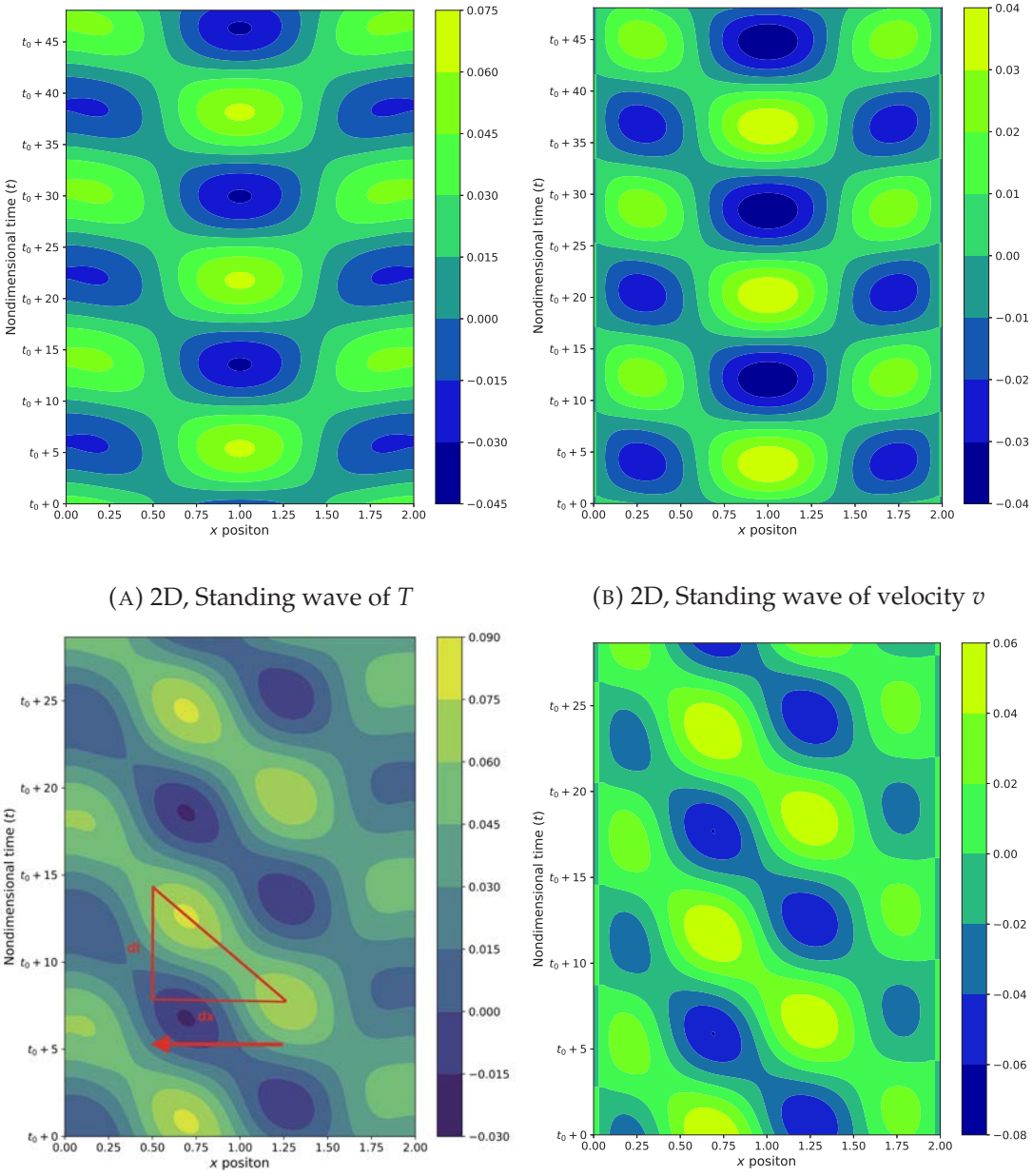

(A) 2D, Standing wave of T

(B) 2D, Standing wave of velocity v

(C) 3D, Traveling wave of T

(D) 3D, Traveling wave of velocity v

FIGURE 6.7: Spatio-temporal evolution of temperature (left) and v-velocity (right) at central horizontal cross line for 2D (up) and 3D (bottom) conditon. (A, B) standing wave; (C, D) traveling wave at clip of $y = 1/2$.

temperature contour for 2D and 3D (at middle surface with $y = 1/2$), when averaged Nusselt number arrived at the peak value.

Energy transport

Fig. 6.10 depicts the energies transport between different energy forms for 2D and 3D conditions with $Pr = 7.0$ $We = 0.1$, $\beta = 0.2$, $\epsilon = 0.1$ and $\xi = 0.05$. The reverse is standing wave in 2D

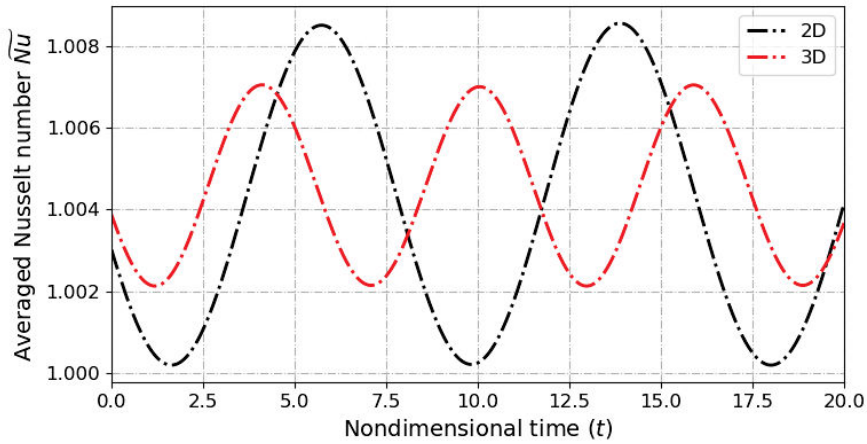

FIGURE 6.8: Averaged Nu changes along time for 2D and 3D with $Ra = 1.01Rac1$.

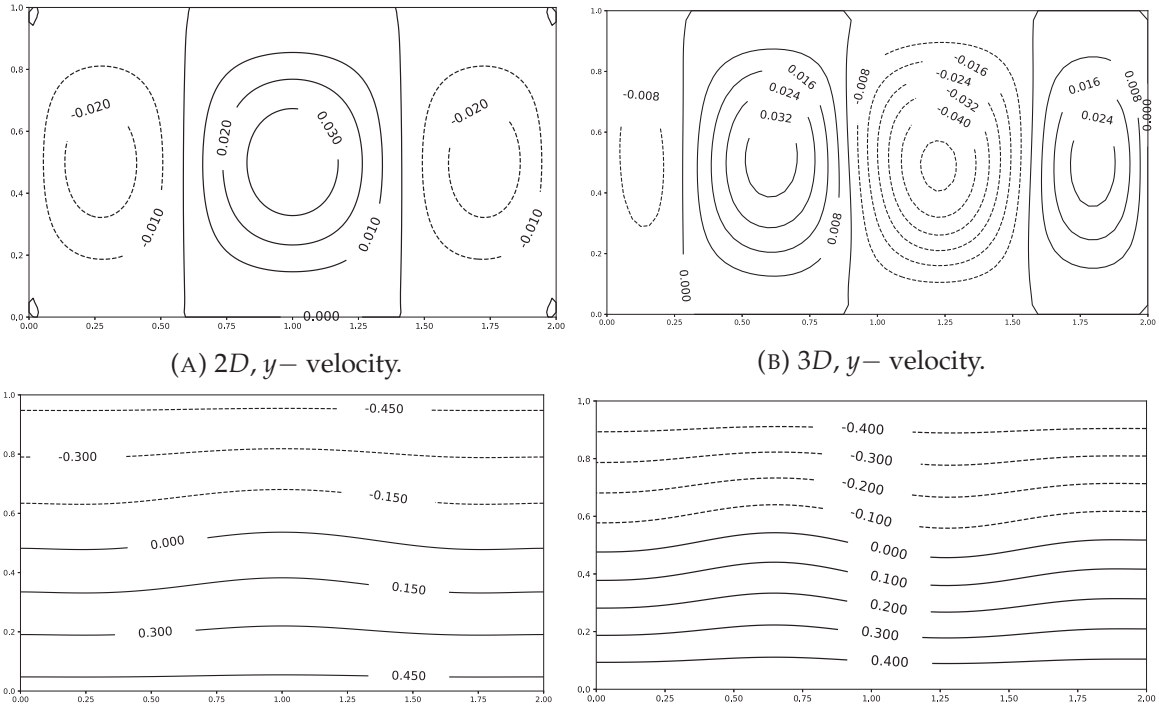

(A) $2D$, $y-$ velocity.

(B) $3D$, $y-$ velocity.

(C) $2D$, temperature

(D) $3D$, temperature

FIGURE 6.9: Contours of the $y-$ velocity and the temperature for 2D (A and C), and for 3D at $x-z$ plane with $y = \frac{L_y}{2}$ (B and D), when spatially averaged Nu arived at peak value.

(Fig. 6.10a) and is travelling wave in 3D (Fig. 6.10b).

In the figure, the (——) corresponding to global kinetic energy ($\langle E \rangle_\omega$); the (——) corresponding to kinetic diffusion ($\langle \Phi_D \rangle_\omega$); the (——) corresponding to buoyancy flux input ($\langle \Phi_F \rangle_\omega$); the (——) corresponding to bulk viscous dissipation of kinetic energy ($\langle \Phi_V \rangle_\omega$); and the (——) corresponding to energy exchange between flow structures and polymer microstructures due to the stretching and relaxation of polymer chains ($\langle \Phi_G \rangle_\omega$). For 2D periodic reversal convection described in detail in Chapter. 4, we know that there is a process of elastic force dragging and then

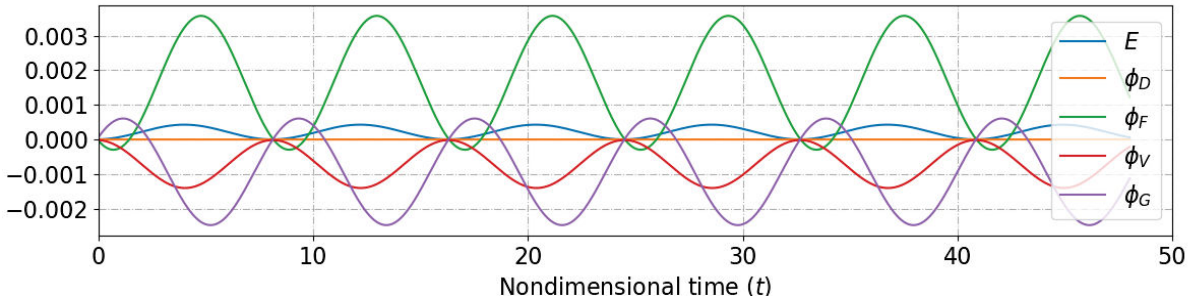

(A) 2D standing reversal convection

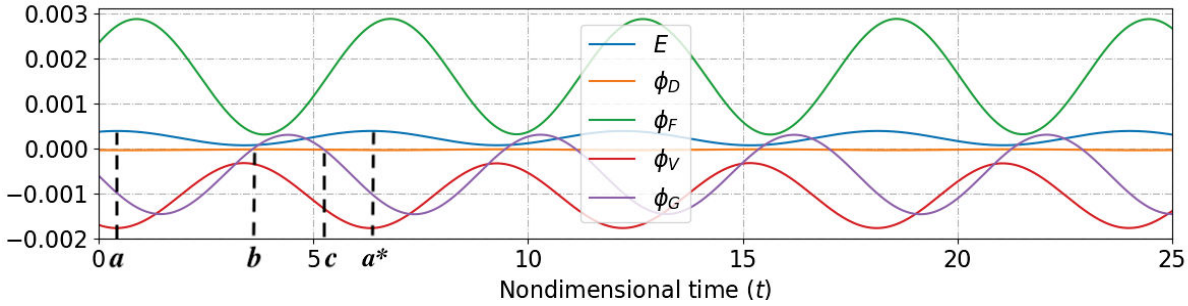

(B) 3D convection with travelling wave.

FIGURE 6.10: Time evolution of energy transport for 2D and 3D convection when $We = 0.1$, $\beta = 0.2$ and $\epsilon = 0.1$. (A) corresponding to 2D stable convection; (B) corresponding to 2D periodic reversal convection; (C) corresponding to 3D convection with travelling wave.

promoting the flow in the flow reversal. This process is mainly reflected in the time difference between the peak value of E (positive), Φ_G (positive) and Φ_F (negative). Obviously, the process of elastic force acting on the flow structure also appears in 3D traveling convection, which even plays a greater role in promoting the development of traveling convection, as shown in Fig. 6.10b. Owing to the higher frequency of new vortices generation (frequency can be observed in Fig. 6.10b) and more complicated interactions between the vortices and boundaries, the viscous dissipation ratio is significantly increased in 3D traveling convection.

Comparing Fig. (6.10a-6.10b), the negative work of Φ_F vanish in 3D cases, therefore, there is no the time point d (when Φ_F crosses the zero value from negative to positive). In 3D, $\langle \Phi_F \rangle > 0$ means that the buoyancy is always a source term. The fact that Φ_G become positive both in 2D and 3D cases means that Φ_G acts during most of the time as a dissipation term but as a source term for a short time (from b to c). Through comparing energy transition process in 2D and 3D, we remark four key time-points ($a - b - c - a^*$) in the half period of reverse, as shown in Fig. 6.10b. In the time line, a and a^* present the time points of kinetic energy peak value with opposite velocity directions, b and c present the time point where Φ_G crosses the zero value from negative value to positive value and from positive value to negative value.

We know that the 3D travelling reverse is a kind of quasi-2D reverse, Fig. 6.11 plots contours of E, T, Φ_G and Φ_F for 3D reversal convection at xz plane with $y = 0.5$ in a half period. In order to easily compare with the 2D reverse, the colored boxes mark the characteristic areas of the reversal convection process, especially the spatial and temporal distribution of the kinetic

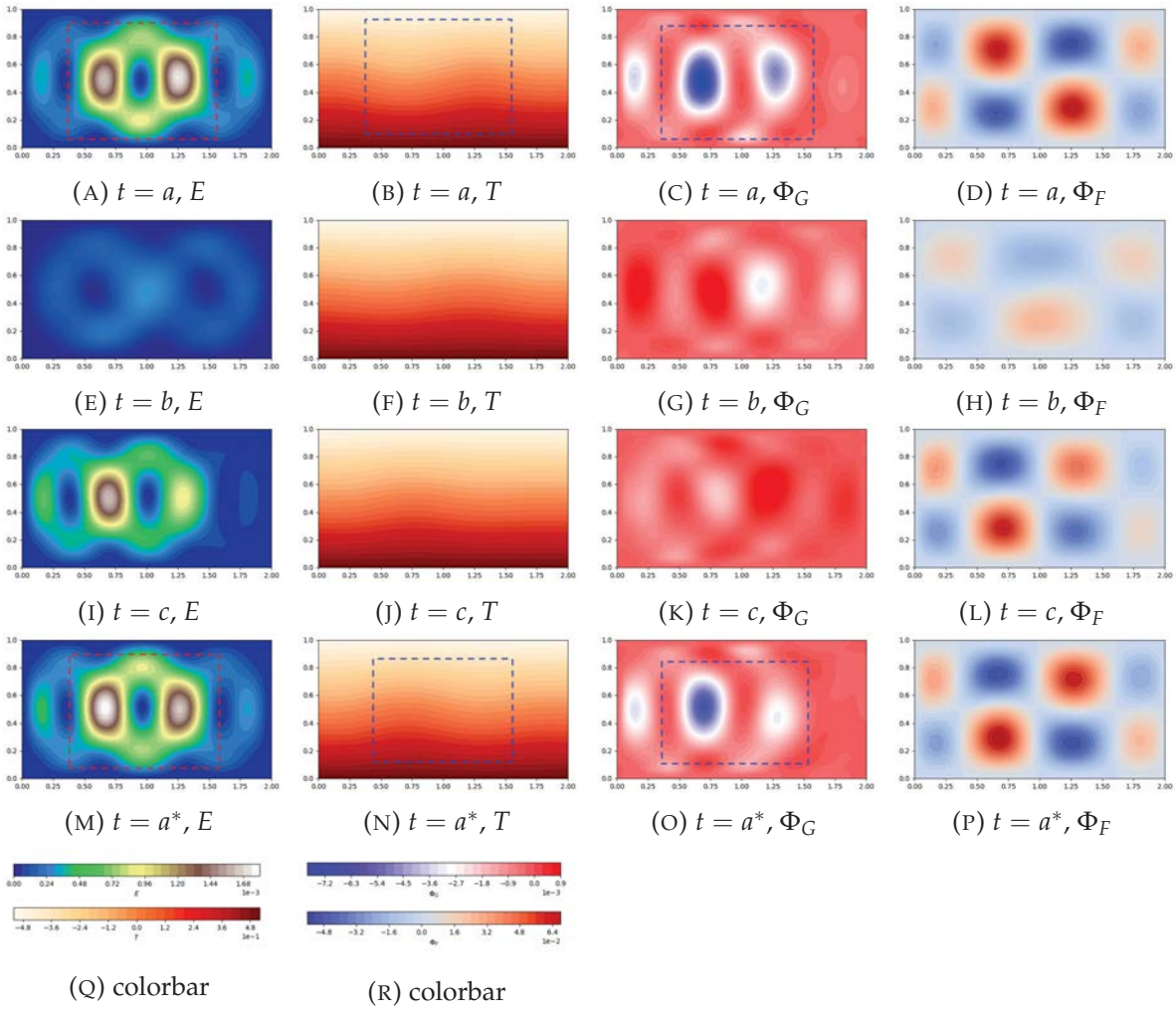

(A) $t = a, E$ (B) $t = a, T$ (C) $t = a, \Phi_G$ (D) $t = a, \Phi_F$

(E) $t = b, E$ (F) $t = b, T$ (G) $t = b, \Phi_G$ (H) $t = b, \Phi_F$

(I) $t = c, E$ (J) $t = c, T$ (K) $t = c, \Phi_G$ (L) $t = c, \Phi_F$

(M) $t = a^*, E$ (N) $t = a^*, T$ (O) $t = a^*, \Phi_G$ (P) $t = a^*, \Phi_F$

(Q) colorbar (R) colorbar

FIGURE 6.11: The contours of E, T, Φ_G and $T\Phi_F$ at four key time-points ($a - b - c - a^*$) for the 3D cases with parameters $Ra = 1600$, $Pr = 7.0$, $We = 0.1$, $\beta = 0.2$, $\epsilon = 0.1$ and $\xi = 0.05$.

energy E, T and Φ_G. We can find that the E, T, and Φ_G fields in 2D (Figs. 4.18-4.19) and 3D cases show highly consistent behavior at the key time points.

6.4 Conclusion

The aim of this chapter is to introduce the preliminary work on 3D viscoelastic Rayleigh-Bénard convection, we extended the solver to have a capacity for solving 3D Newtonian and viscoelastic Rayleigh-Bénard convection. The capability and accuracy of the solver were tested by a benchmark case of 3D Newtonian Rayleigh-Bénard convection, and compared with the result of Pallares, Grau, and Giralt (1999). Independence of time step and grid also was checked for 3D viscoelastic Rayleigh-Bénard convection. Finally, we show the difference of energy evolution between 3D viscoelastic RBC with traveling-wave convection and 2D Rayleigh-Bénard convection with standing wave. Obviously, there needs more work on 3D Rayleigh-Bénard convection due to the need of important computing resources.

Chapter 7

Conclusions and perspectives

Conclusions

The objective of this thesis includes two main parts. The first part is to develop a direct numerical simulation (DNS) solver for the viscoelastic laminar Rayleigh-Bénard convection in 2D/3D rectangular cavities. The second part is to numerically study the flow and heat transfer characteristics in viscoelastic laminar RBC based on the in-house solver.

In Chapter 1 and Chapter 2, we introduced the background of this thesis and state-of-the-art of the viscoelastic Rayleigh-Bénard convection. In Chapter 3, the numerical procedure of the solver is introduced, accuracy and capacity of the solver for studying viscoelastic RBC are investigated. In Chapter 4, the 2D viscoelastic Rayleigh-Bénard convection with PTT model was investigated in a $2:1$ cavity for different $(\epsilon, \xi, \beta, We)$. Following the idea of Chapter 4, the viscoelastic RBC in an inclined cavity was studied in Chapter 5. Finally, in Chapter 6 we extended the solver to 3D, because important computing resources were needed, we only simulated a few cases to investigate the flow structure of viscoelastic RBC in 3D.

Based on the above works, the following conclusions are obtained:

1. A direct numerical simulation solver that can simulate 2D and 3D viscoelastic Rayleigh-Béanrd convection is developed. This solver includes a variety of time and space discrete schemes, and also covers a variety of constitutive models of viscoelastic fluids (such as the Oldroyd-B, Giesekus, PTT model). Then the accuracy and capacity of this solver are verified for viscoelastic Rayleigh-Béanrd convection flow.

2. The influence of rheology parameters $(\beta, We, \epsilon, \xi)$ on the critical Rayleigh number of convection onset $Rac1$ in horizontal 2D viscoelastic (PTT model) RBC with an aspect ratio of $2:1$ was investigated. The flow pattern selection for the onset of RBC strongly depends on the rheology parameters (We and β), steady-state convection takes place when We is small and β is big, but, a regular reversal takes place when We is big and β is small. The results show that the elasticity and concentration of the viscoelastic fluids all make $Rac1$ decrease for oscillating convection.

3. Through the study of the influence of elasticity and concentration on reverse convection, it is found that the relationship between reversal frequency and Ra has two opposite trends

for the Oldroyd model (negative) and PTT model (positive). With increasing Ra the PTT model leads to the existence of a second critical Rayleigh number $Rac2$, which makes the flow transition from periodic reverse convection to steady-state convection. At the same time, the results show that both elasticity and concentration will reduce $Rac2$.

4. For 2D viscoelastic RBC, compared with steady-state convection there will be more system energy dissipation in time-periodic reversal convection, due to the continuous stretching and contraction process of polymer molecules in the fluid. When the Rayleigh number exceeds $Rac2$, the convection flow is always with 2 rolls, and the heat transfer capacity shows more non-linear behavior with Ra. For the reverse convection with 2-roll and 3-roll, the Ra domain of the 3-roll case is often larger, which also means that solution branch of 3-roll periodic reversal convection, will enter the steady-state convection at higher Ra compared to the 2-roll branch.

5. For 2D tilted viscoelastic RBC, we focused on the flow and heat transfer in the case with strong elasticity, because the cases with weak elasticity do not show much difference from those with a Newtonian fluid. The flow and heat transfer with strong elasticity will have a huge change, even if there is a small inclined angle. In the cases we simulated, this angle is less than 1°. The periodic reversal convection still exists in strong elastic RBC, depending on the inlined angle. When inlined angle exceeds a critial value, reverse will vanish and only steady-state convection exists.

6. For the numerical simulation of the 3D viscoelastic RBC, due to the limitation of computational resources and time, we only verified the solving ability and accuracy of the solver and simulated the cases under certain parameters to compare the results with the 2D situation. The important conclusion is that the 3D reversal is due to traveling wave instead of standing wave in 2D cases.

Perspectives

The current solver does not cover parallel calculations in the solution process for three-dimensional viscoelastic Rayleigh-Bénard convection. In the next stage, it would be interesting to optimize the calculation speed of the solver, using openMP and MPI.

In the present work, we have done a lot of research on the time period reversal viscoelastic Rayleigh-Bénard convection in horizontal and inclined two-dimensional rectangular cavities and a three-dimensional cavity. The main content includes the discovery of the threshold of fluid state transitions and the description of reversal formation. However, there is still a lot of work worthy of in-depth study:

1. Since the main purpose of this article is to elaborate on the problem of regular reversal convection in the strong elasticity viscoelastic RBC, it mainly discusses the influence of the relative rheological parameters of the particular viscoelastic fluid model (PTT model)

on the flow and heat transfer. Obviously, this is not enough for a more comprehensive understanding of this reversal phenomenon, so we should consider more relevant parameters, such as Prandtl number, the aspect ratio of geometric shapes, etc.
In fact, the present work on viscoelastic RBC is devoted to $Pr = 7$ due to the existing studies available in the literature. Experimentally speaking, most of viscoelastic fluids are water solutions of polymers, surfactants, etc. and viscoelastic behavior is mainly due to increased viscosity compared to that of water while the corresponding thermal conductivity, specific heat and density of the solutions remain to be more or less the same as water. In this sense most of viscoelastic fluids have much bigger Prandtl numbers. In order to experimentally check the existence of convection reversal observed in the present work and design experimental studies, it will be crucial to explore higher Prandtl number cases

2. Viscoelastic RBC flow has extremely rich flow states, in this work we only explored a small part of them. More flow transitions need to be studied.

3. The research on the viscoelastic RBC within the 3D finite domain is just the beginning. There is still much work to do in the future, such as exploring the flow patterns transition under strong elasticity, the influence of rheological parameters on flow heat transfer, and so on.

Appendix A

Coefficient matrix for quasi-linear terms

Due to space reasons, the coefficient matrix of governing equations after quasi-linearization is not given in Chapter 3 of the main part of thesis. Here I will show this process in detail. The dimensionless governing equations for viscoelastic RBC system are:

$$\nabla \cdot u = 0 \tag{A.1}$$

$$\frac{\partial u}{\partial t} + (u \cdot \nabla)u = -\nabla p + \beta \frac{Pr}{\sqrt{Ra}} \Delta u + \nabla \cdot \tau + PrTe_z \tag{A.2}$$

$$\frac{\partial T}{\partial t} + (u \cdot \nabla)T = \frac{1}{\sqrt{Ra}} \triangle T \tag{A.3}$$

$$\frac{\partial \tau}{\partial t} + (u \cdot \nabla)\tau - \nabla u^T \cdot \tau - \tau \cdot \nabla u + \frac{1}{We}\tau - 2\frac{1-\beta}{Ma^2} D = \boldsymbol{S} \tag{A.4}$$

where $\boldsymbol{S}$ are the source term, as depicted in:

$$\boldsymbol{S} = \begin{cases} 0 & \textbf{(Oldroyd-B model)} \\ -\alpha \frac{\sqrt{Ra}}{(1-\beta)Pr} \tau^2 & \textbf{(Giesekus model)} \\ -\epsilon \frac{\sqrt{Ra}}{(1-\beta)Pr} tr(\tau)\tau - \xi(D\tau + \tau D) & \textbf{(PTT model)} \end{cases} \tag{A.5}$$

In numerical process mass conservation is coupled in the momentum equation, and reoranized the momentum equation and viscoelastic constitutive equation into a quasi-linear system by separating the homogeneous part and the source term:

$$\frac{\partial W}{\partial t} + \sum_{i=1}^{n} A_i \frac{\partial W}{\partial x_i} = S_{ql} \tag{A.6}$$

where S_{ql} is the sorce term as introduced in Chapter 3; $n = 2$ and $n = 3$ for two or three dimension cases, respectively. Correspondingly, the variables verctar are $W = [u_1, u_2, \tau_{11}, \tau_{12}, \tau_{22}]$ (for 2D) and $W = [u_1, u_2, u_3, \tau_{11}, \tau_{12}, \tau_{13}, \tau_{22}, \tau_{23}, \tau_{33}]$ (for 3D). And follow Sec. 3.3.3, we can rewrite A_i as $A_i = L_i \Lambda_i R_i$, where Λ_i is a diagonal matrix containing the eigenvalues of A_i. L_i is the matrix formed by the eigenvectors of A_i and R_i is the inverse of L_i. The convective terms of the Eq.A.6 can then be transformed into $A_i \frac{\partial W}{\partial x_i} = L_i \Lambda_i \frac{\partial R_i W}{\partial x_i}$. In following, I will introduce the coefficient maxtrixs $\boldsymbol{A_i}$ and corresponding matrix (L_i, Λ_i and R_i) for 2D and 3D separatly. The eigenvalue vector Λ_i and eigenvector matrix R_i are calculated by a Maxima application

("Maxima, a Computer Algebra System"), which a system for the manipulation of symbolic and numerical expressions.

A.1 For 2D cases

The coefficient matrix in x_1 direction:

$$A_1 = \begin{pmatrix} u_1 & 0 & -1 & 0 & 0 \\ 0 & u_1 & 0 & -1 & 0 \\ -2(\frac{1-\beta}{Ma^2}+\tau_{11}) & 0 & u_1 & 0 & 0 \\ -\tau_{12} & -(\frac{1-\beta}{Ma^2}+\tau_{11}) & 0 & u_1 & 0 \\ 0 & -2\tau_{12} & 0 & 0 & u_1 \end{pmatrix} \tag{A.7}$$

$$L_{A_1} = \begin{pmatrix} 1 & 1 & 0 & 0 & 0 \\ 0 & 0 & 1 & 1 & 0 \\ \sqrt{2}\sqrt{\tau_{11}+\frac{1-\beta}{Ma^2}} & -\sqrt{2}\sqrt{\tau_{11}+\frac{1-\beta}{Ma^2}} & 0 & 0 & 0 \\ 0 & 0 & \sqrt{\tau_{11}+\frac{1-\beta}{Ma^2}} & -\sqrt{\tau_{11}+\frac{1-\beta}{Ma^2}} & 0 \\ 0 & 0 & \frac{2\tau_{12}}{\sqrt{\tau_{11}+\frac{1-\beta}{Ma^2}}} & -\frac{2\tau_{12}}{\sqrt{\tau_{11}+\frac{1-\beta}{Ma^2}}} & 1 \end{pmatrix} \tag{A.8}$$

$$\Lambda_1 = \begin{pmatrix} u_1 - \sqrt{2(\tau_{11}+\frac{1-\beta}{Ma^2})} \\ u_1 + \sqrt{2(\tau_{11}+\frac{1-\beta}{Ma^2})} \\ u_1 - \sqrt{\tau_{11}+\frac{1-\beta}{Ma^2}} \\ u_1 + \sqrt{\tau_{11}+\frac{1-\beta}{Ma^2}} \\ u_1 \end{pmatrix} \tag{A.9}$$

$$R_{A_1} = \begin{pmatrix} \frac{1}{2} & 0 & \frac{1}{2\sqrt[2]{2}\sqrt{\tau_{11}+\frac{1-\beta}{Ma^2}}} & 0 & 0 \\ \frac{1}{2} & 0 & -\frac{1}{2\sqrt[2]{2}\sqrt{\tau_{11}+\frac{1-\beta}{Ma^2}}} & 0 & 0 \\ 0 & \frac{1}{2} & 0 & \frac{1}{2\sqrt{\tau_{11}+\frac{1-\beta}{Ma^2}}} & 0 \\ 0 & \frac{1}{2} & 0 & -\frac{1}{2\sqrt{\tau_{11}+\frac{1-\beta}{Ma^2}}} & 0 \\ 0 & 0 & 0 & -\frac{2\tau_{12}}{\tau_{11}+\frac{1-\beta}{Ma^2}} & 1 \end{pmatrix} \tag{A.10}$$

The coefficient matrix in x_2 direction:

$$A_2 = \begin{pmatrix} u_2 & 0 & 0 & -1 & 0 \\ 0 & u_2 & 0 & 0 & -1 \\ -2\tau_{12} & 0 & u_2 & 0 & 0 \\ -(\frac{1-\beta}{Ma^2}+\tau_{22}) & -\tau_{12} & 0 & u_2 & 0 \\ 0 & -2(\frac{1-\beta}{Ma^2}+\tau_{22}) & 0 & 0 & u_2 \end{pmatrix} \tag{A.11}$$

$$L_{A_2} = \begin{pmatrix} 0 & 0 & 1 & 1 & 0 \\ 1 & 1 & 0 & 0 & 0 \\ 0 & 0 & \frac{2\tau_{12}}{\sqrt{\tau_{22}+\frac{1-\beta}{Ma^2}}} & -\frac{2\tau_{12}}{\sqrt{\tau_{22}+\frac{1-\beta}{Ma^2}}} & 1 \\ 0 & 0 & \sqrt{\tau_{22}+\frac{1-\beta}{Ma^2}} & -\sqrt{\tau_{22}+\frac{1-\beta}{Ma^2}} & 0 \\ \sqrt{2}\sqrt{\tau_{22}+\frac{1-\beta}{Ma^2}} & -\sqrt{2}\sqrt{\tau_{22}+\frac{1-\beta}{Ma^2}} & 0 & 0 & 0 \end{pmatrix} \tag{A.12}$$

$$\Lambda_2 = \begin{pmatrix} u_2 - \sqrt{2(\tau_{22}+\frac{1-\beta}{Ma^2})} \\ u_2 + \sqrt{2(\tau_{22}+\frac{1-\beta}{Ma^2})} \\ u_2 - \sqrt{\tau_{22}+\frac{1-\beta}{Ma^2}} \\ u_2 + \sqrt{\tau_{22}+\frac{1-\beta}{Ma^2}} \\ u_2 \end{pmatrix} \tag{A.13}$$

$$R_{A_2} = \begin{pmatrix} 0 & \frac{1}{2} & 0 & 0 & \frac{1}{2^{\frac{3}{2}}\sqrt{\tau_{22}+\frac{1-\beta}{Ma^2}}} \\ 0 & \frac{1}{2} & 0 & 0 & -\frac{1}{2^{\frac{3}{2}}\sqrt{\tau_{22}+\frac{1-\beta}{Ma^2}}} \\ \frac{1}{2} & 0 & 0 & \frac{1}{2\sqrt{\tau_{22}+\frac{1-\beta}{Ma^2}}} & 0 \\ \frac{1}{2} & 0 & 0 & -\frac{1}{2\sqrt{\tau_{22}+\frac{1-\beta}{Ma^2}}} & 0 \\ 0 & 0 & 1 & -\frac{2\tau_{12}}{\tau_{11}+\frac{1-\beta}{Ma^2}} & 0 \end{pmatrix} \tag{A.14}$$

A.2 For 3D cases

The coefficient matrix in x_1 direction, and in order to facilitate the display, we define $H = \sqrt{\frac{1-\beta}{Ma^2}+\tau_{11}}$:

$$A_1 = \begin{pmatrix} u_1 & 0 & 0 & -1 & 0 & 0 & 0 & 0 & 0 \\ 0 & u_1 & 0 & 0 & -1 & 0 & 0 & 0 & 0 \\ 0 & 0 & u_1 & 0 & 0 & -1 & 0 & 0 & 0 \\ -2H^2 & 0 & 0 & u_1 & 0 & 0 & 0 & 0 & 0 \\ -\tau_{12} & -H^2 & 0 & 0 & u_1 & 0 & 0 & 0 & 0 \\ -\tau_{13} & 0 & -H^2 & 0 & 0 & u_1 & 0 & 0 & 0 \\ 0 & -2\tau_{12} & 0 & 0 & 0 & 0 & u_1 & 0 & 0 \\ 0 & -\tau_{13} & -\tau_{12} & 0 & 0 & 0 & 0 & u_1 & 0 \\ 0 & 0 & -2\tau_{13} & 0 & 0 & 0 & 0 & 0 & u_1 \end{pmatrix} \tag{A.15}$$

$$L_1 = \begin{pmatrix} 1 & 1 & 0 & 0 & 0 & 0 & 0 & 0 & 0 \\ 0 & 0 & 1 & 0 & 1 & 0 & 0 & 0 & 0 \\ 0 & 0 & 0 & 1 & 0 & 1 & 0 & 0 & 0 \\ \sqrt{2}H & -\sqrt{2}H & 0 & 0 & 0 & 0 & 0 & 0 & 0 \\ 0 & 0 & H & 0 & -H & 0 & 0 & 0 & 0 \\ 0 & 0 & 0 & H & 0 & -H & 0 & 0 & 0 \\ 0 & 0 & 2\frac{\tau_{12}}{H} & 0 & -2\frac{\tau_{12}}{H} & 0 & 1 & 0 & 0 \\ -\frac{\tau_{23}}{H} & \frac{\tau_{23}}{\sqrt{2}H} & \frac{\tau_{13}}{H} & \frac{\tau_{12}}{H} & -\frac{\tau_{13}}{H} & -\frac{\tau_{12}}{H} & 0 & 1 & 0 \\ 0 & 0 & 0 & 2\frac{\tau_{13}}{H} & 0 & -2\frac{\tau_{13}}{H} & 0 & 0 & 1 \end{pmatrix} \tag{A.16}$$

$$\Lambda_1 = \begin{pmatrix} u_1 - \sqrt{2}H \\ u_1 + \sqrt{2}H \\ u_1 - H \\ u_1 - H \\ u_1 + H \\ u_1 + H \\ u_1 \\ u_1 \\ u_1 \end{pmatrix} \tag{A.17}$$

$$R_1 = \begin{pmatrix} \frac{1}{2} & 0 & 0 & \frac{1}{2^{\frac{3}{2}}H} & 0 & 0 & 0 & 0 & 0 \\ \frac{1}{2} & 0 & 0 & -\frac{1}{2^{\frac{3}{2}}H} & 0 & 0 & 0 & 0 & 0 \\ 0 & \frac{1}{2} & 0 & 0 & \frac{1}{2H} & 0 & 0 & 0 & 0 \\ 0 & 0 & \frac{1}{2} & 0 & 0 & \frac{1}{2H} & 0 & 0 & 0 \\ 0 & \frac{1}{2} & 0 & 0 & -\frac{1}{2H} & 0 & 0 & 0 & 0 \\ 0 & 0 & \frac{1}{2} & 0 & 0 & -\frac{1}{2H} & 0 & 0 & 0 \\ 0 & 0 & 0 & 0 & -2\frac{\tau_{12}}{H^2} & 0 & 1 & 0 & 0 \\ 0 & 0 & 0 & \frac{\tau_{23}}{2H^2} & -\frac{\tau_{13}}{H^2} & -\frac{\tau_{12}}{H^2} & 0 & 1 & 0 \\ 0 & 0 & 0 & 0 & 0 & -2\frac{\tau_{13}}{H^2} & 0 & 0 & 1 \end{pmatrix} \tag{A.18}$$

The coefficient matrix in x_2 direction with $H = \sqrt{\frac{1-\beta}{Ma^2} + \tau_{22}}$:

$$A_2 = \begin{pmatrix} u_2 & 0 & 0 & 0 & -1 & 0 & 0 & 0 & 0 \\ 0 & u_2 & 0 & 0 & 0 & 0 & -1 & 0 & 0 \\ 0 & 0 & u_2 & 0 & 0 & 0 & 0 & -1 & 0 \\ -2\tau_{12} & 0 & 0 & u_2 & 0 & 0 & 0 & 0 & 0 \\ -H^2 & -\tau_{12} & 0 & 0 & u_2 & 0 & 0 & 0 & 0 \\ -\tau_{23} & 0 & -\tau_{12} & 0 & 0 & u_2 & 0 & 0 & 0 \\ 0 & -2H^2 & 0 & 0 & 0 & 0 & u_2 & 0 & 0 \\ 0 & -\tau_{23} & -H^2 & 0 & 0 & 0 & 0 & u_2 & 0 \\ 0 & 0 & -2\tau_{23} & 0 & 0 & 0 & 0 & 0 & u_2 \end{pmatrix} \tag{A.19}$$

$$L_2 = \begin{pmatrix} 0 & 0 & 1 & 0 & 1 & 0 & 0 & 0 & 0 \\ 1 & 1 & 0 & 0 & 0 & 0 & 0 & 0 & 0 \\ 0 & 0 & 0 & 1 & 0 & 1 & 0 & 0 & 0 \\ 0 & 0 & 2\frac{\tau_{12}}{H} & 0 & -2\frac{\tau_{12}}{H} & 0 & 1 & 0 & 0 \\ 0 & 0 & H & 0 & -H & 0 & 0 & 0 & 0 \\ -\frac{\tau_{13}}{\sqrt{2}H} & \frac{\tau_{13}}{\sqrt{2}H} & \frac{\tau_{23}}{H} & \frac{\tau_{12}}{H} & -\frac{\tau_{23}}{H} & -\frac{\tau_{12}}{H} & 0 & 1 & 0 \\ \sqrt{2}H & -\sqrt{2}H & 0 & 0 & 0 & 0 & 0 & 0 & 0 \\ 0 & 0 & 0 & H & 0 & -H & 0 & 0 & 0 \\ 0 & 0 & 0 & 2\frac{\tau_{23}}{H} & 0 & -2\frac{\tau_{23}}{H} & 0 & 0 & 1 \end{pmatrix} \tag{A.20}$$

$$\Lambda_2 = \begin{pmatrix} u_2 - \sqrt{2}H \\ u_2 + \sqrt{2}H \\ u_2 - \sqrt{2}H \\ u_2 - \sqrt{2}H \\ u_2 + \sqrt{2}H \\ u_2 + \sqrt{2}H \\ u_2 \\ u_2 \\ u_2 \end{pmatrix} \quad \text{(A.21)} \qquad R_2 = \begin{pmatrix} 0 & \frac{1}{2} & 0 & 0 & 0 & 0 & \frac{1}{2^{\frac{3}{2}}H} & 0 & 0 \\ 0 & \frac{1}{2} & 0 & 0 & 0 & 0 & -\frac{1}{2^{\frac{3}{2}}H} & 0 & 0 \\ \frac{1}{2} & 0 & 0 & 0 & \frac{1}{2H} & 0 & 0 & 0 & 0 \\ 0 & 0 & \frac{1}{2} & 0 & 0 & 0 & 0 & \frac{1}{2H} & 0 \\ \frac{1}{2} & 0 & 0 & 0 & -\frac{1}{2H} & 0 & 0 & 0 & 0 \\ 0 & 0 & \frac{1}{2} & 0 & 0 & 0 & 0 & -\frac{1}{2H} & 0 \\ 0 & 0 & 0 & 1 & -2\frac{\tau_{12}}{H^2} & 0 & 0 & 0 & 0 \\ 0 & 0 & 0 & 0 & -\frac{\tau_{23}}{H^2} & 1 & \frac{\tau_{13}}{2H^2} & -\frac{\tau_{12}}{H^2} & 0 \\ 0 & 0 & 0 & 0 & 0 & 0 & 0 & -2\frac{\tau_{23}}{H^2} & 1 \end{pmatrix} \quad \text{(A.22)}$$

The coefficient matrix in x_3 direction with $H = \sqrt{\frac{1-\beta}{Ma^2} + \tau_{33}}$:

$$A_3 = \begin{pmatrix} u_3 & 0 & 0 & 0 & 0 & -1 & 0 & 0 & 0 \\ 0 & u_3 & 0 & 0 & 0 & 0 & 0 & -1 & 0 \\ 0 & 0 & u_3 & 0 & 0 & 0 & 0 & 0 & -1 \\ -2\tau_{13} & 0 & 0 & u_3 & 0 & 0 & 0 & 0 & 0 \\ -\tau_{23} & -\tau_{13} & 0 & 0 & u_3 & 0 & 0 & 0 & 0 \\ -H^2 & 0 & -\tau_{13} & 0 & 0 & u_3 & 0 & 0 & 0 \\ 0 & -2\tau_{23} & 0 & 0 & 0 & 0 & u_3 & 0 & 0 \\ 0 & -H^2 & -\tau_{23} & 0 & 0 & 0 & 0 & u_3 & 0 \\ 0 & 0 & -2H^2 & 0 & 0 & 0 & 0 & 0 & u_3 \end{pmatrix} \quad \text{(A.23)}$$

$$L_3 = \begin{pmatrix} 0 & 0 & 1 & 0 & 1 & 0 & 0 & 0 & 0 \\ 0 & 0 & 0 & 1 & 0 & 1 & 0 & 0 & 0 \\ 1 & 1 & 0 & 0 & 0 & 0 & 0 & 0 & 0 \\ 0 & 0 & 2\frac{\tau_{13}}{H} & 0 & -2\frac{\tau_{13}}{H} & 0 & 1 & 0 & 0 \\ -\frac{\tau_{12}}{\sqrt{2}H} & \frac{\tau_{12}}{\sqrt{2}H} & \frac{\tau_{23}}{H} & \frac{\tau_{13}}{H} & -\frac{\tau_{23}}{H} & -\frac{\tau_{13}}{H} & 0 & 1 & 0 \\ 0 & 0 & H & 0 & -H & 0 & 0 & 0 & 0 \\ 0 & 0 & 0 & 2\frac{\tau_{23}}{H} & 0 & -2\frac{\tau_{23}}{H} & 0 & 0 & 1 \\ 0 & 0 & 0 & H & 0 & -H & 0 & 0 & 0 \\ \sqrt{2}H & -\sqrt{2}H & 0 & 0 & 0 & 0 & 0 & 0 & 0 \end{pmatrix} \quad \text{(A.24)}$$

$$\Lambda_3 = \begin{pmatrix} u_3 - \sqrt{2}H \\ u_3 + \sqrt{2}H \\ u_3 - H \\ u_3 - H \\ u_3 + H \\ u_3 + H \\ u_3 \\ u_3 \\ u_3 \end{pmatrix} \quad \text{(A.25)} \qquad R_3 = \begin{pmatrix} 0 & 0 & \frac{1}{2} & 0 & 0 & 0 & 0 & 0 & \frac{1}{2^{\frac{3}{2}}H} \\ 0 & 0 & \frac{1}{2} & 0 & 0 & 0 & 0 & 0 & -\frac{1}{2^{\frac{3}{2}}H} \\ \frac{1}{2} & 0 & 0 & 0 & 0 & \frac{1}{2H} & 0 & 0 & 0 \\ 0 & \frac{1}{2} & 0 & 0 & 0 & 0 & 0 & \frac{1}{2H} & 0 \\ \frac{1}{2} & 0 & 0 & 0 & 0 & -\frac{1}{2H} & 0 & 0 & 0 \\ 0 & \frac{1}{2} & 0 & 0 & 0 & 0 & 0 & -\frac{1}{2H} & 0 \\ 0 & 0 & 0 & 1 & 0 & -2\frac{\tau_{13}}{H^2} & 0 & 0 & 0 \\ 0 & 0 & 0 & 0 & 1 & -\frac{\tau_{23}}{H^2} & 0 & -\frac{\tau_{13}}{H^2} & \frac{\tau_{12}}{2H^2} \\ 0 & 0 & 0 & 0 & 0 & 0 & 1 & -2\frac{\tau_{23}}{H^2} & 0 \end{pmatrix} \quad \text{(A.26)}$$

Appendix B

Coding improve for saving calculating time

For a CFD solver, with the demand for increasing the calculation accuracy and the scale of the calculating nodes, the resulting high-intensity calculation load problem will become more prominent. The existing two main aspects to solve this problem are: improve the accuracy and convergence characteristics of the algorithm and/or improve computing efficiency, such as parallel computing or algorithm optimization. In the early stage of coding the solver, we have done some work on the optimization algorithm, to reduce the calculation time of the solver.

Initially, we solved linear large sparse systems of linear algebraic equations by preconditioned conjugate gradient (PCG) method through a software package named Nonsymmetric Preconditioned Conjugate Gradient $(NSPCG)$, which is designed to solve large sparse systems of linear algebraic equations by a variety of different iterative methods and developed by Oppe, Joubert, and Kincaid (1989).

B.1 Test for Newtonian cases

Firstly, we take a Newtonian Rayleigh-Bénard convection in cavity with aspect ratio $1:1$, the Prandtl number and Rayleigh number are $Pr = 7.0$ and $Ra = 10^5$, respectively. The function, $cpu\_time()$ in *Fortran*, is used to record CPU time. Tab. B.1 shows the time cost of each part of the calculating procedure in one time step for different grid node numbers in 2D and 3D configurations.

cpu time	128^2	256^2	512^2	32^3	64^3	128^3
Advection terms	0.004	0.02	0.076	0.028	0.196	1.68
NSPCG T	0.004	0.028	0.2	0.032	0.288	2.36
NSPCG U	0.008	0.048	0.3	0.09	0.762	7.26
NSPCG P	0.02	0.164	1.54	0.08	1.588	14.62
Rest	0.012	0.032	0.116	0.042	0.298	4.24
Total	0.048	0.292	2.232	0.272	3.132	30.16

TABLE B.1: Time cost summary for each part of the solver.

Fig. B.1 shows the pie chart of the proportion of time cost by each part in different grid node sets. It can be easily found that the time cost for calculating the pressure is the largest part, followed by the solution for velocity and temperature. The proportion of the time cost of pressure solution increases as the number of grid nodes increases.

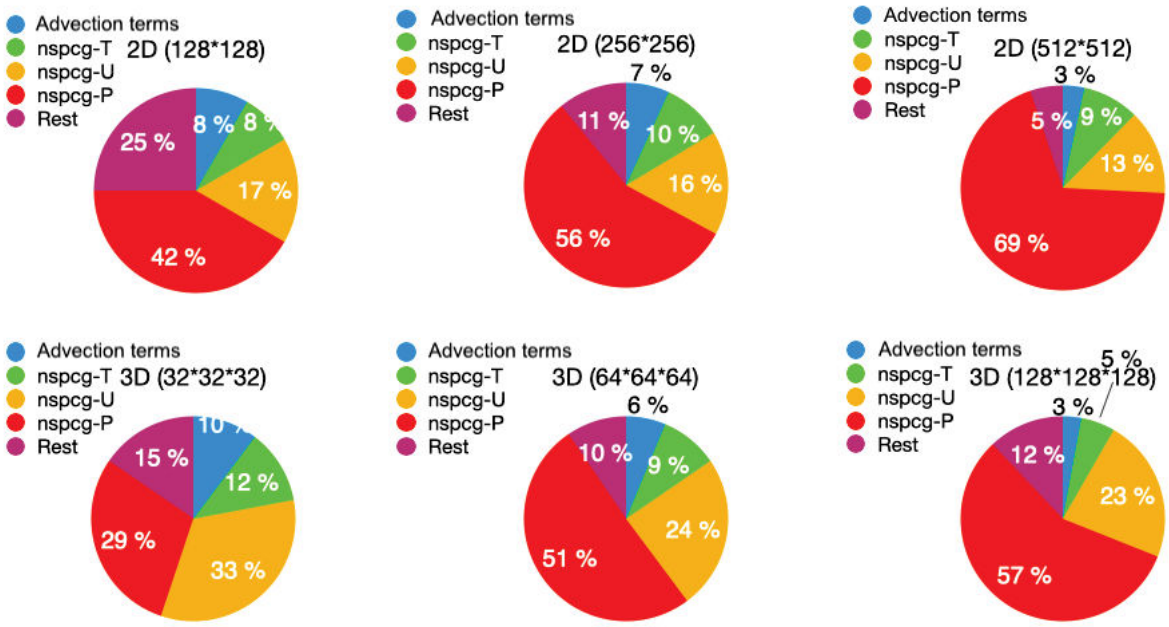

FIGURE B.1: Proportion of the time cost of each part in one time step procedure.

In order to know if they are better solver for the solution of linear equations, we used Alternative Direction Implicite method (ADI) instead of the PCG method, and checked the cost time of each part, as shown in Tab. B.2. It was found that the total time cost is saved by almost 22% for solver using ADI. It can be concluded that ADI solver are more interesting and reduce the computational cost.

	256^2	512^2
NSPCG	Total: 0.292 *A* terms: 0.02 *P* terms: 0.164	Total: 2.232 *A* terms: 0.076 *P* terms: 1.54
ADI	Total: 0.230 *A* terms: 0.022 *P* terms: 0.12	Total: 1.782 *A* terms:0.08 *P* terms: 0.72

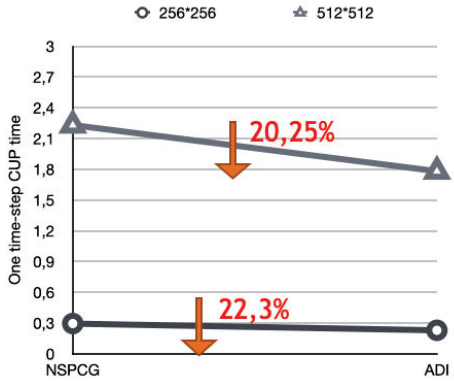

FIGURE B.2: Time cost summary for solver with ADI and NSPCG in 2D Newtonian Rayleigh-Bénard convection. *A* presents the Advection terms in the table. The figure shows the total time cost for solver with NSPCG and ADI.

B.2 Test for viscoelastic cases

In fact, most of the matrix operations in the quasi-linearization process (embodied in *hyperbolic terms*) are sparse matrix operations, which means that a large part of the operations are not useful operations ($*0$). Take the calculation $R_1 \cdot \boldsymbol{W}$ as example, as shown in Eq. **??**, the computation including red color item in the matrix R_1 are not necessary and can be avoided.

$$R_1 \cdot \boldsymbol{W} = \begin{pmatrix} \frac{1}{2} & 0 & 0 & \frac{1}{2^{\frac{3}{2}}H} & 0 & 0 & 0 & 0 & 0 \\ \frac{1}{2} & 0 & 0 & -\frac{1}{2^{\frac{3}{2}}H} & 0 & 0 & 0 & 0 & 0 \\ 0 & \frac{1}{2} & 0 & 0 & \frac{1}{2H} & 0 & 0 & 0 & 0 \\ 0 & 0 & \frac{1}{2} & 0 & 0 & \frac{1}{2H} & 0 & 0 & 0 \\ 0 & \frac{1}{2} & 0 & 0 & -\frac{1}{2H} & 0 & 0 & 0 & 0 \\ 0 & 0 & \frac{1}{2} & 0 & 0 & -\frac{1}{2H} & 0 & 0 & 0 \\ 0 & 0 & 0 & 0 & -2\frac{\tau_{12}}{H^2} & 0 & 1 & 0 & 0 \\ 0 & 0 & 0 & \frac{\tau_{23}}{2H^2} & -\frac{\tau_{13}}{H^2} & -\frac{\tau_{12}}{H^2} & 0 & 1 & 0 \\ 0 & 0 & 0 & 0 & 0 & -2\frac{\tau_{13}}{H^2} & 0 & 0 & 1 \end{pmatrix} \cdot \begin{pmatrix} u_1 \\ u_2 \\ u_3 \\ \tau_{11} \\ \tau_{12} \\ \tau_{13} \\ \tau_{22} \\ \tau_{23} \\ \tau_{33} \end{pmatrix} \tag{B.1}$$

Algorithm 1 Calculate hyperbolic term $L_1\Lambda_1\frac{\partial R_1\boldsymbol{W}}{\partial x}$ using original coding.

Require: $\boldsymbol{W} = (u_1, u_2, u_3, \tau_{11}, \tau_{12}, \tau_{13}, \tau_{22}, \tau_{23}, \tau_{33})$: variables; Nx, Ny, Nz: number of the space node at three direction
Output: $L_1\Lambda_1\frac{\partial R_1\boldsymbol{W}}{\partial x}$

```
for i = 1; Nx; i++ do
    for j = 1; Ny; j++ do
        for k = 1; Nz; k++ do
            compute L1; Λ1; R1
            compute R1W_{i-2,j,k}, R1W_{i-1,j,k}, R1W_{i,j,k}, R1W_{i+1,j,k}, R1W_{i+2,j,k}
            if Λ1 < 0 then
                compute (∂R1W/∂x)_{i,j,k} using backward HOUC3
            else if Λ1 = 0 then
                do not compute (∂R1W/∂x)_{i,j,k}
            elseΛ1 > 0
                compute (∂R1W/∂x)_{i,j,k} using forward HOUC3 (Eq. 3.61).
            end if
            compute (Λ1 ∂R1W/∂x)_{i,j,k}
            compute (L1Λ1 ∂R1W/∂x)_{i,j,k}
        end for
    end for
end for
```

So we further optimized this part by expanding the eigenvector matrix L_1 and R_1 (here we take $L_1\Lambda_1\frac{\partial R_1\boldsymbol{W}}{\partial x}$ as an example, the operation using the red matrices can be improved). Because we already know the expression of the matrix coefficients of hyperbolic terms, we use manual multiplications and avoid $(*0)$ calculations (instead of matrix multiplication function : $matmul(R_1, \boldsymbol{W})$ in Fortran) to reduce the operation number.

Algorithm 1 shows the original program for calculating hyperbolic part, it is ealy found that there is many unnecessary operating for steps 6-11 to compute $R_1 \cdot \boldsymbol{W}$, especially, when we use high order discrete form (such as HOUC3). We know that HOUC3 for $\frac{\partial R_1 \boldsymbol{W}}{\partial x}$ will need one or two grid nodes informaton around the central point, for example, $(R_1 \cdot \boldsymbol{W})_{i-2,j,k}$, $(R_1 \cdot \boldsymbol{W})_{i-1,j,k}$, $(R_1 \cdot \boldsymbol{W})_{i,j,k}$, $(R_1 \cdot \boldsymbol{W})_{i+1,j,k}$ will be calculated for $\Lambda_1 > 0$. In fact, R_1 is related to the grid point (i, j) and independent of x, therefore we have $R_1 \cdot \frac{\partial \boldsymbol{W}}{\partial x} = \frac{\partial R_1 \boldsymbol{W}}{\partial x}$. So we can impove this part by computing $(\frac{\partial \boldsymbol{W}}{\partial x})_{i,j,k}$ first, and then compute $(R_1 \frac{\partial \boldsymbol{W}}{\partial x})_{i,j,k}$ to save computing resource. The improved promgram **Algorithm** 2 is shown as follows:

Algorithm 2 Calculate hyperbolic term $L_1 \Lambda_1 \frac{\partial R_1 \boldsymbol{W}}{\partial x}$ using imporved coding.

Require: $\boldsymbol{W} = (u_1, u_2, u_3, \tau_{11}, \tau_{12}, \tau_{13}, \tau_{22}, \tau_{23}, \tau_{33})$: variables; Nx, Ny, Nz: number of the space node at three direction

Output: $L_1 \Lambda_1 \frac{\partial R_1 \boldsymbol{W}}{\partial x}$

```
for i = 1; Nx; i++ do
    for j = 1; Ny; j++ do
        for k = 1; Nz; k++ do
            compute L_1; Λ_1; R_1
        end for
    end for
end for
for i = 1; Nx; i++ do
    for j = 1; Ny; j++ do
        for k = 1; Nz; k++ do
            if Λ_1 < 0 then
                compute (∂W/∂x)_{i,j,k} using backward HOUC3
            else if Λ_1 = 0 then
                do not compute (∂W/∂x)_{i,j,k}
            elseΛ_1 > 0
                compute (∂W/∂x)_{i,j,k} using forward HOUC3, where backward and forward
                HOUC3 has been introduced by Eq. 3.61.
            end if
            compute (Λ_1 R_1 ∂W/∂x)_{i,j,k} using only the non-zero element of R_1
            compute (L_1 Λ_1 R_1 ∂W/∂x)_{i,j,k} using only the non-zero element of L_1
        end for
    end for
end for
where red matrixes means that has been improved as Eq. ??.
```

Tab. B.2 shows the comparasion of total time cost for three improved solver stages in 3D Newtonian Rayleigh-Bénard convection cases. The results show that through hyperbolic term optimization, for 3D Newtonian fluid RBC, the time cost of one time step calculation for the same nodes number (128^3) can be saved 30%.

Through the test for Newtonian cases, we know that ADI is more effectively than NSPCG for sovling linear algebraic equation in saving time. In following viscoelastic cases, we all adapt

CPU time	16^3	32^3	64^3	128^3
NSPCG + Original **Algorithm** 1	0.032	0.28	3.22	30.16
ADI + Original **Algorithm** 1	0.016	0.18	2.12	21.26
ADI + improved **Algorithm** 2	0.014	0.16	2.06	18.28

TABLE B.2: Time cost for three coding conditions with different grid numbers in 3D Newtonian Rayleigh-Bénard convection cases.

ADI to sovle linear algebraic equation. Tab. B.3 shows time cost at each sovle part for 2D viscoelastic cases with original **Algorithm** 1 and improved **Algorithm** 2, respectively. We named the case with grid of 128×128 with **Algorithm** 1 for 2D as 2D128Al1. From Tab. B.3, we can find that the total time cost will save about 60% in 2D viscoelastic cases, when we improved **Algorithm** 1 to **Algorithm** 2. Take 2D512Al1 and 2D512Al2 as examples, the total saving time ratio is equal to $(1.956 - 0.82)/1.956 \approx 58\%$.

Case	Grid	Hyper part	τ term	T term	$\boldsymbol{u}$ term	p term	Total
2D128Al1	128^2	0.088	0.016	0.004	0.004	0.008	0.120
2D256Al1	256^2	0.352	0.060	0.012	0.028	0.028	0.480
2D512Al1	512^2	1.412	0.216	0.056	0.108	0.164	1.956
2D128Al2	128^2	0.02	0.012	0.004	0.004	0.008	0.048
2D256Al2	256^2	0.076	0.044	0.012	0.024	0.032	0.188
2D512Al2	512^2	0.304	0.184	0.048	0.092	0.192	0.820

TABLE B.3: Time cost for 2D viscoelastic Rayleigh-Bénard convection cases with original **Algorithm** 1.

Number	Grid	Hyper part	τ term	T term	$\boldsymbol{u}$ term	p term	Total
3D32Al1	32^3	0.584	0.216	0.012	0.036	0.044	0.892
3D64Al1	64^3	4.520	1.696	0.108	0.280	0.328	6.932
3D128Al1	128^3	35.378	12.788	0.828	2.132	2.836	53.964
3D32Al2	32^3	0.208	0.128	0.016	0.032	0.044	0.428
3D64Al2	64^3	1.600	1.000	0.108	0.244	0.340	3.292
3D128Al2	128^3	12.692	7.732	0.868	1.916	2.964	26.176
3D128Al2-1	128^3	16.652	12.780	0.828	2.128	2.964	35.356

TABLE B.4: Time cost for 3D viscoelastic Rayleigh-Bénard convection cases with improved **Algorithm** 2, where 3D128Al2-1 presents using original L_1 and R_1 in **Algorithm** 2 instead of L_1 and R_1 in computing.

Here, we summary the main difference between **Algorithm** 1 and **Algorithm** 2: (1) In actual calculation, we use $R_i \frac{\partial W}{\partial x}$ instead $\frac{\partial R_i W}{\partial x}$, so that we can save computation of four times Matrix multiplication for a certain point; (2) We already found that R and L are sparse matrices, we just calculate nonzero useful operations for $R_i W$ and $L_i(\Lambda \frac{\partial R_i W}{\partial x})$ in **Algorithm** 2. In order to study the influence of (2) on the calculation time, we separately designed the case 3D128Al2-1. We use original R_i and L_i in 3D128Al2-1. Tab. **??** shows time cost at each sovle part for 3D viscoelastic cases with original **Algorithm** 1 and improved **Algorithm** 2, respectively. We can find that the

total time cost will save about 50% in 2D viscoelastic cases, when we improved **Algorithm** 1 to **Algorithm** 2. Take 3D128Al1 and 3D128Al2 as examples, the total saving time ratio is equal to $(53.964 - 26.176)/53.964 \approx 52\%$. In addition, comparing 3D128Al2 and 3D128Al2-1, we can easily find that $L_i \Lambda R_i \frac{\partial W}{\partial x}$ is more effective than $L_i \Lambda R_i \frac{\partial W}{\partial x}$ in saving time, time cost saving is about 26%.

Bibliography

Acharya, S and RJ Goldstein (1985). "Natural convection in an externally heated vertical or inclined square box containing internal energy sources". In:

Afonso, Alexandre et al. (2009). "The log-conformation tensor approach in the finite-volume method framework". In: *Journal of Non-Newtonian Fluid Mechanics* 157.1-2, pp. 55–65.

Ahlers, Guenter and Alexei Nikolaenko (2010). "Effect of a polymer additive on heat transport in turbulent Rayleigh-Bénard convection". In: *Physical review letters* 104.3, p. 034503.

Allgower, Eugene L and Kurt Georg (2012). *Numerical continuation methods: an introduction*. Vol. 13. Springer Science & Business Media.

Arnold, JN, I Catton, and DK Edwards (1976). "Experimental investigation of natural convection in inclined rectangular regions of differing aspect ratios". In:

Asokan, Badrinarayanan Velamur and Nicholas Zabaras (2005). "Using stochastic analysis to capture unstable equilibrium in natural convection". In: *Journal of Computational Physics* 208.1, pp. 134–153.

Bairi, A, N Laraqi, and JM Garcia de Maria (2007). "Numerical and experimental study of natural convection in tilted parallelepipedic cavities for large Rayleigh numbers". In: *Experimental Thermal and Fluid Science* 31.4, pp. 309–324.

Balci, Nusret et al. (2011). "Symmetric factorization of the conformation tensor in viscoelastic fluid models". In: *Journal of Non-Newtonian Fluid Mechanics* 166.11, pp. 546–553.

Bao, Yun et al. (2015). "Enhanced heat transport in partitioned thermal convection". In: *Journal of Fluid Mechanics* 784.

Behringer, RP (1985). "Rayleigh-Bénard convection and turbulence in liquid helium". In: *Reviews of modern physics* 57.3, p. 657.

Bénard, Henri (1900). "Les tourbillons cellulaires dans une nappe liquide". In: *Rev. Gen. Sci. Pures Appl.* 11, pp. 1261–1271.

Benzi, Roberto, Emily SC Ching, and Elisabetta De Angelis (2010). "Effect of polymer additives on heat transport in turbulent thermal convection". In: *Physical review letters* 104.2, p. 024502.

Benzi, Roberto, Emily SC Ching, and Elisabetta De Angelis (2016). "Turbulent Rayleigh-Bénard convection with polymers: Understanding how heat flux is modified". In: *Physical Review E* 94.6, p. 063110.

Benzi, Roberto, Vivien WS Chu, et al. (2011). "Heat transport by laminar boundary layer flow with polymers". In: *arXiv preprint arXiv:1104.4526*.

Benzi, Roberto et al. (2016). "Heat transport modification by finitely extensible polymers in laminar boundary layer flow". In: *Journal of Fluid Mechanics* 788, pp. 337–357.

Bergies, E Arthur (1999). "The imperative to enhance heat transfer". In: *Heat transfer enhancement of heat exchangers*. Springer, pp. 13–29.

Bouabdallah, Said et al. (2016). "Onset of natural convection and transition laminar-oscillatory convection flow in Rayleigh-Bénard configuration". In: *International journal of heat and technology* 34, pp. 151–157.

Burger, Edward D, Werner R Munk, Harry A Wahl, et al. (1982). "Flow increase in the Trans Alaska Pipeline through use of a polymeric drag-reducing additive". In: *Journal of petroleum Technology* 34.02, pp. 377–386.

Busse, FH (1978). "Non-linear properties of thermal convection". In: *Reports on Progress in Physics* 41.12, p. 1929.

Cai, Weihua et al. (2016). "Study on the Characteristics of Rayleigh-Benard Convection With Viscoelastic Fluids". In: *Fluids Engineering Division Summer Meeting*. Vol. 50299. American Society of Mechanical Engineers, V01BT14A006.

Castaing, Bernard et al. (1989). "Scaling of hard thermal turbulence in Rayleigh-Bénard convection". In: *Journal of Fluid Mechanics* 204, pp. 1–30.

Catton, Ivan, PS Ayyaswamy, and RM Clever (1974). "Natural convection flow in a finite, rectangular slot arbitrarily oriented with respect to the gravity vector". In: *International Journal of Heat and Mass Transfer* 17.2, pp. 173–184.

Chandrasekhar, Subrahmanyan (2013). *Hydrodynamic and hydromagnetic stability*. Courier Corporation.

Chavanne, a X et al. (1997). "Observation of the ultimate regime in Rayleigh-Bénard convection". In: *Physical review letters* 79.19, p. 3648.

Cheng, Jian-Ping et al. (2017). "Effect of polymer additives on heat transport and large-scale circulation in turbulent Rayleigh-Bénard convection". In: *Physical Review E* 96.1, p. 013111.

Cheng, Jonathan S et al. (2015). "Laboratory-numerical models of rapidly rotating convection in planetary cores". In: *Geophysical Journal International* 201.1, pp. 1–17.

Cioni, S, Sergio Ciliberto, and Jöel Sommeria (1997). "Strongly turbulent Rayleigh–Bénard convection in mercury: comparison with results at moderate Prandtl number". In: *Journal of Fluid Mechanics* 335, pp. 111–140.

Corcione, Massimo (2003). "Effects of the thermal boundary conditions at the sidewalls upon natural convection in rectangular enclosures heated from below and cooled from above". In: *International Journal of Thermal Sciences* 42.2, pp. 199–208.

Crochet, Marcel J, Arthur Russell Davies, and Kenneth Walters (2012). *Numerical simulation of non-Newtonian flow*. Elsevier.

Curry, James H et al. (1984). "Order and disorder in two-and three-dimensional Bénard convection". In: *Journal of Fluid Mechanics* 147, pp. 1–38.

Curtiss, Charles Francis and Joseph O Hirschfelder (1952). "Integration of stiff equations". In: *Proceedings of the National Academy of Sciences of the United States of America* 38.3, p. 235.

Davis, Stephen H (1967). "Convection in a box: linear theory". In: *Journal of Fluid Mechanics* 30.3, pp. 465–478.

Doering, Charles R (2020). "Turning up the heat in turbulent thermal convection". In: *Proceedings of the National Academy of Sciences* 117.18, pp. 9671–9673.

D'Orazio, Maria Cappelli, Claudio Cianfrini, and Massimo Corcione (2004). "Rayleigh–Bénard convection in tall rectangular enclosures". In: *International journal of thermal sciences* 43.2, pp. 135–144.

Drazin, Philip G and William Hill Reid (2004). *Hydrodynamic stability*. Cambridge university press.

Du, Y-B and Penger Tong (1998). "Enhanced heat transport in turbulent convection over a rough surface". In: *Physical review letters* 81.5, p. 987.

Dubief, Yves (2010). "Heat transfer enhancement and reduction by poylmer additives in turbulent Rayleigh Benard convection". In: *arXiv preprint arXiv:1009.0493*.

Eltayeb, IA (1977). "Nonlinear thermal convection in an elasticoviscous layer heated from below". In: *Proceedings of the Royal Society of London. A. Mathematical and Physical Sciences* 356.1685, pp. 161–176.

Fattal, Raanan and Raz Kupferman (2004). "Constitutive laws for the matrix-logarithm of the conformation tensor". In: *Journal of Non-Newtonian Fluid Mechanics* 123.2-3, pp. 281–285.

— (2005). "Time-dependent simulation of viscoelastic flows at high Weissenberg number using the log-conformation representation". In: *Journal of Non-Newtonian Fluid Mechanics* 126.1, pp. 23–37.

Funfschilling, Denis et al. (2005). "Heat transport by turbulent Rayleigh-Bénard convection in cylindrical samples with aspect ratio one and larger". In: *arXiv preprint physics/0507050*.

Gelfgat, Alexander Yu (1999). "Different modes of Rayleigh–Bénard instability in two-and three-dimensional rectangular enclosures". In: *Journal of Computational Physics* 156.2, pp. 300–324.

Gollub, JoPo and SV Benson (1980). "Many routes to turbulent convection". In: *Journal of Fluid Mechanics* 100.3, pp. 449–470.

Green III, Theodore (1968). "Oscillating convection in an elasticoviscous liquid". In: *The Physics of Fluids* 11.7, pp. 1410–1412.

Groisman, Alexander and Victor Steinberg (2000). "Elastic turbulence in a polymer solution flow". In: *Nature* 405.6782, pp. 53–55.

Hagani, Fouad (2021). "Simulation numérique du transfert convectif dans un écoulement viscoélastique". PhD thesis. Université de Lyon.

Hagani, Fouad et al. (2018). "Numerical Modeling of Phan-Thien-Tanner Viscoelastic Fluid Flow Through a Square Cross-Section Duct: Heat Transfer Enhancement due to Shear-Thinning Effects". In: *ASME International Mechanical Engineering Congress and Exposition*. Vol. 52101. American Society of Mechanical Engineers, V007T09A042.

Hagen, Gotthilf (1839). "Ueber die Bewegung des Wassers in engen cylindrischen Röhren". In: *Annalen der Physik* 122.3, pp. 423–442.

Harlow, Francis H and J Eddie Welch (1965). "Numerical calculation of time-dependent viscous incompressible flow of fluid with free surface". In: *The physics of fluids* 8.12, pp. 2182–2189.

He, Xiaozhou et al. (2012). "Transition to the ultimate state of turbulent Rayleigh-Bénard convection". In: *Physical review letters* 108.2, p. 024502.

Hilst., Robert Van Der (Spring 1998). "Senimar in geophysics: Mantle convection." In: *Massachusetts Institute of Technology: MIT OpenCourseWare*.

Hulsen, Martien A, Raanan Fattal, and Raz Kupferman (2005). "Flow of viscoelastic fluids past a cylinder at high Weissenberg number: stabilized simulations using matrix logarithms". In: *Journal of Non-Newtonian Fluid Mechanics* 127.1, pp. 27–39.

Ivanov, MS, Ye A Bondar, and GN Markelov (2007). "Recent achievements in the DSMC method and its applications to studying jets in vacuum chamber". In: *51st IUVSTA Workshop on Modern Problems & Capability of Vacuum Gas Dynamics*.

Jin, Shi (2007). *Numerical simulations of a dilute polymer solution in isotropic turbulence*.

Johnson, Nelson K (1922). "Weather Prediction by Numerical Process". In:

Kakaç, Sadik et al. (2013). *Heat transfer enhancement of heat exchangers*. Vol. 355. Springer Science & Business Media.

Kaneko, Kunihiko (1986). *Collapse of tori and genesis of chaos in dissipative systems*. World Scientific Publishing Company.

Kays, William Morrow (2011). *Convective heat and mass transfer*. Tata McGraw-Hill Education.

Keunings, R (1987). "Simulation of viscoelastic fluid flow". In:

Khayat, Roger E (1994). "Chaos and overstability in the thermal convection of viscoelastic fluids". In: *Journal of non-newtonian fluid mechanics* 53, pp. 227–255.

— (1995a). "Fluid elasticity and the transition to chaos in thermal convection". In: *Physical Review E* 51.1, p. 380.

— (1995b). "Non-linear overstability in the thermal convection of viscoelastic fluids". In: *Journal of non-newtonian fluid mechanics* 58.2-3, pp. 331–356.

Khezzar, Lyes, Dennis Siginer, and Igor Vinogradov (2012). "Natural convection of power law fluids in inclined cavities". In: *International Journal of Thermal Sciences* 53, pp. 8–17.

King, Eric M et al. (2009). "Boundary layer control of rotating convection systems". In: *Nature* 457.7227, pp. 301–304.

Kline, Stephen J et al. (1967). "The structure of turbulent boundary layers". In: *Journal of Fluid Mechanics* 30.4, pp. 741–773.

Kraichnan, Robert H (1962). "Turbulent thermal convection at arbitrary Prandtl number". In: *The Physics of Fluids* 5.11, pp. 1374–1389.

Kurganov, Alexander and Eitan Tadmor (2000). "New high-resolution central schemes for nonlinear conservation laws and convection–diffusion equations". In: *Journal of Computational Physics* 160.1, pp. 241–282.

Kurzweg, Ulrich H (1965). "Convective instability of a hydromagnetic fluid within a rectangular cavity". In: *International Journal of Heat and Mass Transfer* 8.1, pp. 35–41.

Lappa, Marcello (2011). "Some considerations about the symmetry and evolution of chaotic Rayleigh–Bénard convection: The flywheel mechanism and the "wind" of turbulence". In: *Comptes Rendus Mécanique* 339.9, pp. 563–572.

Lappa, Marcello and Alessio Boaro (2020). "Rayleigh–Bénard convection in viscoelastic liquid bridges". In: *Journal of Fluid Mechanics* 904.

Lee, NY, William W Schultz, and John P Boyd (1989). "Stability of fluid in a rectangular enclosure by spectral method". In: *International journal of heat and mass transfer* 32.3, pp. 513–520.

Li, F-C, Yasuo Kawaguchi, and Koichi Hishida (2004). "Investigation on the characteristics of turbulence transport for momentum and heat in a drag-reducing surfactant solution flow". In: *Physics of Fluids* 16.9, pp. 3281–3295.

Li, Pei-Wen, Yasuo Kawaguchi, and Akira Yabe (2001). "Transitional heat transfer and turbulent characteristics of drag-reducing flow through a contracted channel". In: *Journal of Enhanced Heat Transfer* 8.1.

Li, Peiwen et al. (2001). "Heat transfer enhancement to the drag-reducing flow of surfactant solution in two-dimensional channel with mesh-screen inserts at the inlet". In: *J. Heat Transfer* 123.4, pp. 779–789.

Li, Yu-Ke et al. (2017). "Numerical study on secondary flows of viscoelastic fluids in straight ducts: Origin analysis and parametric effects". In: *Computers & Fluids* 152, pp. 57–73.

Li, Zhenyu and Roger E Khayat (2005). "Finite-amplitude Rayleigh-Bénard convection and pattern selection for viscoelastic fluids". In: *Journal of Fluid Mechanics* 529, p. 221.

Long, Robert R (1975). "Some properties of turbulent convection with shear". In: *Geophysical and Astrophysical Fluid Dynamics* 6.4, pp. 337–358.

Ma, Tian, Shouhong Wang, et al. (2004). "Dynamic bifurcation and stability in the Rayleigh-Bénard convection". In: *Communications in Mathematical Sciences* 2.2, pp. 159–183.

Malkus, WVR and George Veronis (1958). "Finite amplitude cellular convection". In: *Journal of Fluid Mechanics* 4.3, pp. 225–260.

Martinez-Mardones, J and C Perez-Garcia (1992). "Bifurcation analysis and amplitude equations for viscoelastic convective fluids". In: *Il Nuovo Cimento D* 14.9, pp. 961–975.

Maurer, J and A Libchaber (1979). "Rayleigh-Bénard experiment in liquid helium; frequency locking and the onset of turbulence". In: *Journal de Physique Lettres* 40.16, pp. 419–423.

— (1980). "Effect of the Prandtl number on the onset of turbulence in liquid 4He". In: *Journal de Physique lettres* 41.21, pp. 515–518.

Metivier, Christel et al. (2020). "Oscillatory Rayleigh–Bénard Convection in elasto-viscoplastic gels". In: *Journal of Non-Newtonian Fluid Mechanics* 286, p. 104428.

Miesch, Mark S (2005). "Large-scale dynamics of the convection zone and tachocline". In: *Living Reviews in Solar Physics* 2.1, p. 1.

Min, Taegee, Jung Yul Yoo, and Haecheon Choi (2001). "Effect of spatial discretization schemes on numerical solutions of viscoelastic fluid flows". In: *Journal of non-newtonian fluid mechanics* 100.1-3, pp. 27–47.

Mizushima, Jiro (1995). "Onset of the thermal convection in a finite two-dimensional box". In: *Journal of the Physical Society of Japan* 64.7, pp. 2420–2432.

Mizushima, Jiro and Takahiro Adachi (1997). "Sequential transitions of the thermal convection in a square cavity". In: *Journal of the Physical Society of Japan* 66.1, pp. 79–90.

Nourgaliev, Robert R and Theo G Theofanous (2007). "High-fidelity interface tracking in compressible flows: unlimited anchored adaptive level set". In: *Journal of Computational Physics* 224.2, pp. 836–866.

Oliver, D.R. and S.I. Bakhtiyarov (1983). "Drag reduction in exceptionally dilute polymer solutions". In: *Journal of Non-Newtonian Fluid Mechanics* 12.1, pp. 113 –118.

Oppe, TC, WD Joubert, and DR Kincaid (1989). "NSPCG, a package for solving large sparse linear systems by various iterative methods". In: *Center for Numerical Analysis, University of Texas at Austin*.

Ouertatani, Nasreddine et al. (2008). "Numerical simulation of two-dimensional Rayleigh–Bénard convection in an enclosure". In: *Comptes Rendus Mécanique* 336.5, pp. 464–470.

Pallares, J and Lars Davidson (2000). "Large-eddy simulations of turbulent flow in a rotating square duct". In: *Physics of Fluids* 12.11, pp. 2878–2894.

Pallares, Jordi, Francesc Xavier Grau, and Francesc Giralt (1999). "Flow transitions in laminar Rayleigh–Bénard convection in a cubical cavity at moderate Rayleigh numbers". In: *International journal of heat and mass transfer* 42.4, pp. 753–769.

Park, H and D Ryu (2002). "Nonlinear convective stability problems of viscoelastic fluids in finite domains". In: *Rheologica acta* 41.5, pp. 427–440.

Park, HM (2018). "Peculiarity in the Rayleigh-Bénard convection of viscoelastic fluids". In: *International Journal of Thermal Sciences* 132, pp. 34–41.

Park, HM and HS Lee (1995). "Nonlinear hydrodynamic stability of viscoelastic fluids heated from below". In: *Journal of non-newtonian fluid mechanics* 60.1, pp. 1–26.

Park, HM and KS Park (2004). "Rayleigh–Bénard convection of viscoelastic fluids in arbitrary finite domains". In: *International journal of heat and mass transfer* 47.10-11, pp. 2251–2259.

Park, HM and DH Ryu (2001). "Rayleigh–Bénard convection of viscoelastic fluids in finite domains". In: *Journal of non-newtonian fluid mechanics* 98.2-3, pp. 169–184.

Patankar, Suhas (2018). *Numerical heat transfer and fluid flow*. Taylor & Francis.

Paterson, Robert W and FH Abernathy (1970). "Turbulent flow drag reduction and degradation with dilute polymer solutions". In: *Journal of Fluid Mechanics* 43.4, pp. 689–710.

Paul, Supriyo, Pankaj Wahi, and Mahendra K Verma (2011). "Bifurcations and chaos in large-Prandtl number Rayleigh–Bénard convection". In: *International Journal of Non-Linear Mechanics* 46.5, pp. 772–781.

Paul, Supriyo et al. (2012). "Bifurcation analysis of the flow patterns in two-dimensional rayleigh–bénard convection". In: *International Journal of Bifurcation and Chaos* 22.05, p. 1230018.

Phan-Thien, Nhan and Roger I Tanner (1977). "A new constitutive equation derived from network theory". In: *Journal of Non-Newtonian Fluid Mechanics* 2.4, pp. 353–365.

Plumley, Meredith and Keith Julien (2019). "Scaling laws in Rayleigh-Benard convection". In: *Earth and Space Science* 6.9, pp. 1580–1592.

Qi, Yunying (2002). "Investigation of relationships among microstructure, rheology, drag reduction and heat transfer of drag reducing surfactant solutions". PhD thesis. The Ohio State University.

Qi, Yunying et al. (2001). "Enhanced heat transfer of drag reducing surfactant solutions with fluted tube-in-tube heat exchanger". In: *International Journal of Heat and Mass Transfer* 44.8, pp. 1495–1505.

Qi, Yunying et al. (2003). "Enhancing heat transfer ability of drag reducing surfactant solutions with static mixers and honeycombs". In: *International Journal of Heat and Mass Transfer* 46.26, pp. 5161–5173.

Qian, Jin et al. (2013). "Experimental study on convection characteristics of crushed-rock layer". In: *Canadian geotechnical journal* 50.8, pp. 834–840.

Raji, A et al. (2013). "Natural convection heat transfer enhancement in a square cavity periodically cooled from above". In: *Numerical Heat Transfer, Part A: Applications* 63.7, pp. 511–533.

Rayleigh, Lord (1916). "LIX. On convection currents in a horizontal layer of fluid, when the higher temperature is on the under side". In: *The London, Edinburgh, and Dublin Philosophical Magazine and Journal of Science* 32.192, pp. 529–546.

Renardy, Michael and Yuriko Renardy (1992). "Pattern selection in the Bénard problem for a viscoelastic fluid". In: *Zeitschrift für angewandte Mathematik und Physik ZAMP* 43.1, pp. 154–180.

Reynolds, Osborne (1883). "XXIX. An experimental investigation of the circumstances which determine whether the motion of water shall be direct or sinuous, and of the law of resistance in parallel channels". In: *Philosophical Transactions of the Royal society of London* 174, pp. 935–982.

Robinson, Stephen K (1991). "Coherent motions in the turbulent boundary layer". In: *Annual Review of Fluid Mechanics* 23.1, pp. 601–639.

Roh, Sangeun et al. (2013). "Numerical study of transient natural convection in a pressurized LNG storage tank". In: *Applied Thermal Engineering* 52.1, pp. 209–220.

Rosenblat, S (1986). "Thermal convection in a viscoelastic liquid". In: *Journal of non-newtonian fluid mechanics* 21.2, pp. 201–223.

Rossby, HT (1969). "A study of Bénard convection with and without rotation". In: *Journal of Fluid Mechanics* 36.2, pp. 309–335.

Sano, M and Y Sawada (1984). "Chaotic attractors in Rayleigh-Benard systems". In: *Chaos and Statistical Methods*. Springer, pp. 226–231.

Sano, Masaki, Xiao Zhong Wu, and Albert Libchaber (1989). "Turbulence in helium-gas free convection". In: *Physical Review A* 40.11, p. 6421.

Schelter, William. "Maxima, a Computer Algebra System". In: (). https://maxima.sourceforge.io.

Shen, Y, Penger Tong, and K-Q Xia (1996). "Turbulent convection over rough surfaces". In: *Physical review letters* 76.6, p. 908.

Shishkina, Olga and Susanne Horn (2016). "Thermal convection in inclined cylindrical containers". In: *J. Fluid Mech* 790, R3.

Shraiman, Boris I and Eric D Siggia (1990). "Heat transport in high-Rayleigh-number convection". In: *Physical Review A* 42.6, p. 3650.

Siggia, Eric D (1994). "High Rayleigh number convection". In: *Annual review of fluid mechanics* 26.1, pp. 137–168.

Sokolov, M and RI Tanner (1972). "Convective stability of a general viscoelastic fluid heated from below". In: *The Physics of Fluids* 15.4, pp. 534–539.

Somasi, Madan et al. (2002). "Brownian dynamics simulations of bead-rod and bead-spring chains: numerical algorithms and coarse-graining issues". In: *Journal of non-newtonian fluid mechanics* 108.1-3, pp. 227–255.

Soong, CY et al. (1996). "Numerical study on mode-transition of natural convection in differentially heated inclined enclosures". In: *International Journal of Heat and Mass Transfer* 39.14, pp. 2869–2882.

Stevens, Bjorn (2005). "Atmospheric moist convection". In: *Annu. Rev. Earth Planet. Sci.* 33, pp. 605–643.

Stork, K and U Möller (1972). "Convection in boxes: experiments". In: *Journal of Fluid Mechanics* 54.4, pp. 599–611.

Sun, Chao et al. (2005). "Heat transport by turbulent Rayleigh-Bénard convection in 1 m diameter cylindrical cells of widely varying aspect ratio". In: *Journal of Fluid Mechanics* 542, p. 165.

Sureshkumar, R and Antony N Beris (1995). "Effect of artificial stress diffusivity on the stability of numerical calculations and the flow dynamics of time-dependent viscoelastic flows". In: *Journal of Non-Newtonian Fluid Mechanics* 60.1, pp. 53–80.

Takeuchi, Hiromi et al. (2007). "Successful 65% reduction in the energy consumption of a circulating pump by using a surfactant". In:

Taylor, GI (1935). "Statistical theory of turbulence, in Proceedings of the Royal Society of London A: Mathematical, Physical and Engineering Sciences". In:

Toms, Be A (1948). "Some observations on the flow of linear polymer solutions through straight tubes at large Reynolds numbers". In: *Proc. of In. Cong. On Rheology, 1948* 135.

Torres, Juan F et al. (2015). "Transition from multiplicity to singularity of steady natural convection in a tilted cubical enclosure". In: *Physical Review E* 92.2, p. 023031.

Trebotich, David, Phillip Colella, and GH Miller (2005). "A stable and convergent scheme for viscoelastic flow in contraction channels". In: *Journal of Computational Physics* 205.1, pp. 315–342.

Tsai, Wan-Chi and Gregory H Miller (2014). "Numerical simulations of viscoelastic flow in complex geometries using a multi-mode Giesekus model". In: *Journal of Non-Newtonian Fluid Mechanics* 210, pp. 29–40.

Tsukahara, Takahiro et al. (2011). "DNS study on viscoelastic effect in drag-reduced turbulent channel flow". In: *Journal of Turbulence* 12, N13.

Vaithianathan, T et al. (2006). "An improved algorithm for simulating three-dimensional, viscoelastic turbulence". In: *Journal of non-newtonian fluid mechanics* 140.1-3, pp. 3–22.

Velte, Waldemar (1964). "Stabilitätsverhalten und verzweigung stationärer Lösungen der navierstokesschen gleichungen". In: *Archive for Rational Mechanics and Analysis* 16.2, pp. 97–125.

Venturi, Daniele, Xiaoliang Wan, and George Em Karniadakis (2010). "Stochastic bifurcation analysis of Rayleigh-Bénard convection". In: *Journal of fluid mechanics* 650, p. 391.

Vest, Charles M and Vedat S Arpaci (1969). "Overstability of a viscoelastic fluid layer heated from below". In: *Journal of fluid Mechanics* 36.3, pp. 613–623.

Wang, Qi et al. (2018). "Flow reversals in two-dimensional thermal convection in tilted cells". In: *Journal of Fluid Mechanics* 849, pp. 355–372.

Wei, Ping, Rui Ni, Ke-Qing Xia, et al. (2012). "Enhanced and reduced heat transport in turbulent thermal convection with polymer additives". In: *Physical Review E* 86.1, p. 016325.

Xie, Yi-Chao et al. (2015). "Effects of polymer additives in the bulk of turbulent thermal convection". In: *Journal of Fluid Mechanics* 784.

Xu, Guoqiang, Jiandong Ding, and Yuliang Yang (1997). "Monte Carlo simulation of self-avoiding lattice chains subject to simple shear flow. I. Model and simulation algorithm". In: *The Journal of chemical physics* 107.10, pp. 4070–4084.

— (2000). "Monte Carlo simulation of self-avoiding lattice chains subject to simple shear flow Part II. Three-dimensional results and comparison with experiments". In: *Polymer* 41.9, pp. 3289–3295.

Yanagita, Tatsuo and Kunihiko Kaneko (1995). "Rayleigh-Bénard convection patterns, chaos, spatiotemporal chaos and turbulence". In: *Physica D: Nonlinear Phenomena* 82.3, pp. 288–313.

Yang, Liu and Kai Du (2019). "A comprehensive review on the natural, forced, and mixed convection of non-Newtonian fluids (nanofluids) inside different cavities". In: *Journal of Thermal Analysis and Calorimetry*, pp. 1–22.

Ye, Ting et al. (2019). "Smoothed particle hydrodynamics (SPH) for complex fluid flows: Recent developments in methodology and applications". In: *Physics of Fluids* 31.1, p. 011301.

Yu, Bo and Yasuo Kawaguchi (2004). "Direct numerical simulation of viscoelastic drag-reducing flow: a faithful finite difference method". In: *Journal of Non-Newtonian Fluid Mechanics* 116.2-3, pp. 431–466.

Zaleski, S (1998). *Geophysical and astrophysical convection*.

Zhang, Hong-Na et al. (2016). "Characteristics and generation of elastic turbulence in a three-dimensional parallel plate channel using direct numerical simulation". In: *Chinese Physics B* 25.9, p. 094701.

Zhu, J and W Rodi (1991). "A low dispersion and bounded convection scheme". In: *Computer Methods in Applied Mechanics and Engineering* 92.1, pp. 87–96.